MODIFIED METAL OXIDE NANOMATERIALS FOR ENVIRONMENTAL AND ENERGY-SAVING APPLICATIONS

Thesis Submitted to the University of Calicut for the Award of

DOCTOR OF PHILOSOPHY IN CHEMISTRY

By

DEEPAK JOSHY

Under the Supervision of

Dr. Pradeepan Periyat
(Guide)
&
Dr. Yahya A.I.
(Co-guide)

DEPARTMENT OF CHEMISTRY

UNIVERSITY OF CALICUT

KERALA-673 635

JANUARY 2024

Dedicated to

My Amma

"All that I am, or hope to be, I owe to my Amma"

KANNUR UNIVERSITY

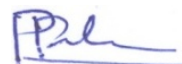## DEPARTMENT OF ENVIRONMENTAL STUDIES

Mangattuparamba Campus

Kannur University (PO); Mangattuparamba, Kannur, Kerala - 670567

Tel: 0497 2781043; E-mail : pperiyat@kannuruniv.ac.in

Certificate

This is to certify that the thesis entitled **"Modified Metal Oxide Nanomaterials for Environmental and Energy-saving Applications"** submitted by **Deepak Joshy** to the University of Calicut for the award of the degree of **Doctor of Philosophy** in Chemistry, is a record of precise research work carried out at the Department of Chemistry, University of Calicut under my guidance and supervision. The contents of the thesis have been checked for plagiarism using the software 'iThenticate' and the similarity index falls under the permissible limit. I further certify that the thesis or part has not previously formed the basis for the award of any degree, diploma or associateship of any other University or Institute.

I also certify that the adjudicators have not suggested any changes/corrections in this thesis and recommend to accept in the present form.

Dr. Pradeepan Periyat

(Guide)
Associate Professor
Department of Environmental Studies
Kannur University

Kannur University

Certificate

This is to certify that the thesis entitled **"Modified Metal Oxide Nanomaterials for Environmental and Energy-saving Applications"** is an authentic report of the precise research work carried out by **Deepak Joshy** under my guidance and supervision for the award of the degree of **Doctor of Philosophy** in Chemistry under the faculty of Sciences, University of Calicut, Kerala. The contents of the thesis have been checked for plagiarism using the software 'iThenticate' and the similarity index falls under the permissible limit. I further certify that the thesis or part has not previously formed the basis for the award of any degree, diploma or associateship of any other University or Institute.

I also certify that the adjudicators have not suggested any changes/corrections in this thesis and recommend to accept in the present form.

Dr. Yahya A.I.
(Co-Guide)
Associate Professor
Department of Chemistry
University of Calicut

Calicut University

DECLARATION

I, **Deepak Joshy**, hereby declare that the thesis entitled **"Modified Metal Oxide Nanomaterials for Environmental and Energy-saving Applications"** submitted to the University of Calicut is a bonafide record of the research work done by me under the joint supervision of **Dr. Pradeepan Periyat** (Guide), Associate Professor, Department of Environmental Studies, Kannur University, and **Dr. Yahya A. I.** (Co-guide), Associate Professor, Department of Chemistry, University of Calicut, in partial fulfillment of the requirements for the award of the degree of Doctor of Philosophy in Chemistry under the Faculty of Sciences, University of Calicut, Kerala. The contents of this thesis have not been presented previously for the award of any Degree/Diploma in any other University or Institution.

Calicut University   **Deepak Joshy**

Acknowledgement

The completion of this thesis happened as a result of the constant support, guidance and contributions of many remarkable individuals with whom I crossed paths in my life. These are people who have influenced me with their affection, encouragement and guidance at various points in my life especially during the last five years and here is my chance to express my affection and gratitude to them. Foremost, I would like to acknowledge my sincere gratitude to my research supervisor, Dr. Pradeepan Periyat for the continuous support, guidance and patience shown to me. I am indebted to his expertise, valuable feedback and motivation. I am grateful for the freedom and research ambience provided by him. Above all, I admire him for his humble and kind nature. I was very fortunate to receive him as my research guide and my research journey would not have been this smooth without his guideship.

I would like to convey my heartfelt gratitude to my research co-guide Dr. Yahya A.I, Associate Professor, Department of Chemistry, University of Calicut for his unwavering support and encouragement. I am indebted to his valuable suggestions and motivation. I thank him for treating me as one of his students and for helping me at various stages of my research. I would like to thank Dr. Rajeev S. Menon, Head of the Department of Chemistry, University of Calicut for his support. Besides, my sincere thanks to the former HODs of the Department. I would also like to use this occasion to express my gratitude to Dr. Abraham Joseph, Dr. P. Raveendran and Dr. N. K Renuka for their valuable suggestions and encouragement. I would like to extend my gratitude and respect to all the present faculty members of the Department. I am grateful to all my

affection to Martin, Roshima and Kichu for their love and support. I am indebted to all the researchers of the Department of Chemistry for their kind words and generosity. I would like to announce my fondness and thankfulness to every individual, whose kind words or gestures influenced me throughout my entire life.

I thank the One, who made me believe in magic. I am so glad our paths crossed and you are the best thing that has ever happened to me in all possible ways. Thank you for everything you do and for everything you are to me.

I am eternally indebted to Papa and my sister Silpa for their love and for always having my back. I am forever grateful to my grandmother for her prayers and endless affection.

"All that I am, or hope to be, I owe to my Amma". Amma, for all the times I didn't thank you enough. There are no words to describe how much admiration and appreciation I have for you. Today I thank you for all you have done for me, for everything you gave me and for walking this journey with me. Above all, I thank you for being my greatest inspiration and strength. Finally, I would like to convey my deepest gratitude to everybody whose prayers, kind words and support led to the completion of this thesis.

Above all, I thank God for all the goodness and strength I have received throughout my life.

I am concluding the acknowledgement with the strong belief that the highest form of appreciation is not to utter words but to live by them.

Deepak Joshy

Table of Contents

Preface

Two of the most important aspects determining our planet's future are energy and the environment. The fundamental building blocks of a habitable world will be how we restore and conserve our energy resources and environment. The environmental and energy domains present the most significant concerns to the global community. Drawing inspiration from the Sustainable Development Goals (SDGs) of the United Nations, this thesis attempts to address environmental and energy-related issues, in particular, SDGs 6 and 7 are highlighted. SDG 6 focuses on access to clean water and sanitation, while SDG 7 strives to provide affordable, clean energy to everyone. The thesis has been subdivided into two sections since it covers objectives relating to the environment and energy. The environmental objective involves attempts to develop efficient water treatment strategies based on adsorption and Fenton-like catalysis. The energy objective is directed towards the development of Near Infrared Reflecting (NIR) cool pigments capable of minimizing the energy spent on cooling purposes in buildings. The present thesis elaborates on employing nanomaterials as an aid to achieve sustainable development of the entire global community. The evolution of affordable and efficient water treatment technologies can improve the living conditions of people in underdeveloped countries. Again, the transformation to a sustainable global community requires the complete shift of our energy practices to renewable ones. This shift towards renewables requires large-scale financial investment and technological backup.

Underdeveloped countries lack the financial and technological resources to keep up with developing countries in the transformation towards renewable energy-based communities. In that case, energy conservation utilizing NIR reflecting inorganic pigments can contribute towards financial gain and reduce the consumption of fossil fuels. Thus, efficient and affordable water treatment strategies and NIR reflecting cool pigments can boost underdeveloped and developing countries in their progression towards a sustainable global society.

The present thesis discusses the application of modified metal oxide nanomaterials as adsorbents, Fenton-like catalysts and NIR-reflecting inorganic pigments. The metal oxides under investigation are CeO_2, MnO_2, Fe_3O_4, ZnO and $TiZn_2O_4$. Modifications were brought about by doping other metal ions, varying synthetic methods and conditions. These metal oxides were used individually or in combination to achieve potential environmental remediation and energy-saving applicability. The developed nanostructures were characterised well and their performances as well as durability were evaluated in detail.

The present thesis comprises seven chapters. A brief introduction to sustainable development is provided in Chapter 1, which also goes into great detail about the strategies used to achieve sustainability. A brief overview of nanoparticles and their characteristics is presented here. Applications of nanomaterials in the fields of environmental remediation and energy were thoroughly examined. The literature available so far has been examined to learn more about the applications of nanoparticles in water treatment

with a focus on Fenton-like catalysts and adsorbents. Additionally, energy-related applications of nanomaterials were included and notable research results were emphasized. Among the many energy-related uses for nanomaterials, the potential for energy saving of NIR reflecting cool pigments was thoroughly discussed. This chapter contains a review of the research on NIR-reflecting inorganic pigments with exceptional solar reflectance and colour properties. An overview of the materials and methods utilised in the investigations can be found in Chapter 2.

The environmental objective of the present thesis is covered in Chapters 3, 4, and 5. The synthesis of surface basicity-enhanced CeO_2 adsorbents for water treatment using sol-gel and sol-hydrothermal techniques is reported in Chapter 3. The CeO_2 lattice was doped with Er^{3+} ions to improve the surface basicity. CO_2-TPD tests were used to assess the surface basicity enhancement and identified a correlation between it and Er^{3+} doping. The rapid and selective adsorption of Congo red by modified CeO_2 was examined, and an adsorption mechanism was put forth. Thus chapter 3 establishes the utility of surface-active sites as a tool for controlling the selectivity and efficiency of an adsorbent material.

The creation of novel adsorbent material with efficient selective adsorption and magnetic recovery is explored in Chapter 4. The resulting core-shell nanostructure consisted of Fe_3O_4 cores enclosed in a mesoporous Mg^{2+} doped CeO_2 shell. A thorough analysis was conducted to determine the synthesized Fe@CMg-1:2 core-shells selectivity towards malachite green. A mechanism for the selective adsorption of malachite green was also proposed. For the

removal of dangerous malachite green from water, Fe@CMg-1:2 core-shells are proven to be extremely effective, economical, selective, stable, reusable, and magnetically retrievable adsorbent materials.

The recycling of spent zinc-carbon batteries into nanostructures that can act as both Fenton-like catalysts and adsorbents is discussed in Chapter 5. Only spent zinc-carbon batteries were used to produce the core-shell nanostructures, which are made up of mesoporous ZnO surrounding a core composed of MnO_2 and Fe_3O_4 nanoparticles. Four distinct dye contaminants were studied in relation to the created nanostructure's adsorption and Fenton-like catalytic activity. A thorough discussion was held on the mechanisms of adsorption and Fenton-like catalytic activity of the produced zinc-carbon battery derived nanostructures. It was determined that the produced adsorbent/catalyst's stability and reusability made them appropriate for practical applications. Here, waste management and water treatment were combined from a circular economic standpoint.

In Chapter 6, which is associated with the energy-saving objective of the present thesis, the design and development of NIR reflecting inorganic pigments based on $TiZn_2O_4$ inverse spinels is reported. Using a solution combustion process based on citric acid, a range of NIR reflecting inorganic pigments with colours spanning from greenish yellow to reddish brown were produced. Thermal shielding and stability experiments were conducted to assess the resulting pigment composition's practical usefulness. It is also important to highlight the developed cool pigment's stability,

affordability, and environmental friendliness. The newly developed NIR reflecting pigments have the advantage of being energy-efficient, and over time, this feature can support sustainable development. A summary of the entire research work is provided in Chapter 7, along with an outlook for the future.

List of Figures

List of Tables

List of Abbreviations

SDG	Sustainable Development Goals
NIR	Near Infrared
HPLC	High Performance Liquid Chromatography
GC-MS	Gas Chromatography-Mass Spectrometry
CA	Cellulose Acetate
PAN	Polyacrylonitrile
PA	Polyamide
DSSC	Dye Sensitized Solar Cells
QDSC	Quantum Dot Sensitized Solar Cells
ASTM	American Society for Testing and Materials
CIE	Commission Internationale de l'éclairage
XRD	X-Ray Diffraction
DRS	Diffuse Reflectance Spectroscopy
FE-SEM	Field Emission-Scanning Electron Microscopy
HR-TEM	High Resolution-Transmission Electron Microscopy
XPS	X-ray Photoelectron Spectroscopy
TPD	Temperature Programmed Desorption
BET	Brunauer–Emmett–Teller
VSM	Vibrating Sample Magnetometer
TGA	Thermogravimetric Analysis
DTA	Differential Thermal Analysis
MG	Malachite Green
MB	Methylene Blue
RB	Rhodamine B
MO	Methyl Orange
CR	Congo red
AOP	Advanced Oxidation Process
LC-MS	Liquid Chromatography-Mass Spectrometry
IP	Isopropanol
CF	Chloroform
TOC	Total Organic Carbon
PPCP	Pharmaceuticals and Personal Care Products

Chapter 1

Introduction and Literature Review

The introduction section emphasizes the need for sustainable development of the entire global community. It highlights the way in which the economically weaker sections of the global population can progress towards sustainability with the help of nanoscience. Two of the crucial factors for sustainable development are clean water and affordable clean energy. From the perspective of sustainable development goals adopted by the United Nations, the possible contributions of metal oxide nanomaterials towards environmental and energy-saving aspects are briefly described here. Literature surveys on adsorbents, Fenton-like catalysts and Near Infrared (NIR) reflecting inorganic pigments are also incorporated in this chapter.

"Our biggest challenge in this new century is to take an idea that seems abstract – sustainable development – and turn it into a reality for all the world's people."

— Kofi Annan

Moving on to the 21st century the world is facing substantial transformations in various fields at a never-before-seen pace. At the same time, we have growing uncertainties regarding the course of our progress. The mankind is going through a period of hope and uncertainties. On one side, we have improved social scenarios, dissolving boundaries and better living standards and on the other hand we are approaching a limit to our growth in terms of environmental aspects and natural resource utilization. We can have high expectations on the course of progress of the global community, as we look into the enhanced literacy rates, reduction in poverty, reduced infant mortality rate, and increased life expectancy. In contradiction to this, environmental constraints, depletion of non-renewable resources, and energy crisis make our trail to the future unsure and full of emerging risks.

Energy and environment are two of the crucial factors deciding the fate of our planet. How we conserve and replenish energy sources and the environment will form the very basis of an inhabitable earth. Among the challenges faced by the global society, the prime ones belong to the domain of energy and environment. The major environmental concerns of the 21st century involve pollution, over population, climate change, global warming, biodiversity loss, natural resource depletion, increased carbon footprint, and waste

management. The extent of contamination of air, water, and soil is increasing at an alarming rate. In addition, pollution emerges as a result of unchecked agricultural practices, plastic disposal, inefficient waste management methods and also from unrestricted mining. Swelling population, unrestricted use of fossil fuels and widespread industrialisation in developing countries are the main contributors to pollution. The greenhouse gas emissions from fossil fuel usage leads to global warming which in turn results in increased atmospheric temperature, melting of solar ice caps, rising sea levels and ocean acidification. The expanding population and widespread industrialisation played crucial roles in accelerating pollution rates. The extent of pollution largely affected the availability of clean air and water. Clean air and water form the most fundamental requirements of living organisms. United Nations has chosen clean water and sanitation as the 6th sustainable development goal (SDG) among the 17 global goals to be achieved by 2030 to end poverty, protect the planet, and ensure prosperity and well-being for all[1-3]. According to the SDG 6 progress report by the United Nations, 2.3 billion people live in water-stressed regions and 733 million of these 2.3 billion live in critically water-stressed countries[4]. The report clearly indicates that 26% of the world's population doesn't have access to safely managed drinking water[4]. UN Water which coordinates United Nations work on water and sanitization, has declared water as a finite or scarce resource. With a growing population and resource-intensive economic development, the demand for water has reached unprecedented levels. A balance between demand and supply of water should be maintained to ensure its accessibility to all. The quantity as well as the quality of

the water resources should be ensured to achieve sustainable water management. Efficient and affordable water treatment strategies can contribute much towards sustainable water management. Polluted water upon being efficiently treated can be added to the existing supplies of clean water, which in turn will meet the increasing demands. Novel and alternative water treatment techniques which are affordable, efficient, and easy to use are inevitable to ensure clean water accessibility on a global scale.

Now as we look into the energy concerns, the energy demand of the global community has reached unexpected levels. A major share of the total energy consumed by the world's population comes from fossil fuels. The unrestricted usage of fossil fuels is already causing the accumulation of greenhouse gases in the atmosphere, causing global warming and climate change. In addition to this, if the overutilization of fossil fuels continues, eventually we will run out of fossil fuel reserves which will lead us to a serious energy crisis. To prevent the depletion of non-renewable energy resources and significant climate changes, an overall change in our energy production habits is inevitable. Foreseeing this scenario, a transformation towards renewable energy resources is being promoted on a global scale. The present energy sector is actually going through this remarkable transformation into a sustainable energy environment. However, fundamental shift in energy production practices is a time-consuming process due to geopolitical, social, and economic constraints. According to the United Nations Department of economic and social affairs, 675 million people on a global scale live in the dark without access to

energy services[5]. Again, one in four people will still be using unsafe and traditional cooking systems by 2030. Clean and affordable energy to everyone by 2030 is the 7th goal among the sustainable development goals announced by the United Nations[6]. According to the Sustainable Development Goals report 2023, the energy efficiency improvement rate is found to be 1.4% whereas the rate required to attain clean and affordable energy by 2030 is 3.4%[5]. The report also reveals that, even though modern renewables constitute 30% of the total electricity generated, their contributions towards heating and transport purpose are only 10.4 % and 4 % respectively. The share of modern renewables in heat and transport should be increased further. As per the current scenario, the world is not on track to achieve this clean and affordable energy goal by 2030 due to the fiscal deficit caused by the Covid-19 crisis. To deal with the scenario, in addition to the wide-scale establishment of modern renewable energy resources, energy conservation and energy efficiency improvement strategies should be followed. A large number of energy-saving practices are already in practice which include the use of energy-efficient appliances and LED lamps, efficient interior heating and cooling technologies, promoting the use of public transport, maximum utilization of daylight and energy-saving building architectures. Globally almost 20% of the energy consumed in a building is used for cooling its interior[7]. Almost 10 % of the total world electricity consumption has been estimated to be used up for maintaining optimum interior temperatures. With the rising atmospheric temperature, the energy consumption for space cooling purposes will be thrice that of now by the year 2050[7, 8]. What if we were able to provide cooler interiors to buildings without

much energy consumption? Here comes the significance of Near Infrared (NIR) reflecting inorganic pigment coatings which can reflect heat from solar radiation[9, 10]. Such cool roofing and walls can save a large amount of energy spent for space cooling purposes. Since the transformation to a modern renewable energy-based sustainable society has been slowed down by economic and geopolitical constraints, any effort to minimise energy consumption is noteworthy. The developing and under developed countries can rely more on energy conservation tactics while slowly shifting to renewable energy practices. Thus, affordable NIR reflecting inorganic pigments capable of ensuring cooler interiors can contribute much towards energy conservation, which in turn can help in achieving the goal - clean and affordable energy to all.

1.1 Nanotechnology – A solution to emerging energy and environmental concerns

Modern science is the only prevailing answer to the energy and environmental concerns we are facing nowadays. Only scientific knowledge and its implementation can bring about remarkable changes to the conventional energy and environmental habits. Widespread research is going on in various fields of science to address the emerging concerns in the fields of energy, environment, and sustainable development. The field of Chemistry has already made immense contributions in the transformation towards sustainable society and will continue to contribute further through the ongoing and future research. Nanotechnology forms the core of

energy and environmental related research and novel discoveries. Nanotechnology as well as nanomaterials has got a wide range of applications in almost all aspects of human life.

In this work, of all the known applications of nanomaterials, we are focusing on energy-saving and environmental remediation applications of nanomaterials.

1.2 Why nanomaterials

The scientific community has been witnessing the developments in nanomaterials for a long time. Ever since the evolution of nanotechnology, it gained enough scientific attention from various fields. Even though various other fields of science emerged recently, with highly sophisticated advancements, the importance of nanomaterials remained the same. This is because every new development in the field of materials science has something to do with nanotechnology. So, nanomaterials form an inevitable component in materials research.

Nanomaterials evolved as a part of humankind's efforts to mimic natural systems. The transition of materials from bulk to nano scale happened as a result of this nature-inspired quest. As we all know, what makes nanomaterials unique compared to their bulk analogues is their size itself. It can be seen that most of the natural processes or biologically derived products are the results of sequences happening at an atomic or molecular level. Such precise build-up of atomic components is responsible for the unmatched efficiency and perfection of natural phenomena. Adopting and incorporating this bottom-up method from nature into material

synthesis resulted in functional materials with better efficiencies and excellent properties. Such atomic and molecular assemblies often fall within the nano regime. Assembling, manipulating, and controlling matter at the nanoscale is nothing but nanotechnology. Using nanotechnology, even highly efficient complex systems can be made by controlled assembly of atoms and molecules. Such nano assemblies will be controlling every aspect of life within a few years. Advanced nanomaterials have got profound influence on energy and environmental sectors. The development of a sustainable society requires an agreement between energy and the environment. Nanomaterials can improve renewable energy production, storage, transmission, and conservation. At the same time, environmental degradation caused by conventional energy production and resource over-exploitation can be addressed properly by nanotechnology.

1.3 Brief history of nanomaterials

Nanomaterials can be found throughout human history in various forms. The Lycurgus cup made by Romans contained nanoparticles of gold and silver and the cup appeared in different colours when illuminated from the inside and the outside. Traditional medicinal systems including Ayurveda had incorporated gold into medicinal preparations. Michael Faraday prepared the earliest form of nanomaterials i.e. colloidal gold in 1856 and named it as 'divided metals'[11]. The inhibition of bacterial growth by fine particles of metallic gold was discovered by Robert Koch in 1890[12]. The concept of nanometre was first introduced by the 1925 chemistry Nobel laureate Richard Zsigmondy, who also

measured for the first time the size of nanoparticles using a microscope[13]. The famous talk delivered by the American physicist Richard Feynman in 1959 at the annual meeting of the American Physical Society titled "There's plenty of room at the bottom" marked the beginning of modern nanotechnology[14]. Japanese scientist Norio Taniguchi was the first to coin the word nanotechnology[15]. The discovery of photocatalytic decomposition of water using TiO_2 in 1972 by Honda and Fujishima was another milestone in the history of nanotechnology[16]. The invention of the scanning tunneling microscope in 1981 was another major breakthrough in the history of nanotechnology[17]. The subsequent development of different scanning probe microscopes helped to observe and manipulate matter at atomic and molecular levels. Further developments in the field of nanotechnology involved the discovery of fullerene in 1985 by Sir Harold W. Kroto, Richard E Smalley, and Robert F. Curl[18]. Later in 1991, Sumio Iijima discovered carbon nanotubes which further fuelled the nanomaterial research[19, 20]. Measures to reduce the space consumed by devices and functional materials is the main objective of present nanotechnology.

1.4 Applications of nanomaterials

The transition of bulk matter into nano dimensions is always accompanied by changes in their physical, chemical, and biological properties. Investigations into the nano realm often help to acquire additional knowledge of material properties. The incorporation of this acquired knowledge into material synthesis results in functional materials with enhanced efficiencies and properties. Such material

manufacturing methods can have a significant influence on all aspects of human life. Most of the critical challenges faced by the human community can be addressed through nanotechnology. The gap between society and technology can be bridged with the help of nanoscience. Nanotechnology known as the future science has got profound influence on economic growth, human health, and sustainability.

Good food, clean water and air, energy and environmental sustainability, and efficient diagnostic technologies are the various sectors where nanotechnology can play a potential role. In 21st century, the scientific priorities of nations are based on nanotechnology. So, exploiting the potential market value of nanomaterials is nothing but the all-round development of the global community. The most important energy and environmental applications of nanomaterials are discussed here.

1.4.1 Environmental applications

The advent of globalization, industrialization, and lifestyle changes marked the beginning of large-scale environmental deterioration. The extensive spread of industrial units along with the excessive exploitation of natural resources caused the increased rate of environmental degradation. Human interventions into the environment without ensuring sustainability were responsible for this hazard. It took several years for the humankind to recognise the emerging environmental concerns as well as the rapid rate of pollution. High energy demand and overpopulation fuelled environmental pollution to a higher level irrespective of all the measures taken to control the pollution rate. Conventional methods

and treatments were found ineffective to deal with this environmental crisis. Climate change and natural resource depletion made people to rethink on their environmental concerns. Later the concept of sustainable development came up with an objective of environmental protection.

As a part of it, the identification and effective utilisation of renewable energy sources as an alternative was suggested. Again, industrial processes were designed in an ecofriendly manner with no malign byproducts. Replacement of harmful components from daily use devices is another solution. Thus, several efforts were made to minimize the extent of pollution. In addition to this, subsequent removal of pollutants from air, water, and soil is also important. Clean water, air, soil, and food can be ensured only by sustainable modes of development.

In order to monitor, regulate, and eliminate pollution, affordable and efficient technologies are required. Nanotechnology is an important tool for environmental remediation. Proper design and employment of nanomaterials can significantly regulate pollution. Here are some of the environmental applications of nanomaterials.

1.4.1.1 Nanosensors

Effective environmental remediation is possible only when the extent of pollution is constantly monitored. Since there are large numbers of natural resources susceptible to pollution, costly methods of pollution monitoring are difficult to afford. Techniques like high-performance liquid chromatography (HPLC), Gas chromatography-mass spectroscopy (GC-MS), Capillary electrophoresis are very effective in monitoring pollution. However,

these are expensive techniques that are not affordable for wide-scale applications. The need for more cost-effective and efficient monitoring methods paved the way for nanosensors. The progress achieved in the field of nanotechnology helped developing large number of nanomaterials that can effectively sense and monitor a wide range of pollutants[21, 22]. These nanosensors are highly sensitive and selective to contaminants present in aqueous and gaseous systems[23]. Often nanosensors are two component systems consisting of a receptor and a transducer. The receptor controls the sensitivity while the transducer uses its electrochemical, optical, or thermal properties to sense the contaminant. The mechanism involved is a charge transfer between the pollutant species and the receptor which manifests as an optical, electrical, or thermal signal that can be detected[24]. Some of the examples for nanosensors include quantum dots [25-29], which use their fluorescence properties, metal nanoparticles[30-33] which employ their optical properties and carbon nanotubes which use their electrochemical properties[34-37]. Since the physical, chemical, optical, magnetic, and electronic properties of nanomaterials can be tuned effectively, they are promising candidates for application as nanosensors for the detection of chemical and biological components.

1.4.1.2 Nanomembranes

Water treatment and purification using nanomembranes for filtration is another mode of environmental remediation. The effectiveness of membrane processes lies in factors such as high separation capacity and convenient operation[24, 38]. Here no

chemical and thermal inputs are required for the filtration process. The membranes as such can be retrieved from the treated water and can be used again. The efficiency of the membrane process depends mainly on the membrane material. The selectivity and permeability of the membranes are the key deciding factors[39]. For water purification, the membrane should be permeable to water and less permeable to solutes and other pollutants[40, 41]. Membrane processes are classified into microfiltration[42], ultrafiltration[43], nanofiltration[44] and reverse osmosis[45, 46]. These classifications are based on the pore size, type of pollutants removed, and level of purification achieved. Microfiltration removes suspended solids, bacterial and protozoa contents. Virus removal can be achieved by ultrafiltration. Nanofiltration ensures the removal of heavy metals and organic pollutants while desalination is done by reverse osmosis. Commonly employed membranes are polymer membranes based on cellulose acetate (CA)[47], polyacrylonitrile (PAN)[48] and polyamide (PA)[49]. Nanomembranes are fabricated by the incorporation of nanomaterials into these polymer membranes[50]. Enhanced permeability, selectivity to particular species, self-cleaning ability and pollutant degradation capability of membranes can be achieved by either blending or surface decoration of nanomaterials[51, 52]. Nanofibrous membrane[53], nanocomposite membranes[54, 55] and osmotic membranes[56, 57] are the different types of nanomembranes. Nanofibrous membranes were developed by electrospinning method using materials like polymers [58-60], ceramics[61], metal oxides[62-64] etc. Electrospun nanofibrous membranes are capable for ultrafiltration and microfiltration. These

membranes can be functionalised further for the removal of heavy metals and organic pollutants[65-68]. Membrane fouling, i.e. deposition of impurities over the membrane, is an important factor that reduces the efficiency and lifetime of membranes[69]. Membrane fouling can be minimised by enhancing the hydrophilicity of the membrane [70-72]. Nanocomposite membranes were introduced with the objective of developing anti-fouling membranes[73-77]. Several modifications were reported for achieving hydrophilicity and reduced fouling. It included incorporation of MWCNT's[78-80], SWCNT's[81, 82] and photocatalysts like TiO_2[73, 83, 84]. Osmotic membranes are another important category for high-purity filtration application. Reverse osmosis[57, 85, 86] and forward osmosis membranes[87-89] are the two membrane types that fall under this category.

1.4.1.3 Adsorbents

The application of nanomaterials for the adsorptive removal of pollutants from water is more efficient and convenient than conventional adsorbents. Superiority of nanomaterial adsorbents arises due to their high surface area, large amount of surface active sites, and tunable pore structures[90]. The number of acidic, basic, and other functional sites on the nanomaterial surface can be controlled and can be tailored to target specific pollutants [91]. Even selective adsorptive removal can be carried out by suitable functional groups present on the surface[92, 93]. The cost effectiveness of the adsorptive removal technique can be ensured by the utilization of agricultural waste, biomass, and industrial

byproducts for the production of adsorbents[90]. Adsorbents mainly belong to either one of these categories

i)   activated carbon adsorbents

ii)   low-cost adsorbents

iii) natural adsorbents

iv)   agricultural wastes

v)   industrial wastes

vi)   biomass-based adsorbents

vii) nanoadsorbents

Nanoadsorbents are further classified into carbon-based nanoadsorbents[94, 95], boron nitride materials[96-98], metallic nanoparticles, metal oxide nanoadsorbents[99-101], spinel ferrite adsorbents[102-105], silicon nanomaterials, nanocomposite adsorbents[106-109], nanofibers, nanoclays, polymer-based nanomaterials, xerogels, and aerogels. The most widely employed carbon-based adsorbents are activated carbon [110-113], cabon nanostructures like carbon nanotubes (SWCNT's and MWCNT's)[106, 114-117], graphene[118-122] and graphene oxide[122-126]. Several modifications of boron nitrides were employed as adsorbents for a wide range of pollutants [127, 128]. Metal oxide nanoadsorbents such as ZnO[129-131], TiO_2 [132-136], CeO_2 and several spinel ferrites[137-140] were investigated thoroughly. If magnetic property can be incorporated into these adsorbents, the separation of adsorbents from treated medium becomes easy[141-144]. Several such magnetically separable metal oxide adsorbents were also introduced. The composites of these metal oxides with above mentioned adsorbent materials were also designed. Silicon-based nanomaterials for adsorption applications

include silicon nanotubes, silicon nanoparticles, and silicon nanosheets. Again, polymer composites like Fe_3O_4-coated polypyrrole (PPy) were found to be excellent adsorbents [145, 146]. The reinforcement of polymer materials can be acquired by the incorporation of inorganic materials into the polymer matrix. Such incorporations can facilitate higher chemical and mechanical stabilities in association with improved adsorption capacities. Nylon 6 is an example of a nanofiber adsorbent and montmorillonite (MMT) is an example of a nanoclay adsorbent. Large surface area and enhanced porous nature are characteristics of xerogels and aerogels. Various examples of xerogels include Silica and γ-alumina xerogels. Compared to xerogels, aerogels are superior in surface area and pore volume. Alumina and $CaCl_2$-doped SiO_2 aerogels are examples.

Among the different classes of adsorbents mentioned above, the widely employed metal oxide adsorbents are ZnO, TiO_2, Al_2O_3, MnO_2, MgO, Fe_2O_3, Fe_3O_4, and CeO_2. ZnO is a low-cost sorbent having high surface area and porous character. ZnO is used for the adsorption of cationic and anionic dyes, heavy metal ions and also for the adsorption of gaseous pollutants. The electrostatic attractions, surface functionalities, and high porosity are the crucial factors controlling the adsorption capacity of ZnO[131, 147]. In the case of TiO_2, the surface area, photoactivity, easy availability, and stability make it a potential photocatalyst material[134, 148-150]. Several works were reported in which TiO_2 can act both as an adsorbent and as a photocatalyst for pollutant removal. Non-toxicity, low-cost availability, enhanced surface area, and porous character make

Al_2O_3 a potential adsorbent material[151]. Arsenic and Fluorides are the major targeted pollutants for Al_2O_3 adsorbents.

High surface area, possible layer structure, and high redox potential are the characteristics of MnO_2 which makes it a potential adsorbent[152]. MnO_2 is found highly effective in adsorbing cationic dyes and cationic heavy metal ions such as Pb^{2+}, Cd^{2+}, Ni^{2+}, and As^{5+}[153].

MgO is another low-cost and eco-friendly adsorbent material used for the adsorptive removal of organic dyes like Congo red[110]. The most widely investigated iron oxides as adsorbents are α-Fe_2O_3, Fe_3O_4, and γ-Fe_2O_3. They are eco-friendly, easy to synthesize, abundant, and economically affordable adsorbents used for the adsorption of organic species as well as heavy metal ions.

1.4.1.4 Advanced Oxidation Processes

Advanced Oxidation Processes (AOPs) are a set of environmental friendly and highly effective modes of removing pollutants from water. AOPs involve the in situ generation of powerful oxidising species like hydroxyl radicals capable of effectively degrading persistent organic pollutants in wastewater. The oxidising agents such as hydroxyl radicals are generated in required amounts by various chemical, photochemical, electrochemical, and sonochemical means. Besides hydroxyl radicals, superoxide anion, hydrogen peroxide, and singlet oxygen can also be generated through AOP as secondary oxidising agents from primary oxidants such as ozone and hydrogen peroxide. The hydroxyl radicals formed through AOP are non-selective in nature towards pollutants and can degrade the contaminants by mainly three routes; electron transfer,

abstraction of hydrogen, and addition reaction between radicals. By making use of these pathways, hydroxyl radicals can easily degrade a wide range of organic and inorganic contaminants present in polluted waters. The main types of AOPs on the basis of reaction conditions are

    i)   Photocatalytic oxidation

    ii)   Fenton oxidation

    iii)   Photo-Fenton oxidation

    iv)   Fenton like oxidation

    v)   Electrochemical oxidation

    vi)   Ozonation

    vii)   UV/O_3

    viii) UV/H_2O_2

    ix)   Radiolysis

    x)   Sonolysis

Among the above mentioned AOPs, the electrical, ultraviolet, microwave, and ultrasonic field employed techniques require high energy and economic investment. Such techniques are therefore not widely adopted by the industry. In order to address the energy consumption and capital investment concerns, we have prioritized the development of AOPs which do not require expensive physical fields or the ones which can utilize sources such as solar energy. Several nanomaterials were developed with an objective of carrying out AOPs in a cleaner, affordable, and efficient manner. Based on the reaction conditions and nature of the materials they can fall into the categories of photocatalysts, Fenton catalysts, photo-Fenton catalysts and Fenton-like catalysts.

1.4.1.4.1 Photocatalysts

Photocatalysts were introduced as an innovative, efficient, low cost reusable, and environmental friendly method for water treatment[24]. Photocatalysts ensured minimum energy consumption and chemical utilization. Photocatalysts rely more on renewable energy sources such as solar energy. By utilizing the input energy, photocatalysts generate strong reactive species like hydroxyl and superoxide radicals which in turn degrade the non-biodegradable organic pollutants and pathogens[38]. Semiconductors are often used as photocatalysts and upon irradiation by light of certain energy, the photocatalyst generates holes and electrons having oxidation and reduction capacities. These generated holes and electrons participate in the pollutant degradation process as well as in the formation of other reactive oxygen species (ROS). Upon degradation, the pollutants are converted into harmless species like CO_2, H_2O etc. A wide range of nanomaterials are employed as photocatalysts. The easy tunability of band gap, high surface area to volume ratio and stability made nanomaterials suitable for photocatalytic applications[38, 154].

Heterogeneous photocatalysis also gained popularity as a water purification technique during the last few years. Among nanomaterials, the most widely investigated photocatalytic material is TiO_2[155]. Tunable band structure, non-toxicity, low cost, and easy availability of TiO_2 made them efficient candidates for organic pollutant degradation and pathogen removal[150, 156]. One of the major limitations of TiO_2 is that they can utilise only 5% of incoming solar radiation. To offset this low solar absorption, several modifications were made to TiO_2. It includes doping of cations and

anions [148, 149, 157-160], formation of heterojunctions[161-167] and composites[168-172] with other nanomaterials, and morphology modification[173-176] (several morphologies like nanotube[177-179], nanowire[180-183], nanorod[184-187], hollow spheres[188-191] etc. were investigated). There are a wide range of materials other than TiO_2 showing photocatalytic behaviour. WO_3[192-195], ZnO[196-201], $SrTiO_3$[202-204] and CeO_2 [205-207] are some of the examples. Band gap engineering, surface area enhancement, amount of surface-active sites, and surface morphology are the possible factors through which photocatalytic efficiency can be tuned leading to the development of next-generation photocatalysts.

1.4.1.4.2 Fenton catalysts:

In 1894, a pioneering work by Henry John Horstman Fenton on the oxidative degradation of tartaric acid using Fe^{2+} and H_2O_2 paved the way for Fenton chemistry[208]. The mixture of Fe^{2+} and H_2O_2 was later known as Fenton's reagent. The Fenton reagent generates extremely reactive hydroxyl radicals having potential oxidising character. The involvement of a radical chain reaction in the Fenton process was first proposed by Haber and Weiss in the 1930s[209]. Even though the Fenton reagent was discovered in 1894, its application to organic pollutant removal was reported later[210, 211]. Hydroxyl radical initiated the mechanism of the Fenton reaction and the resultant degradation of organic pollutants was investigated in detail[212-214]. In short, the Fenton reaction involves a chain initiation (eqn. 1) and a termination (eqn. 2) steps[215, 216]. Again, it involves the reaction of Fe^{3+} with H_2O_2,

which is known as Fenton-like reaction (eqn. 3)[217]. The overall reactions involved in the Fenton process is given below[218-220].

$$Fe^{+2} + H_2O_2 \rightarrow Fe^{+3} + OH^\bullet + OH^- \tag{1}$$

$$Fe^{+2} + OH \rightarrow OH^- + Fe^{+3} \tag{2}$$

$$Fe^{+3} + H_2O_2 \leftrightarrow Fe-OOH^{+2} + H^+ \tag{3}$$

$$Fe-OOH^{+2} \rightarrow HO_2^\bullet + Fe^{+2} \tag{4}$$

$$Fe^{+2} + HO_2^\bullet \rightarrow Fe^{+3} + HO_2^- \tag{5}$$

$$Fe^{+3} + HO_2^\bullet \rightarrow Fe^{+2} + O_2 + H^+ \tag{6}$$

$$OH^\bullet + H_2O_2 \rightarrow H_2O + HO_2^\bullet \tag{7}$$
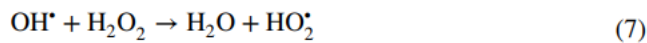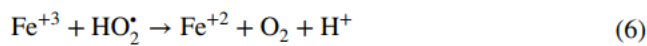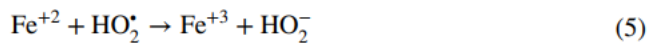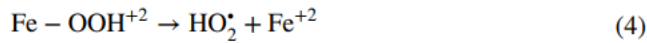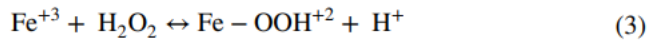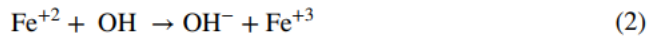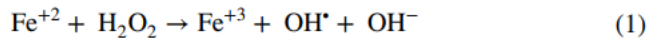
A simplified version of the mechanism is given by the equation

$$Fe^{+2} + H_2O_2 + 2H^+ \rightarrow 2\,Fe^{+3} + 2H_2O_2 \tag{8}$$
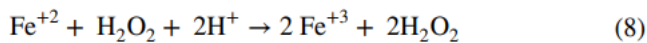
The formed hydroxyl radicals then react with organic contaminants to yield unstable radicals which further undergo oxidative degradation into secondary and tertiary metabolites.

The advantages of the Fenton process include easy and flexible operation, economic affordability, and minimum energy consumption[219, 220]. They can be easily incorporated into existing water treatment facilities. Fenton process has limitations too. The efficiency of the Fenton reaction depends on the dissolution of the Fe catalyst and an acidic pH near 3 which favours the dissolution[219]. When pH exceeds 4, the formed Fe^{3+} ions will get converted to Ferric hydroxide sludge. So, near neutral pH values are not suitable for the best performance of Fenton catalysts. Again, chemicals and additional expenses are required to maintain the

optimum pH conditions. Another drawback is the accumulation of iron sludge and secondary pollution arising from it. The recycling of iron sludge again requires additional expenses and time.

1.4.1.4.3 Photo- Fenton catalysts

Traditional Fenton processes experiences a limitation in their performance due to the deficient Fe^{3+}-Fe^{2+} reduction cycle[221]. The rate of oxidation of Fe^{2+} to Fe^{3+} by H_2O_2 occurs at a rate 10^4 times that of the reduction of Fe^{3+} to Fe^{2+} by H_2O_2. This will result in the accumulation of Fe^{3+} ions and the reaction rate retards as the Fe^{2+} ions are once consumed completely[222]. In order to address this limitation of the Fenton process, Photo Fenton reactions were introduced. A combination of Fenton reagents with UV-Visible light is employed here[222, 223]. The association of UV-Visible light with the Fenton reaction can yield more hydroxyl radicals through the photoreduction of Fe^{3+} to Fe^{2+} and through the photolysis of H_2O_2. The newly generated hydroxyl radicals and Fe^{2+} ions continue the Fenton cycle more effectively. There are several studies in which the Photo-Fenton reaction yields better degradation of organic contaminants[222-227]. Like Fenton reactions, Photo-Fenton processes are also pH dependent and favours pH values around 3[222]. Here UV irradiation can be replaced with solar radiation which makes the process cost-effective but less efficient.

1.4.1.4.4 Fenton-like catalysts

To overcome the drawbacks of the Fenton reaction, we have tried replacing Fe^{2+} with Fe^{3+} or other transition metal ions which lead to the foundation of Fenton-like catalysis[228, 229]. Fenton-like

catalysis can be of two types; homogeneous and heterogenous. Heterogeneous Fenton-like reaction involves the use of a solid catalyst containing Fe^{3+} or any other transition metal ion while homogeneous Fenton-like reaction employs metal ions other than Fe^{3+} or their complexes with organic ligands[228]. Heterogeneous Fenton-like catalysis was put forward with the objective of overcoming the limitations of Fenton reactions such as catalyst loss, iron sludge formation, and large chemical inputs. Insoluble forms of Ferric ions such as naturally occurring minerals are used mainly as Fenton-like catalysts[219]. A few examples include magnetite, haematite, maghemite, and pyrite[228]. Besides mineral forms, Fe^{3+} impregnated into various solid matrices of high surface area such as silica, zeolites, clay, etc. are also employed as Fenton-like catalysts[230]. The other transition metal ions capable of showing Fenton-like catalytic activity are Co, Mn, Cu, Cr, Ni, Al and Mg.

The heterogeneous Fenton-like catalysis involves three main steps. The first one is the adsorption of organic contaminants on the catalyst surface, the second step involves the generation of hydroxyl radicals and their attack on organic pollutants, and the third step is the desorption of degradation products from the catalyst surface[219, 229]. The adsorption occurring during the Fenton-like catalytic oxidation follows the Langmuir adsorption model and the rate of adsorption is controlled by the monolayer adsorption capacity of the catalyst[229]. Thus, surface area and porosity are the key factors determining the efficiency of catalytic degradation. Catalyst loading, pH, concentration of H_2O_2 and temperature are the controlling factors for Fenton-like catalytic oxidation[228]. The pH regulation into acidic conditions requires additional processing and

expenses. Also, the consequent leaching of active metal ions under acidic conditions results in decreased efficiency of the catalytic process[219, 228-230]. Thus, efforts are being made to improve the stability of Fenton-like catalysts without compromising their efficiencies. The chosen metal ions should exhibit multiple oxidation states which can promote the generation of hydroxyl radicals from H_2O_2. Also, these oxidation states should be stable over a wide pH range to avoid the loss of catalyst through metal leaching. The selected metal candidate should also resist hydration forces to remain insoluble during the catalytic process. The most widely employed metals in Fenton-like catalysis are Fe, Mn, Cu, and Ce.

Table 1.1- Some of the significant works in the field of Fenton-like catalysis where catalyst systems containing Fe^{3+} or other metal ions were employed.

Catalyst system	Targeted pollutant	Time taken	Percentage degradation	Reference
GO-Fe_3O_4	Acid orange 7	180 min	99%	[231]
δ-FeOOH	Methylene blue	120 min	100%	[232]
V-doped Fe_2O_3	Methylene blue	30 min	60%	[233]
$Fe_{2.79}Nb_{0.19}O_4$	Methylene blue	180 min	100%	[234]
Cu/$CuFe_2O_4$	Methylene blue	4 min	100 %	[235]

Fe_3O_4@SiO_2	Methylene blue	120 min	91 %	[236]
Fe_3O_4@C	Methylene blue	300 min	100 %	[237]
Au-Fe_2O_3@mesoporous SiO_2	Methylene blue	180 min	100 %	[238]
rGO/Fe_2O_3/polypyrrole	Methylene blue	80 min	100 %	[239]
Fe_2O_3-SiO_2	Methyl orange	20 min	98.5 %	[240]
Fe_3O_4/RGO	Methyl orange	60 min	94 %	[241]
$NiFe(C_2O_4)x$	Methyl orange	20 min	98 %	[242]
Fe_3O_4-MWCNTs	Orange II	30 min	94 %	[243]
Carbon aerogel-Fe	Orange II	120 min	100 %	[244]
Zeolite Y-Fe	Orange II	120 min	100 %	[245]
$BiFeO_3$	Rhodamine B	90 min	95.2 %	[246]
Fe_3O_4	Rhodamine B	120 min	98.9 %	[247]
CuFeZSM-5	Rhodamine 6G	120 min	100 %	[248]
Fe_3O_4/γ Al_2O_3	4-chlorophenol	180 min	100 %	[249]
Fe_3O_4/CeO_2	4-Chlorophenol	60 min	100 %	[250]
Fe_3O_4	2,4-Dichlorophenol	180 min	100 %	[251]
Fe_3O_4/MWCNT	Bisphenol A	360 min	97 %	[252]

Fe_3O_4	Catechol	180 min	100 %	[253]
$Fe_3O_4@SiO_2@Cu$	Acetaminophen	20 min	100 %	[254]
FeS_2	Chloramphenicol	24 min	83.3 %	[255]
FeS_2/SiO_2	Ciprofloxacin	60 min	100 %	[256]
FeCeOx	Diclofenac	40 min	84 %	[257]
Fe_3O_4	Ibuprofen	12 hours	80.1 %	[258]
Fe_3O_4/Mn_3O_4	Sulfamethazine	240 min	100 %	[259]
$MnFe_2O_4$	Norfloxacin	180 min	90.6 %	[260]
FeS_2	Alachlor	60 min	100 %	[261]
$Fe_3O_4/MWCNTs$	Atrazine	120 min	81.4 %	[262]
MnO_2	Methylene blue	0.3 hours	99 %	[263]
$Mn_3O_4/silicate$	Methylene blue	4 hours	100 %	[264]
$MnO_2-MWCNT$	reactive blue 19	3 hours	99 %	[265]
$Mn_3O_4-FeS_2/Fe_2O_3$	Orange II	60 minutes	99 %	[266]
Mesoporous MnOx	Norfloxacin	60 minutes	60 %	[267]
Cu-doped mesoporous silica	Ibuprofen	120 min	100 %	[268]
CuO nanoparticles	Enrofloxacin	4 hours	90 %	[269]
CuFe/ZSM-5	Rhodamine 6G	120 min	100 %	[248]

Cu–CuFe$_2$O$_4$/SiO$_2$	Methylene blue	120 min	98 %	[270]
Cu-Fe$_3$O$_4$@SiO$_2$	Acetaminophen	120 min	100 %	[271]
CeO$_2$	Acid orange 7	5 hours	90 %	[272]
FeCeOx	Rhodamine B	2.5 hours	90 %	[273]
Fe$_2$O$_3$-CeO$_2$	Sulfamerazine	120 min	70 %	[274]
Fe^0/CeO$_2$	Tetracycline	60 min	90 %	[275]

1.4.2 Nanomaterials for energy applications

The energy-related applications of nanomaterials involve energy production, storage, conversion, transmission, and conservation. In order to tackle with the increasing global energy demand and to ensure a sustainable energy habitat, the effective employment of nanotechnology is sufficient. The various stages present between the production and utilization of energy can be made more economical and sustainable with the help of nanomaterials. The significant contributions and recent advances made by nanotechnology, in each of these stages, are discussed here.

1.4.2.1 Energy production/conversion

Major energy production/conversion systems where nanomaterials found their applications are solar cells[276-284], fuel cells[285-290], thermo-electric[291, 292], piezo-electric[293, 294], and tribo-electric materials[295].

1.4.2.1.1 Solar cells

Being hailed as one of the most promising renewable energy sources, solar energy, and its exploitation are significantly important. Solar cells are one of the widely employed solar energy capture techniques available. Solar cells are generally classified into three generations. The first-generation solar cells are based on silicon p-n junctions. Practically silicon solar cells are constructed by diffusing an n-type dopant into one end of p-type silicon or vice versa. Silicon solar cells dominate the photovoltaic industry due to their high conversion efficiency (~27%) and solar absorbance[283, 284, 296, 297]. Later thin-film solar cells were introduced in an attempt to construct cost-effective and more efficient solar cells. Thin film solar cells are regarded as second-generation solar cells, even though they haven't achieved efficiency higher than first-generation [282, 298-300]. Further reduction in cost was achieved by third-generation solar cells such as dye-sensitized solar cells (DSSCs)[278, 279, 301, 302], quantum dot solar cells[280, 281] and polymer/organic solar cells[303, 304]. The efficiencies of third-generation solar cells are lower than silicon solar cells. DSSCs have the potential of being economically viable and technically relevant mode of photovoltaic energy conversion. Apart from conventional solar cells in which a semiconductor absorbs and transports charge carriers, DSSC's employs a sensitizer (dye) for light absorption and a semiconductor for charge transport. At the same time, quantum dots serve as the light-absorbing material in quantum dot solar cells (QDSCs)[280, 281]. An important advantage of QDSC's is that their bandgap can be easily tuned with respect to the choice of charge

carrier material. Organic/plastic solar cells employ conducting polymers or organic molecules for light absorption and charge transport. Another important class of solar cells is perovskite solar cells. Low cost, flexibility, increased diffusion length, and higher light absorption of perovskites are responsible for their high photovoltaic performance [276, 277, 305-310].

Nanomaterials find wide applications among third-generation solar cells, in which they are widely employed as photoanode and counter electrode materials. The overall performance of DSSCs depends strongly on the size, shape, morphology, and band gap of the electrode material employed. The most commonly employed electrode nanomaterials are metal oxides such as TiO_2[311, 312], ZnO[147, 313], SnO_2[314-316], WO_3[317, 318] and Nb_2O_5[319-321]. The electronic structure and stability of metal oxide photoelectrode materials can be modified by doping other elements[322-325]. Band edge modifications and electron mobility improvements were achieved with the help of doping[326]. Apart from efficiency and stability improvements, several efforts were made to increase the flexibility[327-330], transparency[331-333] and lightweightness[304, 334, 335] of solar cells. Wearable solar cell modules are also under development [328, 336-338].

1.4.2.1.2 Fuel cells

A Fuel cell is a device that converts the chemical energy evolved during a reaction into electricity with the evolution of heat and water as byproducts. The energy generation is based on a pair of redox reactions which involves a fuel (often hydrogen) and an

oxidising agent. Fuel cells attracted considerable attention due to their high efficiency, cleanliness, and cost effectiveness[339]. Fuel cell architecture consists of an anode and a cathode with an electrolyte layer in between. Hydrogen fuel is continuously supplied to the anode while oxygen is supplied to the cathode. Hydrogen ions generated at the anode are selectively transported by the electrolyte to the cathode. At the same time, electrons evolved flow through the external circuit and reaches the cathode. The protons and oxidant (oxygen) combine in the presence of electrons to form water[289, 290]. Fuel cell performance depends mainly on the electrode material and electrolyte. Based on the type of electrolyte employed, fuel cells are classified into Proton Exchange Membrane Fuel Cells (PEMFCs), Alkaline Fuel Cells (AFCs), Direct Methanol Fuel Cells (DMFCs), Phosphoric Acid Fuel Cells (PAFCs), Molten Carbonate Fuel Cells (MCFCs) and Solid Oxide Fuel Cells (SOFCs)[339]. Among these, Proton Exchange Membrane Fuel Cells (PEMFCs), Direct Methanol Fuel Cells (DMFCs) and Solid Oxide Fuel Cells (SOFC's) are the most promising ones.

1.4.2.2 Energy storage

The energy produced from renewable energy sources must be stored properly for the timely consumption. So, the development of low-cost and efficient energy storage solutions must go hand in hand with renewable energy production. Nanotechnology can help in developing efficient and stable energy storage materials which are ecofriendly and sustainable.

1.4.2.2.1 Batteries

Batteries are common energy storage devices which convert stored chemical energy into electrical energy. Batteries are nowadays the most widely commercialized energy storage devices[340]. Low power density and shorter life cycles are the main drawbacks of batteries. Better energy and power densities, extended lifetime and safety are the essential requirements for next-generation batteries[341]. Electrode materials and electrolytes are under continuous investigation for better performance and stability. The performance of electrodes depends on the active surface area available. Here comes the importance of nanoscale structures having a high surface-area-to-volume ratio. Nano electrode materials can thus achieve near theoretical storage capacity[342]. Different types of batteries where nanomaterials were employed include lithium-ion batteries [343-345], sodium-ion batteries [346-350], zinc-air batteries [351-353] etc. Several nanocomposites were also investigated for battery applications.

1.4.2.2.2 Supercapacitors

In order to account for the limitations of capacitors and batteries in energy storage, supercapacitors were introduced. Supercapacitors bridge the gap between batteries and ordinary capacitors[354]. Supercapacitors are known for their high power density, long cycle life, rapid charge-discharge, low-cost and safety[285]. Supercapacitors are often used for instant charge-discharge applications rather than high-energy storage needs. Supercapacitors can produce power bursts within a fraction of seconds[355]. Energy storage in supercapacitors takes place either

by ion adsorption or by redox reaction and the charge transfer occurs at the surface of electrode material[356]. Based on the mechanism of charge storage, supercapacitors are classified into electrostatic and faradaic supercapacitors[357].

The capacitance of a supercapacitor depends strongly on the electrochemically active surface area of electrode materials i.e., the surface area accessible for electrochemical activity. Thus increase in surface area available for the electrolyte, can increase the capacitance[358]. Nanostructures are known for their high specific surface area. Several nanomaterial-based electrodes were developed for supercapacitor applications. The specific capacitance of materials depends on the surface area, pore size distribution, electrical conductivity, charge transport, and their electrochemical and mechanical stability[358]. The above-mentioned parameters can be tuned easily for nanomaterials, which makes them suitable candidates for supercapacitor applications. Incorporation of nanomaterials into conventional electrode materials can induce a synergic effect leading to high performance [359-361]. The most commonly employed electrode materials are carbon-based materials, metal oxides and conducting polymers. Activated carbon [362-365], carbon nanotubes [366-370], graphene[371-375] etc are the widely used carbon-based materials. In the case of metal oxide-based electrodes, RuO_2 [376-380], MnO_2 [381-383], NiO [384-386], Co_2O_3 [387], V_2O_5 [388-390]etc are some of the promising candidates. Another direction in which the supercapacitor research progresses is the development of lightweight, flexible and wearable supercapacitor modules [391-393].

1.4.2.3 Energy saving applications

Technologies employing nanomaterials such as solar cells, lithium-ion batteries, light-emitting diodes (LEDs), supercapacitors, and fuel cells are capable of achieving better energy efficiency, energy conservation, and sustainability. Apart from direct energy production, storage, and transmission applications of nanomaterials, they also play a crucial role in energy-saving and energy efficiency-improving applications. Reduction in fuel consumption by the introduction of lightweight building materials for automobiles and aircrafts is one such strategy. Nanocomposites can contribute considerably towards enhancing the lightweightness. Other energy-conserving tactics include the fabrication of wear-resistant and lightweight engine parts along with tyres having low rolling resistance. Nanomaterial additives in fuels can also improve energy efficiency. Modern building technology employs various energy saving strategies like switchable windows, thermal insulation materials as well as cool pigment coatings. Cool coatings made up of Near Infrared reflecting (NIR) inorganic pigments can considerably reduce the energy consumed for cooling. In addition to reducing electricity bills, NIR reflecting pigments can prevent the urban heat island effect. The energy conservation attributes of NIR reflecting pigments can eventually lead to cleaner air and can prevent climate change. The cool pigment application enhances the aesthetic appearance, stability and durability of the roofs and walls.

1.4.2.3.1 Inorganic pigments

Pigments are small particles that are insoluble in solvents and binders which forms their application medium. Pigments form an

important part of human life and they have enhanced the aesthetic beauty of objects. Apart from the aesthetic attributes inorganic pigments are nowadays having a wide range of advantages. The colour exhibited by the inorganic pigments is derived from the stimulation of cone cells in the human eye by the visible light radiations entering into the eye. The optical characteristics of a coated layer of paint depend on the size, shape and optical properties of the pigment particles constituting the paint. From ancient days onwards, several compounds were in use as pigments. Charcoal, ocher, clays etc were the initially used colourants. Oxides of iron and chromium were also employed as pigments. Manganese ores, Arsenic sulfide, Naples yellow, ultramarine, artificial lapis lazuli, Egyptian blue, Han blue, Maya blue, Malachite *etc* are some of the ancient pigments. The pigment industry started in 18th century and flourished by developing and introducing pigments such as Berlin blue, Cobalt blue, Scheele's green, Chrome yellow, ultramarine, cobalt and iron oxide pigments, cadmium red, manganese blue, molybdenum red and titanium dioxide.

1.4.2.3.2 Classification of inorganic pigments

There are different classifications available for pigments based on their origin, chemical composition, crystal structure, colour and functional properties. The major classifications of pigments are given in **Figure 1.1**. Here we are focusing on inorganic pigments having the functional property of Near Infrared (NIR) reflectance.
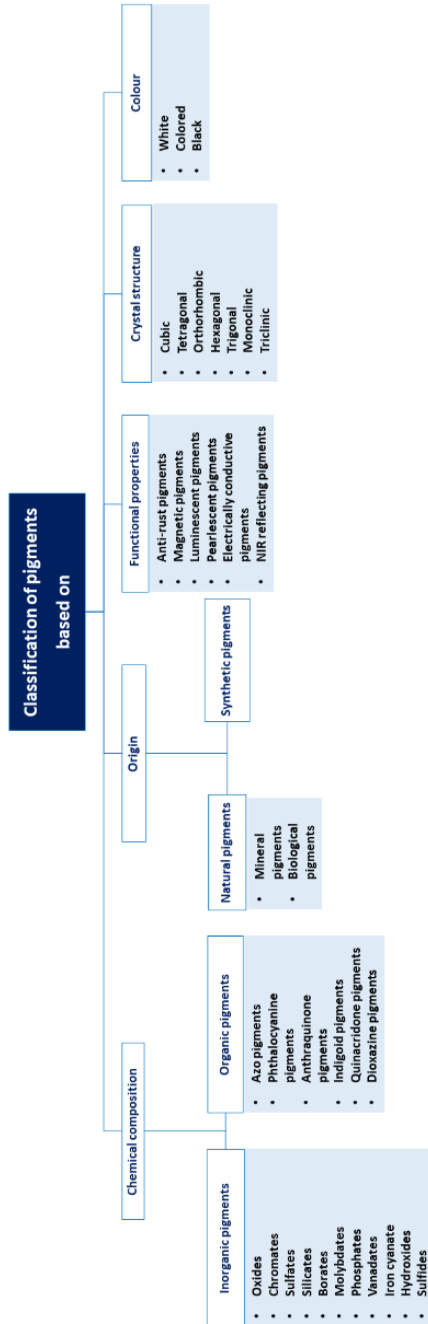
Figure 1.1 - Classification of pigments

1.4.2.3.3 Near Infrared (NIR) reflecting inorganic pigments

The solar energy distribution is given in Figure. The solar radiation reaching the earth's atmosphere consists of 5% ultraviolet, 43% visible and 52% near infrared radiations. More than half of the solar radiation is constituted by near infrared (NIR) radiations which are responsible for the heating up of surfaces and objects when irradiated with sunlight. The growing urbanization and industrialization have led to global warming and caused a rise in atmospheric temperature. The effects of rising temperatures are severe in urban and industrial areas. It may even cause an urban heat island effect, a phenomenon in which the urban core areas experience considerably higher temperatures compared to adjacent suburban and rural areas. Due to increasing heat, maintaining optimum interior temperatures in buildings requires the consumption of a significant amount of energy. Air conditioners and electric fans are the mostly used cooling solutions for buildings. Soaring temperatures and urbanization are further increasing the demand for energy for cooling purposes. A viable strategy to minimize the energy consumption for cooling purposes in buildings is the use of cool pigments, otherwise known as Near Infrared (NIR) reflecting pigments. NIR reflecting cool pigments minimize the heat absorbed by buildings by reflecting the incident solar radiation, especially the NIR portion. Thus, cool roofs eventually provide cooler interiors compared to normal roofing. NIR reflecting inorganic pigments are classified based on their colour into white, black and coloured. There are different classes of NIR reflecting pigments based on their chemical composition and crystal structure.

The pigment particle size is an important factor determining the NIR reflectance. To have better NIR reflectance, the particle size should be more than half of the wavelength of the light to be reflected. For cool pigments, in addition to the reflectance located in the NIR region and absorptions can also exist in the visible region, imparting attractive colours to pigments. Thus, NIR reflecting pigments can impart colours which resembles or exceeds conventional colourants. NIR reflecting pigments are synthesized by subjecting metal precursors like metal nitrates, acetates, hydroxides and oxides to various synthetic strategies. The widely employed synthetic methods for NIR reflecting pigments are solid state, combustion, sol-gel and hydrothermal methods.

One of the most widely used white pigment is TiO_2 and it has got remarkable NIR reflectance. A common strategy to improve the NIR reflectance of pigments is to mix them with TiO_2. The optical properties of TiO_2 are characteristic of its reduced visible light absorption and non-selective scattering. Other white pigments include Zinc sulfide (ZnS), Zinc white (ZnO) and lithopone. Various coloured pigments were developed by tuning visible light absorption in various compounds having different crystal structures by doping different elements or by varying the synthetic conditions. **Table 1.2** gives a brief idea of important NIR reflecting pigments developed so far.

Table 1.2 Important NIR reflecting pigments and characteristics

Name	Crystal structure	Synthesis method	Colour	NIR reflectance	Reference
Nd^{3+} doped $CoAl_2O_4$	Spinel	Solid state	Blue	39%	[394]
$CoCr_2O_4$	Spinel	Sol-gel method	Bluish green	44.1%	[395]
$Zn_{0.9}Co_{0.1}Al_2O_4$	Spinel	Solution combustion	Blue	63%	[396]
Mn^{3+} substituted $YInO3$	Hexagonal	Solid state	Blue	40%	[397]
$YMnO_3$	Perovskite	Polyacrylamide gel synthesis	Blue-green	53.4%	[398]
Nanocomposite $YIn_{0.9}Mn_{0.1}O_3$-ZnO	Hexagonal $YInO_3$ and ZnO phase	Sol-gel combustion	Blue	70%	[399]
La^{3+} and Li^+ doped $SrCuSi_4O_{10}$	Tetragonal	Solid-state synthesis	Blue	67%	[400]
Ti doped Cr_2O_3	Trigonal symmetry	Solid-state synthesis	Green	91.25%	[401]

$BaCr_2(P_2O_7)_2$	Triclinic	Solid-state synthesis	Green	90%	[402]
Y_2BaCuO_5	Orthorhombic	Nano-emulsion synthesis	Green	61%	[403]
$NiTiO_3$	Rhombohedral	Polymer pyrolysis	Yellow	62.1%	[404]
$NiTiO_3@TiO_2$	Ilmenite and rutile	Sol-precipitation	Yellow	76%	[405]
Y^{3+} and Nb^{5+} doped $BiVO_4$	Monoclinic	Solid-state synthesis	Yellow	90.8%	[406]
Mo^{6+} doped $Y_2Ce_2O_7$	Cubic Fluorite	Solid state synthesis	Yellow	>90%	[407]
Fe^{3+} doped $La_2Mo_2O_7$	Cubic Fluorite	Sol-gel synthesis	Yellow	71–93%	[408]
Cr_2O_3-$3TiO_2$	Trigonal	Polymer-pyrolysis method	Orange	53%	[409]
$M(Ti_{1-x}Cr_x)O_3$ where M=Mg, Ca, Sr, Ba and x=0.01, 0.03, 0.05, 0.1	Orthorhombic perovskite	Solid state reaction	Light green, pink and Yellow	-	[410]

$Zn_{1-x}Mg_xFe_2O_4$	Cubic spinel	Sol-gel method	Brick red to dark brown	>51%	[411]
Pr^{4+} doped Y_6MoO_{12}	Cubic	Solid state reaction	Light yellow to dark brown	78%	[412]
$Yb_6Mo_2O_{15}$	Trigonal structure	Solid state reaction	Yellow	93.7%	[413]
Pr^{4+} doped $Y_2Ce_2O_7$	Cubic Fluorite	Solid state reaction	Brick red to dark brown	93.5%	[407]
Pr^{4+} and Tb^{4+} doped $La_2Ce_2O_7$	Cubic Fluorite	Sol-gel synthesis	Light yellow to dark orange	>72.47 % (Pr^{4+}) doping) 87.41% (Tb^{4+})	[414]
Bi_3YO_6	Cubic Fluorite	High temperature calcination	Bright yellow to dark orange	53-99.5%	[415]
Vanadium doped $FePO_4$	Hexagonal	Co-precipitation method	Mustard yellow	72%	[416]
Co doped $LiMgPO_4$	Orthorhombic	Solid state synthesis	Magenta	67%	[417]

Ni^{2+} and La^{3+}-doped hibonite (Ca$_{1-x}$La$_x$Al$_{12-x}$Ni$_x$O$_{19}$)	Hexagonal	Combustion synthesis	Blue	89.7%	[418]
Li$_3$AlMnO$_5$	Monoclinic	Solid state synthesis	Red	87%	[419]
Gd^{3+}-doped cerium vanadates, (Ce$_{1-x}$Gd$_x$VO$_4$)	Tetragonal	Solid state synthesis	Black	77.5%	[420]
Al-doped Y$_3$Fe$_5$O$_{12}$	Tetragonal	Solution combustion method	Yellow-green	87.66%	[421]
Li$_2$MnO$_3$	Monoclinic	Solid state synthesis	Red	85%	[422]
V-doped LaPO$_4$	Monoclinic	Hydrothermal	Light green	87.86%	[423]
YFeO$_3$	Hexagonal	Solid state synthesis	Brown	88.65%	[424]

There are a large number of NIR reflecting inorganic pigments based on spinel and inverse spinel systems. Economic affordability and stability are the major deciding factors of the practical applicability of NIR reflecting inorganic pigments. Here with the energy-saving

objective in mind, a series of NIR reflecting inorganic pigments based on the inverse spinel $TiZn_2O_4$ system were developed. The colour tuning in the developed pigment compositions are brought about by the introduction of Cu^{2+} and Fe^{3+} as dopants. $TiZn_2O_4$ is a very less explored potential NIR reflecting inorganic pigment candidate due to its low cost and high stability.

1.5 Objectives of the thesis

1.5.1 Environmental objective

1. Development of pure and Er^{3+} doped CeO_2 nanoparticles by sol-gel and sol-hydrothermal routes. Quantitative investigation of surface basicity enhancement by Er^{3+} doping into the CeO_2 lattice with the help CO_2-TPD. To employ surface basicity as a tool for achieving rapid and selective adsorptive removal of model pollutants from water.

2. Synthesis of Mg^{2+} doped mesoporous CeO_2 for the selective adsorption of malachite green. To impart magnetic character to the developed Mg^{2+} doped mesoporous CeO_2 by designing a core-shell structure consisting of Fe_3O_4 as the core. The development of a magnetically retrievable, stable and efficient adsorbent material for the selective adsorption of malachite green from water.

3. To recycle spent zinc-carbon batteries into nanostructures suitable for water purification applications. To investigate the adsorption and Fenton-like catalytic activity of the developed nanostructures towards different dye molecules taken as model pollutants.

1.5.2   Energy-saving objective

1. To design and develop a series of colour tunable NIR reflecting pigments based on $TiZn_2O_4$ inverse spinel system. To investigate the variation of NIR reflectance and chromatic characteristics of the developed pigment compositions with Cu^{2+} and Fe^{3+} substitution into the $TiZn_2O_4$ lattice. Evaluation of the practical applicability of the developed pigment compositions by coating and stability studies forms another objective of the study.

1.6.   References

1.   Allen, C., G. Metternicht, and T. Wiedmann, *National pathways to the Sustainable Development Goals (SDGs): A comparative review of scenario modelling tools.* Environmental Science & Policy, 2016. **66**: p. 199-207.

2.   Hoekstra, A.Y., A.K. Chapagain, and P.R. Van Oel, *Advancing water footprint assessment research: Challenges in monitoring progress towards sustainable development goal 6*. 2017, MDPI. p. 438.

3.   Assembly, U.N.G., *Transforming our world: the 2030 Agenda for Sustainable Development.* United Nations: New York, NY, USA, 2015.

4.   Water, U., *Summary Progress Update 2021: SDG 6—water and sanitation for all.* Geneva, Switzerland, 2021.

5.   *The Sustainable Development Goals Report 2023: Special Edition.* United Nations, (2023).

6.   McCollum, D., et al., *Sdg7: Ensure access to affordable, reliable, sustainable and modern energy for all.* 2017.

7.   *The Future of Cooling-Opportunities for energyefficient air conditioning.* International Energy Agency, (2018).

8.   Santamouris, M., *Cooling the buildings–past, present and future.* Energy and Buildings, 2016. **128**: p. 617-638.

9.   Jose, S., et al., *Recent advances in infrared reflective inorganic pigments.* Solar Energy Materials and Solar Cells, 2019. **194**: p. 7-27.

10. Rosati, A., M. Fedel, and S. Rossi, *NIR reflective pigments for cool roof applications: A comprehensive review.* Journal of Cleaner Production, 2021. **313**: p. 127826.

11. Edwards, P.P. and J.M. Thomas, *Gold in a metallic divided state—from faraday to present-day nanoscience.* Angewandte Chemie International Edition, 2007. **46**(29): p. 5480-5486.
12. Higby, G.J., *Gold in medicine.* Gold bulletin, 1982. **15**(4): p. 130-140.
13. Tekmen, S. and Z. Alım, *Ethics in Nanotechnology and Society Perception*, in *Nanotoxicology*. 2018, CRC Press. p. 19-33.
14. Feynman, R.P. *Plenty of Room at the Bottom*. in *APS annual meeting*. 1959.
15. Dusastre, V., *The invisible revolution.* Nature, 2008. **451**(7180): p. 770-771.
16. Fujishima, A. and K. Honda, *Electrochemical Photolysis of Water at a Semiconductor Electrode.* Nature, 1972. **238**(5358): p. 37-38.
17. Binnig, G. and H. Rohrer, *Scanning tunneling microscopy—from birth to adolescence.* reviews of modern physics, 1987. **59**(3): p. 615.
18. Ananthaiah, R., *Discovery of fullerenes.* Resonance, 1997. **2**(1): p. 68-73.
19. Iijima, S., *The background of the discovery of carbon nanotubes.* appl. Phys, 1971. **42**: p. 5891-5893.
20. Ajayan, P. and S. Lijima, *Smallest carbon nanotube.* Nature, 1992. **358**(6381): p. 23-23.
21. Su, S., et al., *Nanomaterials-based sensors for applications in environmental monitoring.* Journal of Materials Chemistry, 2012. **22**(35): p. 18101-18110.
22. Bochenkov, V.E.e. and G.B. Sergeev, *Nanomaterials for sensors.* Russian Chemical Reviews, 2007. **76**(11): p. 1084.
23. Riu, J., A. Maroto, and F.X. Rius, *Nanosensors in environmental analysis.* Talanta, 2006. **69**(2): p. 288-301.
24. Ibrahim, R.K., et al., *Environmental application of nanotechnology: air, soil, and water.* Environmental Science and Pollution Research, 2016. **23**(14): p. 13754-13788.
25. Devi, P., et al., *Recent advances in carbon quantum dot-based sensing of heavy metals in water.* TrAC Trends in Analytical Chemistry, 2019. **114**: p. 171-195.
26. Nsibande, S. and P. Forbes, *Fluorescence detection of pesticides using quantum dot materials–a review.* Analytica chimica acta, 2016. **945**: p. 9-22.
27. Maduraiveeran, G. and W. Jin, *Nanomaterials based electrochemical sensor and biosensor platforms for environmental applications.* Trends in Environmental Analytical Chemistry, 2017. **13**: p. 10-23.
28. Yue, Z., et al., *Quantum-dot-based photoelectrochemical sensors for chemical and biological detection.* ACS applied materials & interfaces, 2013. **5**(8): p. 2800-2814.

29. Chen, X., Y. Liu, and Q. Ma, *Recent advances in quantum dot-based electrochemiluminescence sensors.* Journal of Materials Chemistry C, 2018. **6**(5): p. 942-959.

30. Kim, Y., R.C. Johnson, and J.T. Hupp, *Gold nanoparticle-based sensing of "spectroscopically silent" heavy metal ions.* Nano letters, 2001. **1**(4): p. 165-167.

31. Huang, C.-C. and H.-T. Chang, *Selective gold-nanoparticle-based "turn-on" fluorescent sensors for detection of mercury (II) in aqueous solution.* Analytical Chemistry, 2006. **78**(24): p. 8332-8338.

32. Fernández-Sánchez, C., *Analytical microsystems integrating metal nanoparticle-based chemical sensors to detect water contaminants.*

33. Zhao, X., et al., *Recent developments in detection using noble metal nanoparticles.* Critical Reviews in Analytical Chemistry, 2020. **50**(2): p. 97-110.

34. Saxena, S. and A.K. Srivastava, *Carbon nanotube-based sensors and their application*, in *Nano-Optics*. 2020, Elsevier. p. 265-291.

35. Sinha, N., J. Ma, and J.T. Yeow, *Carbon nanotube-based sensors.* Journal of nanoscience and nanotechnology, 2006. **6**(3): p. 573-590.

36. Jacobs, C.B., M.J. Peairs, and B.J. Venton, *Carbon nanotube based electrochemical sensors for biomolecules.* Analytica chimica acta, 2010. **662**(2): p. 105-127.

37. Vashist, S.K., et al., *Advances in carbon nanotube based electrochemical sensors for bioanalytical applications.* Biotechnology advances, 2011. **29**(2): p. 169-188.

38. Tong, H., et al., *Nano-photocatalytic materials: possibilities and challenges.* Advanced materials, 2012. **24**(2): p. 229-251.

39. Raval, H.D. and J.M. Gohil, *Nanotechnology in water treatment: an emerging trend.* International Journal of Nuclear Desalination, 2010. **4**(2): p. 184-188.

40. Rehman, F., et al., *Chapter 8 - Nanomembranes for water treatment*, in *Nanotechnology in the Beverage Industry*, A. Amrane, et al., Editors. 2020, Elsevier. p. 207-240.

41. Gehrke, I., A. Geiser, and A. Somborn-Schulz, *Innovations in nanotechnology for water treatment.* Nanotechnology, science and applications, 2015. **8**: p. 1-17.

42. Lee, J.-D., et al., *Effect of Coagulation Conditions on Membrane Filtration Characteristics in Coagulation–Microfiltration Process for Water Treatment.* Environmental Science & Technology, 2000. **34**(17): p. 3780-3788.

43. Bixler, H.J. and G.C. Rappe, *Ultrafiltration process.* 1970, Google Patents.

44. Diawara, C.K., *Nanofiltration process efficiency in water desalination.* Separation & purification reviews, 2008. **37**(3): p. 302-324.

45. Mallevialle, J., P.E. Odendaal, and M.R. Wiesner, *Water treatment membrane processes*. 1996: American Water Works Association.

46. Tamura, M. and A. Shinbo, *Reverse osmosis process and equipment*. 2001, Google Patents.

47. Arthanareeswaran, G., et al., *Synthesis, characterization and thermal studies on cellulose acetate membranes with additive.* European Polymer Journal, 2004. **40**(9): p. 2153-2159.

48. Scharnagl, N. and H. Buschatz, *Polyacrylonitrile (PAN) membranes for ultra-and microfiltration.* Desalination, 2001. **139**(1-3): p. 191-198.

49. Tan, Z., et al., *Polyamide membranes with nanoscale Turing structures for water purification.* Science, 2018. **360**(6388): p. 518-521.

50. Rehman, F., et al., *Nanomembranes for water treatment*, in *Nanotechnology in the Beverage Industry*. 2020, Elsevier. p. 207-240.

51. Kang, E., et al., *Large-Scale, Ultrapliable, and Free-Standing Nanomembranes.* Advanced materials, 2013. **25**(15): p. 2167-2173.

52. Cavallo, F. and M.G. Lagally, *Semiconductors turn soft: inorganic nanomembranes.* Soft Matter, 2010. **6**(3): p. 439-455.

53. Tijing, L.D., et al., *Recent progress of membrane distillation using electrospun nanofibrous membrane.* Journal of Membrane Science, 2014. **453**: p. 435-462.

54. Merkel, T.C., et al., *Ultrapermeable, reverse-selective nanocomposite membranes.* Science, 2002. **296**(5567): p. 519-522.

55. Yin, J. and B. Deng, *Polymer-matrix nanocomposite membranes for water treatment.* Journal of membrane science, 2015. **479**: p. 256-275.

56. Lonsdale, H.K., U. Merten, and R.L. Riley, *Transport properties of cellulose acetate osmotic membranes.* Journal of applied polymer science, 1965. **9**(4): p. 1341-1362.

57. Kang, G.-d. and Y.-m. Cao, *Development of antifouling reverse osmosis membranes for water treatment: a review.* Water research, 2012. **46**(3): p. 584-600.

58. Liao, Y., et al., *Progress in electrospun polymeric nanofibrous membranes for water treatment: Fabrication, modification and applications.* Progress in Polymer Science, 2018. **77**: p. 69-94.

59. Lee, J.-W., et al., *Fouling-tolerant nanofibrous polymer membranes for water treatment.* ACS applied materials & interfaces, 2014. **6**(16): p. 14600-14607.

60. Suja, P.S., et al., *Electrospun nanofibrous membranes for water purification.* Polymer reviews, 2017. **57**(3): p. 467-504.

61.   Si, Y., et al., *Ultralight and fire-resistant ceramic nanofibrous aerogels with temperature-invariant superelasticity.* Science advances, 2018. **4**(4): p. eaas8925.

62.   Song, J., et al., *Soft Zr-doped TiO 2 nanofibrous membranes with enhanced photocatalytic activity for water purification.* Scientific reports, 2017. **7**(1): p. 1-12.

63.   Subjalearndee, N., et al., *Structural development of nanosilver on metal oxide nanofibrous membrane by plasma enhanced chemical vapor deposition (PECVD).* Applied Surface Science, 2018. **452**: p. 306-313.

64.   Zhao, R., et al., *Highly flexible magnesium silicate nanofibrous membranes for effective removal of methylene blue from aqueous solution.* Chemical Engineering Journal, 2019. **359**: p. 1603-1616.

65.   Taha, A.A., et al., *Preparation and application of functionalized cellulose acetate/silica composite nanofibrous membrane via electrospinning for Cr (VI) ion removal from aqueous solution.* Journal of environmental management, 2012. **112**: p. 10-16.

66.   Shahabadi, S.M.S., et al., *Superhydrophobic dual layer functionalized titanium dioxide/polyvinylidene fluoride-co-hexafluoropropylene (TiO2/PH) nanofibrous membrane for high flux membrane distillation.* Journal of Membrane Science, 2017. **537**: p. 140-150.

67.   Ma, H., B.S. Hsiao, and B. Chu, *Functionalized electrospun nanofibrous microfiltration membranes for removal of bacteria and viruses.* Journal of membrane science, 2014. **452**: p. 446-452.

68.   Wu, C., et al., *Polydopamine-mediated surface functionalization of electrospun nanofibrous membranes: preparation, characterization and their adsorption properties towards heavy metal ions.* Applied Surface Science, 2015. **346**: p. 207-215.

69.   Guo, W., H.-H. Ngo, and J. Li, *A mini-review on membrane fouling.* Bioresource technology, 2012. **122**: p. 27-34.

70.   Zhang, M., et al., *Effects of hydrophilicity/hydrophobicity of membrane on membrane fouling in a submerged membrane bioreactor.* Bioresource technology, 2015. **175**: p. 59-67.

71.   Sun, W., et al., *Pretreatment and membrane hydrophilic modification to reduce membrane fouling.* Membranes, 2013. **3**(3): p. 226-241.

72.   Luo, M.-L., et al., *Hydrophilic modification of poly (ether sulfone) ultrafiltration membrane surface by self-assembly of TiO2 nanoparticles.* Applied Surface Science, 2005. **249**(1-4): p. 76-84.

73.   Bae, T.-H. and T.-M. Tak, *Preparation of TiO2 self-assembled polymeric nanocomposite membranes and examination of their fouling mitigation effects in a membrane bioreactor system.* Journal of membrane science, 2005. **266**(1-2): p. 1-5.

74. Jhaveri, J.H. and Z.V.P. Murthy, *A comprehensive review on anti-fouling nanocomposite membranes for pressure driven membrane separation processes.* Desalination, 2016. **379**: p. 137-154.

75. Safarpour, M., A. Khataee, and V. Vatanpour, *Preparation of a novel polyvinylidene fluoride (PVDF) ultrafiltration membrane modified with reduced graphene oxide/titanium dioxide (TiO2) nanocomposite with enhanced hydrophilicity and antifouling properties.* Industrial & Engineering Chemistry Research, 2014. **53**(34): p. 13370-13382.

76. Lee, J., et al., *Graphene oxide nanoplatelets composite membrane with hydrophilic and antifouling properties for wastewater treatment.* Journal of membrane science, 2013. **448**: p. 223-230.

77. Yang, Z., et al., *Hydrophilic silver nanoparticles induce selective nanochannels in thin film nanocomposite polyamide membranes.* Environmental science & technology, 2019. **53**(9): p. 5301-5308.

78. Bai, L., et al., *Surface modification of UF membranes with functionalized MWCNTs to control membrane fouling by NOM fractions.* Journal of Membrane Science, 2015. **492**: p. 400-411.

79. Vatanpour, V. and N. Zoqi, *Surface modification of commercial seawater reverse osmosis membranes by grafting of hydrophilic monomer blended with carboxylated multiwalled carbon nanotubes.* Applied Surface Science, 2017. **396**: p. 1478-1489.

80. Rahimi, Z., A.A.L. Zinatizadeh, and S. Zinadini, *Preparation of high antibiofouling amino functionalized MWCNTs/PES nanocomposite ultrafiltration membrane for application in membrane bioreactor.* Journal of Industrial and Engineering Chemistry, 2015. **29**: p. 366-374.

81. Celik, E., et al., *Carbon nanotube blended polyethersulfone membranes for fouling control in water treatment.* Water Research, 2011. **45**(1): p. 274-282.

82. Park, S.-M., et al., *Fouling and rejection behavior of carbon nanotube membranes.* Desalination, 2014. **343**: p. 180-186.

83. Luo, M.-L., et al., *Hydrophilic modification of poly(ether sulfone) ultrafiltration membrane surface by self-assembly of TiO2 nanoparticles.* Applied Surface Science, 2005. **249**(1): p. 76-84.

84. Bae, T.-H. and T.-M. Tak, *Effect of TiO2 nanoparticles on fouling mitigation of ultrafiltration membranes for activated sludge filtration.* Journal of Membrane Science, 2005. **249**(1): p. 1-8.

85. Petersen, R.J., *Composite reverse osmosis and nanofiltration membranes.* Journal of Membrane Science, 1993. **83**(1): p. 81-150.

86. Saleem, H. and S.J. Zaidi, *Nanoparticles in reverse osmosis membranes for desalination: A state of the art review.* Desalination, 2020. **475**: p. 114171.

87. Suwaileh, W., et al., *Forward osmosis membranes and processes: A comprehensive review of research trends and future outlook.* Desalination, 2020. **485**: p. 114455.

88. Wei, J., et al., *Synthesis and characterization of flat-sheet thin film composite forward osmosis membranes.* Journal of Membrane Science, 2011. **372**(1): p. 292-302.

89. Yadav, S., et al., *Recent developments in forward osmosis membranes using carbon-based nanomaterials.* Desalination, 2020. **482**: p. 114375.

90. Singh, N., G. Nagpal, and S. Agrawal, *Water purification by using adsorbents: a review.* Environmental technology & innovation, 2018. **11**: p. 187-240.

91. Jing, L., et al., *Surface tuning for oxide-based nanomaterials as efficient photocatalysts.* Chemical Society Reviews, 2013. **42**(24): p. 9509-9549.

92. Tang, L., et al., *Facile synthesis of silver bromide-based nanomaterials and their efficient and rapid selective adsorption mechanisms toward anionic dyes.* ACS Sustainable Chemistry & Engineering, 2016. **4**(9): p. 4617-4625.

93. Wu, Y., et al., *Environmental remediation of heavy metal ions by novel-nanomaterials: a review.* Environmental pollution, 2019. **246**: p. 608-620.

94. Creamer, A.E. and B. Gao, *Carbon-based adsorbents for postcombustion CO2 capture: a critical review.* Environmental science & technology, 2016. **50**(14): p. 7276-7289.

95. Yang, X., et al., *Surface functional groups of carbon-based adsorbents and their roles in the removal of heavy metals from aqueous solutions: a critical review.* Chemical Engineering Journal, 2019. **366**: p. 608-621.

96. Li, J., et al., *Activated boron nitride as an effective adsorbent for metal ions and organic pollutants.* Scientific reports, 2013. **3**: p. 3208.

97. Pang, J., et al., *Silver nanoparticle-decorated boron nitride with tunable electronic properties for enhancement of adsorption performance.* ACS Sustainable Chemistry & Engineering, 2018. **6**(4): p. 4948-4957.

98. Ye, J., et al., *Few-layered graphene-like boron nitride: a highly efficient adsorbent for indoor formaldehyde removal.* Environmental Science & Technology Letters, 2017. **4**(1): p. 20-25.

99. Kumar, K.Y., et al., *Low-cost synthesis of metal oxide nanoparticles and their application in adsorption of commercial dye and heavy metal ion in aqueous solution.* Powder technology, 2013. **246**: p. 125-136.

100. Zhang, Y., K. Li, and J. Liao, *Facile synthesis of reduced-graphene-oxide/rare-earth-metal-oxide aerogels as a highly efficient*

adsorbent for Rhodamine-B. Applied Surface Science, 2020. **504**: p. 144377.

101.   Sarma, G.K., S.S. Gupta, and K.G. Bhattacharyya, *Nanomaterials as versatile adsorbents for heavy metal ions in water: a review.* Environmental Science and Pollution Research, 2019. **26**(7): p. 6245-6278.

102.   Olusegun, S.J., et al., *Synergistic effect of a spinel ferrite on the adsorption capacity of nano bio-silica for the removal of methylene blue.* Environmental Technology, 2019: p. 1-14.

103.   Reddy, D.H.K. and Y.-S. Yun, *Spinel ferrite magnetic adsorbents: alternative future materials for water purification?* Coordination Chemistry Reviews, 2016. **315**: p. 90-111.

104.   Wang, L., et al., *Adsorption capability for Congo red on nanocrystalline MFe2O4 (M= Mn, Fe, Co, Ni) spinel ferrites.* Chemical Engineering Journal, 2012. **181**: p. 72-79.

105.   Kefeni, K.K., B.B. Mamba, and T.A. Msagati, *Application of spinel ferrite nanoparticles in water and wastewater treatment: a review.* Separation and Purification Technology, 2017. **188**: p. 399-422.

106.   Gong, J.-L., et al., *Removal of cationic dyes from aqueous solution using magnetic multi-wall carbon nanotube nanocomposite as adsorbent.* Journal of hazardous materials, 2009. **164**(2-3): p. 1517-1522.

107.   Sharma, M., et al., *Efficient oil removal from wastewater based on polymer coated superhydrophobic tetrapodal magnetic nanocomposite adsorbent.* Applied Materials Today, 2019. **17**: p. 130-141.

108.   Liu, S., et al., *Magnetic Nanocomposite Adsorbents*, in *Composite Nanoadsorbents*. 2019, Elsevier. p. 295-316.

109.   Ali, N., et al., *Characterization and deployment of surface-engineered chitosan-triethylenetetramine nanocomposite hybrid nano-adsorbent for divalent cations decontamination.* International Journal of Biological Macromolecules, 2020. **152**: p. 663-671.

110.   Yang, C., et al., *Bifunctional ZnO-MgO/activated carbon adsorbents boost H2S room temperature adsorption and catalytic oxidation.* Applied Catalysis B: Environmental, 2020. **266**: p. 118674.

111.   Mashile, G.P., et al., *Recyclable magnetic waste tyre activated carbon-chitosan composite as an effective adsorbent rapid and simultaneous removal of methylparaben and propylparaben from aqueous solution and wastewater.* Journal of Water Process Engineering, 2020. **33**: p. 101011.

112.   Zhang, G., et al., *CuFe2O4/activated carbon composite: a novel magnetic adsorbent for the removal of acid orange II and catalytic regeneration.* Chemosphere, 2007. **68**(6): p. 1058-1066.

113.   Ghaedi, M., et al., *Application of activated carbon as adsorbents for efficient removal of methylene blue: Kinetics and equilibrium study.*

Journal of Industrial and Engineering Chemistry, 2014. **20**(4): p. 2317-2324.

114. Hu, J., et al., *Plasma-induced grafting of cyclodextrin onto multiwall carbon nanotube/iron oxides for adsorbent application.* The Journal of Physical Chemistry B, 2010. **114**(20): p. 6779-6785.

115. Tofighy, M.A. and T. Mohammadi, *Adsorption of divalent heavy metal ions from water using carbon nanotube sheets.* Journal of hazardous materials, 2011. **185**(1): p. 140-147.

116. Mashkoor, F., A. Nasar, and Inamuddin, *Carbon nanotube-based adsorbents for the removal of dyes from waters: A review.* Environmental Chemistry Letters, 2020. **18**(3): p. 605-629.

117. Duman, O., et al., *Carbon nanotube-based magnetic and non-magnetic adsorbents for the high-efficiency removal of diquat dibromide herbicide from water: OMWCNT, OMWCNT-Fe3O4 and OMWCNT-κ-carrageenan-Fe3O4 nanocomposites.* Environmental Pollution, 2019. **244**: p. 723-732.

118. Ali, I., et al., *Graphene based adsorbents for remediation of noxious pollutants from wastewater.* Environment International, 2019. **127**: p. 160-180.

119. Baig, N., et al., *Graphene-based adsorbents for the removal of toxic organic pollutants: A review.* Journal of Environmental Management, 2019. **244**: p. 370-382.

120. Chen, L., et al., *Three-dimensional graphene-based adsorbents in sewage disposal: a review.* Environmental Science and Pollution Research, 2018. **25**(26): p. 25840-25861.

121. Liu, H. and H. Qiu, *Recent advances of 3D graphene-based adsorbents for sample preparation of water pollutants: A review.* Chemical Engineering Journal, 2020. **393**: p. 124691.

122. Ramesha, G.K., et al., *Graphene and graphene oxide as effective adsorbents toward anionic and cationic dyes.* Journal of Colloid and Interface Science, 2011. **361**(1): p. 270-277.

123. Su, H., Z. Ye, and N. Hmidi, *High-performance iron oxide–graphene oxide nanocomposite adsorbents for arsenic removal.* Colloids and Surfaces A: Physicochemical and Engineering Aspects, 2017. **522**: p. 161-172.

124. Kyzas, G.Z., E.A. Deliyanni, and K.A. Matis, *Graphene oxide and its application as an adsorbent for wastewater treatment.* Journal of Chemical Technology & Biotechnology, 2014. **89**(2): p. 196-205.

125. Robati, D., et al., *Removal of hazardous dyes-BR 12 and methyl orange using graphene oxide as an adsorbent from aqueous phase.* Chemical Engineering Journal, 2016. **284**: p. 687-697.

126. Karimi-Maleh, H., et al., *The role of magnetite/graphene oxide nano-composite as a high-efficiency adsorbent for removal of phenazopyridine residues from water samples, an*

experimental/theoretical investigation. Journal of Molecular Liquids, 2020. **298**: p. 112040.

127. Song, Q., et al., *Enhanced adsorption of fluoride on Al-modified boron nitride nanosheets from aqueous solution.* Journal of Alloys and Compounds, 2019. **793**: p. 512-518.

128. Song, Q., et al., *Nickel (II) modified porous boron nitride: An effective adsorbent for tetracycline removal from aqueous solution.* Chemical Engineering Journal, 2020. **394**: p. 124985.

129. Wang, J., et al., *Reduced Graphene Oxide/ZnO Composite: Reusable Adsorbent for Pollutant Management.* ACS Applied Materials & Interfaces, 2012. **4**(6): p. 3084-3090.

130. Sharma, M., et al., *ZnO tetrapods and activated carbon based hybrid composite: Adsorbents for enhanced decontamination of hexavalent chromium from aqueous solution.* Chemical Engineering Journal, 2019. **358**: p. 540-551.

131. Sharma, M., et al., *Adsorption of heavy metal ions by mesoporous ZnO and TiO2@ZnO monoliths: Adsorption and kinetic studies.* Microchemical Journal, 2019. **145**: p. 105-112.

132. George, R., et al., *Environmentally Benign TiO2 Nanomaterials for Removal of Heavy Metal Ions with Interfering Ions Present in Tap Water.* Materials Today: Proceedings, 2016. **3**(2): p. 162-166.

133. Chen, J., et al., *Adsorbent synthesis of polypyrrole/TiO2 for effective fluoride removal from aqueous solution for drinking water purification: Adsorbent characterization and adsorption mechanism.* Journal of Colloid and Interface Science, 2017. **495**: p. 44-52.

134. MiarAlipour, S., et al., *TiO2/porous adsorbents: Recent advances and novel applications.* Journal of Hazardous Materials, 2018. **341**: p. 404-423.

135. Seo, H.O., et al., *Nanoporous TiO2/SiO2 prepared by atomic layer deposition as adsorbents of methylene blue in aqueous solutions.* Chemical Engineering Journal, 2012. **183**: p. 381-386.

136. Zhang, W., L. Zou, and L. Wang, *Photocatalytic TiO2/adsorbent nanocomposites prepared via wet chemical impregnation for wastewater treatment: A review.* Applied Catalysis A: General, 2009. **371**(1): p. 1-9.

137. Lingamdinne, L.P., et al., *Preparation and characterization of porous reduced graphene oxide based inverse spinel nickel ferrite nanocomposite for adsorption removal of radionuclides.* Journal of Hazardous Materials, 2017. **326**: p. 145-156.

138. Lingamdinne, L.P., et al., *Biogenic reductive preparation of magnetic inverse spinel iron oxide nanoparticles for the adsorption removal of heavy metals.* Chemical Engineering Journal, 2017. **307**: p. 74-84.

139. Tatarchuk, T., et al., *Synthesis, morphology, crystallite size and adsorption properties of nanostructured Mg–Zn ferrites with*

enhanced porous structure. Journal of Alloys and Compounds, 2020. **819**: p. 152945.

140. Alam, N. and D. Sarma, *Tunable Metallogels Based on Bifunctional Ligands: Precursor Metallogels, Spinel Oxides, Dye and CO2 Adsorption.* ACS Omega, 2020. **5**(28): p. 17356-17366.

141. Zhu, H.-Y., et al., *A novel magnetically separable γ-Fe2O3/crosslinked chitosan adsorbent: Preparation, characterization and adsorption application for removal of hazardous azo dye.* Journal of Hazardous Materials, 2010. **179**(1): p. 251-257.

142. Li, S., et al., *Fe3O4 modified mesoporous carbon nanospheres: Magnetically separable adsorbent for hexavalent chromium.* Journal of Alloys and Compounds, 2017. **698**: p. 20-26.

143. Zeng, S., et al., *Magnetically separable Ni0.6Fe2.4O4 nanoparticles as an effective adsorbent for dye removal: Synthesis and study on the kinetic and thermodynamic behaviors for dye adsorption.* Chemical Engineering Journal, 2014. **258**: p. 218-228.

144. Behbahani, E.S., K. Dashtian, and M. Ghaedi, *Fe/Co-chalcogenide-stabilized Fe3O4 nanoparticles supported MgAl-layered double hydroxide as a new magnetically separable sorbent for the simultaneous spectrophotometric determination of anionic dyes.* Microchemical Journal, 2020. **152**: p. 104431.

145. Bhaumik, M., et al., *Enhanced removal of Cr(VI) from aqueous solution using polypyrrole/Fe3O4 magnetic nanocomposite.* Journal of Hazardous Materials, 2011. **190**(1): p. 381-390.

146. Muliwa, A.M., et al., *Magnetic adsorption separation (MAS) process: An alternative method of extracting Cr(VI) from aqueous solution using polypyrrole coated Fe3O4 nanocomposites.* Separation and Purification Technology, 2016. **158**: p. 250-258.

147. Theerthagiri, J., et al., *A review on ZnO nanostructured materials: energy, environmental and biological applications.* Nanotechnology, 2019. **30**(39): p. 392001.

148. Basavarajappa, P.S., et al., *Recent progress in metal-doped TiO2, non-metal doped/codoped TiO2 and TiO2 nanostructured hybrids for enhanced photocatalysis.* International Journal of Hydrogen Energy, 2020. **45**(13): p. 7764-7778.

149. Zaleska, A., *Doped-TiO2: a review.* Recent patents on engineering, 2008. **2**(3): p. 157-164.

150. Nakata, K. and A. Fujishima, *TiO2 photocatalysis: Design and applications.* Journal of photochemistry and photobiology C: Photochemistry Reviews, 2012. **13**(3): p. 169-189.

151. Chai, L., et al., *Sulfate-doped Fe3O4/Al2O3 nanoparticles as a novel adsorbent for fluoride removal from drinking water.* Water Research, 2013. **47**(12): p. 4040-4049.

152. Husnain, S.M., et al., *Recent trends of MnO2-derived adsorbents for water treatment: a review.* New Journal of Chemistry, 2020. **44**(16): p. 6096-6120.

153. Zhang, H., et al., *Enhanced removal of heavy metal ions from aqueous solution using manganese dioxide-loaded biochar: Behavior and mechanism.* Scientific Reports, 2020. **10**(1): p. 6067.

154. Khin, M.M., et al., *A review on nanomaterials for environmental remediation.* Energy & Environmental Science, 2012. **5**(8): p. 8075-8109.

155. Lee, S.-Y. and S.-J. Park, *TiO2 photocatalyst for water treatment applications.* Journal of Industrial and Engineering Chemistry, 2013. **19**(6): p. 1761-1769.

156. Schneider, J., et al., *Understanding TiO2 photocatalysis: mechanisms and materials.* Chemical reviews, 2014. **114**(19): p. 9919-9986.

157. Kim, S., S.-J. Hwang, and W. Choi, *Visible light active platinum-ion-doped TiO2 photocatalyst.* The Journal of Physical Chemistry B, 2005. **109**(51): p. 24260-24267.

158. Ohno, T., T. Mitsui, and M. Matsumura, *Photocatalytic activity of S-doped TiO2 photocatalyst under visible light.* Chemistry letters, 2003. **32**(4): p. 364-365.

159. Klosek, S. and D. Raftery, *Visible light driven V-doped TiO2 photocatalyst and its photooxidation of ethanol.* The Journal of Physical Chemistry B, 2001. **105**(14): p. 2815-2819.

160. Kumaravel, V., et al., *Indium-doped TiO2 photocatalysts with high-temperature anatase stability.* The Journal of Physical Chemistry C, 2019. **123**(34): p. 21083-21096.

161. Bessekhouad, Y., D. Robert, and J.-V. Weber, *Photocatalytic activity of Cu2O/TiO2, Bi2O3/TiO2 and ZnMn2O4/TiO2 heterojunctions.* Catalysis Today, 2005. **101**(3-4): p. 315-321.

162. Bessekhouad, Y., D. Robert, and J. Weber, *Bi2S3/TiO2 and CdS/TiO2 heterojunctions as an available configuration for photocatalytic degradation of organic pollutant.* Journal of Photochemistry and Photobiology A: Chemistry, 2004. **163**(3): p. 569-580.

163. Zhao, W., et al., *Synthesis, characterization, and photocatalytic properties of SnO2/rutile TiO2/anatase TiO2 heterojunctions modified by Pt.* The Journal of Physical Chemistry C, 2014. **118**(40): p. 23117-23125.

164. Pan, D., et al., *Efficient separation of electron–hole pairs in graphene quantum dots by TiO2 heterojunctions for dye degradation.* ACS Sustainable Chemistry & Engineering, 2015. **3**(10): p. 2405-2413.

165. Ganguly, P., et al., *Theoretical and experimental investigation of visible light responsive AgBiS2-TiO2 heterojunctions for enhanced photocatalytic applications.* Applied Catalysis B: Environmental, 2019. **253**: p. 401-418.

166. Gündoğmuş, P., J. Park, and A. Öztürk, *Preparation and photocatalytic activity of g-C3N4/TiO2 heterojunctions under solar light illumination.* Ceramics International, 2020.

167. Chen, C., et al., *Perovskite LaNiO3/TiO2 step-scheme heterojunction with enhanced photocatalytic activity.* Applied Surface Science, 2020. **503**: p. 144287.

168. Perović, K., et al., *Recent Achievements in Development of TiO2-Based Composite Photocatalytic Materials for Solar Driven Water Purification and Water Splitting.* Materials, 2020. **13**(6): p. 1338.

169. Woan, K., G. Pyrgiotakis, and W. Sigmund, *Photocatalytic carbon-nanotube–TiO2 composites.* Advanced Materials, 2009. **21**(21): p. 2233-2239.

170. Zhu, Q., et al., *A novel P/Ag/Ag2O/Ag3PO4/TiO2 composite film for water purification and antibacterial application under solar light irradiation.* Science of the Total Environment, 2017. **577**: p. 236-244.

171. Paušová, Š., et al., *Composite materials based on active carbon/TiO2 for photocatalytic water purification.* Catalysis Today, 2019. **328**: p. 178-182.

172. Berberidou, C., et al., *Photocatalytic disinfection and purification of water employing reduced graphene oxide/TiO2 composites.* Journal of Chemical Technology & Biotechnology, 2019. **94**(12): p. 3905-3914.

173. Chen, X. and A. Selloni, *Introduction: titanium dioxide (TiO2) nanomaterials.* 2014, ACS Publications.

174. Banerjee, A.N., *The design, fabrication, and photocatalytic utility of nanostructured semiconductors: focus on TiO2-based nanostructures.* Nanotechnology, science and applications, 2011. **4**: p. 35.

175. Reddy, C.V., et al., *Recent progress in TiO2-and ZnO-based nanostructured hybrid photocatalysts for water purification and hydrogen generation*, in *Nanoscale Materials in Water Purification*. 2019, Elsevier. p. 815-843.

176. Gao, P., et al., *Effects of various TiO2 nanostructures and graphene oxide on photocatalytic activity of TiO2.* Journal of Hazardous materials, 2014. **279**: p. 96-104.

177. Zhou, D., et al., *In-situ construction of all-solid-state Z-scheme g-C3N4/TiO2 nanotube arrays photocatalyst with enhanced visible-light-induced properties.* Solar Energy Materials and Solar Cells, 2016. **157**: p. 399-405.

178. Zheng, X., et al., *Direct Z-scheme MoSe2 decorating TiO2 nanotube arrays photocatalyst for water decontamination.* Electrochimica Acta, 2019. **298**: p. 663-669.

179. Macak, J.M., et al., *Self-Organized TiO2 Nanotube Layers as Highly Efficient Photocatalysts.* Small, 2007. **3**(2): p. 300-304.

180. Lin, Y., *Photocatalytic activity of TiO2 nanowire arrays.* Materials Letters, 2008. **62**(8): p. 1246-1248.
181. Wu, H.B., H.H. Hng, and X.W. Lou, *Direct Synthesis of Anatase TiO2 Nanowires with Enhanced Photocatalytic Activity.* Advanced Materials, 2012. **24**(19): p. 2567-2571.
182. Al-Hajji, L.A., et al., *Impact of calcination of hydrothermally synthesized TiO2 nanowires on their photocatalytic efficiency.* Journal of Molecular Structure, 2020. **1200**: p. 127153.
183. Dou, H., et al., *Core–shell g-C3N4/Pt/TiO2 nanowires for simultaneous photocatalytic H2 evolution and RhB degradation under visible light irradiation.* Catalysis Science & Technology, 2019. **9**(18): p. 4898-4908.
184. Hu, K., et al., *Facile synthesis of Z-scheme composite of TiO2 nanorod/g-C3N4 nanosheet efficient for photocatalytic degradation of ciprofloxacin.* Journal of Cleaner Production, 2020. **253**: p. 120055.
185. Jiang, N., et al., *Facile preparation of flake-like blue TiO2 nanorod arrays for efficient visible light photocatalyst.* Ceramics International, 2019. **45**(8): p. 9754-9760.
186. Wang, Y., et al., *Low Temperature Synthesis and Photocatalytic Activity of Rutile TiO2 Nanorod Superstructures.* The Journal of Physical Chemistry C, 2007. **111**(6): p. 2709-2714.
187. Lu, Q., et al., *Photocatalytic Synthesis and Photovoltaic Application of Ag-TiO2 Nanorod Composites.* Nano Letters, 2013. **13**(11): p. 5698-5702.
188. Xuan, S., et al., *Magnetically Separable Fe3O4/TiO2 Hollow Spheres: Fabrication and Photocatalytic Activity.* The Journal of Physical Chemistry C, 2009. **113**(2): p. 553-558.
189. Shang, S., X. Jiao, and D. Chen, *Template-Free Fabrication of TiO2 Hollow Spheres and Their Photocatalytic Properties.* ACS Applied Materials & Interfaces, 2012. **4**(2): p. 860-865.
190. Zhang, S., et al., *Spatially confined Fe2O3 in hierarchical SiO2@TiO2 hollow sphere exhibiting superior photocatalytic efficiency for degrading antibiotics.* Chemical Engineering Journal, 2020. **380**: p. 122583.
191. Bao, R., et al., *Biotemplated synthesis of 3D rare earth–doped TiO2 hollow spheres for photocatalytic application.* Journal of Physics and Chemistry of Solids, 2019. **126**: p. 78-84.
192. Kim, J., C.W. Lee, and W. Choi, *Platinized WO3 as an Environmental Photocatalyst that Generates OH Radicals under Visible Light.* Environmental Science & Technology, 2010. **44**(17): p. 6849-6854.
193. Cui, L., et al., *Facile preparation of Z-scheme WO3/g-C3N4 composite photocatalyst with enhanced photocatalytic performance under visible light.* Applied Surface Science, 2017. **391**: p. 202-210.

194. Chen, J., et al., *Fabrication of hierarchical sheet-on-sheet WO3/g-C3N4 composites with enhanced photocatalytic activity.* Journal of Alloys and Compounds, 2019. **777**: p. 325-334.

195. Mohamed, H.H., *Rationally designed Fe2O3/GO/WO3 Z-Scheme photocatalyst for enhanced solar light photocatalytic water remediation.* Journal of Photochemistry and Photobiology A: Chemistry, 2019. **378**: p. 74-84.

196. Gröttrup, J., et al., *Porous ceramics based on hybrid inorganic tetrapodal networks for efficient photocatalysis and water purification.* Ceramics International, 2017. **43**(17): p. 14915-14922.

197. Behnajady, M.A., N. Modirshahla, and R. Hamzavi, *Kinetic study on photocatalytic degradation of C.I. Acid Yellow 23 by ZnO photocatalyst.* Journal of Hazardous Materials, 2006. **133**(1): p. 226-232.

198. Georgekutty, R., M.K. Seery, and S.C. Pillai, *A Highly Efficient Ag-ZnO Photocatalyst: Synthesis, Properties, and Mechanism.* The Journal of Physical Chemistry C, 2008. **112**(35): p. 13563-13570.

199. Zheng, Y., et al., *Photocatalytic Activity of Ag/ZnO Heterostructure Nanocatalyst: Correlation between Structure and Property.* The Journal of Physical Chemistry C, 2008. **112**(29): p. 10773-10777.

200. Zarezadeh, S., A. Habibi-Yangjeh, and M. Mousavi, *BiOBr and AgBr co-modified ZnO photocatalyst: A novel nanocomposite with p-n-n heterojunctions for highly effective photocatalytic removal of organic contaminants.* Journal of Photochemistry and Photobiology A: Chemistry, 2019. **379**: p. 11-23.

201. Juabrum, S., T. Chankhanittha, and S. Nanan, *Hydrothermally grown SDS-capped ZnO photocatalyst for degradation of RR141 azo dye.* Materials Letters, 2019. **245**: p. 1-5.

202. Konta, R., et al., *Photocatalytic Activities of Noble Metal Ion Doped SrTiO3 under Visible Light Irradiation.* The Journal of Physical Chemistry B, 2004. **108**(26): p. 8992-8995.

203. Hsieh, P.-L., et al., *Shape-Tunable SrTiO3 Crystals Revealing Facet-Dependent Optical and Photocatalytic Properties.* The Journal of Physical Chemistry C, 2019. **123**(22): p. 13664-13671.

204. Chang, C.-W. and C. Hu, *Graphene oxide-derived carbon-doped SrTiO3 for highly efficient photocatalytic degradation of organic pollutants under visible light irradiation.* Chemical Engineering Journal, 2020. **383**: p. 123116.

205. Wetchakun, N., et al., *BiVO4/CeO2 Nanocomposites with High Visible-Light-Induced Photocatalytic Activity.* ACS Applied Materials & Interfaces, 2012. **4**(7): p. 3718-3723.

206. Wen, X.-J., et al., *A novel Ag2O/CeO2 heterojunction photocatalysts for photocatalytic degradation of enrofloxacin: possible degradation*

pathways, mineralization activity and an in depth mechanism insight. Applied Catalysis B: Environmental, 2018. **221**: p. 701-714.

207. Ma, R., et al., *A critical review on visible-light-response CeO2-based photocatalysts with enhanced photooxidation of organic pollutants.* Catalysis Today, 2019. **335**: p. 20-30.

208. Fenton, H.J.H., *LXXIII.—Oxidation of tartaric acid in presence of iron.* Journal of the Chemical Society, Transactions, 1894. **65**: p. 899-910.

209. Haber, F. and J. Weiss, *Über die katalyse des hydroperoxydes.* Naturwissenschaften, 1932. **20**(51): p. 948-950.

210. Huang, C., C. Dong, and Z. Tang, *Advanced chemical oxidation: its present role and potential future in hazardous waste treatment.* Waste management, 1993. **13**(5-7): p. 361-377.

211. Andreozzi, R., et al., *Advanced oxidation processes (AOP) for water purification and recovery.* Catalysis today, 1999. **53**(1): p. 51-59.

212. Rush, J.D. and B.H. Bielski, *Pulse radiolytic studies of the reactions of HO2/O2 with Fe (II)/Fe (III) ions. The reactivity of HO2/O2 with ferric ions and its implication on the occurrence of the Haber-Weiss reaction.* J. Phys. Chem.;(United States), 1985. **89**(23).

213. Lindsey, M.E. and M.A. Tarr, *Quantitation of hydroxyl radical during Fenton oxidation following a single addition of iron and peroxide.* Chemosphere, 2000. **41**(3): p. 409-417.

214. Walling, C., *Intermediates in the reactions of Fenton type reagents.* Accounts of Chemical Research, 1998. **31**(4): p. 155-157.

215. Barhoumi, N., et al., *Enhanced degradation of the antibiotic tetracycline by heterogeneous electro-Fenton with pyrite catalysis.* Environmental Chemistry Letters, 2017. **15**: p. 689-693.

216. Buxton, G.V., et al., *Critical Review of rate constants for reactions of hydrated electrons, hydrogen atoms and hydroxyl radicals ($\cdot$ OH/$\cdot$ O− in Aqueous Solution.* Journal of Physical and Chemical Reference Data, 1988. **17**(2): p. 513-886.

217. Walling, C. and A. Goosen, *Mechanism of the ferric ion catalyzed decomposition of hydrogen peroxide. Effect of organic substrates.* Journal of the American Chemical Society, 1973. **95**(9): p. 2987-2991.

218. Wang, S., *A comparative study of Fenton and Fenton-like reaction kinetics in decolourisation of wastewater.* Dyes and Pigments, 2008. **76**(3): p. 714-720.

219. Hussain, S., E. Aneggi, and D. Goi, *Catalytic activity of metals in heterogeneous Fenton-like oxidation of wastewater contaminants: a review.* Environmental Chemistry Letters, 2021. **19**: p. 2405-2424.

220. Oturan, M.A. and J.-J. Aaron, *Advanced oxidation processes in water/wastewater treatment: principles and applications. A review.* Critical Reviews in Environmental Science and Technology, 2014. **44**(23): p. 2577-2641.

221. Ghasemi, H., et al., *Decolorization of wastewater by heterogeneous Fenton reaction using MnO2-Fe3O4/CuO hybrid catalysts.* Journal of Environmental Chemical Engineering, 2021. **9**(2): p. 105091.

222. Babuponnusami, A. and K. Muthukumar, *A review on Fenton and improvements to the Fenton process for wastewater treatment.* Journal of Environmental Chemical Engineering, 2014. **2**(1): p. 557-572.

223. Ma, D., et al., *Critical review of advanced oxidation processes in organic wastewater treatment.* Chemosphere, 2021. **275**: p. 130104.

224. Sayın, F.E., et al., *Treatment of real printing and packaging wastewater by combination of coagulation with Fenton and photo-Fenton processes.* Chemosphere, 2022. **306**: p. 135539.

225. Tanveer, R., et al., *Comparison of ozonation, Fenton, and photo-Fenton processes for the treatment of textile dye-bath effluents integrated with electrocoagulation.* Journal of Water Process Engineering, 2022. **46**: p. 102547.

226. Kim, S.M. and A. Vogelpohl, *Degradation of organic pollutants by the photo-Fenton-process.* Chemical Engineering & Technology: Industrial Chemistry-Plant Equipment-Process Engineering-Biotechnology, 1998. **21**(2): p. 187-191.

227. Wang, F.-X., et al., *Efficient removal of emerging organic contaminants via photo-Fenton process over micron-sized Fe-MOF sheet.* Chemical Engineering Journal, 2022. **429**: p. 132495.

228. Wang, N., et al., *A review on Fenton-like processes for organic wastewater treatment.* Journal of Environmental Chemical Engineering, 2016. **4**(1): p. 762-787.

229. Shokri, A. and M.S. Fard, *A critical review in Fenton-like approach for the removal of pollutants in the aqueous environment.* Environmental Challenges, 2022. **7**: p. 100534.

230. Pereira, M.C., L.C.A. Oliveira, and E. Murad, *Iron oxide catalysts: Fenton and Fentonlike reactions – a review.* Clay Minerals, 2018. **47**(3): p. 285-302.

231. Zubir, N.A., et al., *The sacrificial role of graphene oxide in stabilising a Fenton-like catalyst GO–Fe3O4.* Chemical Communications, 2015. **51**(45): p. 9291-9293.

232. Pinto, I.S.X., et al., *Nanostructured δ-FeOOH: An efficient Fenton-like catalyst for the oxidation of organics in water.* Applied Catalysis B: Environmental, 2012. **119-120**: p. 175-182.

233. Oliveira, H.S., et al., *Nanostructured vanadium-doped iron oxide: catalytic oxidation of methylene blue dye.* New Journal of Chemistry, 2015. **39**(4): p. 3051-3058.

234. Rahim Pouran, S., et al., *Niobium substituted magnetite as a strong heterogeneous Fenton catalyst for wastewater treatment.* Applied Surface Science, 2015. **351**: p. 175-187.

235. Li, Z., J. Lyu, and M. Ge, *Synthesis of magnetic Cu/CuFe2O4 nanocomposite as a highly efficient Fenton-like catalyst for methylene blue degradation.* Journal of Materials Science, 2018. **53**(21): p. 15081-15095.

236. Yang, S.-T., et al., *Fe3O4@SiO2 nanoparticles as a high-performance Fenton-like catalyst in a neutral environment.* RSC Advances, 2015. **5**(7): p. 5458-5463.

237. Shao, Y., et al., *A facile approach to the fabrication of rattle-type magnetic carbon nanospheres for removal of methylene blue in water.* Carbon, 2015. **89**: p. 378-391.

238. Chen, Z., et al., *Noncontact Synergistic Effect between Au Nanoparticles and the Fe2O3 Spindle Inside a Mesoporous Silica Shell as Studied by the Fenton-like Reaction.* Langmuir, 2016. **32**(48): p. 12774-12780.

239. Zhang, J., et al., *One-pot preparation of ternary reduced graphene oxide nanosheets/Fe2O3/polypyrrole hydrogels as efficient Fenton catalysts.* Journal of Colloid and Interface Science, 2017. **505**: p. 130-138.

240. Panda, N., H. Sahoo, and S. Mohapatra, *Decolourization of Methyl Orange using Fenton-like mesoporous Fe2O3–SiO2 composite.* Journal of Hazardous Materials, 2011. **185**(1): p. 359-365.

241. Xu, H.-Y., et al., *Nanoparticles of magnetite anchored onto few-layer graphene: A highly efficient Fenton-like nanocomposite catalyst.* Journal of Colloid and Interface Science, 2018. **532**: p. 161-170.

242. Liu, Y., et al., *NiFe(C2O4)x as a heterogeneous Fenton catalyst for removal of methyl orange.* Journal of Environmental Management, 2017. **192**: p. 150-155.

243. Deng, J., X. Wen, and Q. Wang, *Solvothermal in situ synthesis of Fe3O4-multi-walled carbon nanotubes with enhanced heterogeneous Fenton-like activity.* Materials Research Bulletin, 2012. **47**(11): p. 3369-3376.

244. Ramirez, J.H., et al., *Azo-dye Orange II degradation by heterogeneous Fenton-like reaction using carbon-Fe catalysts.* Applied Catalysis B: Environmental, 2007. **75**(3): p. 312-323.

245. Rache, M.L., et al., *Azo-dye orange II degradation by the heterogeneous Fenton-like process using a zeolite Y-Fe catalyst— Kinetics with a model based on the Fermi's equation.* Applied Catalysis B: Environmental, 2014. **146**: p. 192-200.

246. Luo, W., et al., *Efficient Removal of Organic Pollutants with Magnetic Nanoscaled BiFeO3 as a Reusable Heterogeneous Fenton-Like Catalyst.* Environmental Science & Technology, 2010. **44**(5): p. 1786-1791.

247. Chen, F., et al., *Ionothermal synthesis of Fe3O4 magnetic nanoparticles as efficient heterogeneous Fenton-like catalysts for*

degradation of organic pollutants with H2O2. Journal of Hazardous Materials, 2017. **322**: p. 152-162.

248. Dükkancı, M., et al., *Characterization and catalytic activity of CuFeZSM-5 catalysts for oxidative degradation of Rhodamine 6G in aqueous solutions.* Applied Catalysis B: Environmental, 2010. **95**(3): p. 270-278.

249. Munoz, M., et al., *A ferromagnetic γ-alumina-supported iron catalyst for CWPO. Application to chlorophenols.* Applied Catalysis B: Environmental, 2013. **136-137**: p. 218-224.

250. Xu, L. and J. Wang, *Magnetic Nanoscaled Fe3O4/CeO2 Composite as an Efficient Fenton-Like Heterogeneous Catalyst for Degradation of 4-Chlorophenol.* Environmental Science & Technology, 2012. **46**(18): p. 10145-10153.

251. Xu, L. and J. Wang, *Fenton-like degradation of 2,4-dichlorophenol using Fe3O4 magnetic nanoparticles.* Applied Catalysis B: Environmental, 2012. **123-124**: p. 117-126.

252. Cleveland, V., J.-P. Bingham, and E. Kan, *Heterogeneous Fenton degradation of bisphenol A by carbon nanotube-supported Fe3O4.* Separation and Purification Technology, 2014. **133**: p. 388-395.

253. He, J., et al., *Heterogeneous Fenton oxidation of catechol and 4-chlorocatechol catalyzed by nano-Fe3O4: Role of the interface.* Chemical Engineering Journal, 2014. **258**: p. 433-441.

254. Do, Q.C., D.-G. Kim, and S.-O. Ko, *Nonsacrificial Template Synthesis of Magnetic-Based Yolk–Shell Nanostructures for the Removal of Acetaminophen in Fenton-like Systems.* ACS Applied Materials & Interfaces, 2017. **9**(34): p. 28508-28518.

255. Wu, D., et al., *Enhanced oxidation of chloramphenicol by GLDA-driven pyrite induced heterogeneous Fenton-like reactions at alkaline condition.* Chemical Engineering Journal, 2016. **294**: p. 49-57.

256. Diao, Z.-H., et al., *Enhanced catalytic degradation of ciprofloxacin with FeS2/SiO2 microspheres as heterogeneous Fenton catalyst: Kinetics, reaction pathways and mechanism.* Journal of Hazardous Materials, 2017. **327**: p. 108-115.

257. Chong, S., et al., *Diclofenac degradation in water by FeCeOx catalyzed H2O2: Influencing factors, mechanism and pathways.* Journal of Hazardous Materials, 2017. **334**: p. 150-159.

258. Sun, S.-P., X. Zeng, and A.T. Lemley, *Nano-magnetite catalyzed heterogeneous Fenton-like degradation of emerging contaminants carbamazepine and ibuprofen in aqueous suspensions and montmorillonite clay slurries at neutral pH.* Journal of Molecular Catalysis A: Chemical, 2013. **371**: p. 94-103.

259. Wan, Z. and J. Wang, *Degradation of sulfamethazine antibiotics using Fe3O4–Mn3O4 nanocomposite as a Fenton-like catalyst.*

Journal of Chemical Technology & Biotechnology, 2017. **92**(4): p. 874-883.

260. Wang, G., et al., *Removal of norfloxacin by surface Fenton system (MnFe2O4/H2O2): Kinetics, mechanism and degradation pathway.* Chemical Engineering Journal, 2018. **351**: p. 747-755.

261. Liu, W., et al., *Hydrothermal Synthesis of FeS2 as a High-Efficiency Fenton Reagent to Degrade Alachlor via Superoxide-Mediated Fe(II)/Fe(III) Cycle.* ACS Applied Materials & Interfaces, 2015. **7**(51): p. 28534-28544.

262. Yu, L., et al., *Efficient removal of atrazine in water with a Fe3O4/MWCNTs nanocomposite as a heterogeneous Fenton-like catalyst.* RSC Advances, 2015. **5**(57): p. 46059-46066.

263. Kim, E.-J., et al., *Manganese oxide nanorods as a robust Fenton-like catalyst at neutral pH: Crystal phase-dependent behavior.* Catalysis Today, 2017. **282**: p. 71-76.

264. Tušar, N.N., et al., *Manganese Functionalized Silicate Nanoparticles as a Fenton-Type Catalyst for Water Purification by Advanced Oxidation Processes (AOP).* Advanced Functional Materials, 2012. **22**(4): p. 820-826.

265. Fathy, N.A., et al., *Oxidative degradation of RB19 dye by a novel γ-MnO2/MWCNT nanocomposite catalyst with H2O2.* Journal of Environmental Chemical Engineering, 2013. **1**(4): p. 858-864.

266. Xu, Y., et al., *Efficient photocatalytic removal of orange II by a Mn3O4–FeS2/Fe2O3 heterogeneous catalyst.* Journal of Environmental Management, 2020. **253**: p. 109695.

267. Sui, M., et al., *Ordered mesoporous manganese oxide as catalyst for hydrogen peroxide oxidation of norfloxacin in water.* Chinese Journal of Catalysis, 2013. **34**(3): p. 536-541.

268. Lyu, L., L. Zhang, and C. Hu, *Enhanced Fenton-like degradation of pharmaceuticals over framework copper species in copper-doped mesoporous silica microspheres.* Chemical Engineering Journal, 2015. **274**: p. 298-306.

269. Fink, L., I. Dror, and B. Berkowitz, *Enrofloxacin oxidative degradation facilitated by metal oxide nanoparticles.* Chemosphere, 2012. **86**(2): p. 144-149.

270. Wu, X., F. Xia, and Z. Nan, *Facile synthesis of double-mesoporous-shelled hollow spheres of Cu–CuFe2O4/SiO2 composite as excellent Fenton catalyst.* Materials Chemistry and Physics, 2020. **242**: p. 122490.

271. Do, Q.C., D.-G. Kim, and S.-O. Ko, *Catalytic activity enhancement of a Fe3O4@SiO2 yolk-shell structure for oxidative degradation of acetaminophen by decoration with copper.* Journal of Cleaner Production, 2018. **172**: p. 1243-1253.

272. Ji, P., et al., *Ce3+-Centric Organic Pollutant Elimination by CeO2 in the Presence of H2O2.* ChemCatChem, 2010. **2**(12): p. 1552-1554.

273. Zhang, N., et al., *Critical role of oxygen vacancies in heterogeneous Fenton oxidation over ceria-based catalysts.* Journal of Colloid and Interface Science, 2020. **558**: p. 163-172.

274. Gao, P., et al., *Oxygen vacancy enhancing the Fe2O3-CeO2 catalysts in Fenton-like reaction for the sulfamerazine degradation under O2 atmosphere.* Chemosphere, 2019. **228**: p. 521-527.

275. Zhang, N., et al., *Ceria accelerated nanoscale zerovalent iron assisted heterogenous Fenton oxidation of tetracycline.* Chemical Engineering Journal, 2019. **369**: p. 588-599.

276. Lin, Q., et al., *Electro-optics of perovskite solar cells.* Nature Photonics, 2015. **9**(2): p. 106-112.

277. Park, N.-G., *Perovskite solar cells: an emerging photovoltaic technology.* Materials today, 2015. **18**(2): p. 65-72.

278. Nazeeruddin, M.K., E. Baranoff, and M. Grätzel, *Dye-sensitized solar cells: a brief overview.* Solar energy, 2011. **85**(6): p. 1172-1178.

279. Hagfeldt, A., et al., *Dye-sensitized solar cells.* Chemical reviews, 2010. **110**(11): p. 6595-6663.

280. Nozik, A.J., *Quantum dot solar cells.* Physica E: Low-dimensional Systems and Nanostructures, 2002. **14**(1-2): p. 115-120.

281. Kamat, P.V., *Quantum dot solar cells. Semiconductor nanocrystals as light harvesters.* The Journal of Physical Chemistry C, 2008. **112**(48): p. 18737-18753.

282. Chopra, K., P. Paulson, and V. Dutta, *Thin-film solar cells: an overview.* Progress in Photovoltaics: Research and applications, 2004. **12**(2-3): p. 69-92.

283. Green, M.A., *The path to 25% silicon solar cell efficiency: History of silicon cell evolution.* Progress in Photovoltaics: Research and Applications, 2009. **17**(3): p. 183-189.

284. Perlin, J., *Silicon solar cell turns 50*. 2004, National Renewable Energy Lab., Golden, CO.(US).

285. Winter, M. and R.J. Brodd, *What are batteries, fuel cells, and supercapacitors?* 2004, ACS Publications.

286. Linden, D., *Handbook of batteries and fuel cells.* mgh, 1984.

287. Ishihara, T. and T. Ishihara, *Nanomaterials for advanced electrode of low temperature solid oxide fuel cells (SOFCs).* Journal of the Korean Ceramic Society, 2016. **53**(5): p. 469-477.

288. Abdalla, A.M., et al., *Nanomaterials for solid oxide fuel cells: a review.* Renewable and Sustainable Energy Reviews, 2018. **82**: p. 353-368.

289. Bagotsky, V.S., *Fuel cells: problems and solutions*. Vol. 56. 2012: John Wiley & Sons.

290. Carrette, L., K. Friedrich, and U. Stimming, *Fuel cells-fundamentals and applications.* Fuel cells, 2001. **1**(1): p. 5-39.

291. Gayner, C. and K.K. Kar, *Recent advances in thermoelectric materials.* Progress in Materials Science, 2016. **83**: p. 330-382.

292. Chen, G., et al., *Recent developments in thermoelectric materials.* International materials reviews, 2003. **48**(1): p. 45-66.
293. Dineva, P., et al., *Piezoelectric materials*. 2014: Springer.
294. Uchino, K., *Advanced piezoelectric materials: Science and technology*. 2017: Woodhead Publishing.
295. Yu, A., et al., *Progress in triboelectric materials: toward high performance and widespread applications.* Advanced Functional Materials, 2019. **29**(41): p. 1900098.
296. Andreani, L.C., et al., *Silicon solar cells: toward the efficiency limits.* Advances in Physics: X, 2019. **4**(1): p. 1548305.
297. Bhattacharya, S. and S. John, *Beyond 30% conversion efficiency in silicon solar cells: a numerical demonstration.* Scientific reports, 2019. **9**(1): p. 1-15.
298. Katagiri, H., et al., *Development of CZTS-based thin film solar cells.* Thin Solid Films, 2009. **517**(7): p. 2455-2460.
299. Ramanujam, J., et al., *Flexible CIGS, CdTe and a-Si: H based thin film solar cells: A review.* Progress in Materials Science, 2020. **110**: p. 100619.
300. Wang, W., et al., *Device characteristics of CZTSSe thin-film solar cells with 12.6% efficiency.* Advanced Energy Materials, 2014. **4**(7): p. 1301465.
301. Mathew, S., et al., *Dye-sensitized solar cells with 13% efficiency achieved through the molecular engineering of porphyrin sensitizers.* Nature chemistry, 2014. **6**(3): p. 242-247.
302. Urbani, M., et al., *Phthalocyanines for dye-sensitized solar cells.* Coordination Chemistry Reviews, 2019. **381**: p. 1-64.
303. Zhao, W., et al., *Molecular optimization enables over 13% efficiency in organic solar cells.* Journal of the American Chemical Society, 2017. **139**(21): p. 7148-7151.
304. Kaltenbrunner, M., et al., *Ultrathin and lightweight organic solar cells with high flexibility.* Nature communications, 2012. **3**(1): p. 1-7.
305. Green, M.A., A. Ho-Baillie, and H.J. Snaith, *The emergence of perovskite solar cells.* Nature photonics, 2014. **8**(7): p. 506-514.
306. Eperon, G.E., et al., *Inorganic caesium lead iodide perovskite solar cells.* Journal of Materials Chemistry A, 2015. **3**(39): p. 19688-19695.
307. Lin, J., et al., *Thermochromic halide perovskite solar cells.* Nature materials, 2018. **17**(3): p. 261-267.
308. Jiang, Q., et al., *Planar-structure perovskite solar cells with efficiency beyond 21%.* Advanced materials, 2017. **29**(46): p. 1703852.
309. Zheng, X., et al., *Managing grains and interfaces via ligand anchoring enables 22.3%-efficiency inverted perovskite solar cells.* Nature Energy, 2020. **5**(2): p. 131-140.

310. You, P., et al., *Ultrafast laser-annealing of perovskite films for efficient perovskite solar cells.* Energy & Environmental Science, 2020. **13**(4): p. 1187-1196.

311. Ahmad, M.S., A.K. Pandey, and N. Abd Rahim, *Advancements in the development of TiO2 photoanodes and its fabrication methods for dye sensitized solar cell (DSSC) applications. A review.* Renewable and Sustainable Energy Reviews, 2017. **77**: p. 89-108.

312. Hegazy, A., et al., *TiO2 nanoparticles optimized for photoanodes tested in large area Dye-sensitized solar cells (DSSC).* Solar Energy Materials and Solar Cells, 2016. **153**: p. 108-116.

313. Vittal, R. and K.-C. Ho, *Zinc oxide based dye-sensitized solar cells: A review.* Renewable and Sustainable energy reviews, 2017. **70**: p. 920-935.

314. Ramasamy, E. and J. Lee, *Ordered mesoporous SnO2– based photoanodes for high-performance dye-sensitized solar cells.* The Journal of Physical Chemistry C, 2010. **114**(50): p. 22032-22037.

315. Xiao, J., et al., *CdS/CdSe co-sensitized solar cells based on a new SnO2 photoanode with a three-dimensionally interconnected ordered porous structure.* The Journal of Physical Chemistry C, 2014. **118**(8): p. 4007-4015.

316. Zhou, L., et al., *High light absorption and charge separation efficiency at low applied voltage from Sb-doped SnO2/BiVO4 core/shell nanorod-array photoanodes.* Nano letters, 2016. **16**(6): p. 3463-3474.

317. Younas, M., et al., *Fabrication of cost effective and efficient dye sensitized solar cells with WO3-TiO2 nanocomposites as photoanode and MWCNT as Pt-free counter electrode.* Ceramics International, 2019. **45**(1): p. 936-947.

318. Roy, A., et al., *Incorporating Solution-Processed Mesoporous WO3 as an Interfacial Cathode Buffer Layer for Photovoltaic Applications.* The Journal of Physical Chemistry A, 2020.

319. Nunes, B.N., et al., *Nb2O5 dye-sensitized solar cells*, in *Nanomaterials for Solar Cell Applications*. 2019, Elsevier. p. 287-322.

320. Ou, J.Z., et al., *Elevated temperature anodized Nb2O5: a photoanode material with exceptionally large photoconversion efficiencies.* ACS nano, 2012. **6**(5): p. 4045-4053.

321. Ghosh, R., et al., *Nanoforest Nb2O5 photoanodes for dye-sensitized solar cells by pulsed laser deposition.* ACS Applied Materials & Interfaces, 2011. **3**(10): p. 3929-3935.

322. Lim, S.P., et al., *Boosting photovoltaic performance of dye-sensitized solar cells using silver nanoparticle-decorated N, S-Co-doped-TiO 2 photoanode.* Scientific reports, 2015. **5**: p. 11922.

323. Gupta, A., et al., *Novel synergistic combination of Cu/S co-doped TiO2 nanoparticles incorporated as photoanode in dye sensitized solar cell.* Solar Energy, 2020. **203**: p. 296-303.

324. Ünlü, B. and M. Özacar, *Effect of Cu and Mn amounts doped to TiO2 on the performance of DSSCs.* Solar Energy, 2020. **196**: p. 448-456.

325. Zhang, J., et al., *Effect of cerium doping in the TiO2 photoanode on the electron transport of dye-sensitized solar cells.* The Journal of Physical Chemistry C, 2012. **116**(36): p. 19182-19190.

326. Sengupta, D., et al., *Effects of doping, morphology and film-thickness of photo-anode materials for dye sensitized solar cell application–A review.* Renewable and Sustainable Energy Reviews, 2016. **60**: p. 356-376.

327. Wang, R., et al., *Highly Transparent, Thermally Stable, and Mechanically Robust Hybrid Cellulose-Nanofiber/Polymer Substrates for the Electrodes of Flexible Solar Cells.* ACS Applied Energy Materials, 2020. **3**(1): p. 785-793.

328. Hashemi, S.A., S. Ramakrishna, and A.G. Aberle, *Recent progress in flexible–wearable solar cells for self-powered electronic devices.* Energy & Environmental Science, 2020. **13**(3): p. 685-743.

329. Roldán-Carmona, C., et al., *Flexible high efficiency perovskite solar cells.* Energy & Environmental Science, 2014. **7**(3): p. 994-997.

330. Fu, X., et al., *Flexible solar cells based on carbon nanomaterials.* Carbon, 2018. **139**: p. 1063-1073.

331. Miyazaki, T., A. Akisawa, and T. Kashiwagi, *Energy savings of office buildings by the use of semi-transparent solar cells for windows.* Renewable energy, 2005. **30**(3): p. 281-304.

332. Kang, S.B., et al., *Stretchable and colorless freestanding microwire arrays for transparent solar cells with flexibility.* Light: Science & Applications, 2019. **8**(1): p. 1-13.

333. Husain, A.A., et al., *A review of transparent solar photovoltaic technologies.* Renewable and sustainable energy reviews, 2018. **94**: p. 779-791.

334. Zhang, X., et al., *Extremely lightweight and ultra-flexible infrared light-converting quantum dot solar cells with high power-per-weight output using a solution-processed bending durable silver nanowire-based electrode.* Energy & Environmental Science, 2018. **11**(2): p. 354-364.

335. Kang, S., et al., *Ultrathin, lightweight and flexible perovskite solar cells with an excellent power-per-weight performance.* Journal of Materials Chemistry A, 2019. **7**(3): p. 1107-1114.

336. Zhang, Y., et al., *Solution-Processed Transparent Electrodes for Emerging Thin-Film Solar Cells.* Chemical Reviews, 2020. **120**(4): p. 2049-2122.

337. Kim, B.J., et al., *Highly efficient and bending durable perovskite solar cells: toward a wearable power source.* Energy & Environmental Science, 2015. **8**(3): p. 916-921.

338. Pu, X., et al., *Wearable power-textiles by integrating fabric triboelectric nanogenerators and fiber-shaped dye-sensitized solar cells.* Advanced Energy Materials, 2016. **6**(20): p. 1601048.

339. Kirubakaran, A., S. Jain, and R. Nema, *A review on fuel cell technologies and power electronic interface.* Renewable and Sustainable Energy Reviews, 2009. **13**(9): p. 2430-2440.

340. Linden, D. *Handbook of batteries*. in *Fuel and energy abstracts*. 1995.

341. Armand, M. and J.-M. Tarascon, *Building better batteries.* nature, 2008. **451**(7179): p. 652-657.

342. Whittingham, M.S., *Inorganic nanomaterials for batteries.* Dalton Transactions, 2008(40): p. 5424-5431.

343. Jiang, C., E. Hosono, and H. Zhou, *Nanomaterials for lithium ion batteries.* Nano Today, 2006. **1**(4): p. 28-33.

344. Bruce, P.G., B. Scrosati, and J.-M. Tarascon, *Nanomaterials for Rechargeable Lithium Batteries.* Angewandte Chemie International Edition, 2008. **47**(16): p. 2930-2946.

345. Sun, Y., N. Liu, and Y. Cui, *Promises and challenges of nanomaterials for lithium-based rechargeable batteries.* Nature Energy, 2016. **1**(7): p. 16071.

346. Jin, T., et al., *1D Nanomaterials: Design, Synthesis, and Applications in Sodium–Ion Batteries.* Small, 2018. **14**(2): p. 1703086.

347. Lu, Y., et al., *Graphene-Based Nanomaterials for Sodium-Ion Batteries.* Advanced Energy Materials, 2018. **8**(17): p. 1702469.

348. Slater, M.D., et al., *Sodium-Ion Batteries.* Advanced Functional Materials, 2013. **23**(8): p. 947-958.

349. Vaalma, C., et al., *A cost and resource analysis of sodium-ion batteries.* Nature Reviews Materials, 2018. **3**(4): p. 18013.

350. Hwang, J.-Y., S.-T. Myung, and Y.-K. Sun, *Sodium-ion batteries: present and future.* Chemical Society Reviews, 2017. **46**(12): p. 3529-3614.

351. Müller, S., F. Holzer, and O. Haas, *Optimized zinc electrode for the rechargeable zinc–air battery.* Journal of Applied Electrochemistry, 1998. **28**(9): p. 895-898.

352. Wang, L., et al., *Nitrogen-doped hierarchically porous carbon networks: synthesis and applications in lithium-ion battery, sodium-ion battery and zinc-air battery.* Electrochimica Acta, 2016. **219**: p. 592-603.

353. Zang, W., et al., *Single Co Atoms Anchored in Porous N-Doped Carbon for Efficient Zinc–Air Battery Cathodes.* ACS Catalysis, 2018. **8**(10): p. 8961-8969.

354. Simon, P., Y. Gogotsi, and B. Dunn, *Where do batteries end and supercapacitors begin?* Science, 2014. **343**(6176): p. 1210-1211.

355. Wang, H., et al., *Multifunctional inorganic nanomaterials for energy applications.* Nanoscale, 2020. **12**(1): p. 14-42.

356. Lu, M., *Supercapacitors: materials, systems, and applications*. 2013: John Wiley & Sons.

357. González, A., et al., *Review on supercapacitors: Technologies and materials.* Renewable and Sustainable Energy Reviews, 2016. **58**: p. 1189-1206.

358. Zhang, S. and N. Pan, *Supercapacitors performance evaluation.* Advanced Energy Materials, 2015. **5**(6): p. 1401401.

359. Liu, Y., R. Wang, and X. Yan, *Synergistic effect between ultra-small nickel hydroxide nanoparticles and reduced graphene oxide sheets for the application in high-performance asymmetric supercapacitor.* Scientific reports, 2015. **5**: p. 11095.

360. Wang, Y., et al., *CeO 2 nanoparticles/graphene nanocomposite-based high performance supercapacitor.* Dalton Transactions, 2011. **40**(24): p. 6388-6391.

361. Xu, X., et al., *Structural and chemical synergistic effect of NiCo2S4 nanoparticles and carbon cloth for high performance binder-free asymmetric supercapacitors.* Applied Surface Science, 2019. **465**: p. 635-642.

362. Li, J., et al., *Porous Fe2O3 nanospheres anchored on activated carbon cloth for high-performance symmetric supercapacitors.* Nano Energy, 2019. **57**: p. 379-387.

363. Kesavan, T., et al., *Hierarchical nanoporous activated carbon as potential electrode materials for high performance electrochemical supercapacitor.* Microporous and Mesoporous Materials, 2019. **274**: p. 236-244.

364. Wei, H., et al., *Advanced porous hierarchical activated carbon derived from agricultural wastes toward high performance supercapacitors.* Journal of Alloys and Compounds, 2020. **820**: p. 153111.

365. Gamby, J., et al., *Studies and characterisations of various activated carbons used for carbon/carbon supercapacitors.* Journal of power sources, 2001. **101**(1): p. 109-116.

366. Yu, D. and L. Dai, *Self-assembled graphene/carbon nanotube hybrid films for supercapacitors.* The Journal of Physical Chemistry Letters, 2010. **1**(2): p. 467-470.

367. An, K.H., et al., *Electrochemical properties of high-power supercapacitors using single-walled carbon nanotube electrodes.* Advanced functional materials, 2001. **11**(5): p. 387-392.

368. Fan, Z., et al., *A three-dimensional carbon nanotube/graphene sandwich and its application as electrode in supercapacitors.* Advanced materials, 2010. **22**(33): p. 3723-3728.

369. Adusei, P.K., et al., *Fabrication and study of supercapacitor electrodes based on oxygen plasma functionalized carbon nanotube fibers.* Journal of Energy Chemistry, 2020. **40**: p. 120-131.

370. Mapleback, B.J., et al., *Structural composite supercapacitor using carbon nanotube mat electrodes with interspersed metallic iron nanoparticles.* Electrochimica Acta, 2020. **331**: p. 135233.

371. Yan, J., et al., *Fast and reversible surface redox reaction of graphene–MnO2 composites as supercapacitor electrodes.* Carbon, 2010. **48**(13): p. 3825-3833.

372. Cao, X., et al., *Preparation of novel 3D graphene networks for supercapacitor applications.* small, 2011. **7**(22): p. 3163-3168.

373. Liu, C., et al., *Graphene-based supercapacitor with an ultrahigh energy density.* Nano letters, 2010. **10**(12): p. 4863-4868.

374. Wang, Y., et al., *Supercapacitor devices based on graphene materials.* The Journal of Physical Chemistry C, 2009. **113**(30): p. 13103-13107.

375. Li, S., et al., *Three-dimensional porous carbon/Co3O4 composites derived from graphene/Co-MOF for high performance supercapacitor electrodes.* Applied Surface Science, 2020. **503**: p. 144090.

376. Hu, C.-C., et al., *Design and tailoring of the nanotubular arrayed architecture of hydrous RuO2 for next generation supercapacitors.* Nano letters, 2006. **6**(12): p. 2690-2695.

377. Subramanian, V., et al., *Mesoporous anhydrous RuO2 as a supercapacitor electrode material.* Solid State Ionics, 2004. **175**(1-4): p. 511-515.

378. Jiang, Q., et al., *All pseudocapacitive MXene-RuO2 asymmetric supercapacitors.* Advanced Energy Materials, 2018. **8**(13): p. 1703043.

379. Edison, T.N.J.I., R. Atchudan, and Y.R. Lee, *Facile synthesis of carbon encapsulated RuO2 nanorods for supercapacitor and electrocatalytic hydrogen evolution reaction.* International Journal of Hydrogen Energy, 2019. **44**(4): p. 2323-2329.

380. Jeon, S., et al., *RuO2 Nanorods on Electrospun Carbon Nanofibers for Supercapacitors.* ACS Applied Nano Materials, 2020. **3**(4): p. 3847-3858.

381. Yi, T.-F., et al., *Construction of spherical NiO@ MnO2 with core-shell structure obtained by depositing MnO2 nanoparticles on NiO nanosheets for high-performance supercapacitor.* Ceramics International, 2020. **46**(1): p. 421-429.

382. Zhao, Z., et al., *Facile fabrication of binder-free reduced graphene oxide/MnO2/Ni foam hybrid electrode for high-performance supercapacitors.* Journal of Alloys and Compounds, 2020. **812**: p. 152124.

383. Chen, S., et al., *Graphene oxide– MnO2 nanocomposites for supercapacitors.* ACS nano, 2010. **4**(5): p. 2822-2830.

384. Yuan, C., et al., *Facile synthesis and self-assembly of hierarchical porous NiO nano/micro spherical superstructures for high*

performance supercapacitors. Journal of Materials Chemistry, 2009. **19**(32): p. 5772-5777.

385.   Kim, S.-I., et al., *Facile route to an efficient NiO supercapacitor with a three-dimensional nanonetwork morphology.* ACS applied materials & interfaces, 2013. **5**(5): p. 1596-1603.

386.   Xiong, S., et al., *A high-performance hybrid supercapacitor with NiO derived NiO@ Ni-MOF composite electrodes.* Electrochimica Acta, 2020: p. 135956.

387.   Jayalakshmi, M. and K. Balasubramanian, *Simple capacitors to supercapacitors-an overview.* Int. J. Electrochem. Sci, 2008. **3**(11): p. 1196-1217.

388.   Chen, Z., et al., *High-performance supercapacitors based on intertwined CNT/V2O5 nanowire nanocomposites.* Advanced materials, 2011. **23**(6): p. 791-795.

389.   Saravanakumar, B., K.K. Purushothaman, and G. Muralidharan, *Interconnected V2O5 nanoporous network for high-performance supercapacitors.* ACS applied materials & interfaces, 2012. **4**(9): p. 4484-4490.

390.   Hu, B., et al., *La-doped V2O5·nH2O@OAB and flexible Fe2O3@rGO as binder-free thin film electrodes for asymmetric supercapacitors.* Chemical Engineering Journal, 2020. **389**: p. 123534.

391.   Lu, X., et al., *Flexible solid-state supercapacitors: design, fabrication and applications.* Energy & Environmental Science, 2014. **7**(7): p. 2160-2181.

392.   Liu, L., et al., *Wearable energy-dense and power-dense supercapacitor yarns enabled by scalable graphene–metallic textile composite electrodes.* Nature Communications, 2015. **6**(1): p. 7260.

393.   Muralee Gopi, C.V.V., et al., *Recent progress of advanced energy storage materials for flexible and wearable supercapacitor: From design and development to applications.* Journal of Energy Storage, 2020. **27**: p. 101035.

394.   Radhika, S.P., K.J. Sreeram, and B.U. Nair, *Rare earth doped cobalt aluminate blue as an environmentally benign colorant.* Journal of Advanced Ceramics, 2012. **1**(4): p. 301-309.

395.   Hedayati, H.R., et al., *Synthesis and characterization of Co1−xZnxCr2−yAlyO4 as a near-infrared reflective color tunable nano-pigment.* Dyes and Pigments, 2015. **113**: p. 588-595.

396.   Ianoş, R., et al., *Combustion synthesis of a blue Co-doped zinc aluminate near-infrared reflective pigment.* Dyes and Pigments, 2017. **142**: p. 24-31.

397.   Li, J., et al., *From Serendipity to Rational Design: Tuning the Blue Trigonal Bipyramidal Mn3+ Chromophore to Violet and Purple through Application of Chemical Pressure.* Inorganic Chemistry, 2016. **55**(19): p. 9798-9804.

398. Han, A., et al., *Crystal structure and optical properties of YMnO3 compound with high near-infrared reflectance.* Solar Energy, 2013. **91**: p. 32-36.

399. Jose, S., et al., *YIn0.9Mn0.1O3–ZnO nano-pigment exhibiting intense blue color with impressive solar reflectance.* Dyes and Pigments, 2016. **124**: p. 120-129.

400. Jose, S. and M.L. Reddy, *Lanthanum–strontium copper silicates as intense blue inorganic pigments with high near-infrared reflectance.* Dyes and Pigments, 2013. **98**(3): p. 540-546.

401. Liang, S.-t., et al., *Preparation of Cr2O3-based pigments with high NIR reflectance via thermal decomposition of CrOOH.* Transactions of Nonferrous Metals Society of China, 2015. **25**(8): p. 2646-2647.

402. Tao, Z., et al., *A novel pyrophosphate BaCr2(P2O7)2 as green pigment with high NIR solar reflectance and durable chemical stability.* Solid State Sciences, 2014. **34**: p. 78-84.

403. Jose, S., et al., *Green colored nano-pigments derived from Y2BaCuO5: NIR reflective coatings.* Dyes and Pigments, 2014. **107**: p. 118-126.

404. Wang, J.-L., et al., *Synthesis and characterization of NiTiO3 yellow nano pigment with high solar radiation reflection efficiency.* Powder Technology, 2013. **235**: p. 303-306.

405. He, X., et al., *Fabrication of highly dispersed NiTiO3@TiO2 yellow pigments with enhanced NIR reflectance.* Materials Letters, 2017. **208**: p. 82-85.

406. Sameera, S.F., et al., *Potential NIR Reflecting Yellow Pigments in (BiV)1−x(YNb)xO4 Solid Solutions.* Chemistry Letters, 2013. **42**(5): p. 521-523.

407. Vishnu, V. and M. Reddy, *Near-infrared reflecting inorganic pigments based on molybdenum and praseodymium doped yttrium cerate: Synthesis, characterization and optical properties.* Solar Energy Materials and Solar Cells - SOLAR ENERG MATER SOLAR CELLS, 2011. **95**: p. 2685-2692.

408. Han, A., et al., *Estimating thermal performance of cool coatings colored with high near-infrared reflective inorganic pigments: Iron doped La2Mo2O7 compounds.* Energy and Buildings, 2014. **84**: p. 698-703.

409. Li, Y.-Q., et al., *Highly Solar Radiation Reflective Cr2O3–3TiO2 Orange Nanopigment Prepared by a Polymer-Pyrolysis Method.* ACS Sustainable Chemistry & Engineering, 2014. **2**(2): p. 318-321.

410. García, A., et al., *Ceramic pigments based on chromium doped alkaline earth titanates.* Ceramics International, 2013. **39**(4): p. 4125-4132.

411. Liu, L., et al., *The evaluation of thermal performance of cool coatings colored with high near-infrared reflective nano-brown inorganic pigments: Magnesium doped ZnFe2O4 compounds.* Solar Energy, 2015. **113**: p. 48-56.

412. George, G., V.S. Vishnu, and M.L.P. Reddy, *The synthesis, characterization and optical properties of silicon and praseodymium doped Y6MoO12 compounds: Environmentally benign inorganic pigments with high NIR reflectance.* Dyes and Pigments, 2011. **88**(1): p. 109-115.

413. Schildhammer, D., et al., *Synthesis and characterization of a new high NIR reflective ytterbium molybdenum oxide and related doped pigments.* Dyes and Pigments, 2017. **138**: p. 90-99.

414. Huang, B., et al., *Environment-friendly pigments based on praseodymium and terbium doped La2Ce2O7 with high near-infrared reflectance: Synthesis and characterization.* Dyes and Pigments, 2017. **147**: p. 225-233.

415. Chen, J., et al., *Near infrared reflective pigments based on Bi3YO6 for heat insulation.* Ceramics International, 2020. **46**(15): p. 24575-24584.

416. Elakkiya, V. and S. Sumathi, *Vanadium and bismuth doped FePO4 as Near Infra Red (NIR) reflective pigment for energy saving application.* Materials Chemistry and Physics, 2022. **290**: p. 126561.

417. Thejus, P.K., K.V. Krishnapriya, and K.G. Nishanth, *NIR reflective, anticorrosive magenta pigment for energy saving sustainable building coatings.* Solar Energy, 2021. **222**: p. 103-114.

418. Ianoş, R., et al., *Near-infrared reflective Ni, La-doped hibonite pigments for cool blue coatings.* Ceramics International, 2022. **48**(23, Part A): p. 34428-34436.

419. Divya, S. and S. Das, *New red pigments based on Li3AlMnO5 for NIR reflective cool coatings.* Ceramics International, 2021. **47**(21): p. 30381-30390.

420. Moriomoto, T., et al., *Novel near-infrared reflective black inorganic pigment based on cerium vanadate.* RSC Advances, 2022. **12**(26): p. 16570-16575.

421. Zhou, W., et al., *Synthesis and characterization of novel yellow-green Al-doped Y3Fe5O12 nano-pigments with high NIR reflectance.* Journal of Alloys and Compounds, 2022. **896**: p. 162883.

422. Gramm, G., et al., *Development of High NIR-Reflective Red Li2MnO3 Pigments.* Zeitschrift für anorganische und allgemeine Chemie, 2020. **646**(21): p. 1722-1729.

423. Ding, C., et al., *V-doped LaPO4 new solar heat-reflective pigments and its improvement on the aging resistance of poly-methyl methacrylate.* Solar Energy, 2020. **195**: p. 660-669.

424. Li, Y., et al., *A promising inorganic YFeO3 pigments with high near-infrared reflectance and infrared emission.* Solar Energy, 2021. **226**: p. 180-191.

Chapter 2

Materials and Methods
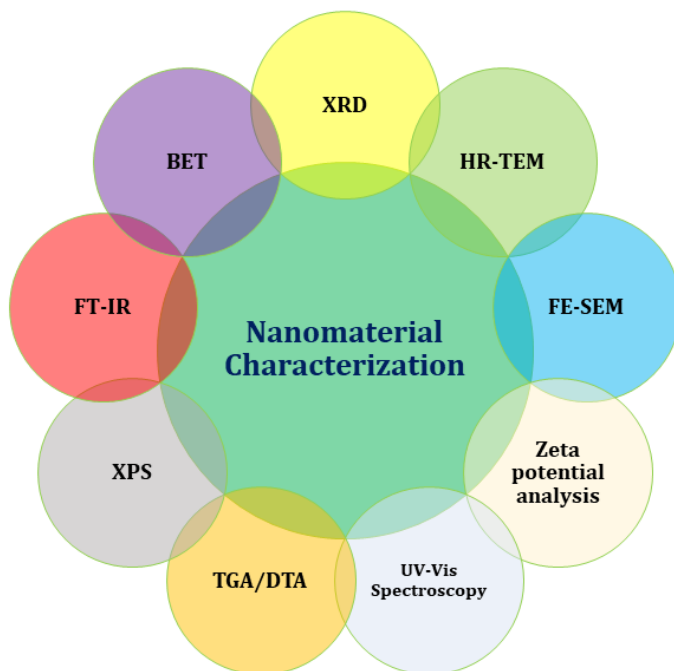
An overview of the materials and methods utilised in the investigations are described here. The basic principles behind the nanomaterial characterization techniques are incorporated in this chapter. Detailed procedures for adsorption studies, Fenton-like catalytic studies and NIR reflecting pigment characterisation are discussed.

2.1 Introduction

The chemicals, synthetic routes, characterisation techniques and analysis methods determine the overall solution to a research problem under investigation. The present work involves mainly the synthesis of nanomaterials for environmental and energy-saving applications. This chapter discusses the nanomaterial synthesis strategies used, characterisation details and experimental procedures for specific applications. The materials and synthetic routes were chosen to get the best performance towards specific applications.

2.2 Materials used

Cerium nitrate ($Ce(NO_3)_3.6H_2O$)(Aldrich 99 %) and Erbium nitrate ($Er(NO_3)_3.5H_2O$)(Sigma Aldrich 99.9 %) were used as the metal precursors for sol-gel and sol-hydrothermal synthesis of pure and Er^{3+} doped CeO_2. NH_4OH (Merck Emplura, 25 %) was used as the precipitating agent. Congo red purchased from Himedia was used as such for the adsorption studies.

Cerium nitrate ($Ce(NO_3)_3.6H_2O$) (Aldrich 99 %) and Magnesium nitrate ($Mg(NO_3)_2.6H_2O$ (Nice chemicals) were used as the precursors for Mg^{2+} doped CeO_2 synthesis along with NH_4OH (Merck Emplura, 25%) as the precipitating agent. For Fe_3O_4 synthesis, $FeCl_3.6H_2O$ (Qualigens), Ethylene glycol (Merck Emplura), Sodium acetate (Nice chemicals) and PEG (poly-ethylene glycol) (Merck) were used. Malachite green (Nice chemicals) was used to carry out adsorption studies using $Fe_3O_4@Mg^{2+}$ doped CeO_2 core shells.

Spent Zinc carbon batteries (Panasonic AA cells) were used for the synthesis of ZC BAT. Other reagents used include Hydrochloric acid (HCl)(Merck Emplura 35%), Sulphuric acid (H_2SO_4)(Merck 98%), Hydrogen peroxide (H_2O_2)(Merck Emparta 30%), Acetic acid glacial (CH_3COOH) (Merck Emparta 100%), Methanol (CH_3OH)(Merck 99%) and Ammonium hydroxide (NH_4OH) (Merck Emplura, 25%). Methylene blue (Qualigens), Rhodamine B (Sigma Aldrich), methyl orange (Qualigens) and Congo red (Himedia) were used for adsorption and catalytic studies.

Zinc nitrate ($Zn(NO_3)_2.6H_2O$)(Alfa Aesar 98 %), Titanium isopropoxide ($Ti(OCH(CH_3)_2)_4$)(Aldrich Chemistry 97 %), Cupric nitrate trihydrate ($Cu(NO_3)_2.3H_2O$) (Alfa Aesar 98 %), Ferric nitrate nonahydrate ($Fe(NO_3)_3.9H_2O$)(Alfa Aesar 98 %) and Citric acid monohydrate ($C_6H_8O_7.H_2O$) (Vetec AR 99.5 %) were used as received for the synthesis of NIR reflecting cool pigments. Commercial TiO_2 powder and acrylic repair material (DPI RR cold cure) were used for coating application studies of the developed pigment compositions.

2.3 Experimental procedures

2.3.1 Surface basicity mediated selective adsorption application

2.3.1.1 Synthesis of pure CeO_2 and Er^{3+}doped CeO_2

Pure CeO_2 and Er^{3+}doped CeO_2 were synthesized by two separate synthetic routes via the sol-hydrothermal and aqueous sol-gel methods. 43.2 g of $Ce(NO_3)_3.6H_2O$ (Aldrich 99 %) was stirred in 500 ml distilled water for half an hour to ensure complete dissolution. NH_4OH (Merck Emplura, 25%) solution was then added dropwise to precipitate cerium (IV) hydroxide. The addition of NH_4OH was

continued until the pH attained a value of 10 to ensure that all $Ce(NO_3)_3.6H_2O$ had been precipitated as $Ce(OH)_4$. The precipitate of $Ce(OH)_4$ was centrifuged and washed several times with distilled water. To confirm the absence of nitrate in the precipitate, concentrated H_2SO_4 was added to the centrifugate and the resulting solution was boiled. To this solution, a paper ball was dropped, the absence of brown fumes indicated that the centrifugate was nitrate-free. After achieving nitrate-free centrifugate, the precipitate was then dispersed in 1000 ml distilled water, to this, 10% HCl (Emplura Merck, 35%) was added dropwise until the pH value reached 2. The solution was then stirred for 2 days to obtain the sol. The sol was then divided into two portions. The first portion was used for the synthesis of CeO_2 *via* the hydrothermal method. For this, the sol was transferred into a Teflon-lined stainless-steel autoclave and heated at 150 °C for 48 hours. The components in the autoclave were then transferred into a Petri dish and were dried in an oven set at 150 °C for 2 days to obtain hydrothermally synthesised CeO_2(CeO_2-HT). The second portion of the sol was used for the synthesis of CeO_2 by the aqueous sol-gel method. The sol was dried directly in an oven set at 150 °C for 48 hours. The dried precursor was then calcined at 500 °C for 2 hours and the compound thus obtained is represented as CeO_2-Sol. Er^{3+} doped CeO_2 sol was prepared by the same procedure by adding a calculated quantity (5 mmol) of $Er(NO_3)_3.5H_2O$ into 100 mmol CeO_2 sol. The Er^{3+} doped sol was subjected to both hydrothermal and sol-gel methods to obtain CEr-HT and CEr-Sol samples.

2.3.1.2 *Surface basicity measurements using Temperature Programmed Desorption (TPD)*

CO_2-Temperature Programmed Desorption (TPD) studies were carried out using the BELCAT-M analyser. For this, 0.1 g of the prepared sample was weighed into a quartz tube sample holder and then subjected to pre-treatment at 200 °C for 30 minutes under He atmosphere. The sample was then cooled to room temperature and then CO_2 was passed over the sample for 30 minutes to carry out adsorption. Then it was followed by He purging for another 30 minutes at 50 °C for the removal of physisorbed CO_2 from the sample surface. The desorption measurements were performed by increasing the temperature from 50 °C to 650 °C at a heating rate of 12 K/min. The amount of different types of basic sites was calculated by integrating the CO_2-TPD curves over different temperature ranges of desorption corresponding to very weak, weak, medium and strong basic sites.

2.3.1.3 *Adsorption experiments using pure CeO_2 and Er^{3+}doped CeO_2*

Adsorption studies were carried out on all four synthesized CeO_2 samples ($1g.L^{-1}$) using Congo red as the model pollutant of concentration 20 $mg.L^{-1}$. The adsorption experiments were carried out in magnetically stirred glass vessels at the ambient pH of the Congo red solution. At regular contact intervals, samples were withdrawn, centrifuged and analysed using a Jasco V-770 UV-Vis-NIR spectrophotometer. To evaluate the selectivity, adsorption analysis was made with methylene blue and methyl orange. The effect of dye concentration and pH on adsorption activity was evaluated by varying the initial dye concentrations (10, 15, 20, 25 and 30 $mg.L^{-1}$)

and by carrying out the adsorption studies under 3 different pH conditions (3,6.5 (ambient pH) and 10). Besides this, the pH of the point of zero charge (pH$_{PZC}$) of the adsorbent material was determined using the pH drift method[1]. After the adsorption process, the Congo red adsorbed CeO$_2$ samples were collected and washed several times with distilled water. Then the samples were dried and calcined at 500 °C for 2 hours. The adsorption efficiency of the recycled adsorbents was also determined.

2.3.2 Magnetically retrievable core-shell materials for selective adsorption application

2.3.2.1 Synthesis of CeO$_2$ and Mg^{2+} doped CeO$_2$

Pure and Mg^{2+} doped CeO$_2$ were synthesized by coprecipitation route. For the synthesis of pure CeO$_2$, 1.259g of Ce(NO$_3$)$_3$.6H$_2$O was dissolved in 50 ml of distilled water and NH$_4$OH (Merck Emplura, 25%) solution was then added dropwise to precipitate cerium (IV) hydroxide. The addition of NH$_4$OH was continued until the pH attained a value of 10 to ensure the complete precipitation of Ce(NO$_3$)$_3$.6H$_2$O as Ce(OH)$_4$. Then the precipitate was centrifuged and washed several times with distilled water to completely remove the nitrate ions and then dried in a hot air oven at a temperature of 180 °C for 24 hours. To synthesize Mg^{2+} doped CeO$_2$ *ie* CMg-10, CMg-20 and CMg-30, Mg(NO$_3$)$_2$.6H$_2$O and Ce(NO$_3$)$_3$.6H$_2$O were weighed in the molar ratios 10:100 mmol, 20:100 mmol and 30:100 mmol and dissolved in 50 ml distilled water. Then the complete precipitation of the reactants was attained by the addition of NH$_4$OH. The precipitate was then centrifuged, washed several times with distilled water and dried in a hot air oven at 180 °C.

2.3.2.2 Synthesis of Fe₃O₄ nanoparticles

1.35 g $FeCl_3.6H_2O$ was dissolved in 40 ml of ethylene glycol to form a clear solution. Then 3.6 g of Sodium acetate and 1.0 g of PEG (poly-ethylene glycol) were added into the above solution and stirred for 30 minutes. Then the solution was transferred to a Teflon-lined stainless-steel autoclave and kept at 200 ^{o}C for 8 hours[2, 3]. The autoclave was then cooled to room temperature and its contents were transferred and washed several times with distilled water and ethanol. Then the obtained Fe_3O_4 nanoparticles were dried at 80 ^{o}C for 12 hours.

2.3.2.3 Synthesis of Fe₃O₄@Mg²⁺ doped CeO₂ core-shells

$Fe_3O_4@Mg^{2+}$ doped CeO_2 core-shells having two different compositions were synthesized *ie* Fe@CMg-1:2 having Fe_3O_4: Mg^{2+} doped CeO_2 weight ratio of 1:2 and Fe@CMg-1:3 having Fe_3O_4: Mg^{2+} doped CeO_2 weight ratio of 1:3. For the synthesis of Fe@CMg-1:2, 0.25 g of Fe_3O_4 nanoparticles were thoroughly dispersed in 50ml distilled water by ultrasonication. In the case of Fe@CMg-1:3, the weight of Fe_3O_4 nanoparticles dispersed into 50 ml distilled water is 0.166 g. Then 1.259 g of $Ce(NO_3)_3.6H_2O$ and 0.147 g of $Mg(NO_3)_2.6H_2O$ were dissolved into the above dispersions followed by the slow addition of NH_4OH until the pH of the dispersion reached a value of 10. Then the obtained products were magnetically separated, washed several times with distilled water and then dried at 180 ^{o}C for 12 hours to obtain the core-shell structures.

2.3.2.4 Adsorption studies using $Fe_3O_4@Mg^{2+}$ doped CeO_2 core-shells

Adsorption studies were carried out using Mg^{2+} doped CeO_2 samples (CMg-10, CMg-20 and CMg-30) as well as using the two developed $Fe_3O_4@Mg^{2+}$ doped CeO_2 core-shell compositions. In a typical adsorption experiment, 50 ml malachite green dye solution (2 – 6 mg.L^{-1}) was taken in a 100 ml conical flask, and 25 mg of adsorbent material was added and stirred in a magnetic stirrer with a constant speed of 250 rpm. During regular intervals, the mixture was collected, ultracentrifuged and the supernatant solution was separated and analysed the residual dye concentration at a wavelength of 617 nm using a Jasco V-770 UV-Vis-NIR spectrometer.

The following equations were used for the determination of percentage removal and equilibrium adsorption capacity, q_e

$$\% \ removal = \frac{C_o - C_t}{C_o} \ X \ 100 \qquad (2.1)$$

$$q_e = \frac{(C_o - C_e) \ V}{W} \qquad (2.2)$$

where C_o is the initial dye concentration in mg.L^{-1}, C_t is the dye concentration at time t, C_e is the equilibrium dye concentration, V is the volume of the dye solution in litres and W is the adsorbent weight given in grams. The optimal adsorption conditions were evaluated by varying various parameters such as adsorbent loading, initial dye concentration, contact time and pH. For pH-dependent studies, the pH of the dye solutions was adjusted using 0.1M HCl and 0.1M NaOH solutions. For adsorption isotherm and kinetic studies, the concentration of malachite green varied from 2 to 6 mg.L^{-1}. The experimental adsorption data was then correlated to various

adsorption isotherm and kinetic models by linear regression analysis. The reusability studies were done using magnetically recovered adsorbent materials.

2.3.3 Spent zinc-carbon battery derived magnetically retrievable material for Fenton-like catalyst application

2.3.3.1 Recycling of MnO_2 from spent zinc-carbon batteries

Spent zinc-carbon batteries (Panasonic AA cells) were collected, discharged further and dismantled into various components such as steel casing, cathode material, zinc can (anode) and separators. The obtained cathode material is a mix of oxides of Manganese and activated/graphitic carbon and was washed several times with distilled water. The cathode material was then treated with 5 molar H_2SO_4 for 1 hour and again washed till neutralisation with distilled water, centrifuged and treated with H_2O_2 for 5 hours under constant magnetic stirring to facilitate the oxidation of Mn^{2+} and Mn^{3+} into Mn^{4+}. The obtained graphitic/activated carbon-containing MnO_2 was then centrifuged, separated and dried at 80 °C for 24 hours[4].

2.3.3.2 Synthesis of Fe_3O_4 from steel casing of zinc-carbon battery

The dismantled steel casing from the zinc-carbon battery was cleaned with acetone and cut into small pieces. About 4 g of steel casing pieces were then dissolved in a minimum quantity of hot concentrated HCl. Upon ensuring complete dissolution, the solution was filtered, collected and made up to 100 ml in a standard flask. The solution was then transferred into a beaker and its pH was raised to 9 by the addition of NH_4OH. The controlled pH facilitates the selective precipitation of Fe from a solution containing Fe, Cr and

other trace amounts of metal ions. The obtained precipitates were then collected washed with distilled water several times and then dried at 80 °C for 24 hours to obtain Fe_3O_4 nanoparticles.

2.3.3.3 Synthesis of ZnO from anode zinc can of a zinc carbon battery

About 3 g of the Zinc metal pieces obtained from the dismantled anodic zinc can of zinc carbon battery were cleaned with acetone and dissolved in concentrated HCl to obtain a $ZnCl_2$ solution. The obtained $ZnCl_2$ solution was then filtered and made up to 100 ml in a standard flask. 10 ml of the $ZnCl_2$ solution was then transferred to a pre-weighed crucible and calcined at 300 °C to obtain ZnO nanoparticles. The amount of ZnO nanoparticles that can be prepared from 10 ml of the $ZnCl_2$ solution was thus obtained and thereby the concentration of $ZnCl_2$ solution. Now required volume of $ZnCl_2$ solution was transferred into a beaker followed by the addition of NH_4OH till the complete precipitation of $ZnCl_2$ into $Zn(OH)_2$. The precipitates obtained were washed several times with distilled water and dried at 180 °C for 24 hours to obtain ZnO nanoparticles.

2.3.3.4 Synthesis of ZC BAT nanostructures

To prepare ZC BAT nanostructures, already synthesized MnO_2 and Fe_3O_4 nanoparticles were taken as such. ZC BAT nanostructures have a composition in which MnO_2:Fe_3O_4: ZnO are in the weight ratio 1:1:1.5. As the primary step of ZC BAT synthesis, 0.2 g each of MnO_2 and Fe_3O_4 nanoparticles were weighed and dispersed into 100 ml distilled water by ultrasonication for 15 minutes. The dispersion of MnO_2 and Fe_3O_4 was then kept for stirring and the calculated volume of the already prepared $ZnCl_2$ solution was added into the dispersion

slowly. The volume of $ZnCl_2$ was calculated in such a way as to maintain the weight ratio of 1:1:1.5 between MnO_2: Fe_3O_4: ZnO. Now NH_4OH was added slowly into the dispersion with constant magnetic stirring till the pH reached 9. The mixture was kept stirring for about 30 minutes. The precipitate, which consists of MnO_2 and Fe_3O_4 nanoparticles encapsulated by mesoporous ZnO was then washed several times with distilled water, centrifuged and separated. The products obtained were then dried at 150 ℃ for 12 hours to get the ZC BAT nanostructures.

2.3.3.5 Adsorption Studies using ZC BAT nanostructures

All adsorption studies were carried out at room temperature using MB, RB, MO and CR as the model dyes. The optimum adsorbent dosage was evaluated first by analysing three different adsorbent loadings (500, 1000 and 1500 mg.L^{-1}). The adsorption studies were performed in a 100 ml conical flask in which 50 ml of the model dye solution was taken and 50 mg ZC BAT nanostructures were added followed by constant stirring at 300 rpm for about 180 minutes. The progress of the adsorption process was evaluated using a Jasco V-770 UV-Vis-NIR spectrometer. The effect of initial dye concentration on the adsorption efficiency was evaluated by carrying out the adsorption experiments using various dye concentrations. For MB and RB, the concentrations chosen for investigation are 1,2,3,4 and 5 ppm. In the case of MO, 5, 7.5, 10,12.5 and 15 ppm solutions were used. For CR, 25, 30, 35, 40 and 45 ppm solutions were used. Once the optimum adsorbent dosage and optimum dye concentrations were obtained, the adsorption efficiencies of individual components were also evaluated. The effect of pH on the adsorption efficiencies

was studied by performing the adsorption experiments under three different pH conditions (pH -3, 7 and 10). The pH_{pzc} value was determined using the pH drift method. The desorption studies were performed using a mixture of 20:1 volume ratio mixture of methanol and glacial acetic acid. The adsorbent reusability studies were done by following three steps i) desorption of adsorbed dye molecules from the ZC BAT surface ii) continuous washing with distilled water followed by drying at 150 ℃ iii) performing the next adsorption cycle using the recycled ZC BAT.

2.3.3.6 Catalytic studies using ZC BAT nanostructures

Fenton-like catalytic oxidation of MB, RB, MO and CR by ZC BAT was carried out at room temperature under dark conditions in the presence of H_2O_2. As the preliminary step, the optimum amount of H_2O_2 was determined by performing the catalytic oxidation of dyes in the presence of three different concentrations of H_2O_2 (0.048, 0.098 and 0.146 $mol.L^{-1}$). The catalytic activity of ZC BAT towards each of the dyes was performed by taking 50 ml of the dye solution and 50 mg of ZC BAT nanostructures were dispersed into the dye solution followed by the addition of 0.5 ml H_2O_2 (0.098 $mol.L^{-1}$) with constant stirring. At regular intervals, a fixed amount of the reaction mixture was withdrawn, and the catalyst was removed magnetically before being analysed using a Jasco V-770 UV-Vis-NIR spectrometer. The effect of initial dye concentration and pH on the catalytic efficiency was studied as done in the case of adsorption. Catalytic efficiencies of individual components were also determined. The rate of decomposition of H_2O_2 by MnO_2, Fe_3O_4, ZnO and ZC BAT nanostructures was also examined. For this 0.5 ml H_2O_2 was added

to 50 ml of distilled water followed by 50 mg of the catalyst. The rate of decomposition of H_2O_2 was evaluated by withdrawing fixed amounts of catalyst-dispersed H_2O_2 solution at regular intervals and by titrating it with 2 mmolar $KMnO_4$ solution. The reactive oxygen species responsible for the catalytic degradation of dyes were identified using isopropanol and chloroform as the radical scavengers. The catalytic studies were done in the absence and presence of free radical scavengers (0, 100 and 200 mmoles of isopropanol and chloroform) and the catalytic efficiencies were determined. Desorption studies were done using a mixture of 20:1 volume ratio mixture of methanol and glacial acetic acid. The extent of completion of the catalytic oxidation by ZC BAT was monitored by desorption studies. Very low values of desorption efficiencies can ensure the complete degradation of the dye molecules by Fenton-like catalysis. Reusability studies were also done by magnetic recovery of the catalyst followed by desorption, continuous washing with distilled water and drying at 150 °C.

2.3.4 Energy saving NIR reflecting colour tunable cool pigments application

2.3.4.1 Synthesis of $TiZn_2O_4$ and Cu^{2+} and Fe^{3+} doped $TiZn_2O_4$ compositions

The pigments of formulated stoichiometries were developed by the solution combustion method. Stoichiometric amounts of metal nitrate precursors were dissolved in water and titanium isopropoxide was separately dissolved in a 10% HNO_3 solution followed by mixing with the former solution of metal nitrates. A calculated amount of Citric acid was added as fuel. Then the

precursor solution was placed on a hotplate with constant stirring at a temperature of 250 ℃. Then the reactant mixture slowly transformed into a viscous gel which underwent combustion to form a fluffy voluminous solid. The obtained solids were ground using a mortar and pestle and transferred to crucibles. The finely powdered samples taken in crucibles were then placed in a muffle furnace for calcination at a temperature of 800 ℃ to obtain the pigment powders of desired compositions. The structural compositions of the Cu^{2+} and Fe^{3+} doped series of pigments are given in Table 1 along with their abbreviations.

Table 2.1 – Composition and corresponding abbreviations of developed $TiZn_2O_4$-based pigments

Composition	Abbreviation
$TiZn_2O_4$	TZ
$TiZn_{1.8}Cu_{0.2}O_4$	TZC-0.2
$TiZn_{1.6}Cu_{0.4}O_4$	TZC-0.4
$TiZn_{1.4}Cu_{0.6}O_4$	TZC-0.6
$TiZn_{1.2}Cu_{0.8}O_4$	TZC-0.8
$TiZn_1Cu_1O_4$	TZC-1
$TiZn_{1.8}Fe_{0.2}O_{4.1}$	TZF-0.2
$TiZn_{1.6}Fe_{0.4}O_{4.2}$	TZF-0.4
$TiZn_{1.4}Fe_{0.6}O_{4.3}$	TZF-0.6
$TiZn_{1.2}Fe_{0.8}O_{4.4}$	TZF-0.8
$TiZn_1Fe_1O_{4.5}$	TZF-1

2.3.4.2 Preparation of coatings and NIR reflecting cool pigment application studies

Selected pigment compositions were used to make NIR-reflecting coatings over concrete and Aluminium sheets. The preparation of NIR reflecting coating was done in two steps. The first step involves the coating of concrete cement block/Al sheet with TiO_2, which is a highly NIR-reflecting pigment. In the next step, the designed pigments are coated onto the TiO_2-precoated concrete/Al sheets. For this, the developed pigments are mixed with acrylic-acralyn emulsion in a weight ratio of 1:1. The mixture is ultrasonicated thoroughly for 30 minutes to ensure the even dispersion of the pigment particles in the binder. The resultant emulsion was coated onto a TiO_2-coated concrete/ Al sheet and was allowed to dry in the air. The concrete coatings were then subjected to solar reflectance measurements and chromatic studies using ASTM standard number G173-03 model and CIE 1976 *L*a*b** colour scheme respectively.

The thermal shielding effect of the developed pigment compositions was evaluated by an experimental setup. The setup consists of two foam boxes (8 X 8 X 8 cm) with Al sheet roofing of dimension 10 X 10 cm coated with the developed pigments as per the procedure mentioned above. A thermocouple was inserted into the foam box just 2 cm below the roof. The foam boxes with pigment-coated roofs were then placed under an IR lamp (Philips, 250 watts), 40 cm below, for 1 hour. The temperatures were recorded at 10-minute intervals.

2.3.4.3 *Near Infrared (NIR) reflectance measurements and CIELAB colour characterisation.*

The developed pigment samples and pigment coatings were subjected to near-infrared measurements according to the ASTM standard number G173-03. By using the integrating sphere attachment along with Teflon (poly-tetrafluoroethylene) as the reference standard, the diffuse reflectance measurements were carried out in the visible-near infrared range of 700-2500 nm with a measurement interval of 5 nm. The calculation of the NIR solar reflectance (R*) was done according to the equation

$$R* = \frac{\int_{700}^{2500} r(\lambda) i(\lambda) d(\lambda)}{\int_{700}^{2500} i(\lambda) d(\lambda)} \qquad (2.3)$$

where $r(\lambda)$ is the spectral reflectance of sample obtained experimentally and $i(\lambda)$ is the standard solar spectral irradiance ($Wm^{-2} mm^{-1}$) according to ASTM standard model G173-03[5].

The chromatic characteristics were calculated using the CIE 1976 L*a*b* colour scheme of Commission Internationale De l'eclairage (CIE)[6]. Here L* represents the lightness scale which ranges from 0 (black) to 100 (white). The transition from green (-ve) to red (+ve) is represented by a* coordinate and b* gives blue (-ve) to yellow (+ve) transition. Another factor c* known as chroma represents the saturation of colour and was calculated using the equation

$$C* = [(a*)^2 + (b*)^2]^{1/2} \qquad (2.4)$$

The hue angle h^o is expressed in degrees and ranges from 0° to 360° and is calculated using the formula,

$$h^o = \tan^{-1}(b*/a*) \qquad (2.5)$$

2.4 Characterisation Techniques

2.4.1 X-Ray Diffraction Analysis (XRD)

X-ray diffraction can be regarded as the best available technique for availing information like crystal structure, chemical composition, size of the crystallites, lattice parameters and phase purity of a material. XRD is a widely employed non-destructive analysis technique which can be applied to a broad range of materials such as solids, powders, films, nanomaterials and liquids. The principle of X-ray diffraction is the constructive interference between a crystalline sample and monochromatic X-rays. The crystalline planes can act as three-dimensional diffraction gratings for X-rays having wavelengths similar to their interplanar spacings leading to constructive and destructive interference. The obtained diffraction pattern can be interpreted with the help of Bragg's law which is given by

$$2d\sin\theta = n\,\lambda \qquad (2.6)$$

Here d is the interplanar spacing, θ is the angle of incidence, n is an integer and λ is the wavelength of X-ray used. Constructive interference occurs upon incident of X-rays on the sample, when the path difference is a multiple of X-ray wavelength λ. Thus sharp intensities result only at angles where Bragg's law holds and these measured intensities provide information about the structure, phase, lattice parameters, specific orientations and crystallinity of the sample. An X-ray diffractometer consists of an X-ray source, a sample holder and a detector. The sample is irradiated by X-rays produced from the source and the diffracted rays then reach the

detector. To change the diffraction angle, the source and detector are moved, intensities are collected and diffraction data is obtained. The main applications of XRD analysis involve microstructure analysis and phase change studies. XRD analysis was used as the fundamental characterisation technique throughout this work. The phase purity, extent of doping and lattice parameters were confirmed through XRD analysis.

2.4.2 Fourier Transform- Infra Red Spectroscopy (FT-IR)

Infrared spectroscopy involves the interaction between infrared radiation and matter. Covalent bonds present in a molecule will selectively absorb infrared radiations and change the vibrational energy. The nature of the vibrational transition depends on the atoms involved in the bond and thus different bonding species and functional groups will have different frequencies of absorption. So different molecules having different structures will give rise to distinct infrared spectra which can act as their characteristic fingerprints. Fourier Transform- Infra Red Spectroscopy is faster, more precise and sensitive than conventional infrared spectroscopy. Fourier transform is a mathematical function which converts waves from the time domain to the frequency domain. In this work FTIR spectroscopy was employed to understand the interactions between adsorbent and adsorbates, to identify the surface functional groups and to indicate the possible surface changes before and after the adsorption process.

2.4.3 UV-Visible Spectroscopy

The interaction of ultraviolet and visible light with matter is the subject of UV-Visible spectroscopy. The amount of light absorbed by a sample at various ultraviolet and visible wavelengths can be assessed using UV-Visible spectroscopy. From the UV-Visible absorption spectra, both qualitative as well as quantitative information regarding the samples can be availed. Thus UV-Visible spectroscopy can be used in the identification and estimation of chemical species. The basic principle behind UV-Visible spectroscopy is the Beer-Lambert law which is given by

$$A = \varepsilon c l \qquad\qquad (2.7)$$

where ε is the molar extinction coefficient which is a constant indicating the extent of absorption of a particular wavelength by the sample, c is the concentration in moles.L^{-1} and l is the path length in cm. The main instrumental parts of a UV-Visible spectrometer consist of a light source, a monochromator, a quartz cuvette (sample holder) and a detector. Depending on the optical arrangement, single-beam and double-beam UV-Visible spectrometers are available. In both cases, light from the light source reaches the monochromator and gets dispersed using a diffraction grating into monochromatic light. The sample is then irradiated with the monochromatic light and the transmitted light is detected which gives transmittance(I/I_0). In the case of double beam spectrometers, a beam splitter is employed to split the monochromatic radiation into two, one of which passes through the sample and the other through the reference. Here both I and I_0 can be determined

simultaneously using optical bifurcation. In this work, UV-Visible spectroscopy was utilized mainly to monitor the progress of the adsorption and catalytic processes. Adsorption and catalytic degradation efficiencies were estimated using UV-Visible spectroscopy.

2.4.4 UV-Visible-NIR Diffuse Reflectance Spectroscopy (DRS)

Diffuse Reflectance is a widely used method for the determination of material spectroscopic information by employing ultraviolet, visible and near-infrared radiations. When light falls on a material, apart from absorption and transmission, reflection also occurs. There are two types of reflection, specular and diffuse reflection. When the angle of reflection is the same as the angle of incidence it is a specular reflection. When the angle of reflection is different from the angle of incidence, it is a diffused reflection. The surface-reflected electromagnetic radiations are collected and interpreted into reflectance spectra. An integrating sphere is used to record diffuse reflectance spectra. The integrating sphere collects most of the diffuse reflected light from the sample to achieve a better measurement of the sample spectra. An integrating sphere consists of a spherical cavity coated by highly light-reflecting materials such as Barium sulphate. For the diffuse reflectance measurement, the sample is placed at the reflectance port of the integrating sphere. The reflected light from the sample undergoes a series of reflections inside the integrating sphere before it reaches the detector. The baseline measurements are carried out by using Barium sulphate or Teflon as the standard. A Kubelka-Munk conversion is employed to

transform the diffuse reflectance spectra equivalent to the transmission spectra. The Kubelka-Munk function is given by

$$F(R) = \frac{(1-R)^2}{2R} = \frac{k}{s} \qquad (2.8)$$

where R is the reflectance, k is the molar absorption coefficient and s is the scattering coefficient. The precise determination of the band gap of materials was done using the Kubelka-Munk remission function. The bandgap E_g is given by

$$E_g = \frac{hc}{\lambda} \qquad (2.9)$$

2.4.5 Field Emission Scanning Electron Microscopy (FE-SEM)

To overcome the resolution limitations of conventional microscopes, electron microscopes were developed. Since electrons have smaller wavelengths, they can achieve better resolutions. In Scanning Electron Microscopy (SEM) the surface of the sample is irradiated with a focused beam of high-energy electrons and the interactions between the sample and electrons yield valuable information on the morphology, chemical composition, orientation and crystallinity of the samples under analysis. The main components of a Scanning Electron Microscope involve an electron source or electron gun, electromagnetic lenses, a sample stage and detectors. In SEM, the electrons from the electron source are accelerated towards the sample through a set of electromagnetic lenses to produce a focused beam scanning over the sample surface. As the electron beam scans the sample surface, due to electron-sample interactions, secondary electrons and backscattered electrons are generated along with characteristic x-rays. These signals are collected separately by

detectors and are interpreted into high-resolution images. While secondary electrons give information on surface morphology, backscattered electrons can display contrasts between various phases in images. Characteristic x-rays yield information about the chemical composition of the sample. Field Emission Scanning Electron Microscopes can give images with higher depth of field, better resolution and less electrostatical distortion. In FE-SEM, the electron consists of a field emission cathode capable of producing narrow beams of both high and low energies.

2.4.6 High-Resolution Transmission Electron Microscopy (HR-TEM)

Transmission Electron Microscopes (TEM) employ a beam of electrons to visually probe specimens to capture highly magnified images. TEM analysis is an inevitable tool used widely for the characterisation of nanostructures as well as for the determination of elemental composition and electronic structure. The basic working principle of TEM includes the generation of a high-energy electron beam from an electron gun and the stream of electrons is accelerated towards the sample using an applied potential. The electron beam is then focused on the sample utilizing electromagnetic lenses and apertures. Upon striking the sample, a major portion of the beam gets transmitted through the sample. The transmitted beam is again focussed using objective lenses to form an image. The image is enlarged and produced over a screen using a combination of electromagnetic lenses known as intermediate and projector lenses. Thus HR-TEM is a well-established characterisation technique which can help to understand material strcutures down to

atomic arrangements. Such a detailed understanding of material structures is very essential in nanomaterial synthesis.

2.4.7 BET Surface Area Analysis

The surface area and porosity of the developed nanomaterials play a crucial role in their adsorption and catalytic efficiency. BET surface area analysis is used to get insights into the surface characteristics of materials. The BET (Brunauer, Emmett and Teller) theory is given by the equation

$$\frac{p}{v_{total}(p_o - p)} = \frac{1}{v_{mono}c} + \frac{c-1}{v_{mono}c}\left(\frac{p}{p_o}\right) \qquad (2.10)$$

where v_{total} is the volume of gas adsorbed at pressure p, v_{mono} is the volume of the gas molecules adsorbed in the case of monolayer coverage and c is a constant, characteristic of the gas. The BET equation forms the basis of BET surface area analysis. During BET analysis, an inert gas such as nitrogen is passed over the sample surface and the resultant monolayer formation and adsorption rate are used to estimate the specific surface area and porosity of the sample. The BET analysis involves the measurement of an adsorption isotherm which gives a plot of relative pressure against the amount of gas molecules adsorbed. The various steps involved in a BET measurement are transferring the samples into a sample container followed by pretreatment by outgassing to remove adsorbed impurities and other gases. Then the pressure is increased slowly measuring the amount of gas adsorbed at each stage and allowing the system to attain equilibrium before each increment. The saturation vapour pressure is also measured alongside. Usually,

the BET surface area analyser employs nitrogen as the adsorbate at the boiling temperature of liquid nitrogen.

2.4.8 X-ray Photoelectron Spectroscopy (XPS)

X-ray Photoelectron Spectroscopy (XPS) is a surface-sensitive non-destructive characterisation technique which can provide relevant information on elemental composition, quantitative surface composition and the chemical oxidation states of various elements. With the help of XPS, material surfaces can be probed up to 10 nm thickness and elemental information can be obtained. The basic principle behind X-ray Photoelectron Spectroscopy (XPS) is the photoelectric effect. According to Einstein's description of the photo-electric effect, when a material is irradiated with electromagnetic radiation having energy higher than the binding energy of electrons in that material, photoelectrons are ejected from the material. The kinetic energy of the ejected photoelectrons is proportional to the frequency of the incident electromagnetic radiation. Also, the kinetic energies of the ejected photoelectrons can be related to the binding energies of electrons present at different energy levels according to the equation

$$E_{kinetic} = h\nu - E_{binding} - \phi \qquad (2.11)$$

Where $E_{kinetic}$ is the kinetic energy of the ejected photoelectron, $h\nu$ is the known energy of the x-rays used, $E_{binding}$ is the binding energy of that specific electron and ϕ is the work function of the material. Thus, the energies of the emitted photoelectrons are characteristic of constituent elements of the material. An XPS give binding energy values on the x-axis plotted against measured photoelectron counts

on the y-axis. XPS analysis has been employed in various research fields such as adsorption, catalysis, corrosion etc.

2.4.9 Thermogravimetric Analysis (TGA)

Thermogravimetric Analysis (TGA) is the most widely used technique for the thermal stability estimation of materials. In thermogravimetry, the variation of weight of the material under investigation is evaluated as a function of temperature or time after subjecting it to a controlled temperature programme under specific atmospheric conditions. In summary, the increase or decrease in weight of the sample is measured during a heating or cooling process. The thermogravimetric analyser consists of a sample pan residing inside a furnace capable of both heating and cooling. The sample is connected to a high precision balance and the atmosphere within the furnace can be regulated by purging either reactive or inert gases. The resultant plot will have weight percentage on the Y-axis and temperature or time on the X-axis. A TGA plot can give information on material stability, quantitative composition, dehydration, pyrolysis, oxidation, carbon/filler content, thermogravimetric kinetics and interactions with reactive gases.

2.4.10 Zeta Potential Analysis

Zeta potential is one of the important physical properties of particles, suspensions, macromolecules and material surfaces which can influence the stability of nanodispersions and their interactions with other chemical species. When nanoparticles form a dispersion, the liquid layer surrounding the nanoparticles forms two regions, a stern layer where ionic species are strongly bound and a diffused

layer where ions are loosely bound. Another boundary exists within the diffused layer within which particles and ions remain associated. When the particle moves, the species within this boundary remain attached to the core. Zeta potential is the potential of this boundary. The zeta potential value predicts the stability of colloids as well as the possible interactions of material surfaces with other chemical entities. The zeta potential values can be directly correlated to the electrophoretic mobility of the particles. In a zeta potential analyser, the electrophoretic mobility is measured with the help of a laser source. The laser source illuminates the sample cell. The sample cell is placed between two electrodes and upon applying an electric field, the particles move within the sample cell by electrophoresis and the electrophoretic mobility is estimated from the scattered light reaching the detector. The electrophoretic mobility can give the zeta potential value of the sample under investigation.

2.5 References

1. Xie, A., et al., *Hierarchical porous carbon materials derived from a waste paper towel with ultrafast and ultrahigh performance for adsorption of tetracycline.* RSC Advances, 2016. **6**(77): p. 72985-72998.
2. Kozakova, Z., et al., *The formation mechanism of iron oxide nanoparticles within the microwave-assisted solvothermal synthesis and its correlation with the structural and magnetic properties.* Dalton Transactions, 2015. **44**(48): p. 21099-21108.
3. Namikuchi, E.A., et al., *PEG size effect and its interaction with Fe3O4 nanoparticles synthesized by solvothermal method: morphology and effect of pH on the stability.* Nano Express, 2021. **2**(2): p. 020022.
4. Mekhalfi, H., et al., *Recycling of manganese dioxide from spent Zn–MnO 2 cells.* Russian Journal of Applied Chemistry, 2015. **88**: p. 879-884.
5. Marzo, A., et al. *Comparison of Atacama desert solar spectra vs. ASTM G173–03 reference spectra for solar energy application.* in *Conference Proceedings EuroSun*. 2016.

6.   Millard, R., R. Peterson, and B. Hunter, *CAS: 528: DyaK2MXosFOks7s% 3D: Study of the cubic to tetragonal transition in Mg2TiO4 and Zn2TiO4 spinels by17O MAS NMR and Rietveld refinement of X-ray diffraction data. vol. 80.* Am Mineral, 1995: p. 885-896.

Chapter 3

Surface Basicity Mediated Rapid and Selective Adsorptive Removal of Congo Red Over Nanocrystalline Mesoporous CeO$_2$
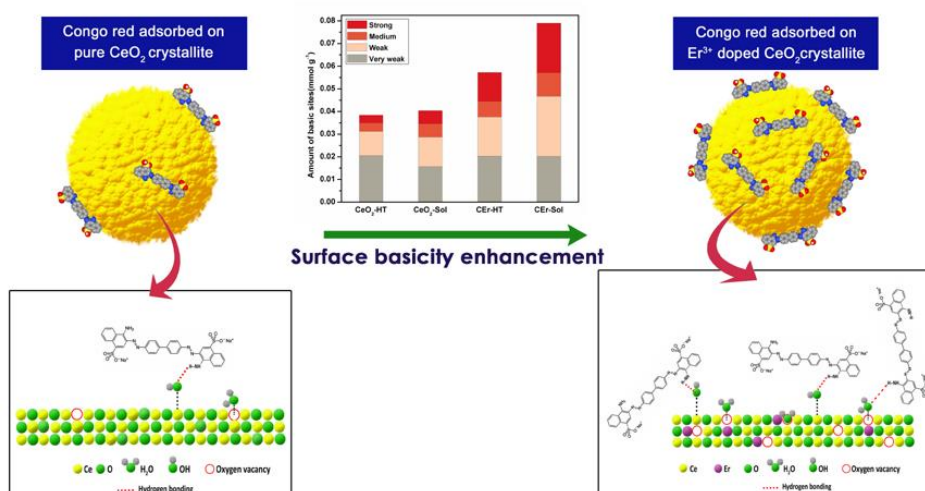
The role of surface features in controlling the selectivity and efficiency of adsorption is well known. Nevertheless, the possibility of tuning the adsorption capacity and selectivity of adsorbents through their surface characteristics remained less explored. In this work, the surface basicity of mesoporous CeO$_2$ nanoparticles was improved by Er^{3+} doping under two different reaction conditions via; sol-gel and sol-hydrothermal methods. The nature and amount of surface basic sites were determined with the help of CO$_2$ Temperature Programmed Desorption (TPD). The adsorption capacity and selectivity of the four different CeO$_2$ samples were investigated using Congo red, methyl orange, and methylene blue as the model pollutants.

3.1 Introduction

CeO$_2$ is one of the most widely employed semiconducting metal oxides in the field of catalysis and environmental remediation [1-5], mainly due to (i) it's high abundance and low cost[6], (ii) wide band-gap, non-toxicity and high stability[7], (iii) tendency for oxygen uptake into the lattice and the possibility of reversible transition redox system between Ce^{+3} and Ce^{+4} [8, 9] and (iv) the chance of formation of solid solutions with other oxides [6]. CeO$_2$ has already emerged as a promising choice for a wide range of catalytic processes such as; promoter in three-way catalysts in automobiles[10, 11], solid oxide fuel cells [12, 13], reforming of hydrocarbons [14-16], water gas shift reaction [17-19], CO oxidation [20-22], catalytic combustion of volatile organic compounds (VOC's) [23-26], hydrogenation of alkynes [27, 28], syngas conversion to alcohols [29], thermochemical water splitting [30, 31], photocatalysis[32-34] *etc*. Nevertheless, efforts to further improve its catalytic efficiency are still in progress[35]. Besides this, the environmental remediation applications of CeO$_2$ mainly include photocatalytic degradation[36, 37] and adsorptive removal of pollutants from water resources [38, 39]. Textile and dyestuff industries are one of the major sources of water pollution, as they release these dye species into water resources. The total world production of dyes is around 700000 tonnes annually. About 10-15 % of these dyes are lost during their application and a major share is discharged into water bodies. Many of these dyes have a very complex chemical structure and are found to be non-biodegradable. Studies revealed that many of these dyes are carcinogenic and

mutagenic in nature. In addition, the dyes may be present in different forms in different aqueous environments. In such cases we should be able to tune our remediation technique according to the requirements of the target dye molecules. For *e.g.* Congo red is such a widely employed benzidine-based azo dye for various applications such as textiles, printing, plastics, rubber and dyeing industries. Due to high water solubility, Congo red can disperse easily into water resources. Also depending on pH, Congo red is capable of being present in different ionic forms in water. Such a malign and widely distributed water pollutant should be treated individually by highly efficient means[40-42]. Adsorptive removal is one such effective way to remove organic pollutants. While developing the adsorbent material, we have in mind Congo red as our target pollutant.

The adsorption capacity and selectivity of an adsorbent depend on several factors such as high surface area, porosity, amount of surface active sites, pH, electrostatic interaction between the adsorbent surface and dye species, weak interactions such as hydrogen bonding between adsorbent and dye molecules [43, 44]. The adsorption capacity and selectivity of adsorbents can be controlled by the effective tuning of the above factors, especially by regulating surface features. Tailoring surface features according to the requirements of pollutants is our objective.

The present work aims at understanding, analysing and correlating the surface characteristics of CeO_2 with its adsorption capacity and selectivity towards Congo red. The surface characteristics under investigation are surface area, porosity, surface basicity and

hydrogen bonding. Variations in surface characteristics were brought by doping Er^{3+} into the CeO_2 lattice under two different reaction conditions via sol-gel and sol-hydrothermal methods. Er^{3+} doping succeeded in improving surface features such as surface area, porosity, and surface basicity and thereby the weak interactions between CeO_2 surface and Congo red molecules. The effect of improved surface features was then correlated with the adsorption ability of CeO_2. In this work, surface features of CeO_2 were tuned to develop highly efficient and selective adsorbents for Congo red adsorption and removal. This work aims at maximizing the adsorption efficiency and selectivity of CeO_2 with minimum modifications. This work will prompt future investigators to see adsorption, also from the perspective of surface basicity.

3.2 Results and Discussions

3.2.1 XRD

Pure CeO_2 and Er^{3+} doped CeO_2 were synthesized via hydrothermal and aqueous sol-gel methods. The PXRD pattern of all the samples synthesized is given in **Figure 3.1**. As shown in **Figure 3.1**, well-defined peaks are obtained for all samples. The peaks can be indexed to the cubic fluorite structure of CeO_2 (JCPDS 34–0394) belonging to the Fm3m space group[7]. Characteristic reflections of the (111), (200), (220), (311), (222) and (400) planes are indicated in **Figure 3.1**. A small shift in the peaks towards the lower 2θ for Er^{3+}doped samples was observed in the PXRD pattern, this can be attributed to the increased ionic size of Er^{3+}compared to Ce^{4+}(Ionic radii of Ce = 97 pm; Er = 100.4 pm). The crystallite size of the synthesized

samples determined from the Scherrer equation is reported in **Table 3.1.**
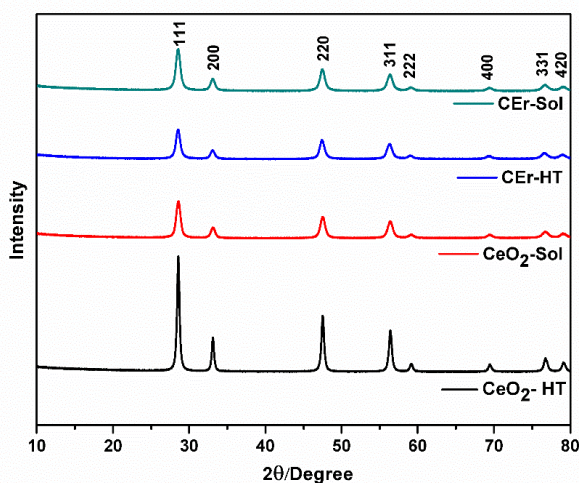
Figure 3.1 - X-ray diffraction patterns of pure CeO_2 and Er^{3+} doped CeO_2 samples prepared by aqueous sol-gel and hydrothermal methods.

Table 3.1 - Calculated crystallite sizes of pure CeO_2 and Er^{3+} doped CeO_2 samples prepared by sol-gel and hydrothermal methods.

Samples	Crystallite Size (nm)
CeO_2-HT	19.48
CeO_2-Sol	10.74
CEr-HT	10.69
CEr-Sol	11.11

From the crystallite size values, it is evident that CeO_2-HT has the largest crystallite size compared to other samples. This is due to the

enhanced Ostwald ripening and oriented attachment in hydrothermally synthesized samples [45]. However, in the case of CEr-HT, a reduction in the crystallite size was observed which may be due to the inhibition of crystal growth caused by the dopant Er^{3+}. The presence of Er^{3+} in between the Ce^{4+} ions has a significant role in decreasing the frequency of collisions between the ceria particles. As the collisions decrease, oriented attachment and Ostwald ripening rate diminish, resulting in smaller crystallite size. At the same time, crystal growth takes place in a normal manner in the case of CeO_2-Sol and CEr-Sol where strict conditions of pressure and temperature are absent. Thus, the crystal growth conditions are almost the same for CeO_2-Sol and CEr-Sol.

3.2.2 FE-SEM
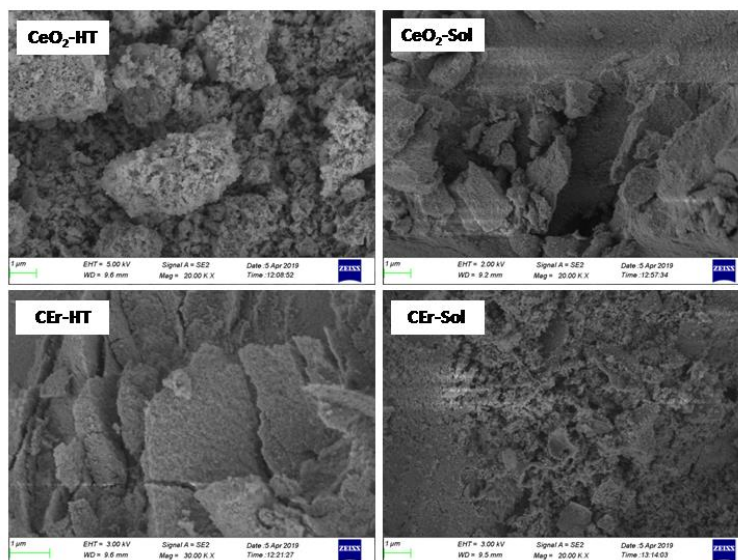
Figure 3.2 – FE-SEM micrographs of pure CeO_2 and Er^{3+} doped CeO_2 samples prepared by sol-gel and hydrothermal methods.

The Field Emission Scanning Electron Microscope (FE-SEM) micrographs of the synthesized samples are given in **Figure 3.2**. An idea about the surface morphology and extent of agglomeration can be obtained from the FE-SEM images. SEM images of CeO_2-HT show large-sized aggregates, distinct from one another. At the same time, CEr-HT exhibits a porous flakes-like structure. The SEM images of pure CeO_2 and Er^{3+} doped CeO_2 particles synthesized via the sol-gel method indicate that CEr-sol exhibits a highly porous appearance and relatively smaller agglomerates when compared to CeO_2-Sol.

3.2.3 HR-TEM

HR-TEM analysis of CeO_2-Sol and CEr-Sol was performed to further confirm the trend observed in crystallite sizes. HR-TEM images of CeO_2 –Sol is given in **Figure 3.3**. The average particle size was found to be 9.93 nm. The SAED patterns can be indexed to (111), (200) and (220) planes. The calculated d spacing for the (111) plane is 3.14 Å in CeO_2-Sol. HR-TEM images of CEr-Sol are shown in **Figure 3.4**. In this case, the average particle size was found to be 12.18 nm. Here the calculated d spacing for the (111) plane is 3.20 Å which is greater than that observed in CeO_2-Sol. This can be attributed to the doping of relatively larger Er^{3+} ions into the CeO_2 lattice. The well-defined fringes in **Figures 3.3b and 3.4b** showed the mesoporous nature of the CeO_2 prepared and it is also well evidenced from the pore size obtained from the BET measurements.
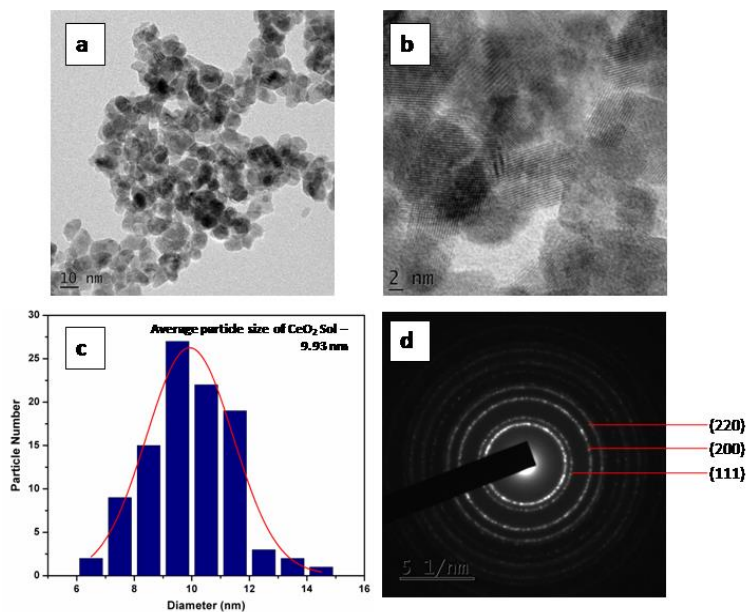
Figure 3.3 - a, b) HR-TEM images c) particle size distribution and d) SAED pattern of CeO$_2$-Sol.
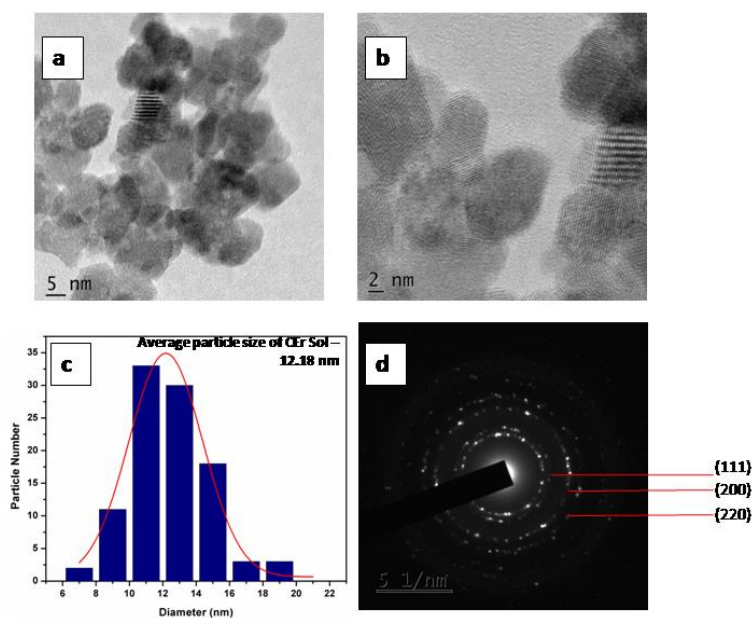
Figure 3.4 - a, b) HR-TEM images c) particle size distribution and d) SAED pattern of CEr-Sol.

3.2.4 BET surface area analysis
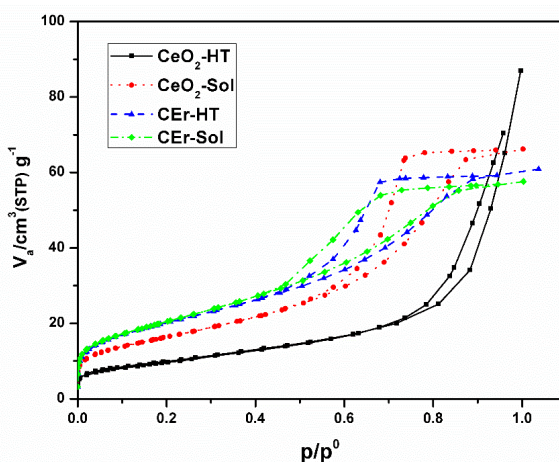
Figure 3.5 - N_2 adsorption isotherms of pure and Er^{3+} doped CeO_2 samples prepared by aqueous sol-gel and hydrothermal methods.

The N_2 adsorption isotherms of the synthesized samples are given in **Figure 3.5**. Parameters such as surface area, pore volume and pore diameters of the synthesized samples were analysed using the BET technique and are tabulated in **Table 3.2**. The Er^{3+} doped CeO_2 samples were found to have a higher surface area than pure CeO_2. Among the samples synthesized, sol-gel derived samples exhibited higher surface areas compared to their hydrothermal analogues. In the case of hydrothermally synthesized samples, CEr-HT exhibited almost double the surface area of CeO_2-HT. This can be partly correlated to the higher crystallite size of CeO_2-HT particles which may result in a decrease in the surface area. The additional enhancement in surface areas of the Er^{3+} doped samples can be the result of oxygen vacancies generated and enriched interconnected pore networks present in them. All the samples synthesized were

mesoporous as evident from their pore size which lies in the range of 4 – 14 nm [46].

Table 3.2. Surface area parameters of pure CeO_2 and Er^{3+} doped CeO_2 samples prepared by aqueous sol-gel and hydrothermal methods

Samples	BET surface area ($m^2.g^{-1}$)	Total pore volume ($cm^3.g^{-1}$)	Pore diameter (nm)
CeO_2-HT	35.114	0.1278	14.563
CeO_2-Sol	58.769	0.102	6.9446
CEr-HT	72.073	0.0929	5.1561
CEr-Sol	73.668	0.0888	4.8198

The mesoporous nature is also evident from the fact that all the samples exhibit type IV adsorption isotherms[47]. According to the IUPAC classification of adsorption hysteresis loops, the loops of CeO_2-Sol, CEr-Sol and CEr-HT belong to type H2[48], which arise from porous materials having networks of interconnected pores of progressive sizes and shapes. At the same time, CeO_2-HT exhibits type H3 adsorption hysteresis loop which is characteristic of materials with slit-shaped pores[49].

3.2.5 FT-IR Spectroscopy

Here we have recorded the FT-IR spectra of all the CeO_2 samples prepared and are given in **Figure 3.6**. In the FT-IR spectra, the broad absorption band within 3400-3450 cm^{-1} corresponds to the OH stretching vibrations of adsorbed H_2O on the sample surfaces[50]. Again the transmission bands at 1380 and 1625 cm^{-1} correspond to

the H-O-H bend mode which confirms the presence of adsorbed moisture and surface hydroxyls in the samples.
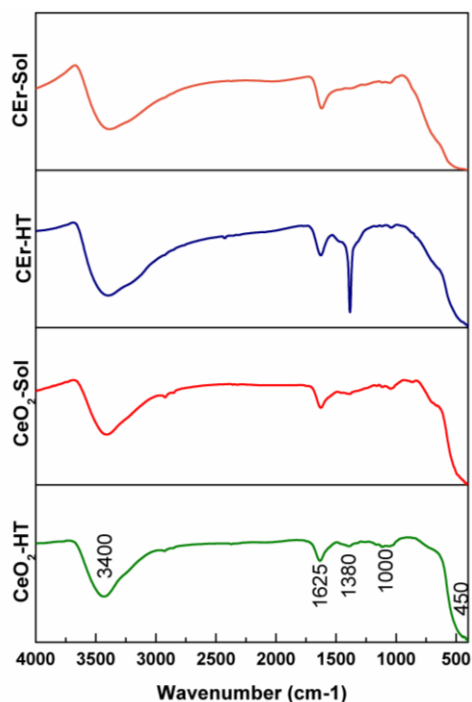
Figure 3.6 - FT-IR spectra of pure and Er^{3+} doped CeO_2 samples prepared by sol-gel and hydrothermal methods.

Thus FT-IR measurements indicated the presence of adsorbed water molecules on the CeO_2 surfaces. The role of adsorbed water on the selective adsorption of Congo red by CeO_2 will be discussed later. The absorption band at 450 cm^{-1} and 850 cm^{-1} corresponds to characteristic Ce-O stretching vibrations. So the observed IR absorption frequencies are in good agreement with previous literature[51, 52]. Other species of strong bands are located around 1000 cm^{-1}, which may be associated with the formation of nano-crystalline CeO_2[51].

3.2.6 CO₂-TPD Measurements

Surface basicity studies performed using CO_2-TPD measurements revealed the strength, distribution and amount of basic sites present on the surface of the synthesized compounds[53, 54]. The strength of basic sites was determined based on the temperature range in which desorption occurs i.e., the higher the temperature at which desorption occurs, the stronger will be the basic sites. Similarly, weaker sites desorb at a lower temperature. Based on the temperature range at which desorption occurs, the basic sites on CeO_2 particles were classified into very weak (<523 K), weak (523-653 K), medium (653-723 K) and strong (>723 K)[55, 56].
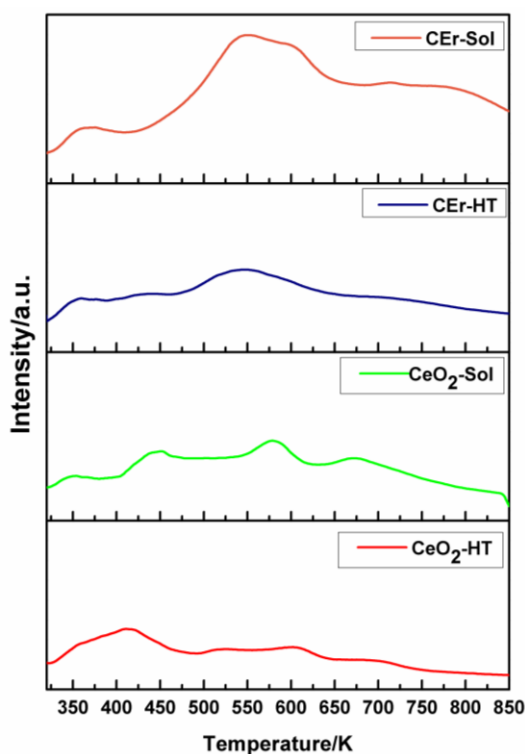
Figure 3.7 - CO_2-TPD curves at the heating rate 12 K/min for CeO_2-HT, CeO_2-Sol, CEr-HT and CEr-Sol

Integrating the CO_2-TPD curves over these temperature ranges provided the amount of different basic sites. The TPD curves of all the samples recorded at 12 K/min are shown in **Figure 3.7** and the amount of basic site calculated by integrating the curves along with the surface area of the respective samples are given in **Table 3.3**.

It is evident from **Figure 3.8** that with the increase in the surface area, there is a simultaneous increment in the number of basic sites. While considering each type of basic site, except for the very weak
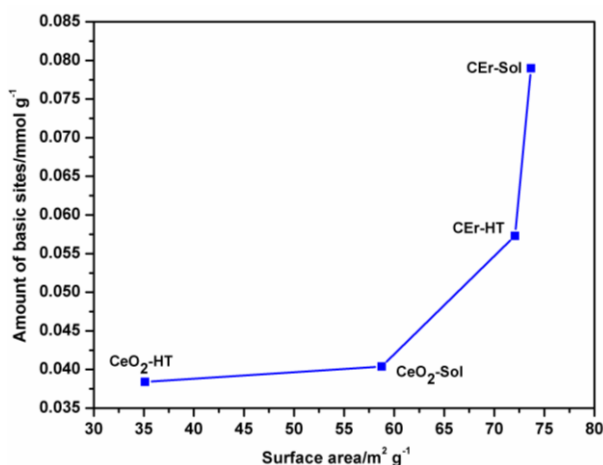
Figure 3.8 - Variation in the amount of basic sites *Vs* surface area of various CeO_2 samples prepared.

type sites, the amount of all other types of basic sites increases with an increase in surface area. However, very weak basic sites are present in almost the same amount in all samples except CeO_2-Sol. The distributions of different types of basic sites among the synthesized samples are shown in **Figure 3.9**. The introduction of Er^{3+} ions into the CeO_2 lattice has had a remarkable influence on the strength of basic sites. For hydrothermally synthesized samples

(CeO$_2$-HT and CEr-HT), the amount of medium-strength basic sites doubled on Er^{3+} doping and the amount of strong basic sites became four times that of CeO$_2$-HT.
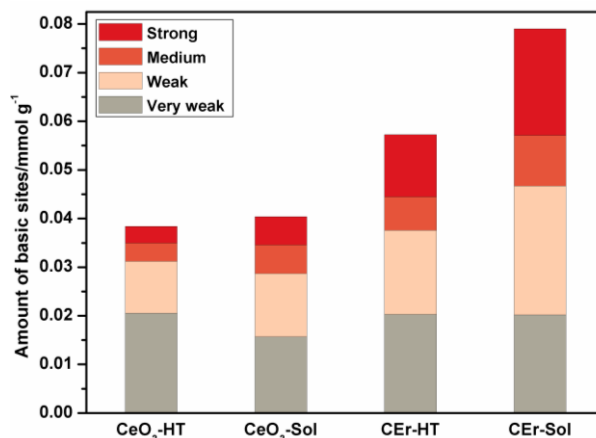
Figure 3.9 - Distribution of different basic sites in various CeO$_2$ samples.

Table 3.3 - Surface area, amount of different basic sites and the total amount of basic sites for CeO$_2$-HT, CeO$_2$-Sol, CEr-HT and CEr-Sol.

Sample	Surface area (m^2.g^{-1})	Type of basic sites (mmol.g^{-1})				Total (mmol.g^{-1})
		Very weak <523K	Weak 523-653K	Medium 653-723K	Strong >723K	
CeO$_2$-HT	35.11	0.0205	0.0107	0.0038	0.0034	0.0384
CeO$_2$-Sol	58.77	0.0157	0.0130	0.0059	0.0058	0.0404
CEr-HT	72.07	0.0203	0.0173	0.00687	0.0128	0.0573
CEr-Sol	73.67	0.0202	0.0265	0.0104	0.0219	0.0790

Similarly, in sol-gel synthesized samples, CEr-Sol has almost double the amount of medium basic sites and approximately four times the

amount of strong basic sites when compared to CeO_2-Sol. The increase in the number of basic sites with Er^{3+} doping can be explained based on the Lewis acid-base concept. The structure of pure CeO_2 and oxygen vacancy generation by Er^{3+} doping into the CeO_2 lattice is illustrated in **Figure 3.10**.
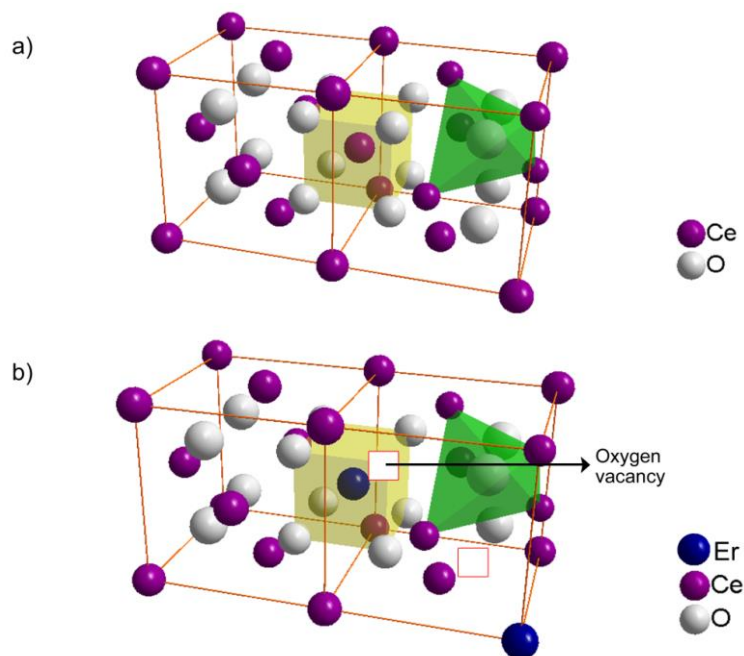
Figure 3.10 - Structure of (a) pure CeO_2 and (b) Er^{3+} doped CeO_2 with oxygen vacancy in the lattice.

The replacement of Ce^{4+} with Er^{3+} in the CeO_2 lattice results in oxygen vacancies, which are electron-rich. According to the Lewis concept, electron donors are basic in nature and electron acceptors are acidic. Hence the electron-rich sites are expected to have basic character[57]. So, the doping of Er^{3+} results in an increased number of oxygen vacancies which are basic in nature.

3.2.7 Adsorption Studies

The adsorption activity of the prepared CeO_2 samples towards Congo red was evaluated using UV-Visible absorption spectroscopy. The adsorptive removal of Congo red (initial concentration of dye solution fixed at 20 mg.L^{-1}) by the CeO_2-HT, CeO_2-Sol, CEr-HT and CEr-Sol samples (1g.L^{-1}) at the ambient pH (6.5) of Congo red solution in terms of their UV -Visible spectra were shown in **Figure 3.11.**
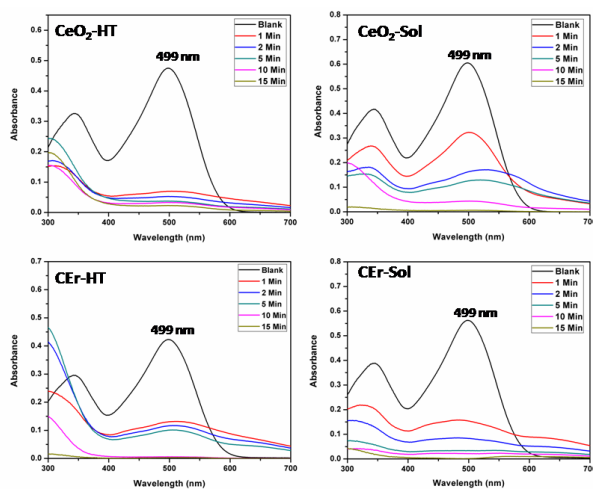
Figure 3.11 - UV-Visible absorbance spectra showing the adsorptive removal of Congo red by CeO_2-HT, CeO_2-Sol, CEr-HT and CEr-Sol samples.

The percentage removal of Congo red by the four different CeO_2 samples is shown in **Figure 3.12**. It can be seen that all four samples show more than 90 % removal of Congo red within 15 minutes. It can be seen that CeO_2-HT and CEr-Sol show 88.9 and 85.16 % removal within 2 minutes. Among the four samples, CEr-Sol is capable of removing almost 100 % of Congo red within 15 minutes.

The adsorption rates of Congo red by the sol-hydrothermal and sol-gel derived samples are given separately in **Figure 3.13**.
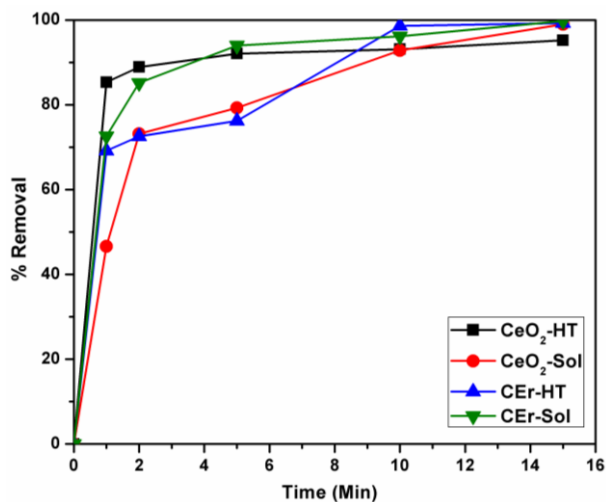
Figure 3.12 - Removal percentages of Congo red by CeO$_2$-HT, CeO$_2$-Sol, CEr-HT and CEr-Sol
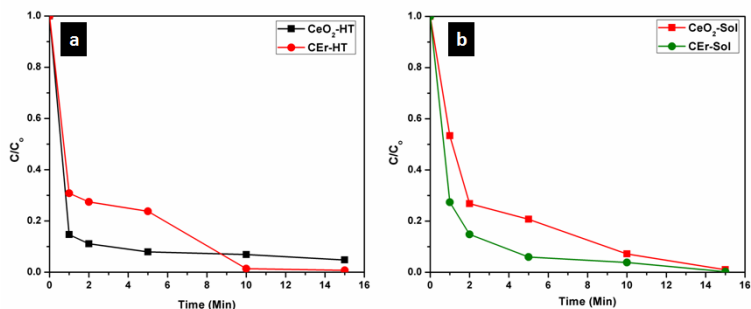
Figure 3.13 - Comparison of adsorption rates of a) sol-hydrothermal derived and b) sol-gel derived CeO$_2$ samples

In the case of hydrothermal-derived samples, it can be seen that CeO$_2$-HT initially shows a higher rate of adsorption which diminishes on the way and then gets dominated by CEr-HT. While comparing the sol-gel derived samples, it can be seen that CEr-Sol is always exhibiting a superior adsorption rate over CeO$_2$-Sol. From the

adsorption studies, it is evident that CEr-Sol is the best adsorbent material among the four CeO$_2$ samples developed. Therefore, further investigations were focussed mainly on CEr-Sol.
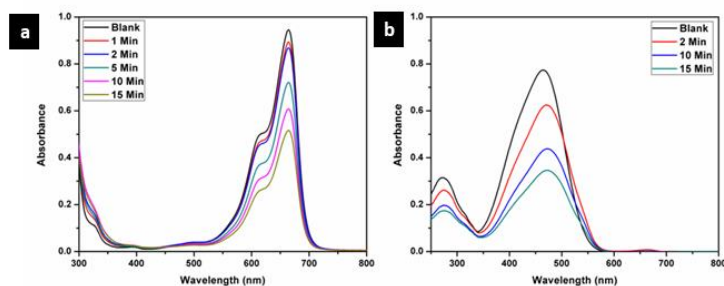
Figure 3.14 - UV-Visible absorbance spectra showing the adsorptive removal of a) methylene blue and b) methyl orange by CEr-Sol.

The higher selectivity of CEr-Sol towards Congo red (CR) was evaluated by carrying out the adsorption analysis with a cationic dye methylene blue (MB) and another azo dye methyl orange (MO). The UV-Visible absorption spectra for MB and MO adsorptions are shown in **Figure 3.14a and 3.14b** respectively. CEr-Sol shows adsorption towards both MB and MO to some extent. The percentage removal of MB and MO by CEr-Sol is shown in **Figure 3.15**. CEr-Sol shows higher adsorption capacity towards MO compared to MB. Compared to the 85 % removal of Congo red by CEr-Sol within 2 minutes, the percentage removal of MB and MO within the same period is less. The adsorption activity of CEr-Sol in a mixed dye solution of MB and CR was also studied using UV-Visible absorption spectroscopy. UV-Visible absorbance spectra of the mixed dye solution before and after introducing CEr-Sol are shown in **Figure 3.16**. The initial dye solution exhibits two absorption maxima, one at 663 nm corresponding to MB and ~480 nm corresponding to CR

respectively. Two minutes after the introduction of CEr-Sol into the dye solution, a considerable reduction in the CR absorption band can be seen.
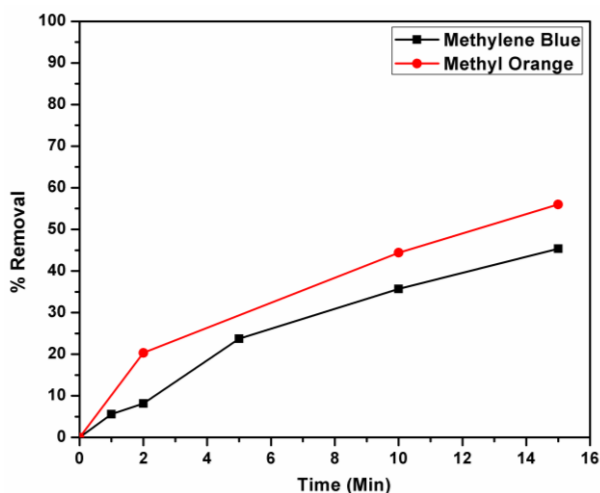
Figure 3.15 - Removal percentages of methylene blue and methyl orange by CEr-Sol
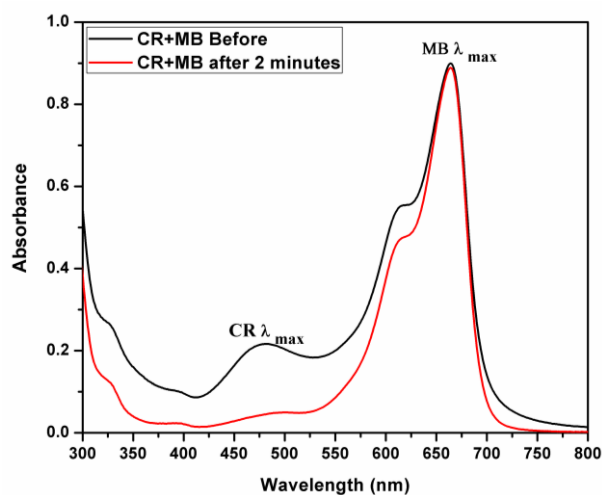
Figure 3.16 - UV-Visible absorbance spectrum showing the selective adsorption of Congo red by CEr-Sol from a mixed solution of Congo red and methylene blue.

At the same time, the MB absorption band around 663 nm is fully retained. Hence the selectivity and rapid adsorption rate of CEr-Sol towards CR even in the presence of other dyes are fully evident.

3.2.8 Effect of pH on adsorption

The effect of pH on the adsorption of Congo red was evaluated by carrying out the adsorption studies under pH conditions of 3, 6.5 and 10. The UV-Visible spectra corresponding to the adsorptions under three different pH conditions are given in **Figure 3.17**.
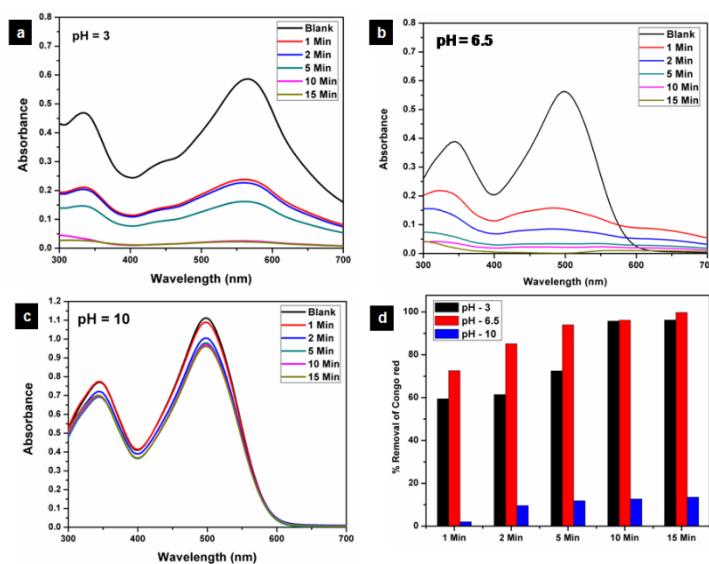
Figure 3.17 – Effect of pH on the adsorptive removal of Congo red by CEr-Sol at a) pH 3 b) pH 6.5 c) pH 10 and d) bar diagram showing the percentage removal at different time intervals.

On varying the pH of the Congo red solution, it was found that the colour of the solution turned dark blue around pH 3 and showed a corresponding red shift in the absorption spectra. At the same time around pH 10, the red colour of the dye solution got more intense

compared to the ambient pH of 6.5. It is evident from the adsorption studies that pH plays a crucial role in Congo red adsorption. CEr-Sol exhibited 99.75 % removal of Congo red under the inherent pH (6.5) of the dye solution. At pH 3, CEr-sol showed a percentage removal of 96.24 % which was reduced to 13.54 % under an alkaline pH of 10. Thus, the inherent pH of the Congo red solution (6.5) was found to be the best environment for maximum adsorption by CEr-Sol. The pH of the point of zero charge (pH$_{PZC}$) of CEr-Sol determined by the pH drift method was 2.16. The role of the pH of Congo red solution and pH$_{PZC}$ of the adsorbent in the adsorption mechanism was discussed in detail in the coming sections. From all the above results, it is clear that CEr-Sol is the superior and fastest adsorbent among the four variants of CeO$_2$ samples synthesized. Adsorption isotherms for CEr-Sol are given in **Figure 3.18.**

3.2.9 Adsorption isotherms

Adsorption isotherm analysis can help to calculate the maximum adsorption capacity of the adsorbents towards a particular species. The adsorbent concentration was optimized at first (1 g.L^{-1}). For the optimized CEr-Sol concentration, the amount of Congo red was varied (10,15, 20, 25 and 30 mg.L^{-1}) and Langmuir and Freundlich adsorption isotherms were plotted.

Langmuir adsorption isotherm model can account for homogeneous systems. According to Langmuir adsorption model

$$q_e = \frac{q_m \, bC_e}{1+bC_e} \qquad (3.1)$$

where q_e is the amount of dye adsorbed at equilibrium, q_m is the maximum amount of dye adsorbed per unit weight of the adsorbent (mg/g) and b is Langmuir adsorption isotherm constant[58].
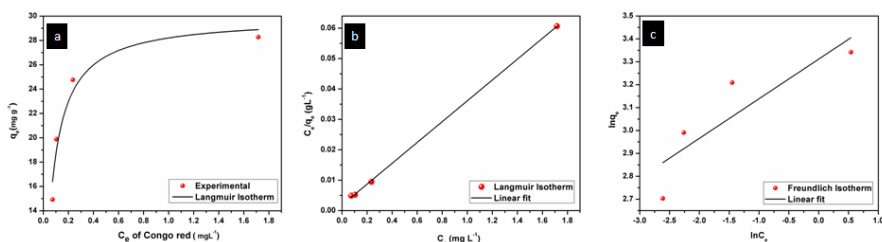
Figure 3.18 - a) Langmuir isotherm (b) linearized Langmuir and (c) linearized Freundlich isotherms of CEr-Sol.

Langmuir adsorption isotherm and linearized Langmuir isotherm of CEr-Sol are given in **Figures 3.18a and 3.18b**. The maximum amount of dye adsorbed per unit weight of CEr-SOl, q_m is found to be 29.19 mg/g. It corresponds to the complete monolayer coverage of the CEr-Sol surface. The experimental data were found to fit well with the Langmuir model with a correlation coefficient R^2 of 0.9996. The value of b is found to be 18.52 L.mg^{-1} and b is a measure of affinity between adsorbent and adsorbate. The Freundlich model can account for multilayer and non-equivalent adsorption sites. According to the Freundlich adsorption model

$$\ln q_e = \frac{1}{n} ln C_e + \ln K_f \qquad (3.2)$$

here K_f and n are Freundlich adsorption isotherm constants and n is a measure of the heterogeneity of the system[58]. The linear fitting analysis of experimental data with the Freundlich model as in **Figure 3.18c** showed a correlation coefficient, R^2 of 0.6447. The K_f and n

values are 27.428 and 5.77 respectively. From the R^2 values, it is obvious that Congo red adsorption on CEr-Sol follows the Langmuir model rather than Freundlich.

In the case of Langmuir adsorption isotherm, the affinity between adsorbent and adsorbate can be quantified by calculating a dimensionless separation factor R_L which is given by the equation

$$R_L = \frac{1}{1+bC_0} \qquad (3.3)$$

Here C_0 is the highest initial adsorbate concentration[58]. Depending on the value of R_L, adsorption can be classified into favourable and unfavourable adsorption. For favourable adsorption $0<R_L<1$ and unfavourable adsorption $R_L>1$ or $R_L=1$. For Congo red adsorption by CEr-Sol, we have obtained an R_L value of 0.0018. From the obtained R-value a favourable parameter K_{C0} can be derived.

$$K_{C0} = \frac{1}{R_L} - 1 \qquad (3.4)$$

Linear isotherms will have a K_{C0} value equal to 1. If K_{C0} is in between 1 and 10 the adsorption is considered favourable. A K_{C0} value higher than 10 denotes a spontaneous and highly favourable adsorption isotherm. The derived value of K_{C0} for CEr-Sol is 557.65 and it indicated the highly favourable nature of its adsorption isotherm.

3.2.10 Kinetics of Congo red adsorption on CEr-Sol

The rate of adsorption of Congo red by CEr-Sol can be determined from kinetic studies. Here we have considered pseudo-first-order

and pseudo-second-order models for kinetic studies as shown in **Figure 3.19**. According to pseudo-first-order adsorption,

$$\log(q_e - q_t) = log q_e - \frac{k_1 t}{2.303} \qquad (3.5)$$

where q_e is the amount of Congo red adsorbed at equilibrium and q_t is the amount adsorbed during various time intervals. Here t is the time in minutes and k_1 is the pseudo-first-order rate constant[43].

In the case of pseudo-second-order adsorption,

$$\frac{t}{q_t} = \frac{1}{k_2 q_e{}^2} + \frac{t}{q_e} \qquad (3.6)$$

where k_2 is the pseudo second order rate constant[43].

Both the pseudo-first-order and second-order kinetic models were applied to the Congo red adsorption by CEr-Sol and the model which fits best for the experimental data was identified from the linear regression correlation coefficient, R^2 values.
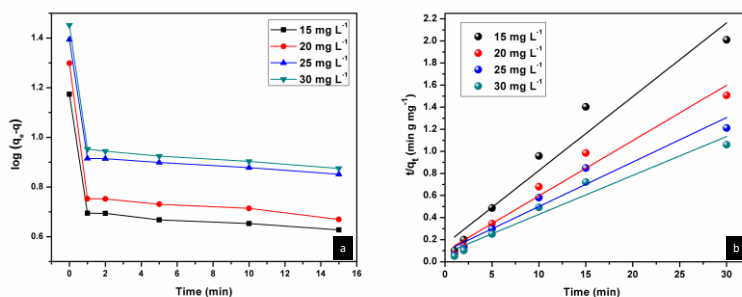
Figure 3.19 - a) Pseudo-first-order and b) pseudo-second-order kinetic plots of CEr-Sol.

Table 3.4. Pseudo-second-order kinetic parameters for the selective adsorption of Congo red by CEr-Sol.

Congo red concentration (mg.L^{-1})	k$_2$ (g.mg^{-1}.min^{-1})	q$_e$ calculated (mg.g^{-1})	q$_e$ experimental (mg.g^{-1})	R^2
15	2.84×10^{-2}	14.95	14.93	0.9442
20	2.64×10^{-2}	19.95	19.89	0.9649
25	1.68×10^{-2}	24.81	24.76	0.9425
30	1.63×10^{-2}	28.34	28.28	0.9534

From the linear regression analysis, it was observed that the experimental results fit well with pseudo-second-order adsorption. The pseudo-second-order rate constant k$_2$, experimental and calculated values of q$_e$ and R^2 values at different concentrations of Congo red are given in **Table 3.4.** R^2 values above 0.944 indicate the best fit of experimental data.

3.2.11 Mechanism of selective adsorption of Congo red

A thorough investigation of the adsorption mechanism was required to understand the selectivity and enhanced adsorption activity of the prepared samples towards Congo red. While evaluating the adsorption mechanism, several factors such as surface area, porosity, pH, electrostatic interaction between adsorbent surface and dye molecules, and weak interactions such as hydrogen bonding and coordination effects should be considered. The surface area and pore size distributions of the developed samples are already given in **Table 3.2**. Among the four CeO$_2$ samples, CEr-Sol has the highest surface area as well as the smallest pore size distribution (4.8 nm).

Adsorption capacity and surface area are directly related. The molecular size of Congo red is 2.62 nm which can fit exactly into the CEr-Sol pores but the molecular sizes of methyl orange and methylene blue are 1.2 and 1.43 nm respectively which is too small to fit into the pores [59]. Thus, surface area enhancement and pore size regulation by doping Er^{3+} into the CeO_2 lattice can influence the adsorption capacity to a certain extent. It is noted that electrostatic interaction between the CeO_2 surface and dye molecules can affect the adsorption capacity. Hence the adsorption activity of CEr-Sol using both cationic (methylene blue) and anionic (Congo red and methyl orange) dyes are also evaluated. Within 2 minutes, 85.1 % of Congo red and 20.3 % of methyl orange were removed by CEr-Sol. However, only 8.1 % of the cationic dye methylene blue was removed in 2 minutes by CEr-Sol. Even though CEr-Sol has more affinity towards anionic dyes rather than cationic dyes, the surface charge on CeO_2 is not the only crucial determining factor of adsorption here. If the surface charge was the only determining factor, CEr-Sol would have adsorbed both anionic dye species to the same extent. A combined effect of pH and adsorbent surface charge emerges during the adsorption of Congo red by CEr-Sol. Here the pH_{PZC} of CEr-Sol was found to be 2.16. Since Congo red is a dipolar molecule, it exists in anionic form in neutral and alkaline pH and cationic form in acidic pH. From the pH_{PZC} value, we know that at pH > 2.16, the CEr-Sol surface is negatively charged and at pH < 2.16, the CEr-Sol surface is positively charged. While considering the possible electrostatic interactions between Congo red and CEr-Sol surface, it can be seen that at neutral pH and above pH 7, the adsorbent surface as well as the Congo red molecule are negatively charged. Thus, the mutual

repulsion between the adsorbent and adsorbate is responsible for the reduced adsorption under alkaline conditions. Again, below pH 2.16, we have both adsorbent and adsorbate as positively charged species and their mutual repulsion tends to decrease the extent of adsorption. This electrostatic repulsion is one of the reasons for reduced adsorption in acidic conditions. At the same time, a pH between 2.16 and 7 can give rise to positively charged Congo red species and negatively charged CEr-Sol surface, enhancing the electrostatic attraction between Congo red and CEr-Sol. Thus, the pH range between 2.16 and 7 is electrostatically favouring Congo red adsorption on the CEr-Sol surface. Further beyond the electrostatic interactions, the deciding factor in this case is hydrogen bonding. Adsorbed water molecules and surface functional groups on the CeO_2 surface can often form hydrogen bonds with the functional groups present on the dye molecules. Here the surface basic sites are significant in controlling the adsorption mechanism. Because the extent of hydrogen bonding depends on surface basicity. Hence further investigation is exclusively dedicated to the surface basicity controlled selective adsorption of Congo red by CeO_2.

3.2.12 Selective adsorption and surface basicity

The type and nature of surface basic sites may be different in different adsorbent materials. Here on the CeO_2 surface, oxygen vacancies are the major basic sites. The basic nature of oxygen vacancies was explained earlier. The doping of low valent ions such as Er^{3+} into the CeO_2 lattice significantly increased the number of oxygen vacancies and thereby the amount of basic sites[57]. These

oxygen vacancies have a strong affinity for moisture[52]. The presence of adsorbed moisture is evident from the FT-IR spectra. The adsorbed water molecules can form hydrogen bonds with solvent water which ensures better dispersion of the adsorbent in water. Also, many of the adsorbed water molecules dissociate near oxygen vacancies to form surface-active hydroxyl groups[60]. The possibilities for hydrogen bonding increase with an increase in surface basicity. Now the selectivity of CEr-Sol towards Congo red can be explained based on hydrogen bonding. The structure of Congo red, methylene blue and methyl orange are shown in **Figure 3.20**.

Congo red

Methylene Blue

Methyl orange
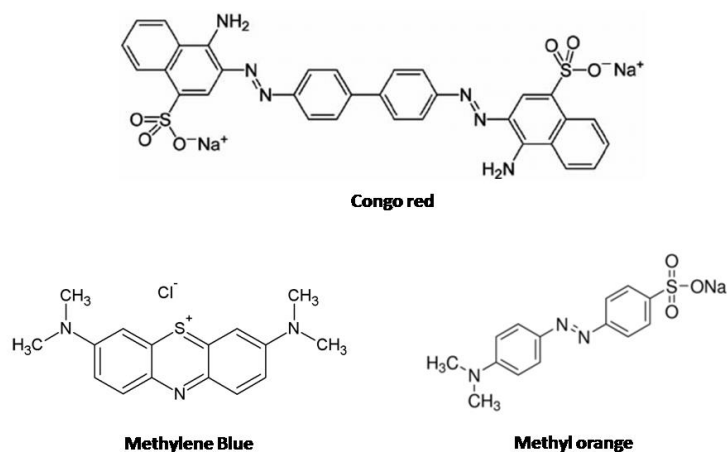
Figure 3.20 - Structures of dye molecules under investigation

From the chemical structures, it is evident that only Congo red has – NH_2 functional groups present in their structure which are capable of forming hydrogen bonds with the adsorbed water molecules and hydroxyl basic sites on the CeO_2 surface. At the same time, methylene blue and methyl orange lack amino groups that are capable of forming hydrogen bonds. Thus, hydrogen bonding can account for

the selective adsorption of Congo red by CeO$_2$. The proposed adsorption mechanism is illustrated in **Figure 3.21**. Since CEr-Sol possess the highest amount of basic sites especially medium and strong type basic sites, a corresponding improvement in adsorption capacity is observed.
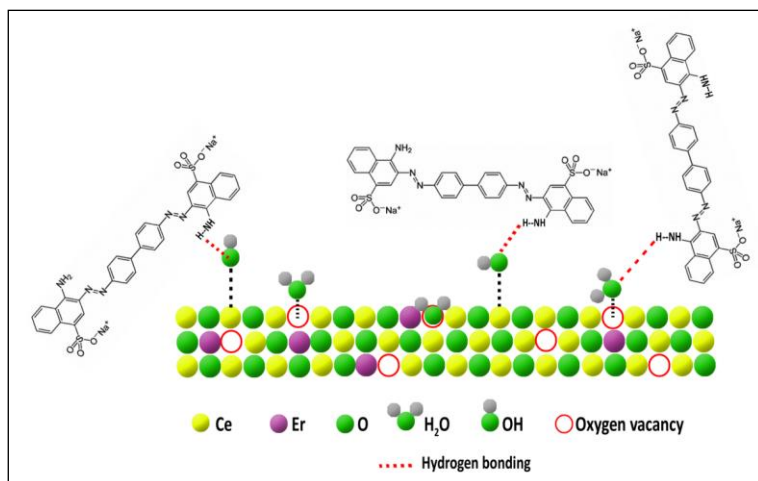
Figure 3.21 - Selective adsorption mechanism of Congo red by CEr-Sol.

So, surface basicity enhancement by Er^{3+} doping into CeO$_2$ lattice increases hydrogen bonding and thereby the selective adsorption of Congo red. These studies revealed that surface basicity can be used as an effective tool for tuning the adsorption capacity and selectivity of CeO$_2$ towards Congo red. Optimising surface basicity can thus lead to the fabrication of the best adsorbent version of CeO$_2$ for environmental remediation.

3.2.13 Reusability tests

Recyclability is an important attribute in sustainable environmental remediation. After several times of washing with distilled water the

regenerated adsorbents were dried and calcined at 500 °C for 2 hours. The adsorption studies were again carried out using the regenerated adsorbents for two more adsorption/regeneration cycles. As given in **Figure 3.22**, the recyclability tests show that the percentage removal of Congo red is 89.33 % in the second cycle and 81.38 % in the third cycle. Better desorption and recycling techniques which can preserve the surface-active sites and thereby the adsorption efficiency of regenerated adsorbents should be further investigated.
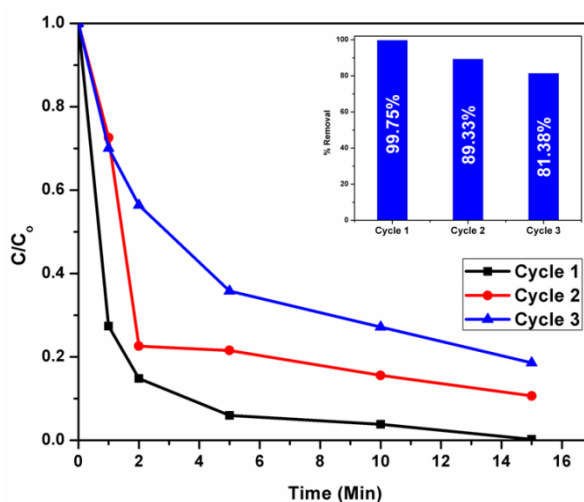
Figure 3.22 – adsorption rates of regenerated CEr-Sol samples in 3 successive cycles (the percentage removals in the inset).

3.3 Conclusions

Nanocrystalline mesoporous CeO_2 and Er^{3+} doped CeO_2 samples were synthesized using sol-gel and sol hydrothermal methods. The selective and rapid adsorption of these nanocrystalline mesoporous CeO_2 samples towards organic pollutants such as Congo red, methyl orange and methylene blue was investigated in detail. From the

adsorption experiments, CEr-Sol was found to be the most efficient and highly selective adsorbent towards Congo red. All these studies revealed that CEr-Sol has the highest selectivity and efficiency for Congo red adsorption. CEr-Sol is capable of removing 85.16 % of Congo red within 2 minutes and 99.75 % removal is observed in 15 minutes. The rapid and selective adsorption mechanism of CEr-Sol was further investigated in detail. Kinetics of the adsorption process was also studied and pseudo second-order kinetics was assigned to it. The main factors controlling the selectivity and adsorption ability are surface area, porosity, electrostatic interactions, surface active sites and hydrogen bondings. Among these, the presence of strong surface basic sites and hydrogen bonding are the crucial factors responsible for the selective and rapid adsorption of Congo red by CEr-Sol. From the surface basicity measurements, the enhancement of adsorption efficiency along with an increase in surface basic sites is evident. The basic mechanism behind the rapid and selective adsorptive removal of Congo red by CEr-Sol is the formation of hydrogen bonds, formed either by the surface hydroxyls or adsorbed water molecules with NH_2 groups present exclusively on Congo red. Surface hydroxyls and oxygen vacancies are prominent basic sites present on the CeO_2 surface. The enhanced number of oxygen vacancies generated upon Er^{3+} doping into the CeO_2 lattice has a significant role in selective adsorption. These oxygen vacancies have a higher affinity for moisture adsorption and the adsorbed water molecules can selectively form hydrogen bonds with NH_2 groups present in Congo red molecules. Since functional groups capable of hydrogen bond formation are absent in methylene blue and methyl orange, the extent of adsorption of these dye molecules on CEr-Sol is

comparatively smaller. This work establishes the possibility of a surface basicity-mediated enhancement in the selectivity and efficiency of Congo red adsorption by CeO_2. Thus, surface basicity can be effectively used to tune the selective adsorption capacity of adsorbents towards pollutants.

3.4 References

1. Trovarelli, A., *Catalytic properties of ceria and CeO2-containing materials.* Catalysis Reviews, 1996. **38**(4): p. 439-520.
2. Wang, S. and G.M. Lu, *Role of CeO2 in Ni/CeO2–Al2O3 catalysts for carbon dioxide reforming of methane.* Applied Catalysis B: Environmental, 1998. **19**(3-4): p. 267-277.
3. Seal, S., et al., *Engineered defects in cerium oxides: tuning chemical reactivity for biomedical, environmental, & energy applications.* Nanoscale, 2020. **12**(13): p. 6879-6899.
4. Sun, C., H. Li, and L. Chen, *Nanostructured ceria-based materials: synthesis, properties, and applications.* Energy & Environmental Science, 2012. **5**(9): p. 8475-8505.
5. Rodriguez, J.A., et al., *Ceria-based model catalysts: fundamental studies on the importance of the metal–ceria interface in CO oxidation, the water–gas shift, CO2 hydrogenation, and methane and alcohol reforming.* Chemical Society Reviews, 2017. **46**(7): p. 1824-1841.
6. Montini, T., et al., *Fundamentals and catalytic applications of CeO2-based materials.* Chemical reviews, 2016. **116**(10): p. 5987-6041.
7. Periyat, P., et al., *A facile aqueous sol–gel method for high surface area nanocrystalline CeO2.* RSC Advances, 2011. **1**(9): p. 1794-1798.
8. Lawrence, N.J., et al., *Defect engineering in cubic cerium oxide nanostructures for catalytic oxidation.* Nano letters, 2011. **11**(7): p. 2666-2671.
9. Wang, J., et al., *The application of CeO2-based materials in electrocatalysis.* Journal of Materials Chemistry A, 2019. **7**(30): p. 17675-17702.
10. Ozawa, M., M. Kimura, and A. Isogai, *The application of Ce⬚ Zr oxide solid solution to oxygen storage promoters in automotive catalysts.* Journal of Alloys and Compounds, 1993. **193**(1-2): p. 73-75.
11. Kašpar, J., P. Fornasiero, and M. Graziani, *Use of CeO2-based oxides in the three-way catalysis.* Catalysis Today, 1999. **50**(2): p. 285-298.

12. Yahiro, H., K. Eguchi, and H. Arai, *Electrical properties and reducibilities of ceria-rare earth oxide systems and their application to solid oxide fuel cell.* Solid State Ionics, 1989. **36**(1-2): p. 71-75.

13. Eguchi, K., et al., *Electrical properties of ceria-based oxides and their application to solid oxide fuel cells.* Solid State Ionics, 1992. **52**(1-3): p. 165-172.

14. Srisiriwat, N., S. Therdthianwong, and A. Therdthianwong, *Oxidative steam reforming of ethanol over Ni/Al2O3 catalysts promoted by CeO2, ZrO2 and CeO2–ZrO2.* International Journal of Hydrogen Energy, 2009. **34**(5): p. 2224-2234.

15. Zhang, R., Y. Wang, and R.C. Brown, *Steam reforming of tar compounds over Ni/olivine catalysts doped with CeO2.* Energy Conversion and Management, 2007. **48**(1): p. 68-77.

16. Marinho, A.L., et al., *Highly active and stable Ni dispersed on mesoporous CeO2-Al2O3 catalysts for production of syngas by dry reforming of methane.* Applied Catalysis B: Environmental, 2021. **281**: p. 119459.

17. Si, R. and M. Flytzani-Stephanopoulos, *Shape and crystal-plane effects of nanoscale ceria on the activity of Au-CeO2 catalysts for the water–gas shift reaction.* Angewandte Chemie International Edition, 2008. **47**(15): p. 2884-2887.

18. Fu, Q., A. Weber, and M. Flytzani-Stephanopoulos, *Nanostructured Au–CeO2 catalysts for low-temperature water–gas shift.* Catalysis Letters, 2001. **77**(1-3): p. 87-95.

19. Andreeva, D., et al., *Low-temperature water-gas shift reaction over Au/CeO2 catalysts.* Catalysis Today, 2002. **72**(1-2): p. 51-57.

20. Avgouropoulos, G. and T. Ioannides, *Selective CO oxidation over CuO-CeO2 catalysts prepared via the urea–nitrate combustion method.* Applied Catalysis A: General, 2003. **244**(1): p. 155-167.

21. Avgouropoulos, G., T. Ioannides, and H. Matralis, *Influence of the preparation method on the performance of CuO–CeO2 catalysts for the selective oxidation of CO.* Applied Catalysis B: Environmental, 2005. **56**(1-2): p. 87-93.

22. Wang, H., et al., *Atomically dispersed Au catalysts supported on CeO2 foam: controllable synthesis and CO oxidation reaction mechanism.* Nanoscale, 2017. **9**(43): p. 16817-16825.

23. Aouad, S., E. Abi-Aad, and A. Aboukaïs, *Simultaneous oxidation of carbon black and volatile organic compounds over Ru/CeO2 catalysts.* Applied Catalysis B: Environmental, 2009. **88**(3-4): p. 249-256.

24. Xingyi, W., K. Qian, and L. Dao, *Catalytic combustion of chlorobenzene over MnOx–CeO2 mixed oxide catalysts.* Applied Catalysis B: Environmental, 2009. **86**(3-4): p. 166-175.

25.   Centeno, M., et al., *Catalytic combustion of volatile organic compounds on Au/CeO2/Al2O3 and Au/Al2O3 catalysts.* Applied Catalysis A: General, 2002. **234**(1-2): p. 65-78.

26.   Kong, J., et al., *Introduce oxygen vacancies into CeO2 catalyst for enhanced coke resistance during photothermocatalytic oxidation of typical VOCs.* Applied Catalysis B: Environmental, 2020. **269**: p. 118755.

27.   Peng, S., et al., *Selective Hydrogenation of acetylene over gold nanoparticles supported on CeO2 pretreated under different atmospheres.* Catalysis Letters, 2019. **149**(2): p. 465-472.

28.   Vilé, G., et al., *Ceria in hydrogenation catalysis: high selectivity in the conversion of alkynes to olefins.* Angewandte Chemie International Edition, 2012. **51**(34): p. 8620-8623.

29.   Liu, Y., et al., *Mixed alcohols synthesis from syngas over Cs-and Ni-modified Cu/CeO2 catalysts.* Fuel, 2013. **104**: p. 62-69.

30.   Meng, Q.-L., et al., *Reactivity of CeO2-based ceramics for solar hydrogen production via a two-step water-splitting cycle with concentrated solar energy.* international journal of hydrogen energy, 2011. **36**(21): p. 13435-13441.

31.   Kaneko, H., et al., *Reactive ceramics of CeO2–MOx (M= Mn, Fe, Ni, Cu) for H2 generation by two-step water splitting using concentrated solar thermal energy.* Energy, 2007. **32**(5): p. 656-663.

32.   Ma, R., et al., *A critical review on visible-light-response CeO2-based photocatalysts with enhanced photooxidation of organic pollutants.* Catalysis Today, 2019. **335**: p. 20-30.

33.   Qi, H., et al., *Constructing CeO2/nitrogen-doped carbon quantum dot/g-C3N4 heterojunction photocatalysts for highly efficient visible light photocatalysis.* Nanoscale, 2020. **12**(37): p. 19112-19120.

34.   Dong, Z., et al., *The fabrication and characterization of CeO2/Cu2O nanocomposites with enhanced visible-light photocatalytic activity.* RSC Advances, 2020. **10**(60): p. 36371-36377.

35.   Huang, W. and Y. Gao, *Morphology-dependent surface chemistry and catalysis of CeO2 nanocrystals.* Catalysis Science & Technology, 2014. **4**(11): p. 3772-3784.

36.   Jiang, H., et al., *One-pot microwave-hydrothermally synthesized carbon nanotube-cerium oxide nanocomposites for enhanced visible photodegradation of acid orange 7.* Physical Chemistry Chemical Physics, 2020. **22**(41): p. 23743-23753.

37.   Sabzehmeidani, M.M., H. Karimi, and M. Ghaedi, *Enhanced visible light-active CeO2/CuO/Ag2CrO4 ternary heterostructures based on CeO2/CuO nanofiber heterojunctions for the simultaneous degradation of a binary mixture of dyes.* New Journal of Chemistry, 2020. **44**(13): p. 5033-5048.

38.   Ye, K., et al., *An ultrathin carbon layer activated CeO2 heterojunction nanorods for photocatalytic degradation of organic pollutants.* Applied Catalysis B: Environmental, 2019. **259**: p. 118085.

39.   Xu, Y., R. Li, and Y. Zhou, *An eco-friendly route for template-free synthesis of high specific surface area mesoporous CeO2 powders and their adsorption for acid orange 7.* RSC Advances, 2019. **9**(39): p. 22366-22375.

40.   Yu, X.-F., et al., *Template- and surfactant-free synthesis of ultrathin CeO2 nanowires in a mixed solvent and their superior adsorption capability for water treatment.* Chemical Science, 2015. **6**(4): p. 2511-2515.

41.   Ouyang, X., et al., *Hierarchical CeO2 nanospheres as highly-efficient adsorbents for dye removal.* New Journal of Chemistry, 2013. **37**(3): p. 585-588.

42.   Lu, X.-h., et al., *Porous CeO2 nanowires/nanowire arrays: electrochemical synthesis and application in water treatment.* Journal of Materials Chemistry, 2010. **20**(34): p. 7118-7122.

43.   Maiti, D., S. Mukhopadhyay, and P.S. Devi, *Evaluation of mechanism on selective, rapid, and superior adsorption of Congo red by reusable mesoporous α-Fe2O3 nanorods.* ACS Sustainable Chemistry & Engineering, 2017. **5**(12): p. 11255-11267.

44.   Wang, L., et al., *Rational design, synthesis, adsorption principles and applications of metal oxide adsorbents: a review.* Nanoscale, 2020. **12**(8): p. 4790-4815.

45.   Lin, M., et al., *Hydrothermal synthesis of CeO2 nanocrystals: Ostwald ripening or oriented attachment?* Crystal Growth & Design, 2012. **12**(6): p. 3296-3303.

46.   Sing, K.S., *Adsorption methods for the characterization of porous materials.* Advances in Colloid and Interface Science, 1998. **76**: p. 3-11.

47.   Barrett, E.P., L.G. Joyner, and P.P. Halenda, *The determination of pore volume and area distributions in porous substances. I. Computations from nitrogen isotherms.* Journal of the American Chemical society, 1951. **73**(1): p. 373-380.

48.   Sing, K.S. and R.T. Williams, *Physisorption hysteresis loops and the characterization of nanoporous materials.* Adsorption Science & Technology, 2004. **22**(10): p. 773-782.

49.   Horikawa, T., D. Do, and D. Nicholson, *Capillary condensation of adsorbates in porous materials.* Advances in colloid and interface science, 2011. **169**(1): p. 40-58.

50.   Yue, L. and X.-M. Zhang, *Structural characterization and photocatalytic behaviors of doped CeO2 nanoparticles.* Journal of Alloys and Compounds, 2009. **475**(1-2): p. 702-705.

51.   Sahoo*, S.K., et al., *Hydrothermal Synthesis of Single Crystalline Nano CeO2 and Its Structural, Optical, and Electronic*

Characterization. Materials and Manufacturing Processes, 2010. **25**(9): p. 982-989.

52. Tomić, N.a.M., et al., *Nanocrystalline CeO2– δ as effective adsorbent of azo dyes.* Langmuir, 2014. **30**(39): p. 11582-11590.

53. Choudhary, V. and V. Rane, *Acidity/basicity of rare-earth oxides and their catalytic activity in oxidative coupling of methane to C2-hydrocarbons.* Journal of Catalysis, 1991. **130**(2): p. 411-422.

54. Fung, J. and I. Wang, *Determination of surface acidity and basicity of TiO2ZrO2 by temperature programmed desorption of ammonia and acetic acid.* Applied Catalysis A: General, 1998. **166**(2): p. 327-334.

55. Azzouz, A., et al., *Assessment of acid–base strength distribution of ion-exchanged montmorillonites through NH3 and CO2-TPD measurements.* Thermochimica Acta, 2006. **449**(1-2): p. 27-34.

56. Cui, Z., et al., *Size-Dependent Surface Basicity of Nano-CeO2 and Desorption Kinetics of CO2 on Its Surface.* Industrial & Engineering Chemistry Research, 2018. **57**(32): p. 10977-10984.

57. Metiu, H., et al., *Chemistry of Lewis acid–base pairs on oxide surfaces.* The Journal of Physical Chemistry C, 2012. **116**(19): p. 10439-10450.

58. Jacob, N.M., et al., *Purifying water containing both anionic and cationic species using a (Zn, Cu) O, ZnO, and cobalt ferrite based multiphase adsorbent system.* Industrial & Engineering Chemistry Research, 2013. **52**(46): p. 16384-16395.

59. Szlachta, M. and P. Wójtowicz, *Adsorption of methylene blue and Congo red from aqueous solution by activated carbon and carbon nanotubes.* Water science and technology : a journal of the International Association on Water Pollution Research, 2013. **68**: p. 2240-8.

60. Yang, Z., et al., *The effect of environment on the reaction of water on the ceria (111) surface: a DFT+ U study.* The Journal of Physical Chemistry C, 2010. **114**(35): p. 14891-14899.

Chapter 4

Mesoporous Mg^{2+} Doped CeO_2 Encapsulated Fe_3O_4 Core-Shells for the Selective Adsorptive Removal of Malachite Green

Economically viable, easy to operate and highly efficient techniques for water treatment are one of the basic amenities that should be provided to every individual in our society. Here we have developed Fe_3O_4@Mg^{2+} doped CeO_2 core-shells by a co-precipitation route as magnetically retrievable adsorbents which are highly selective towards hazardous malachite green. Various parameters affecting the adsorption activity were investigated in detail. Mesoporous Mg^{2+} doped CeO_2 encapsulated Fe_3O_4 core-shell structures are developed focusing on easy separation, high selectivity and cost-effectiveness.

4.1 Introduction

Industrialization and the growing global population have caused a wide variety of social, economic and environmental effects. Among them, the one that requires the highest priority is environmental issues caused by the changing global trends. Water pollution is a serious environmental scenario, the world is facing nowadays. The unavailability of clean water sources and the lack of efficient and cost-effective methods for water purification are always topics of serious concern. Industrial and agricultural activities released a wide variety of pollutants into water in significant quantities[1, 2]. The major category among those released pollutants is dyes expelled from various sources such as textile, leather, food processing and plastic industries[3-6]. The unchecked release of these dyes into water sources without proper treatment can cause severe problems to aquatic life as well as to humans[7-9]. The released dyes are of different types having different chemical structures and properties falling under different categories such as cationic, anionic, azo, acidic and basic dyes[10]. Malachite green is a cationic basic dye widely employed in food processing and pharmaceutical industries[11]. Malachite green is directly employed as a dye over a broad variety of substrates such as cotton, silk, leather, plastic, wood and paper[12]. Malachite green when present in quantities higher than permitted levels can cause adverse effects. Besides being carcinogenic as well as teratogenic, malachite green can cause infections, damage to vital organs and developmental disorders[11, 13]. So, the effective treatment of the discharged malachite green content in waterbodies from various sources is inevitable. Being regarded as one of the most

dangerous dye pollutants, malachite green requires a selective and highly effective removal strategy.

Several water treatment techniques such as ultrafiltration[14, 15], photocatalysis[16, 17], reverse osmosis[18], adsorption[19-22], coagulation-flocculation[23], advanced oxidation process etc. are used for the removal of pollutants from water sources[9, 24, 25]. Some of these techniques are found to be effective for the removal of malachite green from water. Photocatalysts such as TiO_2[26-28], ZnO[29, 30], and $ZnVFeO_4$[31] are found to be effective against malachite green. Besides photocatalysis, other advanced oxidation techniques such as Fenton and Fenton-like oxidation[32, 33], electrochemical[34, 35] and sonochemical[36] oxidations were also reported for malachite green removal. The effectiveness, cost, and ease of operation are the main factors determining the wide-scale applicability of these purification techniques. Among the widely employed malachite green removal methods, the use of adsorbents is found to be cost-effective, easy to operate, highly efficient and widely employable[37-45]. Activated carbon and its modifications[37, 40, 46], sawdust[38], nanoclay[39], fly ash[42], zeolites[43], carbon nanotubes[45], graphite oxide[47], polymer nanocomposites[48, 49], and a wide range of metal oxides and their modifications[44, 50-52] are the most frequently employed adsorbents for malachite green. Out of the wide spectrum of adsorbents choosing the best adsorbent and making it more selective towards a malachite green is the key step here. Metal oxides are the best candidates capable of showing tunable selectivity in adsorption[53, 54]. In addition to high selectivity, easy recovery of

the adsorbent after the treatment process is also important[55]. The ease of operation of the adsorption process depends on the ease with which the adsorbents can be removed from the aqueous medium[56]. Magnetic recovery is one of the most effective ways for adsorbent separation[57-60].

In the present work, CeO_2 is chosen as the adsorbent material which can be selectively tuned towards malachite green[61-64]. Cerium is the most abundant rare earth element present on the earth's crust and thus CeO_2 synthesis is found to be cost-effective [65, 66]. The selectivity towards malachite green is induced by doping Mg^{2+} ions into the CeO_2 lattice by co-precipitation route. To facilitate the easy recovery of adsorbent material, core-shell structures in which Fe_3O_4 nanoparticles are encapsulated within mesoporous Mg^{2+} doped CeO_2 shells are developed. The optimum adsorption conditions and the various factors influencing the process of adsorption are evaluated for the developed core-shell structures. Adsorption isotherms and kinetic models were used to investigate the nature and mechanism of the adsorption. Thus Mg^{2+} doped CeO_2 encapsulated Fe_3O_4 nanoparticles as efficient, cost-effective and easy-to-operate adsorbents for the selective removal of malachite green was evaluated.

4.2 Results and Discussion

4.2.1 XRD

The x-ray diffraction studies of the developed Mg^{2+} doped CeO_2 samples as well as the $Fe_3O_4@Mg$-doped CeO_2 core-shells were carried out to obtain crystallographic information. The x-ray

diffraction patterns of pure CeO_2 and CeO_2 doped with three different concentrations of Mg^{2+} are given in **Figure 4.1a**. The XRD diffraction patterns of pure and doped CeO_2 versions can be indexed to the cubic CeO_2 phase belonging to the Fm3m space group (JCPDS-00-043-1002)[67]. The diffraction peaks at 28.55, 33.07, 47.48, 56.34, 59.09, 69.41, 76.70 and 79.07 arise due to (111), (200), (220), (311), (222), (400), (331) and (420) planes respectively.
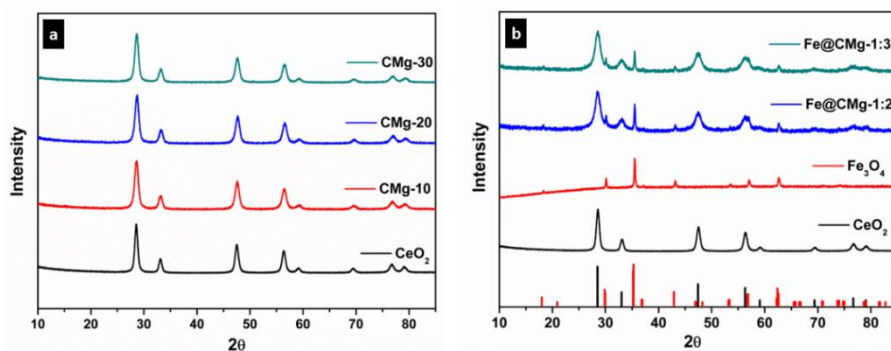
Figure 4.1 – a) X-ray diffraction patterns obtained for pure and Mg^{2+} doped CeO_2 samples; b) x-ray diffraction patterns of CeO_2, Fe_3O_4, core-shell compositions Fe@CMg-1:2 and Fe@CMg-1:3 along with reference patterns.

There are no additional peaks or significant shifts present in the case of Mg^{2+} doped CeO_2 variants, which confirms the successful doping of Mg^{2+} into the CeO_2 lattice. **Figure 4.1b** shows the x-ray diffraction patterns obtained for Fe_3O_4@Mg^{2+}doped CeO_2 core-shells of two different compositions along with XRD patterns of CeO_2, Fe_3O_4 and their corresponding reference peaks. Both the core-shell structures show no additional phases other than that of cubic CeO_2 (JCPDS-00-043-1002) and orthorhombic magnetite phase of Fe_3O_4 (JCPDS- 01-075-1609)[68]. The x-ray diffraction peaks of Fe_3O_4 at 18.27, 30.11,

30.21, 35.42, 35.53, 43.12, 56.96, 57.09, 62.61 and 62.82 corresponds to (011), (112), (200), (121), (103), (004), (231), (321), (224) and (400) respectively and are evident in the x-ray diffraction profile of Fe_3O_4@Mg^{2+}doped CeO_2 core-shell compositions.

4.2.2 FE-SEM

The FE-SEM (Field Emission Scanning Electron Microscopy) micrographs of Mg^{2+} doped CeO_2 and Fe_3O_4@ Mg^{2+} doped CeO_2 core-shells are given in **Figure 4.2.**
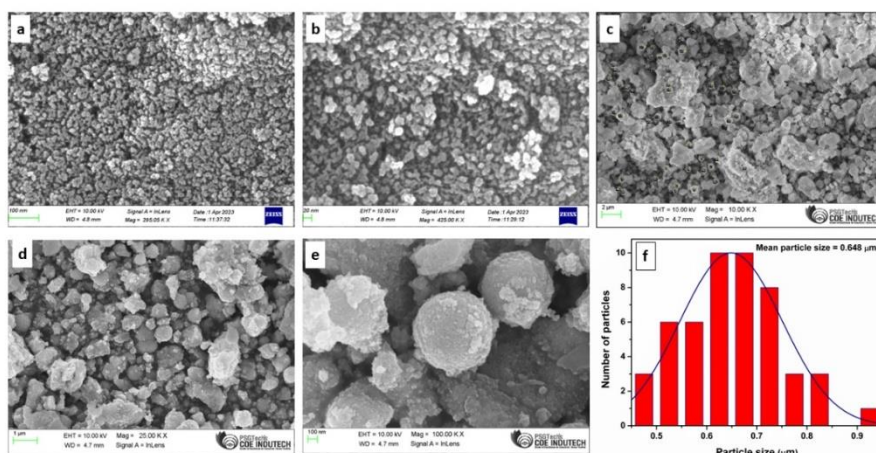
Figure 4.2 – FE-SEM micrographs of a, b) CMg-20; c, d, e) Fe@CMg-1:2 core-shells; f) particle size distribution obtained from SEM images.

Figures 4.2a and **4.2b** depict the FE-SEM images of Mg^{2+} doped CeO_2, where the particles are slightly aggregated and show a uniform size distribution and morphology. From the FE-SEM micrographs, it is evident that the Mg^{2+} doped CeO_2 particles fell exactly within the nanometre regime. In the case of Fe_3O_4@ Mg^{2+} doped CeO_2 core-

shells, as shown in **Figure 4.2c** and **Figure 4.2d**, the spherical particles were found to be in the micrometre range. **Figure 4.2f** gives the particle size distribution obtained from FE-SEM images and the mean particle size was found to be 0.648 μm. The micrometre-sized Fe@CMg-1:2 core-shells exhibited uniform size distribution as well as enhanced surface roughness. The SEM micrographs also revealed a slight degree of aggregation among the developed core-shells.

4.2.3 HR-TEM
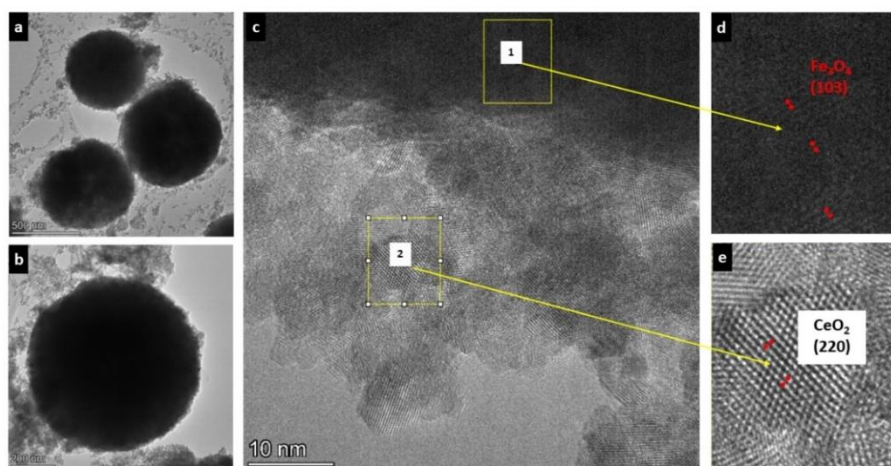
Figure 4.3 – HR-TEM images showing a,b) spherical Fe@CMg-1:2 core-shells in micrometre range; c) region marked 2 indicates the formation of a mesoporous shell of Mg^{2+} doped CeO_2 around a Fe_3O_4 core which is marked as region 1; d) enlarged image of region 1 showing an interplanar spacing corresponding to (103) plane of Fe_3O_4; e) enlarged image of region 2 showing an interplanar spacing corresponding to (220) plane of CeO_2.

The formation of the proposed Fe_3O_4@ Mg^{2+}doped CeO_2 core-shell structure was investigated using HR-TEM (High-Resolution Transmission Electron Microscopy) analysis. The HR-TEM images of

$Fe_3O_4@Mg^{2+}$ doped CeO_2 core-shells, Fe@CMg-1:2 are given in **Figure 4.3**. The Fe@CMg-1:2 core-shells were found to have their particle sizes in the micrometre range. As shown in **Figure 4.3a** and **4.3b**, these core-shells exhibited uniform morphology and size. The average Fe@CMg-1:2 core-shell diameter was found to be 565 nm. A magnified high-resolution image of one of the Fe@CMg-1:2 core-shell shown in **Figure 4.3c** clearly shows the presence of (103) planes of Fe_3O_4 having an interplanar spacing of 2.52 Å in the core region (region marked as 1)[68].

Again, the shell region (region marked as 2) contains (220) planes of CeO_2 having an interplanar spacing of 1.91 Å[67]. Thus, it is evident that the Fe_3O_4 particles are encapsulated within a shell of porous Mg^{2+} doped CeO_2. The TEM images indicate the formation of a uniform shell of CeO_2 around Fe_3O_4 particles having a thickness of around 30 nm.

4.2.4 XPS

The elemental composition as well as elemental oxidation states present in the developed core-shell structure Fe@CMg-1:2 was evaluated using XPS analysis. As per the survey spectra, the elements present in the developed $Fe_3O_4@Mg^{2+}$ doped CeO_2 core-shells were found to be C, Ce, Fe, Mg and O. The core level XPS spectra corresponding to O 1s, Ce 3d, Fe 2p and Mg 1s are given in **Figure 4.4**. The high-resolution O 1s spectrum shown in **Figure 4.4a** was deconvoluted into three peaks having binding energy values at 529.4, 530 and 531.38 eV which were attributed to lattice oxygen, hydroxyl and water adsorbed on the surface vacant sites and also to

oxygen deficit Ce^{+3} bonded regions[69]. In the Ce 3d fine spectrum of Fe@CMg-1:2 shown in **Figure 4.4b**, the spectrum was deconvoluted into 8 peaks [69, 70]. These peaks can be attributed to Ce $3d_{3/2}$ and Ce $3d_{5/2}$ spin-orbit splitting. Both Ce^{3+} and Ce^{4+} oxidation states are present and as evident from the fine spectra of Ce 3d, Ce^{4+} forms the superior valence state here.
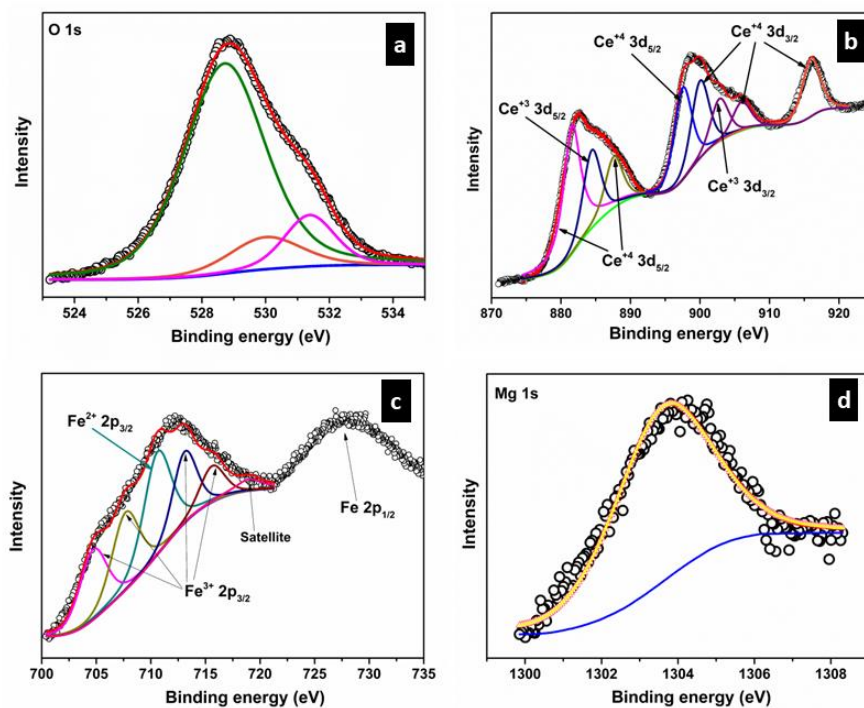
Figure 4.4- High resolution XPS spectra of a) O1s; b) Ce 3d; c) Fe 2p and d) Mg 1s of Fe@CMg-Fe-1:2 core-shells

The peaks at binding energy values 884.1 and 902.4 eV correspond to the $3d_{5/2}$ and $3d_{3/2}$ energy states of Ce^{3+} respectively. $3d_{5/2}$ peaks for Ce^{4+} were observed at 882.1, 888.4 and 897.5 eV. At the same time, Ce^{4+} $3d_{3/2}$ peaks were found at 899.3, 907.5 and 916.6 eV respectively[70]. The fine Fe 2p spectra given in **Figure 4.4c**, the

peaks corresponding to $2p_{3/2}$ and $2p_{½}$ of Fe^{2+} were found at binding energy values 710.6 and 723.8 eV respectively[71, 72]. At the same time due to spin-orbit and electrostatic interactions, each of the $2p_{3/2}$ and $2p_{1/2}$ peaks of Fe^{3+} fine spectra can be further split into four peaks. **Figure 4.4c** shows the splitting of Fe $2p_{3/2}$ into 5 peaks where four arise due to spin-orbit interaction in high spin Fe^{3+} and one due to Fe^{2+} $2p_{3/2}$ peak. A satellite peak was observed at 719 eV which confirms the formation of a pure Fe_3O_4 phase within the core-shell structure[71]. The relative amounts of Fe^{2+} and Fe^{3+} were estimated from the areas of corresponding peaks and were found to be 0.303:0.69 which is close to the actual Fe^{2+}: Fe^{3+} ratio in Fe_3O_4, *i.e.* 0.33:0.67[72].

In the case of Mg 1s xps fine spectra shown in **Figure 4.4d**, there exists only a single peak with a binding energy value of 1303.9 eV which is attributed to Mg^{2+} species in MgO or $Mg(OH)_2$[73]. Thus, the XPS analysis clearly shows that the core-shells consist only of Mg^{2+} doped CeO_2 and Fe_3O_4 phases.

4.2.5 BET surface area analysis

The N_2 adsorption isotherms of the Mg^{2+} doped CeO_2 samples are given in **Figure 4.5a** and the variation of the adsorption isotherms for Fe_3O_4, CMg-20 and Fe@CMg-1:2 core-shells are shown in **Figure 4.5b**. The surface area as well as porosity parameters such as pore volume and pore diameter are tabulated in **Table 4.1**. It can be seen that the surface area decreases gradually with an increase in Mg^{2+} dopant concentration. In the case of Fe_3O_4, the surface area was

found to be very small with large pore diameter and pore volume. Interestingly, the core-shell structures, Fe@CMg-1:2 exhibited better surface characteristics. Fe@CMg-1:2 was found to have almost double the surface area that of CMg-20.
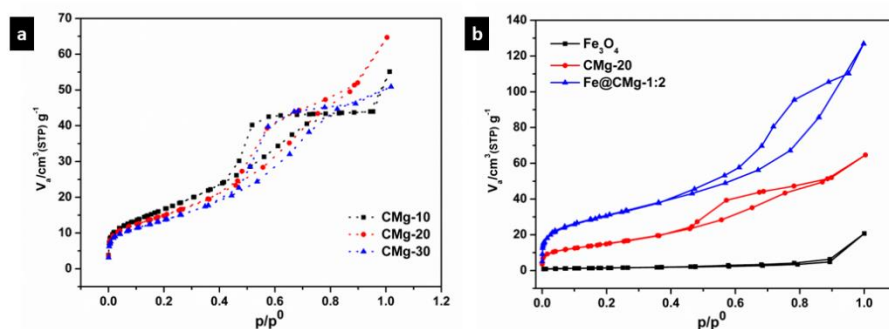
Figure 4.5- a) N_2 gas adsorption-desorption isotherms obtained for Mg^{2+} doped CeO_2 samples; b) the variation in adsorption-desorption isotherms for Fe_3O_4, CMg-20 and Fe@CMg-1:2 core-shells

Table 4.1 – BET surface area parameters obtained for Mg^{2+} doped CeO_2 samples, Fe_3O_4 and Fe@CMg-1:2

Sample	BET surface area $(m^2.g^{-1})$	Total pore volume $(cm^3.g^{-1})$	Pore diameter (nm)
CMg-10	63.30	0.078	4.959
CMg-20	55.73	0.097	7.004
CMg-30	50.23	0.077	6.158
Fe_3O_4	4.95	0.029	23.97
Fe@CMg-1:2	105.9	0.192	7.272

The enhanced surface area is one of the factors determining the adsorption performance towards malachite green. Also, all the

developed adsorbent materials were found to be mesoporous with their pore diameter falling within the 2-50 nm range. The core-shell design with a highly porous Mg^{2+} doped CeO_2 shell wrapped around a Fe_3O_4 core contributed much towards the adsorption capacity through surface area and porosity enhancement.

4.2.6 Magnetic studies

The M-H curve measured by vibrating sample magnetometer (VSM) at room temperature for Fe@CMg-1:2 core-shells is given in **Figure 4.6**. The inset of **Figure 4.6** shows the enlarged view of the M-H curve showing the hysteresis loop. Fe@CMg-1:2 core-shells exhibited a magnetization saturation value of 14.58 emu.g^{-1}. Fe@CMg-1:2 core-shells have an s-shaped hysteresis loop with a coercivity (H_c) of 51.24 O_e and a remanent magnetization (M_r) of 0.5136 emu.g^{-1} reflecting their ferromagnetic nature.
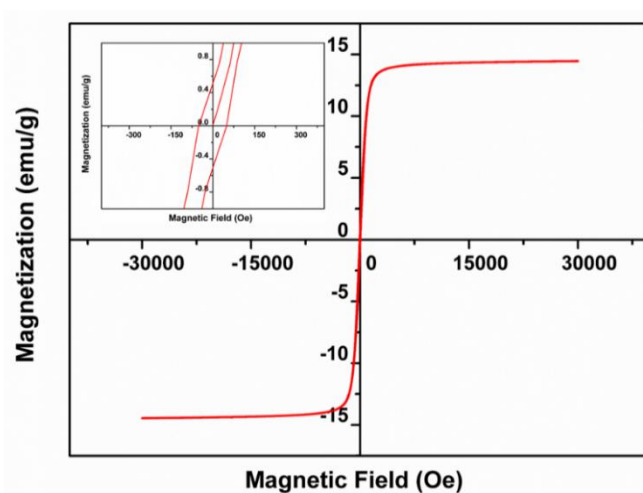
Figure 4.6 – Hysteresis measurement of Fe@CMg-1:2 core-shells at room temperature. The inset shows the enlarged M-H curve showing coercivity and remanent magnetization values.

4.2.7 Adsorption studies

4.2.7.1 Contact time

The adsorption capability of Mg^{2+} doped CeO_2 and $Fe_3O_4@Mg^{2+}$ doped CeO_2 core-shell structures towards malachite green was investigated in detail. The effect of contact time on the adsorption ability was studied using an initial malachite green dye concentration of 4 $mg.L^{-1}$ and an adsorbent dosage of 0.5 $g.L^{-1}$. The extent of adsorption over 60 minutes was investigated.
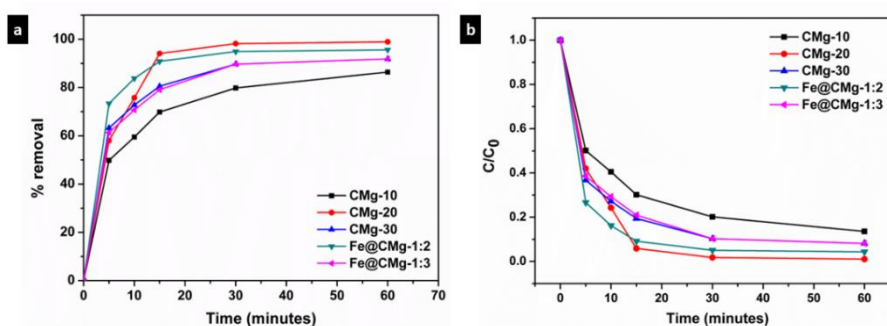
Figure 4.7-a) Malachite green removal percentages; b) adsorption rates obtained for Mg^{2+} doped CeO_2 samples and $Fe_3O_4@Mg^{2+}$ doped CeO_2 core-shell compositions

The percentage removal of malachite green with time for the Mg^{2+} doped CeO_2 and $Fe_3O_4@Mg^{2+}$ doped CeO_2 core-shell compositions are given in **Figure 4.7a**. **Figure 4.7b** shows the rate of adsorption over time for all 5 samples under investigation. CMg-20 shows the highest removal percentage of 98.9 % among all the samples. Coming next to CMg-20 is the Fe@CMg-1:2 core-shell structure having a removal efficiency of 95.1 %. The percentage removal of malachite green increases with Mg^{2+} doping reaches a maximum at a dopant concentration of 20 mmol per 100 mmol of CeO_2 (CMg-20)

and then decreases for 30 mmol Mg^{2+} dopant concentration (CMg-30). Among the core-shell compositions, Fe@CMg-1:2 showed better adsorption relative to Fe@CMg-1:3. As we have introduced the concept of magnetic core-shells for easy separation and recovery of adsorbent materials from solution, further adsorption studies are carried out using better performing Fe@CMg-1:2 core-shells. **Figure 4.8** shows the initial and final stages of malachite green adsorption by magnetically retrievable Fe@CMg-1:2. **Figure 4.8a** shows magnetic Fe@CMg-1:2 core-shells in malachite green solution before adsorption and **Figure 4.8b** shows Fe@CMg-1:2 core-shells collected after 60 minutes upon completion of the adsorption process.

Magnetic Fe@CMg-1:2 core-shells in MG solution before adsorption

Magnetic Fe@CMg-1:2 core-shells in clear solution after the adsorption of MG
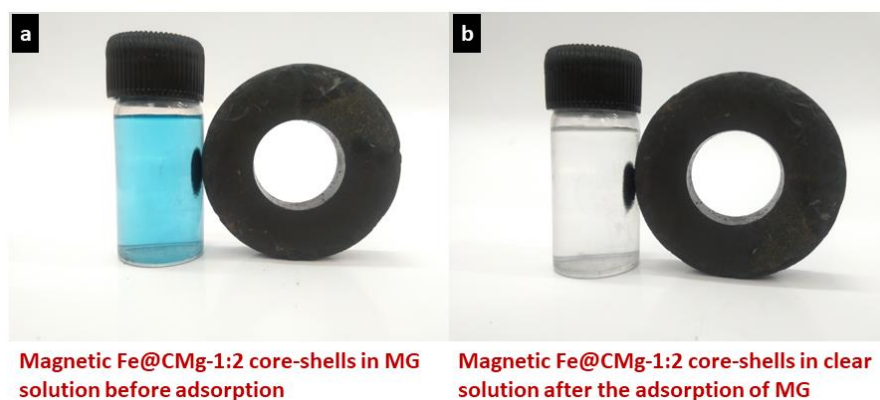
Figure 4.8- a) Initial and b) final stages of malachite green (MG) adsorption by magnetically retrievable Fe@CMg-1:2

4.2.7.2 Adsorbent loading

The optimum Fe@CMg-1:2 loading for the adsorption studies was studied by carrying out the adsorption experiments under four different adsorbent dosages and with a malachite green solution of an initial concentration of 3 mg.L^{-1}. With an increase in adsorbent

loading as shown in **Figure 4.9**, percentage removal starts to increase rapidly and then reaches almost an equilibrium at dosages above 0.5 g.L^{-1}. It has been found that the percentage removal at adsorbent loading of 0.5 g.L^{-1} was 95.6 % while an adsorbent loading of 1 g.L^{-1} exhibited only 96.6 % within 60 minutes.
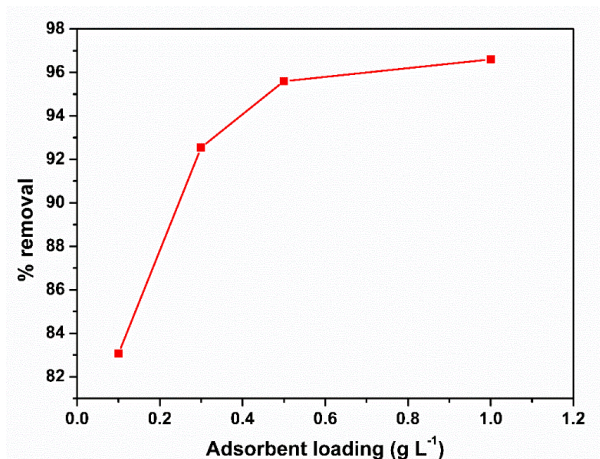
Figure 4.9 – The variation in percentage removal of malachite green with different Fe@CMg-1:2 loading

Almost double the adsorbent dosage yielded only a negligible 1 percentage increase in removal efficiency. Thus, the optimum adsorbent loading was fixed at 0.5 g.L^{-1}. The agglomeration of the adsorbent materials may be responsible for the retarded adsorption ability at higher adsorbent dosages. Further adsorption studies were done using the optimised adsorbent dosage.

4.2.7.3 Initial dye concentration

The effect of initial dye concentration on the adsorption performance was evaluated by varying the dye concentrations from 2 to 6 mg.L^{-1} and by employing an adsorbent dosage of 0.5 mg.L^{-1}.

The variation of percentage removal and q_e with different concentrations of malachite green is given in **Figure 4.10**.
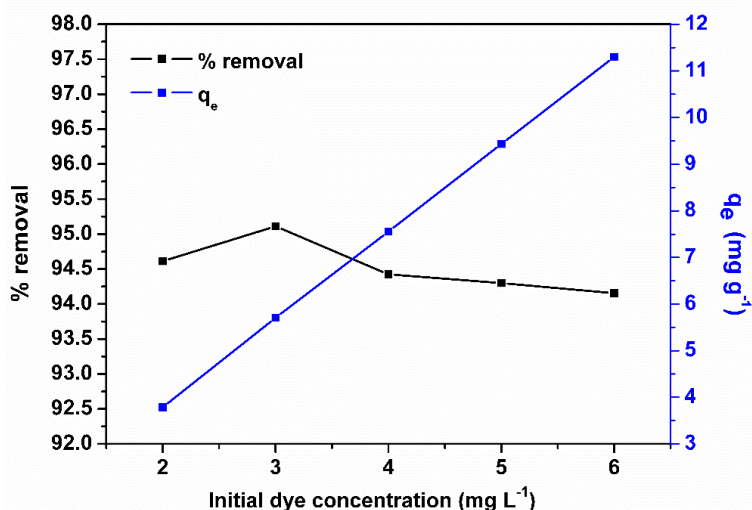
Figure 4.10 - The variation of percentage removal and q_e with different concentrations of malachite green on Fe@CMg-1:2 core-shells

The highest percentage of removal was obtained for an initial dye concentration of 3 mg.L^{-1}. Further increase in malachite green concentrations exhibited a slight decrease in removal efficiency. Even though there existed a decreasing trend, the percentage removals were maintained at around 94 %. At the same time, adsorption capacity showed a steady increase with an increase in initial malachite green concentrations. The reduced removal percentages at higher dye concentrations are mainly due to the saturation of surface adsorbent sites by dye molecules. Thus, the optimum malachite green concentration was found to be 3 mg.L^{-1}.

4.2.7.4 pH dependence studies

The adsorption abilities of developed adsorbents depend strongly on the pH of the solution medium. We have determined the pH_{pzc} value of developed Fe@CMg-1:2 core-shells by the pH drift method. The pH_{pzc} value obtained through the pH drift method was 3.77. Thus, it is clear that at pH values above 3.77, the Fe@CMg-1:2 surface charge is negative due to an increased number of hydroxyl ions and this is in agreement with the zeta potential value of -8.69 mV measured under neutral pH conditions. The zeta potentials of each of the individual components are given in **Table 4.2**.

Table 4.2 - Zeta potentials obtained for individual components and Fe@CMg-1:2 core-shells

Sample	Zeta potential
CeO_2	33 mV
CMg-20	8.16 mV
Fe_3O_4	37.7 mV
Fe@CMg- 1:2	-8.69 mV

At pH values less than 3.77, the Fe@CMg-1:2 adsorbent surface charge is positive. Complete ionisation of malachite green occurs around pH 4 or lower. Besides this, the pK_a value of malachite green is 6.9 where the cationic species change to a carbinol base upon the addition of OH^- ions. The effect of three different pH conditions (pH 3, neutral and pH 9) on the adsorption of malachite green by Fe@CMg-1:2 core-shells was evaluated. The adsorption

performance of Fe@CMg-1:2 at three different pH conditions is given in **Figure 4.11**.
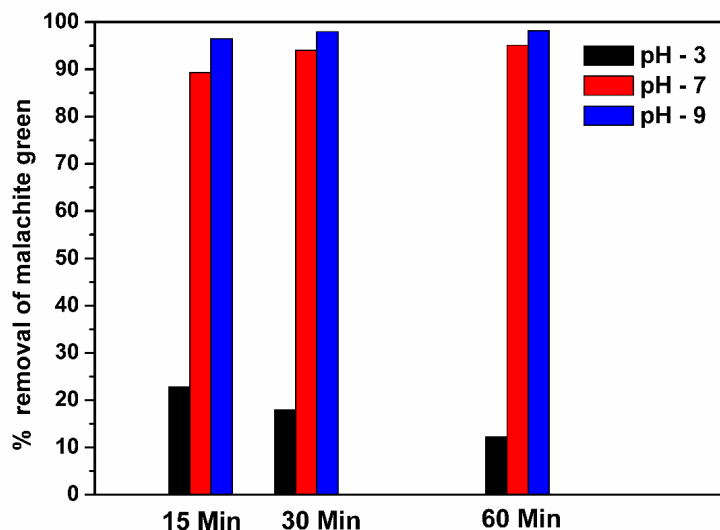
Figure 4.11 – Percentage removal of malachite green by Fe@CMg-1:2 under three different pH conditions over 60 minutes.

At pH 3, which is less than pH_{pzc}, the Fe@CMg-1:2 core-shell surface is positively charged and the malachite green exists as a positively charged species due to the protonation of auxochrome groups present in their structure. This has led to electrostatic repulsion between adsorbate and adsorbent and as shown in **Figure 4.11**, after an initial uptake onto the adsorbent surface, the dye molecules were desorbed back into the solution from the Fe@CMg-1:2 surface. Thus, the final percentage removal of malachite green by Fe@CMg-1:2 under acidic conditions is around 12.2 % only. At neutral pH conditions (pH > pH_{pzc}), Fe@CMg-1:2 surface charge is negative and malachite green exists as a positively charged/neutral species which facilitates the process of adsorption partially through electrostatic

attraction. The other part is due to the presence of H bonding as well as n-π interactions between the electron-deficient π electron system of malachite green and non-bonding electrons present on the O atom in surface hydroxyls. Adsorption carried out under a pH value of 9, exhibited even better percentage removal of malachite green which is around 98.16 %. Here electrostatic attraction between negatively charged Fe@CMg-1:2 surface and cationic dye species facilitate adsorption. Another important factor contributing to the enhanced adsorption is the presence of oxygen vacancies created upon Mg^{2+} doping into the CeO_2 lattice. These oxygen vacancies interact with water molecules to form surface hydroxyl groups which can form hydrogen bonds with malachite green molecules. Also at higher alkaline pH conditions, deprotonated surface hydroxyls or dissociated surface functional groups being negatively charged, form favourable electrostatic interactions with the tertiary amine group present in malachite green. For such interactions, the required high dipole moment for the tertiary amine group arises from the electron-deficient π system present in the aromatic ring of malachite green. To the contrary under acidic pH conditions, H_3O^+ ions compete with malachite green molecules for the surface-active sites.

4.2.7.5 Adsorption isotherms

Adsorption isotherms can be used to get insights about the nature of the adsorption process as well as to determine the adsorption capacity of an adsorbent towards a specific adsorbate. Here adsorption isotherms were plotted by carrying out adsorption experiments with the optimum adsorbent loading of 25 mg.g^{-1} and by varying the malachite green concentrations (2 to 6 mg.L^{-1}).
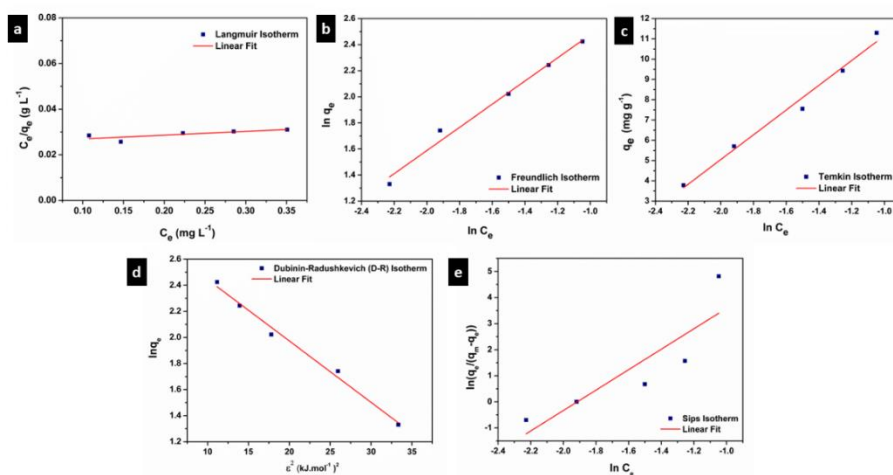
Figure 4.12 – Linearized a) Langmuir; b) Freundlich; c) Temkin; d) Dubinin-Radushkevich (D-R) and e) Sips adsorption isotherms for malachite green adsorption on Fe@CMg-1:2 core-shells.

The Langmuir adsorption model for homogeneous systems is given by

$$q_e = \frac{q_m b C_e}{1 + b C_e} \qquad (4.1)$$

where q_e is the quantity of dye adsorbed at equilibrium, q_m is the maximum quantity of dye adsorbed per unit weight of the adsorbent given in mg.g^{-1} and b is the Langmuir adsorption isotherm constant[74]. **Figure 4.12a** shows the linearized Langmuir adsorption isotherm[75, 76]. The obtained experimental data were fitted with the Langmuir model and various parameters involved were calculated and are given in **Table 4.3**.

According to the Freundlich adsorption model which can account for multilayer adsorption,

$$lnq_e = \frac{1}{n}lnC_e + \ln K_f \qquad (4.2)$$

where K_f and n are Freundlich adsorption isotherm constants[77].

Table 4.3 – Adsorption isotherm parameters and fitting details obtained using Langmuir, Freundlich, Temkin, Dubinin-Radushkevich (D-R) and Sips adsorption models.

Isotherm Model	Isotherm parameters	
Langmuir	q_m (mg.g^{-1})	60.53
	b (L.mg^{-1})	0.653
	R^2	0.505
Freundlich	n	1.125
	K_F (mg$^{(1-1/n)}$ L$^{1/n}$ g^{-1})	28.95
	R^2	0.982
Temkin	b_T (J.mol^{-1})	406.0
	A_T (L.mg^{-1})	16.92
	R^2	0.979
Dubinin-Radushkevich (D-R)	q_m (mg.g^{-1})	18.44
	K_{DR} (mol^2 ·kJ^{-2})	0.0471
	R^2	0.987
	E (kJ·mol^{-1})	3.26
Sips	q_m (mg.g^{-1})	11.39
	b_s (L^n.mg^{-n})	6.788
	n	0.255
	R^2	0.696

 The Freundlich adsorption isotherm obtained from experimental data is given in **Figure 4.12b**. The experimental data is then fitted with the Freundlich adsorption model and the resultant adsorption and fitting parameters are given in **Table 4.3**. Here K_f is a measure of adsorption capacity and $1/n$ determines the strength of the adsorption as well as the heterogeneity of the system[78]. Here the linear fitting analysis of experimental data gives the value of $1/n$ as 0.8885 and n is found to be 1.125. A value of $1/n$ less than one indicates normal adsorption and if it's above 1, it is cooperative adsorption. A value of n between 1 and 10, indicates that the sorption process is favourable[78-80].

As per the Temkin adsorption model, the heat of adsorption of all molecules decreases linearly with an increase in adsorbent surface coverage and it involves the uniform distribution of binding energies up to a certain maximum value of binding energy. The Temkin equation is given by

$$q_e = \frac{RT}{b_T} \ln A_T + \frac{RT}{b_T} \ln C_e \qquad (4.3)$$

where R is the universal gas constant, T is temperature, b_T is the constant related to the heat of sorption, and A_T is the Temkin isotherm equilibrium binding constant (L/g)[78, 80]. The Temkin adsorption isotherm is shown in **Figure 4.12c** and isotherm parameters and fitting details are given in **Table 4.3**.

The Dubinin-Radushkevich (D-R) adsorption model is given by

$$ln q_e = ln q_m - K_{DR} \varepsilon^2 \qquad (4.4)$$

where q_m is the maximum adsorbed amount (mg·g⁻¹), K_{DR} is the D-R model constant ($mol^2·kJ^{-2}$) and ε is the adsorption potential (($kJ·mol^{-1}$)[81, 82]. The Dubinin-Radushkevich (D-R) adsorption isotherm obtained for malachite green adsorption over Fe@CMg-1:2 core-shells is given in **Figure 4.12d** and the D-R model parameters with fitting details are given in **Table 4.3**.

According to the Sips adsorption model,

$$ln\frac{q_e}{q_m - q_e} = \frac{1}{n}lnC_e + ln\ b_s^{\frac{1}{n}} \qquad (4.5)$$

where q_m is the maximum adsorbed amount (mg.g⁻¹), b_s ($L^n.mg^{-n}$) and n are Sips model constants[81, 82]. The Sips adsorption isotherm is given in **Figure 4.12e** and the Sips isotherm fitting parameters are in **Table 4.3.**

Upon fitting experimental adsorption data with Langmuir, Freundlich, Temkin, Dubinin-Radushkevich (D-R) and Sips adsorption models, it was found that the best fit in terms of R^2 value was observed for Freundlich, Dubinin-Radushkevich (D-R) and Temkin adsorption models. Thus, the agreement of experimental data with Dubinin-Radushkevich (D-R), Freundlich and Temkin adsorption models points towards favourable heterogeneous multilayer adsorption.

4.2.7.6 Adsorption Kinetics

Kinetic studies were carried out to determine the rate of adsorption of malachite green over Fe@CMg-1:2. The pseudo-first-order and pseudo-second-order models were chosen for adsorption kinetic studies. According to the pseudo-first-order model

$$\log(q_e - q_t) = log q_e - \frac{k_1 t}{2.303} \qquad (4.6)$$

where q_e is the amount of malachite green adsorbed at equilibrium and q_t is the amount adsorbed over various time intervals[83, 84]. Here, k_1 is the pseudo-first-order rate constant and t is the time in minutes.

As per pseudo second order model,

$$\frac{t}{q_t} = \frac{1}{k_2 q_e^2} + \frac{t}{q_e} \qquad (4.7)$$

where k_2 is the pseudo-second-order rate constant[83, 84].

The experimental data obtained were correlated with both pseudo-first-order and pseudo-second-order kinetic models using linear regression analysis and are presented in **Figure 4.13**.
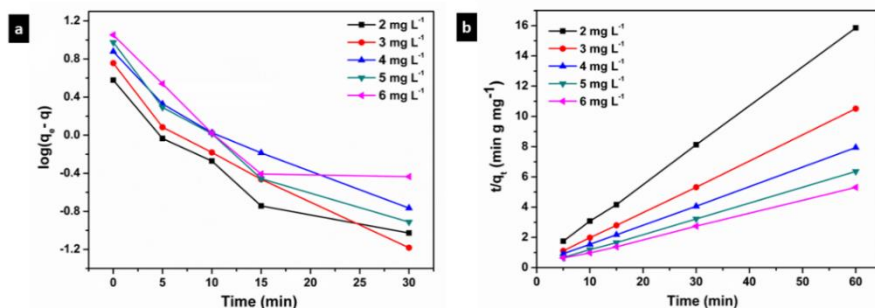
Figure 4.13 – a) Pseudo-first order; b) pseudo-second-order kinetic plots for malachite green adsorption on Fe@CMg-1:2 core-shells.

The calculated kinetic parameters and regression correlation coefficient R^2 values are given in **Table 4.4** along with experimental q_e values. From the kinetic studies, it is evident that the adsorption of malachite green over Fe@CMg-1:2 follows pseudo-second-order kinetics with an R^2 value of 0.999. Also, the experimentally observed

Table 4.4 – Pseudo-first and pseudo-second-order kinetic parameters along with experimental values obtained for malachite green adsorption over Fe@CMg-1:2 core-shells.

Malachite green concentration (mg.L⁻¹)	Pseudo first-order model			Pseudo second order model			q_e experimental (mg.g⁻¹)
	K_1 (min⁻¹)	q_e (mg.g⁻¹)	R^2	K_2 (g.mg⁻¹ min⁻¹)	q_e (mg.g⁻¹)	R^2	
2	0.1167	2.036	0.8257	0.1523	3.895	0.9997	3.784
3	0.1388	3.362	0.9336	0.1180	5.856	0.9999	5.706
4	0.1182	4.705	0.9227	0.0622	7.827	0.9999	7.554
5	0.1371	4.977	0.8743	0.0809	9.651	0.9998	9.429
6	0.1108	5.389	0.6665	0.0557	11.628	0.9991	11.298

q_e values are in agreement with pseudo-second-order kinetic model-derived q_e values. The good agreement of adsorption kinetics with the pseudo-second-order model implies that rather than external diffusion, surface active sites capable of forming electrostatic and Vander Waals interactions are the crucial deciding factors and the process is more of chemisorption in nature[79, 85].

To further understand the role of various kinds of diffusion on the adsorption rate, we have analysed the intraparticle diffusion model. According to the intraparticle diffusion model,

$$q_t = k_{id}t^{1/2} + c \qquad (4.8)$$

where k_{id} is the intraparticle diffusion rate constant (mg.g⁻¹.min⁻¹/²), t is time and c is the intercept in mg.g⁻¹ which gives a measure of

boundary layer thickness[13]. The Weber– Morris intraparticle diffusion plot of q_t versus $t^{1/2}$ is shown in **Figure 4.14**.
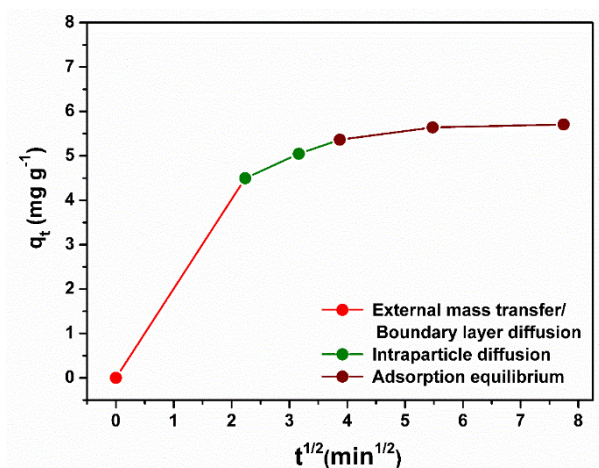
Figure 4.14 – Intraparticle diffusion model for malachite green adsorption over Fe@CMg-1:2 core-shells

The presence of multilinearity in the intraparticle diffusion plot indicates more than one adsorption rate determining factors[86, 87]. Here the first sharper portion represents adsorption due to external mass transfer as well as electrostatic boundary layer diffusion[13, 86]. The second portion of the plot corresponds to intraparticle diffusion into the mesoporous and micropores of the Fe@CMg-1:2 core-shells. The third region shows the adsorption process approaching equilibrium. The linear regression analysis of the intraparticle diffusion model was carried out and the obtained parameters are given in **Table 4.5**. The negative intercept (c_1) value indicates that the adsorption process is a combined effect of surface reaction and film diffusion[88]. The multilinearity and linear regression analysis parameters show that intraparticle diffusion is not the only rate-determining process.

Table 4.5 – Kinetic parameters obtained using intraparticle diffusion model for Fe@CMg-1:2 core-shells

	k_{id1}	C_1	R^2	k_{id2}	C_2	R^2
Intraparticle diffusion model	2.007	-0.017	0.9995	0.5334	3.319	0.987

4.2.7.7 Selectivity towards malachite green
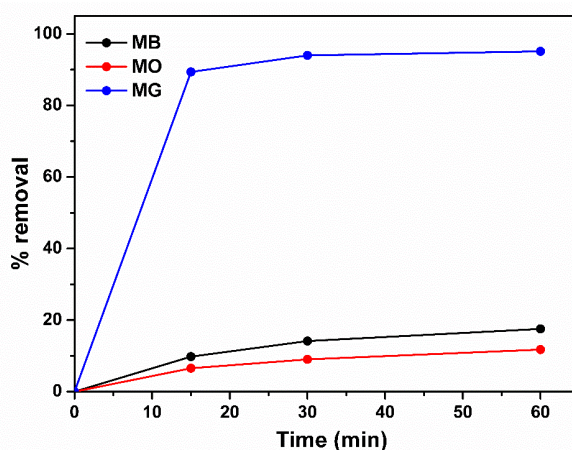
Figure 4.15- Comparison of percentage removals obtained for methylene blue (MB), methyl orange (MO) and malachite green (MG) using Fe@CMg-1:2 core-shells

To understand the extent of selectivity shown by Fe@CMg-1:2 towards malachite green, adsorption experiments were also performed using two other dyes, methylene blue and methyl orange. Here methylene blue is a cationic basic dye and methyl orange is an anionic azo dye. The results of adsorption experiments obtained for all three dyes are shown in **Figure 4.15**. After 60 minutes, Fe@CMg-1:2 core-shells have removed only 17.54 % of methylene blue and it

can be attributed to electrostatic interactions between negatively charged Fe@CMg-1:2 surface and positively charged methylene blue molecules. The electron-rich heterocyclic ring present in methylene blue renders the tertiary amine nitrogen less polarizing and the extent of hydrogen bond formation between tertiary amine nitrogen and surface hydroxyls decreases which in turn reduces the adsorption activity. In the case of methyl orange, the percentage removal was only 11.76 % in 60 minutes and it can be attributed to the electrostatic repulsion between negatively charged adsorbent surface and anionic adsorbate. Now the selective nature of Fe@CMg-1:2 towards malachite green is evident and it can be considered as an adsorbent material exclusively designed for malachite green removal.

4.2.7.8 Adsorption mechanism

The adsorption isotherm analysis and adsorption kinetic studies revealed the nature and possible mechanism of malachite green adsorption over Fe@CMg-1:2 core-shells. There are various factors controlling the adsorption process and the adsorption of malachite green over Fe@CMg-1:2 is the combined output of several physicochemical processes. The first factor playing a crucial role in adsorption is the surface characteristics of the adsorbent as well as the porosity. Enhanced surface area of Fe@CMg-1:2 core-shells as well as the porous shell structure of Mg^{2+} doped CeO_2 around Fe_3O_4 can provide a better area of contact for the malachite green molecules. The porous character of the developed core-shells is obvious from the BET surface area analysis. Another driving factor for the adsorption process is electrostatic interactions between the

adsorbent and adsorbate. Above pH > pH_{pzc} value of 3.77, the Fe@CMg-1:2 surface is found negatively charged and at the same time the malachite green dye molecules exist in their cationic forms, which can enhance the process of adsorption through electrostatic interactions. In the case of highly acidic pH environments (pH< 3.77) there exists electrostatic repulsion between likely charged adsorbent surface and dye molecules and also the H_3O^+ ions compete with malachite green molecules for surface active sites. In contrast to this, under alkaline conditions, in addition to the favourable electrostatic attraction between the adsorbent surface and adsorbate, there occurs deprotonation of surface hydroxyls and this may lead to an enhanced amount of hydrogen bonding between tertiary amine group present in malachite green molecules and deprotonated surface species.

Now the superior factor contributing to the adsorption of malachite green over Fe@CMg-1:2 is found to be the surface-active sites. Upon doping Mg^{2+} ions into the CeO_2 lattice, an optimum concentration of oxygen vacancies was generated. These oxygen vacancies interact with water molecules to yield surface hydroxyls which in turn form hydrogen bonds with malachite green molecules. Also, the Mg-O species present on the surface can form Mg-OH, which leads to an increased amount of hydrogen bonding with malachite green dye molecules. Also, surface ligand complexation between Mg and OH under alkaline conditions leads to Mg-OH formation[13]. A graphical illustration of the selective adsorption mechanism of malachite green over Fe@CMg-1:2 core-shells is given in **Figure 4.16**. Thus, the overall adsorption process is a result of surface characteristics,

electrostatic attraction, intraparticle diffusion into the mesoporous core-shells, surface complexation and hydrogen bond formation.
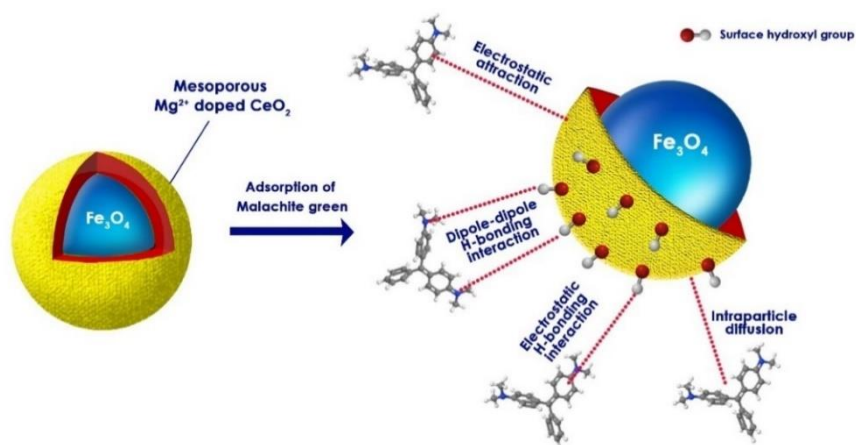
Figure 4.16 – Selective adsorption mechanism of malachite green over Fe@CMg-1:2 core-shells

4.2.8 Thermal stability studies

The thermal stability of the developed Fe@CMg-1:2 core-shell adsorbents was evaluated by thermogravimetric analysis. The TGA and DTA curves obtained for Fe@CMg-1:2 over a temperature range of 30-800 °C are given in **Figure 4.17**. It was found that there was no significant weight loss occurring during the thermal treatment. The weight loss observed in the initial stages can be attributed to the removal of adsorbed moisture and gases on the adsorbent surface. At elevated temperatures occurs the oxidation of Fe_3O_4 into Fe_2O_3[89, 90]. Even then the maximum weight loss experienced was around 3.5 % only, which indicates the high-temperature stability of Fe@CMg-1:2.
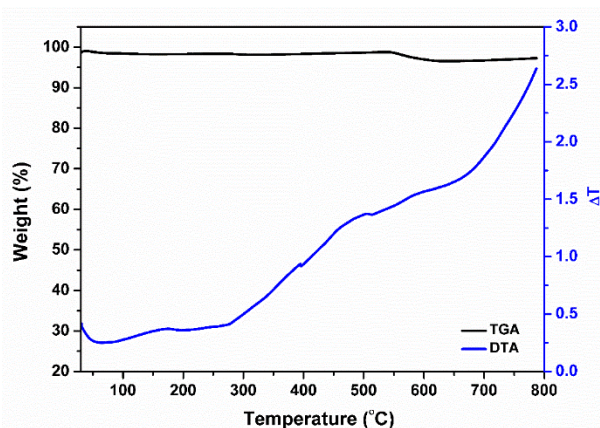
Figure 4.17 – TGA and DTA plots of Fe@CMg-1:2 core-shells

4.2.9 Reusability studies

The recovery and recyclability of the developed adsorbent materials determine their practical applicability and cost-effectiveness. For the reuse of Fe@CMg-1:2, a combination of chemical and thermal regeneration methods was employed. Once the adsorption process is completed, the malachite green adsorbed Fe@CMg-1:2 core-shells were magnetically separated from the aqueous medium and stirred with 20:1 (volume ratio) ethanol-HCl solution for 30 minutes. Then the adsorbent material was collected by centrifugation, washed several times with distilled water and then dried in a hot air oven at 180 °C for 12 hours. These regenerated adsorbents were then used for consecutive cycles of adsorption and percentage removals were measured. The percentage removal obtained over 4 consecutive reusability cycles is given in **Figure 4.18**. Even though there is a gradual decrease in percentage removal from 95.1 % to 82.4 % over 4 cycles, Fe@CMg-1:2 core-shells exhibit good recyclability and economic affordability.
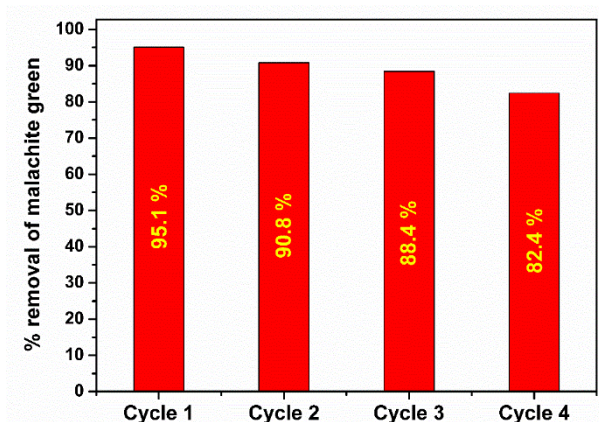
Figure 4.18- MG Percentage removals obtained for Fe@CMg-1:2 core-shells over 4 consecutive reusability cycles.

4.2.10 Comparison with reported adsorbents

Table 4.6 gives a comparison of the malachite green adsorption performance of Fe@CMg-1:2 core-shells with other available adsorbents in the literature. Even though many of the adsorbents are superior to Fe@CMg-1:2 core-shells in adsorption capacity, Fe@CMg-1:2 core-shells are the only candidates which can be applied over a wider pH range with high selectivity, magnetic retrievability, and temperature stability.

Table 4.6 - Comparison of adsorption performance of Fe@CMg-1:2 core-shells with other available adsorbents

Adsorbent	Optimum pH range	q_m (mg.g^{-1})	Selectivity	Mode of recovery	Reusability cycles and retained removal efficiency	Reference
Fe@CMg-1:2 core-shells **(Present work)**	pH 7 and above	18.4	Selective	Magnetic separation	4 cycles (82.4 %)	-
Powdered activated carbon	pH 7 and above	509	Non-selective	Filtration	-	[46]
Activated carbon	pH 7 and above	83.06	Non-selective	Filtration	-	[37]
Rice husk-activated carbon	pH 7 and above	63.85	Non-selective	Filtration		[40]
Rattan sawdust	pH 10-12	62.71	Non-selective	Filtration	-	[38]

Eucalyptus bark	pH 5	59.88	Non-selective	Filtration	-	[41]
Organically modified clay	pH independent	40.48	Non-selective	Physical and chemical methods	-	[39]
Orange peel	-	483.6	Non-selective	-	-	[91]
Fly ash	pH > 6	40.65	Non-selective	Filtration	-	[42]
Surfactant-modified alumina	pH 2.5–4.75	185	Non-selective	Column regeneration with acetone	2 cycles (80 % removal)	[92]
Zeolite	pH 6	46.35	Selective	-	-	[43]
Copper nanowires loaded on activated carbon	pH > 5	434.8	Non-selective	Filtration	-	[93]

ZnO nanoparticles	pH 8	310.5	Selective	Filtration	3 cycles (21 %)	[44]
γ- Fe_2O_3	pH 3	227.3	Selective	Magnetic separation	-	[94]
Functionalized multi-wall carbon nanotubes	pH 7	142.8	Non-selective	Filtration	-	[45]
NiO nanoflakes	-	142.0	Selective	Filtration	-	[50]
Melamine-supported magnetic iron oxide (Fe_3O_4) nanoparticles	pH 6.5	9.06	Selective	Magnetic separation	6 cycles	[51]
Polyaniline–nickel ferrite magnetic nanocomposite	pH 7	4.09	Selective	Magnetic separation	-	[48]

Fe$_3$O$_4$@PANI nanocomposites	pH 7	240	-	Magnetic separation	3 cycles (90 %)	[49]
Graphite oxide (GO)	-	248	Non-selective	Filtration	-	[47]
Magnetic corn straw-derived biochar supported nZVI composite	pH 6	515.7	-	Magnetic recovery	7 cycles (90 %)	[95]
Polycarboxylic magnetic polydopamine sub-microspheres	pH 7	331.0	-	Magnetic recovery	8 cycles (80 %)	[96]
Magnetic Nickel Oxide Nanoparticles	pH 7	87.7	-	Magnetic recovery	4 cycles	[52]
CeO$_2$ nanoparticles	pH 7	558.6	-	Filtration	5 cycles (~70 %)	[64]

4.3 Conclusion

Fe@CMg-1:2 core-shells are developed with Fe_3O_4 nanoparticle core surrounded by a mesoporous shell of Mg^{2+} doped CeO_2. These core-shells are developed to meet the requirement of a cost-effective, highly efficient, selective, reusable and easily recoverable adsorbent material for the removal of malachite green dye, which is carcinogenic and mutagenic. The optimum adsorption conditions for Fe@CMg-1:2 core-shells were evaluated and the effect of pH, dye concentration, contact time, and adsorbent dosage on the adsorption process were investigated in detail. Fe@CMg-1:2 core-shells were found to have attained an adsorption efficiency of 95.1 % with an adsorbent dosage of 0.5 $g.L^{-1}$ in a malachite green solution of concentration 3 $mg.L^{-1}$. Adsorption isotherm analysis showed that the adsorption of malachite green over Fe@CMg-1:2 can be best fitted with Freundlich, Dubinin-Radushkevich (D-R) and Temkin adsorption models and the process is regarded as heterogeneous multilayer adsorption. The maximum adsorption capacity (q_m) was found to be 18.44 $mg.g^{-1}$ according to the Dubinin-Radushkevich (D-R) model. From the adsorption kinetic studies, it is obvious that the adsorption followed a pseudo-second-order model which is related to chemisorption mostly. In addition, the thermal stability as well as reusability of the adsorbent materials were evaluated. During thermal treatment, Fe@CMg-1:2 showed only 3.5 % weight loss till 800 ^{o}C. Fe@CMg-1:2 core-shells were used over four consecutive reusability cycles and the efficiency was retained at 82.4 %. A detailed mechanism for the selective adsorption activity was also

proposed supported by experimental information. The high efficiency and selectivity towards malachite green arise as the combined output of enhanced surface area, porosity, electrostatic attraction, surface functionalities and hydrogen bonding between adsorbate and adsorbent. Thus, magnetically recoverable Fe@CMg-1:2 core-shells are promising adsorbents for malachite green removal. Here we have used malachite green as a model pollutant and now by tuning or modifying the fundamental structure, these core-shell entities can be used as highly selective removal tools for a wide variety of pollutants in various fields.

4.4 References

1. Kumar, M., P. Borah, and P. Devi, *Chapter 3 - Priority and emerging pollutants in water*, in *Inorganic Pollutants in Water*, P. Devi, P. Singh, and S.K. Kansal, Editors. 2020, Elsevier. p. 33-49.
2. Gooty, J.M., et al., *Chapter 12 - Occurrence and fate of micropollutants in surface waters*, in *Environmental Micropollutants*, M.Z. Hashmi, S. Wang, and Z. Ahmed, Editors. 2022, Elsevier. p. 233-269.
3. Maheshwari, K., M. Agrawal, and A.B. Gupta, *Dye Pollution in Water and Wastewater*, in *Novel Materials for Dye-containing Wastewater Treatment*, S.S. Muthu and A. Khadir, Editors. 2021, Springer Singapore: Singapore. p. 1-25.
4. Pereira, L. and M. Alves, *Dyes—Environmental Impact and Remediation*, in *Environmental Protection Strategies for Sustainable Development*, A. Malik and E. Grohmann, Editors. 2012, Springer Netherlands: Dordrecht. p. 111-162.
5. Christie, R.M., *Pigments, dyes and fluorescent brightening agents for plastics: An overview.* Polymer International, 1994. **34**(4): p. 351-361.
6. Wainwright, M., *Dyes in the development of drugs and pharmaceuticals.* Dyes and Pigments, 2008. **76**(3): p. 582-589.
7. Lellis, B., et al., *Effects of textile dyes on health and the environment and bioremediation potential of living organisms.* Biotechnology Research and Innovation, 2019. **3**(2): p. 275-290.

8. Farah Maria Drumond, C., et al., *Textile Dyes: Dyeing Process and Environmental Impact*, in *Eco-Friendly Textile Dyeing and Finishing*, G. Melih, Editor. 2013, IntechOpen: Rijeka. p. Ch. 6.

9. Mani, S., P. Chowdhary, and R.N. Bharagava, *Textile Wastewater Dyes: Toxicity Profile and Treatment Approaches*, in *Emerging and Eco-Friendly Approaches for Waste Management*, R.N. Bharagava and P. Chowdhary, Editors. 2019, Springer Singapore: Singapore. p. 219-244.

10. Benkhaya, S., S. M' rabet, and A. El Harfi, *A review on classifications, recent synthesis and applications of textile dyes.* Inorganic Chemistry Communications, 2020. **115**: p. 107891.

11. Raval, N.P., P.U. Shah, and N.K. Shah, *Malachite green "a cationic dye" and its removal from aqueous solution by adsorption.* Applied Water Science, 2017. **7**(7): p. 3407-3445.

12. ALDERMAN, D.J., *Malachite green: a review.* Journal of Fish Diseases, 1985. **8**(3): p. 289-298.

13. Zhang, Q., et al., *Facile preparation of robust dual MgO-loaded carbon foam as an efficient adsorbent for malachite green removal.* Environmental Research, 2021. **195**: p. 110698.

14. Mustapha, S., et al., *Removal of Pollutants from Wastewater Through Nanofiltration: A Review*, in *Nanofiltration Membrane for Water Purification*, A. Ahmad and M.B. Alshammari, Editors. 2023, Springer Nature Singapore: Singapore. p. 247-268.

15. Siagian, U.W., et al., *High-performance ultrafiltration membrane: Recent progress and its application for wastewater treatment.* Current Pollution Reports, 2021: p. 1-15.

16. Tijani, J.O., et al., *Photocatalytic, electrochemical, antibacterial and antioxidant behaviour of carbon-sulphur Co-doped zirconium (IV) oxide nanocomposite.* Cleaner Chemical Engineering, 2022. **3**: p. 100034.

17. Chong, M.N., et al., *Recent developments in photocatalytic water treatment technology: a review.* Water research, 2010. **44**(10): p. 2997-3027.

18. Greenlee, L.F., et al., *Reverse osmosis desalination: water sources, technology, and today's challenges.* Water research, 2009. **43**(9): p. 2317-2348.

19. Egbosiuba, T.C., et al., *Adsorption of Cr(VI), Ni(II), Fe(II) and Cd(II) ions by KIAgNPs decorated MWCNTs in a batch and fixed bed process.* Scientific Reports, 2021. **11**(1): p. 75.

20. Egbosiuba, T.C., et al., *Activated multi-walled carbon nanotubes decorated with zero valent nickel nanoparticles for arsenic, cadmium and lead adsorption from wastewater in a batch and*

continuous flow modes. Journal of Hazardous Materials, 2022. **423**: p. 126993.

21. Egbosiuba, T.C. and A.S. Abdulkareem, *Highly efficient as-synthesized and oxidized multi-walled carbon nanotubes for copper(II) and zinc(II) ion adsorption in a batch and fixed-bed process.* Journal of Materials Research and Technology, 2021. **15**: p. 2848-2872.

22. Alex Mbachu, C., et al., *Green synthesis of iron oxide nanoparticles by Taguchi design of experiment method for effective adsorption of methylene blue and methyl orange from textile wastewater.* Results in Engineering, 2023. **19**: p. 101198.

23. Teh, C.Y., et al., *Recent advancement of coagulation–flocculation and its application in wastewater treatment.* Industrial & Engineering Chemistry Research, 2016. **55**(16): p. 4363-4389.

24. Crini, G. and E. Lichtfouse, *Advantages and disadvantages of techniques used for wastewater treatment.* Environmental Chemistry Letters, 2019. **17**(1): p. 145-155.

25. De Gisi, S. and M. Notarnicola, *Industrial Wastewater Treatment.* 2017.

26. Amigun, A.T., et al., *Photocatalytic degradation of malachite green dye using nitrogen/sodium/iron-TiO2 nanocatalysts.* Results in Chemistry, 2022. **4**: p. 100480.

27. Amiri-Hosseini, S. and Y. Hashempour, *Photocatalytic removal of Malachite green dye from aqueous solutions by nano-composites containing titanium dioxide: A systematic review.* Environmental Health Engineering And Management Journal, 2021. **8**(4): p. 295-302.

28. Ju, Y., et al., *Microwave-assisted rapid photocatalytic degradation of malachite green in TiO2 suspensions: mechanism and pathways.* The Journal of Physical Chemistry A, 2008. **112**(44): p. 11172-11177.

29. Zhang, Y., et al., *Synthesis of SnO2/ZnO flowerlike composites photocatalyst for enhanced photocatalytic degradation of malachite green.* Optical Materials, 2022. **133**: p. 112978.

30. Saad, A.M., et al., *Photocatalytic degradation of malachite green dye using chitosan supported ZnO and Ce–ZnO nano-flowers under visible light.* Journal of environmental management, 2020. **258**: p. 110043.

31. Mostafa, E.M. and E. Amdeha, *Enhanced photocatalytic degradation of malachite green dye by highly stable visible-light-responsive Fe-based tri-composite photocatalysts.* Environmental Science and Pollution Research, 2022. **29**(46): p. 69861-69874.

32. Hashemian, S., *Fenton-like oxidation of Malachite green solutions: kinetic and thermodynamic study.* Journal of Chemistry, 2013. **2013**.

33. Hameed, B. and T. Lee, *Degradation of malachite green in aqueous solution by Fenton process.* Journal of hazardous materials, 2009. **164**(2-3): p. 468-472.

34. Guenfoud, F., M. Mokhtari, and H. Akrout, *Electrochemical degradation of malachite green with BDD electrodes: effect of electrochemical parameters.* Diamond and Related Materials, 2014. **46**: p. 8-14.

35. Wang, L., et al., *Removal of malachite green by electrochemical oxidation polymerization and electrochemical reduction precipitation: its kinetics and intermediates.* Journal of Solid State Electrochemistry, 2022. **26**(10): p. 2231-2246.

36. Moumeni, O., O. Hamdaoui, and C. Pétrier, *Sonochemical degradation of malachite green in water.* Chemical Engineering and Processing: Process Intensification, 2012. **62**: p. 47-53.

37. Qu, W., et al., *Effect of properties of activated carbon on malachite green adsorption.* Fuel, 2019. **249**: p. 45-53.

38. Hameed, B.H. and M.I. El-Khaiary, *Malachite green adsorption by rattan sawdust: Isotherm, kinetic and mechanism modeling.* Journal of Hazardous Materials, 2008. **159**(2): p. 574-579.

39. Arellano-Cárdenas, S., et al., *Study of malachite green adsorption by organically modified clay using a batch method.* Applied Surface Science, 2013. **280**: p. 74-78.

40. Sharma, Y., *Fast removal of malachite green by adsorption on rice husk activated carbon.* The Open Environmental Pollution & Toxicology Journal, 2009. **1**(1).

41. Boutemedjet, S. and O. Hamdaoui, *Sorption of malachite green by eucalyptus bark as a non-conventional low-cost biosorbent.* Desalination and Water Treatment, 2009. **8**(1-3): p. 201-210.

42. Witek-Krowiak, A., et al., *Removal of Cationic Dyes from Aqueous Solutions using Microspherical Particles of Fly Ash.* Water Environment Research, 2012. **84**(2): p. 162-170.

43. Wang, S. and E. Ariyanto, *Competitive adsorption of malachite green and Pb ions on natural zeolite.* Journal of Colloid and Interface Science, 2007. **314**(1): p. 25-31.

44. Kumar, K.Y., et al., *Low-cost synthesis of metal oxide nanoparticles and their application in adsorption of commercial dye and heavy metal ion in aqueous solution.* Powder Technology, 2013. **246**: p. 125-136.

45. Shirmardi, M., et al., *The adsorption of malachite green (MG) as a cationic dye onto functionalized multi walled carbon nanotubes.*

Korean Journal of Chemical Engineering, 2013. **30**(8): p. 1603-1608.

46.   Kumar, K.V., *Comparative analysis of linear and non-linear method of estimating the sorption isotherm parameters for malachite green onto activated carbon.* Journal of Hazardous Materials, 2006. **136**(2): p. 197-202.

47.   Bradder, P., et al., *Dye Adsorption on Layered Graphite Oxide.* Journal of Chemical & Engineering Data, 2011. **56**(1): p. 138-141.

48.   Patil, M.R. and V.S. Shrivastava, *Adsorption of malachite green by polyaniline–nickel ferrite magnetic nanocomposite: an isotherm and kinetic study.* Applied Nanoscience, 2015. **5**(7): p. 809-816.

49.   Mahto, T.K., A.R. Chowdhuri, and S.K. Sahu, *Polyaniline-functionalized magnetic nanoparticles for the removal of toxic dye from wastewater.* Journal of Applied Polymer Science, 2014. **131**(19).

50.   Wei, A., et al., *Synthesis and formation mechanism of flowerlike architectures assembled from ultrathin NiO nanoflakes and their adsorption to malachite green and acid red in water.* Chemical Engineering Journal, 2014. **239**: p. 141-148.

51.   Mirzajani, R. and S. Ahmadi, *Melamine supported magnetic iron oxide nanoparticles (Fe3O4@Mel) for spectrophotometric determination of malachite green in water samples and fish tissues.* Journal of Industrial and Engineering Chemistry, 2015. **23**: p. 171-178.

52.   Mohanta, J., B. Dey, and S. Dey, *Sucrose-Triggered, Self-Sustained Combustive Synthesis of Magnetic Nickel Oxide Nanoparticles and Efficient Removal of Malachite Green from Water.* ACS Omega, 2020. **5**(27): p. 16510-16520.

53.   Wang, L., et al., *Rational design, synthesis, adsorption principles and applications of metal oxide adsorbents: a review.* Nanoscale, 2020. **12**(8): p. 4790-4815.

54.   Singh, N.B., et al., *Water purification by using Adsorbents: A Review.* Environmental Technology & Innovation, 2018. **11**: p. 187-240.

55.   Dotto, G.L. and G. McKay, *Current scenario and challenges in adsorption for water treatment.* Journal of Environmental Chemical Engineering, 2020. **8**(4): p. 103988.

56.   Momina and K. Ahmad, *Feasibility of the adsorption as a process for its large scale adoption across industries for the treatment of wastewater: Research gaps and economic assessment.* Journal of Cleaner Production, 2023. **388**: p. 136014.

57.   Moosavi, S., et al., *Application of Efficient Magnetic Particles and Activated Carbon for Dye Removal from Wastewater.* ACS Omega, 2020. **5**(33): p. 20684-20697.

58. Kharissova, O.V., H.V.R. Dias, and B.I. Kharisov, *Magnetic adsorbents based on micro- and nano-structured materials.* RSC Advances, 2015. **5**(9): p. 6695-6719.

59. Mehta, D., S. Mazumdar, and S.K. Singh, *Magnetic adsorbents for the treatment of water/wastewater—A review.* Journal of Water Process Engineering, 2015. **7**: p. 244-265.

60. Cheng, S., et al., *Preparation of magnetic adsorbent-photocatalyst composites for dye removal by synergistic effect of adsorption and photocatalysis.* Journal of Cleaner Production, 2022. **348**: p. 131301.

61. Tomić, N.M., et al., *Nanocrystalline CeO2–δ as Effective Adsorbent of Azo Dyes.* Langmuir, 2014. **30**(39): p. 11582-11590.

62. Wu, B. and I.M.C. Lo, *Surface Functional Group Engineering of CeO2 Particles for Enhanced Phosphate Adsorption.* Environmental Science & Technology, 2020. **54**(7): p. 4601-4608.

63. Wang, F., et al., *Preparation of CeO2@SiO2 Microspheres by a Non-sintering Strategy for Highly Selective and Continuous Adsorption of Fluoride Ions from Wastewater.* ACS Sustainable Chemistry & Engineering, 2019. **7**(17): p. 14716-14726.

64. Borgohain, X., E. Das, and M.H. Rashid, *Facile synthesis of CeO2 nanoparticles for enhanced removal of malachite green dye from an aqueous environment.* Materials Advances, 2023. **4**(2): p. 683-693.

65. Yang, C., et al., *Defect Engineering on CeO2-Based Catalysts for Heterogeneous Catalytic Applications.* Small Structures, 2021. **2**(12): p. 2100058.

66. Montini, T., et al., *Fundamentals and Catalytic Applications of CeO2-Based Materials.* Chemical Reviews, 2016. **116**(10): p. 5987-6041.

67. Trusova, E.A. and N.S. Trutnev, *Cryochemical synthesis of ultrasmall, highly crystalline, nanostructured metal oxides and salts.* Beilstein Journal of Nanotechnology, 2018. **9**(1): p. 1755-1763.

68. Wang, Z., et al., *Effect of Steam During Fischer–Tropsch Synthesis Using Biomass-Derived Syngas.* Catalysis Letters, 2017. **147**(1): p. 62-70.

69. Maslakov, K.I., et al., *The electronic structure and the nature of the chemical bond in CeO 2.* Physical Chemistry Chemical Physics, 2018. **20**(23): p. 16167-16175.

70. Bortamuly, R., et al., *CeO2-PANI-HCl and CeO2-PANI-PTSA composites: synthesis, characterization, and utilization as supercapacitor electrode materials.* Ionics, 2020. **26**.

71. Ai, Q., et al., *One-pot co-precipitation synthesis of Fe3O4 nanoparticles embedded in 3D carbonaceous matrix as anode for lithium ion batteries.* Journal of Materials Science, 2019. **54**(5): p. 4212-4224.

72. Yamashita, T. and P. Hayes, *Analysis of XPS spectra of Fe2+ and Fe3+ ions in oxide materials.* Applied surface science, 2008. **254**(8): p. 2441-2449.

73. Morales, M.V., et al., *CuPd Bimetallic Nanoparticles Supported on Magnesium Oxide as an Active and Stable Catalyst for the Reduction of 4-Nitrophenol to 4-Aminophenol.* International Journal of Green Technology, 2018. **3**: p. 51-62.

74. Chukwu Onu, D., et al., *Isotherm, kinetics, thermodynamics, recyclability and mechanism of ultrasonic assisted adsorption of methylene blue and lead (II) ions using green synthesized nickel oxide nanoparticles.* Environmental Nanotechnology, Monitoring & Management, 2023. **20**: p. 100818.

75. Al-Ghouti, M.A. and D.A. Da'ana, *Guidelines for the use and interpretation of adsorption isotherm models: A review.* Journal of Hazardous Materials, 2020. **393**: p. 122383.

76. Wang, J. and X. Guo, *Adsorption isotherm models: Classification, physical meaning, application and solving method.* Chemosphere, 2020. **258**: p. 127279.

77. Egbosiuba, T.C., et al., *Ultrasonic enhanced adsorption of methylene blue onto the optimized surface area of activated carbon: Adsorption isotherm, kinetics and thermodynamics.* Chemical Engineering Research and Design, 2020. **153**: p. 315-336.

78. Dada, O., et al., *Langmuir, Freundlich, Temkin and Dubinin–Radushkevich Isotherms Studies of Equilibrium Sorption of Zn 2+ Unto Phosphoric Acid Modified Rice Husk.* J. Appl. Chem., 2012. **3**: p. 38-45.

79. Guo, F., et al., *Synthesis of MgO/Fe3O4 nanoparticles embedded activated carbon from biomass for high-efficient adsorption of malachite green.* Materials Chemistry and Physics, 2020. **240**: p. 122240.

80. Piccin, J., G. Dotto, and L. Pinto, *Adsorption isotherms and thermochemical data of FD&C Red n 40 binding by chitosan.* Brazilian Journal of Chemical Engineering, 2011. **28**: p. 295-304.

81. Lim, L.B.L., et al., *Parkia speciosa (Petai) pod as a potential low-cost adsorbent for the removal of toxic crystal violet dye.* Scientia Bruneiana, 2016. **15**.

82. Popoola, L.T., et al., *Brilliant green dye sorption onto snail shell-rice husk: statistical and error function models as parametric isotherm predictors.* Journal of Environmental Science and Technology, 2019. **12**(2): p. 65-80.

83. Wang, J. and X. Guo, *Adsorption kinetic models: Physical meanings, applications, and solving methods.* Journal of Hazardous Materials, 2020. **390**: p. 122156.

84. Qiu, H., et al., *Critical review in adsorption kinetic models.* Journal of Zhejiang University-SCIENCE A, 2009. **10**(5): p. 716-724.

85. Swan, N.B. and M.A.A. Zaini, *Adsorption of malachite green and congo red dyes from water: recent progress and future outlook.* Ecological chemistry and engineering S, 2019. **26**(1): p. 119-132.

86. Dr.T.Santhi, D.T.S., M. S, and T.Smitha, *Kinetics And Isotherm Studies On Cationic Dyes Adsorption Onto Annona Squmosa Seed Activated Carbon.* International Journal of Engineering Science and Technology, 2010. **2**.

87. Fierro, V., et al., *Adsorption of phenol onto activated carbons having different textural and surface properties.* Microporous and mesoporous materials, 2008. **111**(1-3): p. 276-284.

88. Tan, K.L. and B.H. Hameed, *Insight into the adsorption kinetics models for the removal of contaminants from aqueous solutions.* Journal of the Taiwan Institute of Chemical Engineers, 2017. **74**: p. 25-48.

89. Liang, Y. and W. Lu, *Gamma-irradiation synthesis of Fe 3 O 4/rGO nanocomposites as lithium-ion battery anodes.* Journal of Materials Science: Materials in Electronics, 2020. **31**: p. 17075-17083.

90. Fattahi, H., N. Arsalani, and M. Nazarpoor, *Synthesis and characterization of PVP-functionalized superparamagnetic Fe3O4 nanoparticles as an MRI contrast agent.* eXPRESS Polymer Letters, 2010. **4**: p. 329.

91. Kumar, K.V. and K. Porkodi, *Batch adsorber design for different solution volume/adsorbent mass ratios using the experimental equilibrium data with fixed solution volume/adsorbent mass ratio of malachite green onto orange peel.* Dyes and Pigments, 2007. **74**(3): p. 590-594.

92. Das, A., et al., *Behaviour of fixed-bed column for the adsorption of malachite green on surfactant-modified alumina.* Journal of Environmental Science and Health, Part A, 2009. **44**(3): p. 265-272.

93. Ghaedi, M., et al., *Isotherm and kinetics study of malachite green adsorption onto copper nanowires loaded on activated carbon: Artificial neural network modeling and genetic algorithm optimization.* Spectrochimica Acta Part A: Molecular and Biomolecular Spectroscopy, 2015. **142**: p. 135-149.

94. Afkhami, A., R. Moosavi, and T. Madrakian, *Preconcentration and spectrophotometric determination of low concentrations of malachite green and leuco-malachite green in water samples by high performance solid phase extraction using maghemite nanoparticles.* Talanta, 2010. **82**(2): p. 785-789.

95. Eltaweil, A.S., et al., *Mesoporous magnetic biochar composite for enhanced adsorption of malachite green dye: Characterization,*

adsorption kinetics, thermodynamics and isotherms. Advanced Powder Technology, 2020. **31**(3): p. 1253-1263.

96. Pan, X., et al., *Polycarboxylic magnetic polydopamine sub-microspheres for effective adsorption of malachite green.* Colloids and Surfaces A: Physicochemical and Engineering Aspects, 2019. **560**: p. 106-113.

Chapter 5

Spent Zinc-Carbon Battery Derived Magnetically Retrievable Fenton-Like Catalyst for Water Treatment
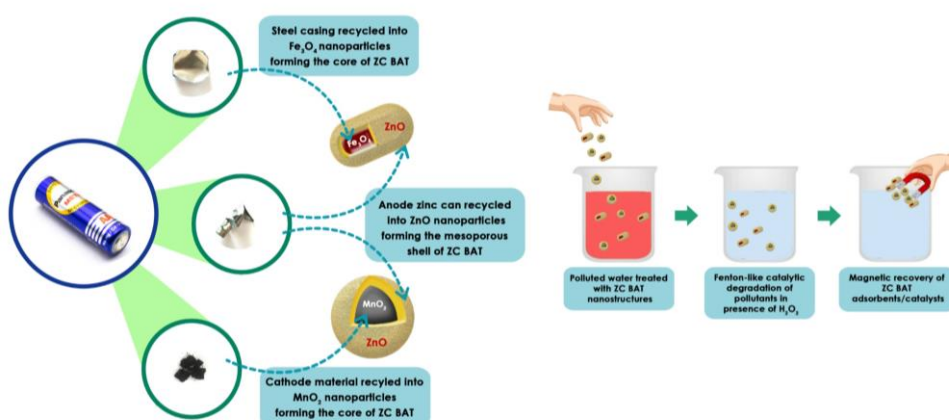
Discarded zinc-carbon batteries were effectively recycled into magnetically retrievable nanostructures that can perform dual roles as adsorbent and Fenton-like catalysts. The developed nanostructures were made exclusively from various components of spent zinc-carbon batteries. The otherwise thrown-away zinc-carbon batteries were thus given a novel role in water treatment. The adsorption and Fenton-like catalytic performance of the developed nanostructures were studied in detail by employing methylene blue (MB), rhodamine B(RB), methyl orange (MO), and Congo red (CR) as the model pollutants.

5.1 Introduction

Dyes are one of the largest classes of organic compounds responsible for water pollution. The dyeing of plastic, textile, and printing industries is mainly responsible for expelling the dyes into water resources. The high chemical stability and non-biodegradability of these molecules make them potentially harmful to humans and aquatic life. Besides the dye molecules; pharmaceutical drugs, pesticides, and other harmful organic compounds are also present at alarming levels in water sources. The dye molecules can be taken as model pollutants representing various classes of water contaminants. Various strategies such as adsorption[1], photocatalysis[2], ultrafiltration[3], and the Advanced Oxidation Process (AOP)[4, 5] are in practice for the removal of these pollutants from water. Among the various AOPs available, one of the promising and widely used methods is Fenton-like catalysis[6]. Fenton-like catalysis is the modified version of the Fenton reaction; which is the aqueous phase oxidation process in the presence of ferrous ions and H_2O_2[7-9]. The process involves the generation of hydroxyl radicals which are capable of degrading organic pollutants in water. However, conventional Fenton reactions have a narrow pH range of activity, an ineffective Fe^{3+}-Fe^{2+} redox cycle, and the production of iron sludge under acidic conditions; which reduces their catalytic activity[7, 10]. Heterogeneous Fenton-like catalysts were introduced to overcome the limitations of Fenton catalysts. Fenton-like catalysis can be regarded as an environmentally friendly heterogeneous process capable of generating a large amount of reactive oxygen species (ROS) which can degrade organic

contaminants into CO_2, H_2O, and various other inorganic species[6]. Heterogeneous Fenton-like catalysis can ensure a wide pH range of activity, minimum input of chemicals, better regeneration of catalysts, and minimal amount of iron sludge generation[8-10]. Besides the most commonly employed Fe^{3+} containing iron-based catalysts, several other transition metals like Ce, Mn, Cu, and Co which are capable of showing multiple oxidation states are also used as heterogeneous Fenton-like catalysts. Fe_3O_4 forms a major component of several Fenton-like catalysts[11, 12]. The presence of transition metals such as Mn[13-17], Ce[18, 19], and Cu[20-22] along with conventional Fenton-like catalysts can further enhance the catalytic activity by taking part in hydroxyl radical generation and by speeding up the Fe^{3+} to Fe^{2+} conversion[10]. The association of transition metals like Mn, Ce, and Cu with Fe_3O_4 can yield highly stable, non-toxic, and economically affordable Fenton-like catalysts[19, 20, 23, 24].

As we look from a circular economy perspective, the development of Fenton-like catalysts from disposed waste materials is worth a try. Zinc-carbon batteries are dry-cell primary batteries (also known as AA batteries) widely used for small-scale power requirements. Spent or discharged zinc-carbon batteries are often thrown into dumping yards or soil without proper recycling or treatment. A zinc-carbon battery consists of a zinc can which acts as the anode, a cathode mixture made of MnO_2 and graphitic/activated carbon, a porous carbon rod serving as the current collector, a paper separator impregnated with electrolyte paste for preventing direct contact between anode and cathode and a steel casing. Here we have

designed a nanostructure, ZC BAT consisting of MnO_2, Fe_3O_4, and ZnO; which are derived from the various components of the spent zinc-carbon battery. The design is such that MnO_2 and Fe_3O_4 nanoparticles are encapsulated by a layer of mesoporous ZnO. Since the prominent factor controlling the rate of heterogeneous Fenton-like catalysis is adsorption, encapsulation within mesoporous ZnO is expected to improve the surface area and porous texture of the catalyst. Besides its Fenton-like catalytic activity, Fe_3O_4 can also facilitate the magnetic retrieval of the catalyst after the reaction. MnO_2 has significant catalytic properties and can reinforce the Fenton-like catalytic efficiency of Fe_3O_4. Thus, a synergic action of MnO_2, Fe_3O_4, and ZnO can be envisaged in the adsorption as well as in the catalytic performance of ZC BAT nanostructures.

The adsorption and Fenton-like catalytic efficiencies of ZC BAT were investigated separately in this work using methylene blue (MB), rhodamine B (RB), methyl orange (MO), and Congo red (CR) as the model pollutants. Here the concept of circular economy is brought into another real-life example by the recycling and transformation of spent zinc-carbon batteries into efficient, affordable, and easy-to-use Fenton-like catalysts capable of water purification.

5.2 Results and discussion

5.2.1 XRD

The phase purity of the compounds was determined by powder X-ray diffraction. **Figure 5.1** represents the XRD patterns of all the components synthesized from disposed zinc-carbon batteries. The XRD pattern of MnO_2 is shown in **Figure 5.1a**, and it matches with

the already-reported Pyrolusite mineral pattern of MnO_2 (JCPDS file No. 00-001-0799)[25].
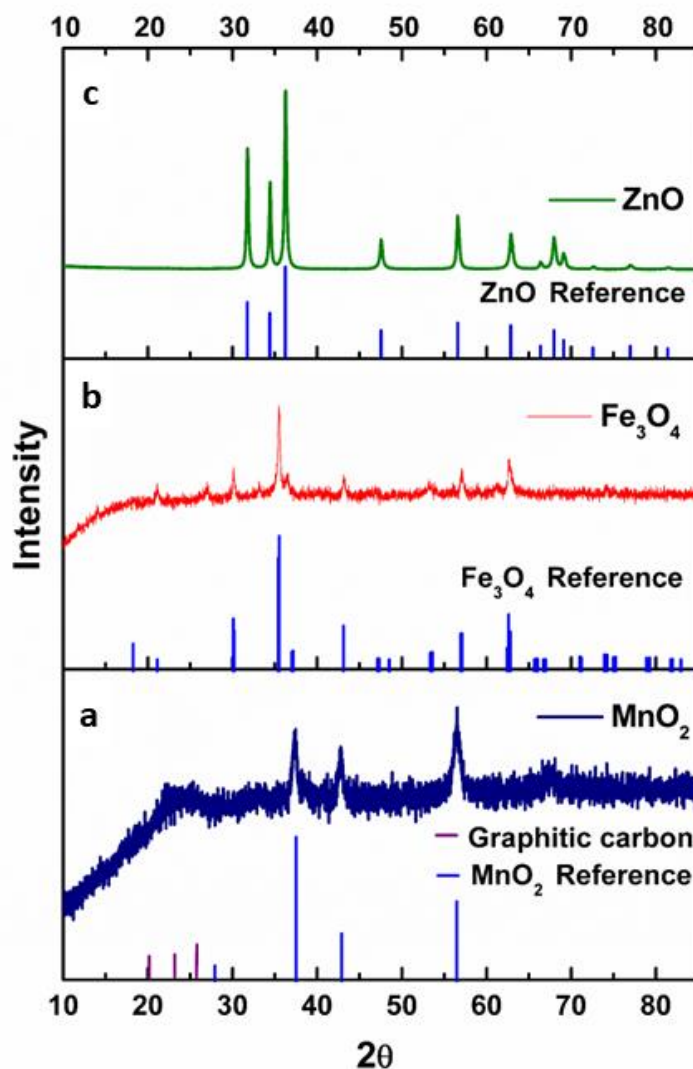
Figure 5.1 - XRD patterns obtained for zinc-carbon battery-derived individual components a) MnO_2 b) Fe_3O_4 and c) ZnO along with their reference patterns.

The compound crystallises in a tetragonal crystal structure belonging to the P42/mnm space group. Since some amount of

activated/graphitic carbon is present along with MnO_2 as the cathode material, the presence of peaks at 23.8° and 26.3° can be attributed to the (002) plane of graphitic carbon (JCPDS file No. 00-041-1487)[26]. Also, a peak corresponding to graphene oxide manifests around 20.1° with a d-spacing of 4.01 Å [26].

Figure 5.1b exhibits the XRD pattern of Fe_3O_4 nanoparticles developed from the steel casing of zinc-carbon batteries. As evident from the **Figure 5.1b**, the XRD pattern matches that of the orthorhombic magnetite crystal structure reported in the literature (JCPDS file No. 01-075-1609)[27-29]. **Figure 5.1c** displays the XRD profile of ZnO nanoparticles derived from the anode zinc can of the zinc-carbon batteries. The obtained ZnO XRD peaks can be assigned to the hexagonal crystal structure of ZnO belonging to the P63mc space group (JCPDS - 00-036-1451)[30, 31]. The individual XRD profiles indicate that each of the zinc-carbon battery-derived components is phase pure. Thus, they can be assembled into a single nanostructure to exploit their individual as well as synergic contributions. The XRD profile obtained for the developed ZC BAT nanostructure comprising MnO_2/Fe_3O_4@ZnO compositions is given in **Figure 5.2**. The XRD pattern obtained for the ZC BAT nanostructures can be indexed to tetragonal MnO_2 (JCPDS file No. 00-001-0799), graphitic carbon (JCPDS file No. 00-041-1487), orthorhombic Fe_3O_4 (JCPDS file No. 01-075-1609) and hexagonal ZnO (JCPDS file No. 00-036-1451) reference patterns. The presence of activated/graphitic carbon in the ZC BAT nanostructures is also evident from the XRD peak around 2θ values of 20.1° , 23.8° , and 26.3° [26]. Thus, it is obvious from the XRD analysis that the ZC BAT

nanostructures contain no additional phases or impurities other than activated/graphitic carbon, MnO_2, Fe_3O_4, and ZnO.
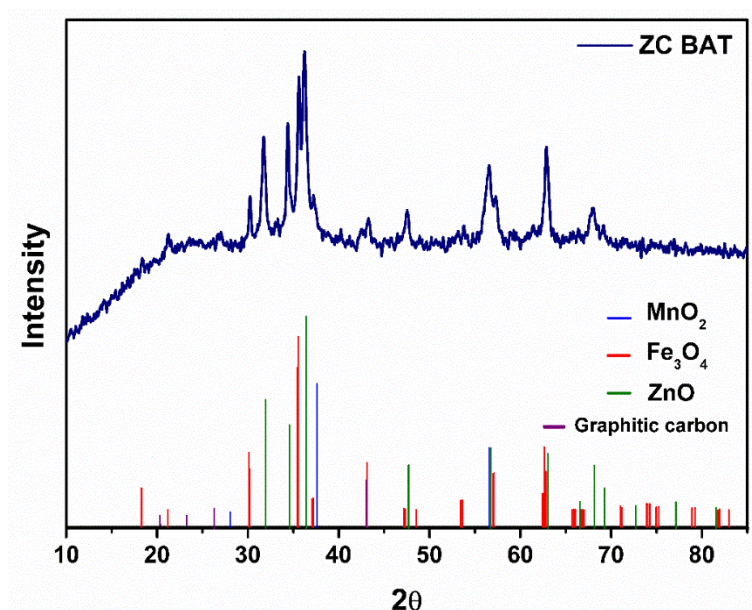
Figure 5.2 - XRD pattern obtained for the developed ZC BAT nanostructure along with the reference peaks for individual components

5.2.2 FE-SEM

The surface morphology of the individual components derived from the disposed zinc-carbon battery and that of the, ZC BAT catalyst was studied using FE-SEM. **Figure 5.3** shows the FE-SEM micrographs of the individual components as well as the developed ZC BAT core-shell nanostructures. **Figure 5.3a** displays the FE-SEM micrographs of MnO_2, it is evident from the FE-SEM image that even though there is a small degree of aggregation, the MnO_2 nanoparticles are distinct from one another and fall within the nanometre regime. **Figure 5.3b** shows the FE-SEM micrographs of Fe_3O_4, which is present in the form of elongated rods having their dimensions within the

nanometre range. Upon examination under FE-SEM, it was observed that ZnO exhibited aggregation of spherical nanoparticles as evident from **Figure 5.3c**.
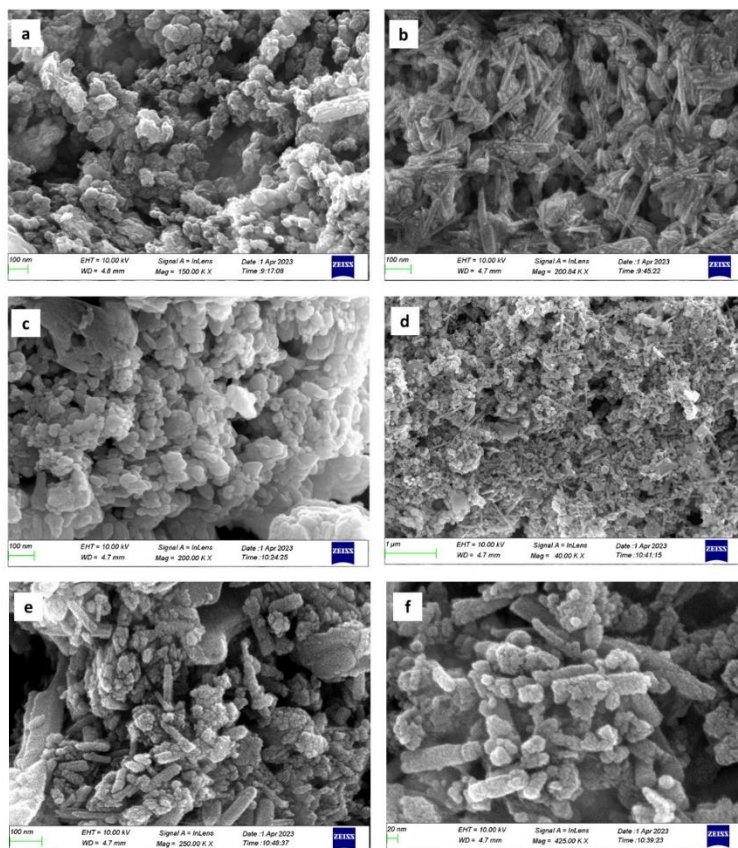
Figure 5.3 - FE-SEM micrographs of the zinc-carbon battery-derived a) MnO_2 b) Fe_3O_4 c) ZnO and d,e,f) the developed ZC BAT nanostructures

Figures 5.3(d-f) represent the FE-SEM images of the developed ZC BAT core-shell-like structures under various magnifications. From the FE-SEM images, the presence of both spherical and rod-shaped morphologies is evident among the ZC BAT nanostructures. Both spherical and rod-shaped nanostructures exhibit rough and porous surfaces which can be attributed to the presence of an outer

encapsulating layer of ZnO around MnO_2 and Fe_3O_4 nanoparticles. The observed surface morphology of ZC BAT nanostructures indicates enhanced surface area and porosity as a result of the synergic effects of all three individual components i.e., MnO_2, Fe_3O_4, and ZnO brought together into a single nanostructure.

5.2.3 HR-TEM

The HR-TEM images obtained for the developed ZC BAT core-shell nanostructures are given in **Figure 5.4**. A uniform distribution of all the components is evident from **Figures 5.4a** and **5.4b.** The nanorod morphologies exhibited by Fe_3O_4 particles are easily visible in **Figure 5.4b**. **Figures 5.4c** and **5.4d** represent the encapsulation of MnO_2 and Fe_3O_4 nanoparticles by a porous layer of ZnO, which was further confirmed by analysing the SAED pattern of one such region. **Figure 5.4e** depicts the HR-TEM image, in which specific regions were labelled and identified with lattice spacings corresponding to graphitic carbon, MnO_2, Fe_3O_4, and ZnO.

In **Figure 5.4e**, the regions were numbered, and an enlarged image of the numbered regions was given alongside. Nine regions were identified and marked with characteristic interplanar spacings. Significant planes corresponding to carbon content from the HR-TEM images are (002) plane of graphitic carbon having a d-spacing of 3.65 A^o and a d-spacing of 4.02 Å corresponding to graphene oxide[26]. In the case of MnO_2, the observed interplanar spacing of 2.4 Å and 2.12 Å correspond to (101) and (111) planes respectively[32, 33]. The (103) and (112) planes corresponding to

Fe_3O_4 are also prominent within the ZC BAT composition with a d-spacing value of 2.52 Å and 2.12 Å respectively[27-29].
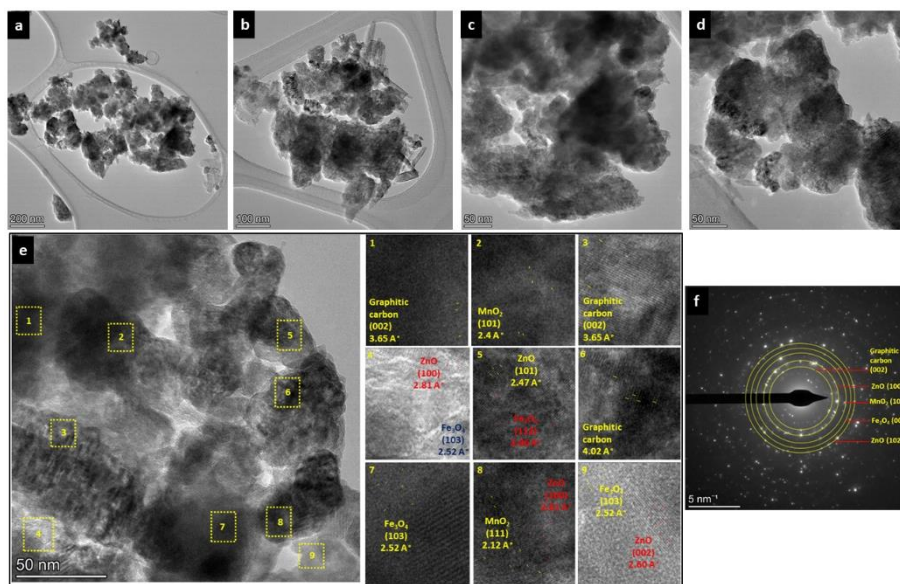
Figure 5.4 – **a,b,c,d)** HR-TEM images obtained for the developed ZC BAT nanostructures **e)** HR-TEM image marked with regions 1-9 and their enlarged images showing the characteristic interplanar spacings of individual components such as graphitic carbon, MnO_2, Fe_3O_4 and ZnO and **f)** SAED pattern obtained for ZC BAT nanostructures where diffraction rings are labelled with characteristic planes of individual components.

The regions marked as 4,5,8 and 9 also display lattice spacings characteristic of (100), (101), and (002) planes of ZnO, which further confirms the formation of an encapsulating layer of ZnO over MnO_2 and Fe_3O_4 nanoparticles[30, 31]. Thus, the HR-TEM images clearly show the formation of core-shell nanostructures in which graphitic carbon, MnO_2, and Fe_3O_4 form the cores and mesoporous ZnO forms the shell. The SAED pattern shown in **Figure 5.4f** can be indexed to

(002) plane of graphitic carbon, (100) and (102) planes of ZnO, (101) plane of MnO_2 and (004) plane of Fe_3O_4.

5.2.4 XPS

X-ray photoelectron spectroscopy (XPS) was used to determine the oxidation states of various elements present in the ZC BAT, as well as to understand the purity of the formed structure. The XPS survey spectrum given in **Figure 5.5** shows no additional peaks corresponding to any other elements other than C, O, Mn, Fe, and Zn.
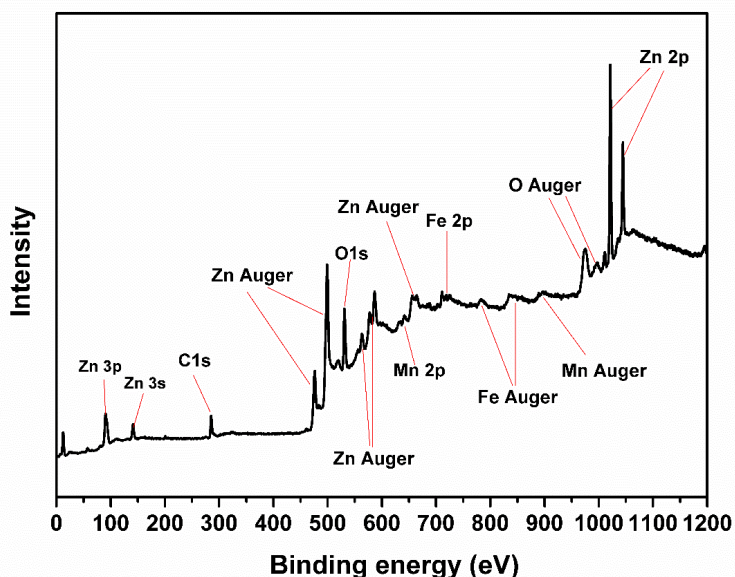
Figure 5.5 - XPS Survey spectrum for ZC BAT nanostructures

Figure 5.6 displays the core level XPS spectra of C 1s, O 1s, Mn 2p, Fe 2p, and Zn 2p energy levels. As evident from **Figure 5.6a**, high-resolution C 1s spectra can be deconvoluted into 5 peaks positioned at binding energy values 284.8, 285.7, 286.7, 288.8, and 290 eV which can be attributed to graphitic carbon, phenolic or alcoholic C-O-, carbonyl, carboxyl/ester and carbonate/π electrons in aromatic

ring respectively[34]. In the case of oxygen, as shown in **Figure 5.6b** the O 1s XPS spectra can be fitted using three peaks situated at 530.2, 531.1, and 532.4 eV representing lattice oxygen, surface hydroxyl, and adsorbed water on surface vacant sites respectively[35]. The deconvoluted core level XPS spectrum of Mn 2p is given in **Figure 5.6c**. The peak corresponding to the $2p_{3/2}$ level of Manganese in Mn^{2+}, $Mn^{3+,}$ and Mn^{4+} states was deconvoluted. Here $2p_{3/2}$ levels of Mn^{2+}, Mn^{3+}, and Mn^{4+} were found to have binding energies at 640, 640.8, and 642.4 eV respectively[36, 37].
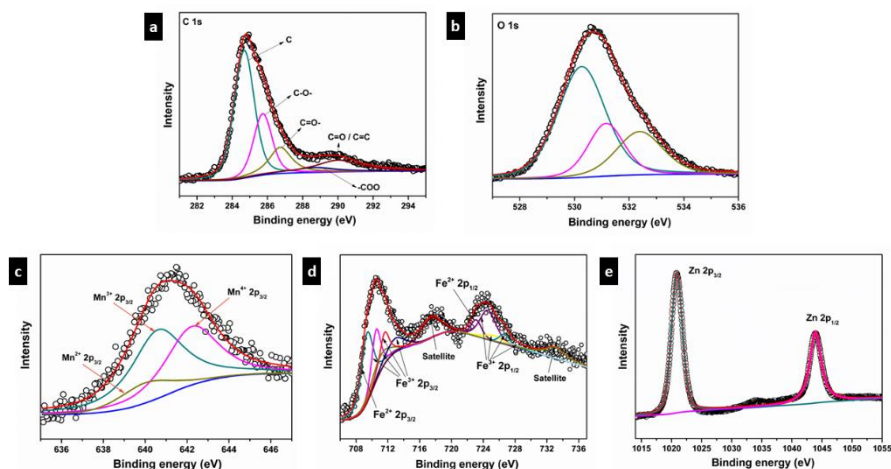
Figure 5.6 – XPS spectra of a) C 1s b) O 1s c) Mn 2p d) Fe 2p and e) Zn 2p of ZC BAT nanostructures

The area under each of these peaks quantitatively represents the amount of respective species, it was observed that among the different oxidation states of Mn, Mn^{2+} was found to be in the least amount. The domination of Mn^{3+} and Mn^{4+} oxidation states over Mn^{2+} can be envisaged to enhance the catalytic efficiency of ZC BAT. In the case of Fe, the high-resolution XPS spectrum consists of Fe

2p$_{3/2}$ and Fe 2p$_{1/2}$ levels of both Fe^{2+} and Fe^{3+} oxidation states. The 2p$_{3/2}$ and 2p$_{1/2}$ peaks for Fe^{2+} were observed at 709.4 and 723 eV[38, 39]. At the same time, due to spin-orbit splitting and electrostatic interactions each of the 2P$_{3/2}$ and 2p$_{1/2}$ states of Fe^{3+} were deconvoluted into four peaks as shown in **Figure 5.6d**[40-42]. In addition, two satellite peaks were also found for Fe^{3+} around 718 and 733 eV. The high-resolution XPS spectrum obtained for Zn 2p is shown in **Figure 5.6e**, which depicts the Zn 2p$_{3/2}$ and Zn 2p$_{1/2}$ energy levels around binding energy values of 1021 and 1044 eV respectively[43].
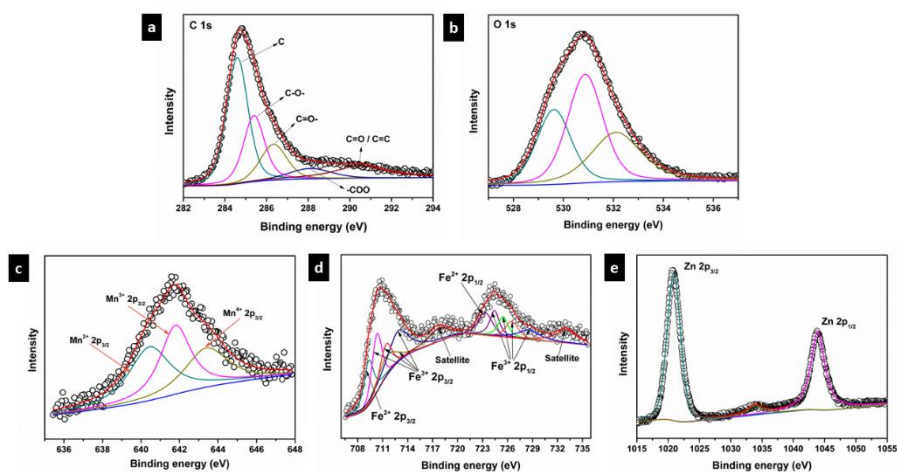
Figure 5.7 - XPS spectra of a) C 1s b) O 1s c) Mn 2p d) Fe 2p and e) Zn 2p of ZC BAT nanostructures after Fenton-like catalysis

Thus, the XPS spectra suggest the formation of ZC BAT nanostructures comprising MnO$_2$, Fe$_3$O$_4$, and ZnO. To verify the stability of the developed ZC BAT nanostructures, the XPS analysis of ZC BAT after Fenton-like catalysis was also carried out. The XPS spectra of ZC BAT analysed after the catalytic process are given in **Figure 5.7**. There are no significant changes in the chemical

oxidation states of Fe, Mn and Zn. But there exists a variation in the ratio of Fe^{2+}: Fe^{3+} and Mn^{2+}: Mn^{3+}: Mn^{4+} species after Fenton-like catalysis which supports the proposed mechanism of Fenton-like catalysis discussed later in this chapter.

5.2.5 BET surface area analysis
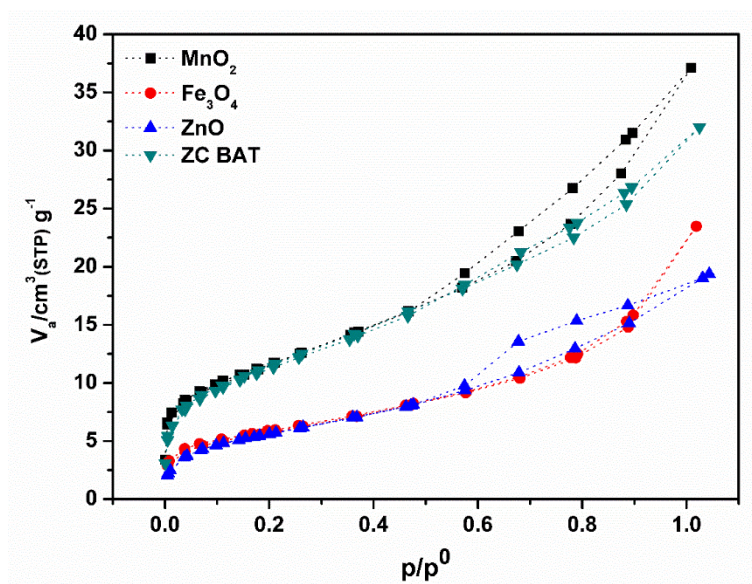
Figure 5.8 –N_2 adsorption isotherms obtained for MnO_2, Fe_3O_4, ZnO and ZC BAT nanostructures

Table -5.1 Surface area parameters obtained for MnO_2, Fe_3O_4, ZnO, and ZC BAT nanostructures from BET measurements.

Sample	BET surface area ($m^2.g^{-1}$)	Total pore volume ($cm^3.g^{-1}$)	Pore diameter (nm)
MnO_2	40.46	0.055	5.48
Fe_3O_4	20.03	0.033	6.66
ZnO	20.39	0.028	5.43
ZC BAT	39.48	0.047	4.76

N_2 adsorption isotherms obtained for MnO_2, Fe_3O_4, ZnO, and ZC BAT core-shell nanostructures are given in **Figure 5.8**. The surface parameters obtained from BET surface area analysis are given in **Table 5.1**. Among the various components recovered from the battery, the highest surface area was obtained for MnO_2, which can be attributed to the presence of activated carbon in the cathodic material of the zinc-carbon battery. Fe_3O_4 and ZnO, when present individually showed only half of the surface area exhibited by MnO_2. It is obvious from the BET analysis that encapsulating both MnO_2 and Fe_3O_4 nanoparticles with ZnO improved the surface area of the developed ZC BAT nanostructures relative to individual ZnO and Fe_3O_4 surface areas. It can be seen that the adsorption isotherms of the individual components as well as the ZC BAT core-shell structures belong to type IV isotherms and exhibited an H3-type hysteresis[44]. Type IV adsorption isotherms are characteristic of mesoporous materials and the pore diameters agree with mesoporous nature[45]. The H3-type hysteresis loop indicates the presence of aggregates having slit-shaped pores[44]. The surface characteristics and porosity of ZC BAT nanostructures can enhance dye adsorption. The adsorbed dye along with H_2O_2 can diffuse through the mesoporous ZnO networks towards MnO_2 and Fe_3O_4 surfaces, which facilitates the catalytic oxidation of dye molecules.

5.2.6 Magnetic studies

Figure 5.9 represents the M-H curve obtained for ZC BAT core-shell nanostructures by Vibrating Sample Magnetometer (VSM) at room temperature. An enlarged view of the hysteresis loop obtained for ZC BAT is given within the inset in **Figure 5.9**. The s-shaped M-H curve

indicates the ferromagnetic nature of ZC BAT core-shell nanostructures. From the M-H curve, the coercivity (Hc) and the remanent magnetization (Mr) were found to be 50.4 O_e and 0.509 emu.g^{-1} respectively. ZC BAT also exhibited a magnetization saturation value of 14.46 emu.g^{-1}.
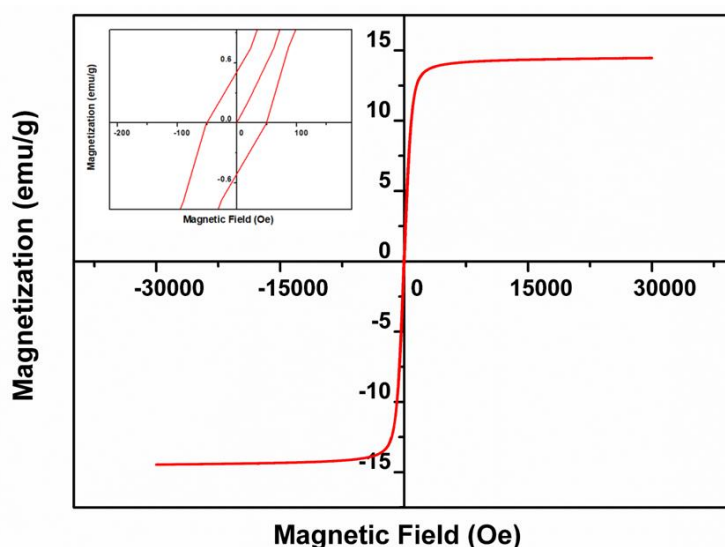
Figure 5.9 - M-H curve obtained for ZC BAT core-shell nanostructures

5.2.7 Adsorption and catalytic optimization studies
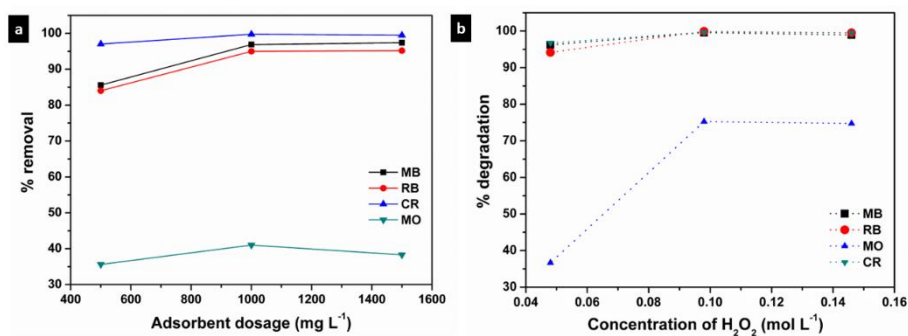
Figure 5.10– a) Variation of adsorption efficiency with ZC BAT dosage b) variation of degradation efficiency with the concentration of H_2O_2.

Adsorption and Fenton-like catalytic studies were carried out to determine the optimum adsorbent dosage and optimum concentration of H_2O_2 for catalytic oxidation.

5.2.7.1 Adsorbent dosage

The effect of adsorbent dosage on the adsorption performance was evaluated by loading 500, 1000, and 1500 mg.L^{-1} of ZC BAT against minimum concentrations of MB (1 ppm), RB (1ppm), MO (5 ppm), and CR (25 ppm). The variation of adsorption efficiency with different adsorbent dosages of ZC BAT is shown in **Figure 5.10a**. The removal percentages of all four dyes under three different ZC BAT dosages are tabulated in **Table 5.2**. The optimum adsorbent dosage was found to be 1000 mg.L^{-1}

Table 5.2 – The effect of ZC BAT dosage and H_2O_2 concentration on the removal efficiency of MB, RB, MO and CR.

Dye	ZC BAT Dosage (mg.L^{-1})			H_2O_2 concentration (moles.L^{-1})		
	500	1000	1500	0.048	0.098	0.146
MB	85.6 %	96.9 %	97.4 %	96.2 %	99.6 %	98.9 %
RB	84.0 %	95.0 %	95.2 %	94.2 %	99.9 %	99.5 %
MO	35.6 %	41.0 %	38.3 %	36.7 %	75.2 %	74.7 %
CR	97.0 %	99.7 %	99.5 %	96.8 %	99.7 %	99.5 %

5.2.7.2 Concentration of H_2O_2

Another crucial factor determining the rate of Fenton-like catalytic degradation of dyes is the concentration of H_2O_2. The catalytic degradation efficiencies exhibited by ZC BAT towards MB, RB, MO

and CR in the presence of three different H_2O_2 concentrations are given in **Figure 5.10 b**. The degradation efficiencies obtained for MB (1 ppm), RB (1 ppm), MO (5 ppm) and CR (25 ppm) in the presence of 0.048, 0.098 and 0.146 moles.L^{-1} H_2O_2 are given in **Table 5.2**. The optimum H_2O_2 concentration was found to be 0.098 moles.L^{-1} as the degradation efficiency reached a limiting value around this concentration.

5.2.8 Estimation of adsorption and catalytic efficiency

The adsorption, as well as Fenton-like catalytic degradation of four model dyes, MB, RB, MO, and CR over ZC BAT core-shell nanostructures, were evaluated separately. **Figure 5.11a** shows the variation of adsorption efficiencies of MB, RB, MO, and CR with time under an optimum catalyst dosage of 1000 mg.L^{-1}.
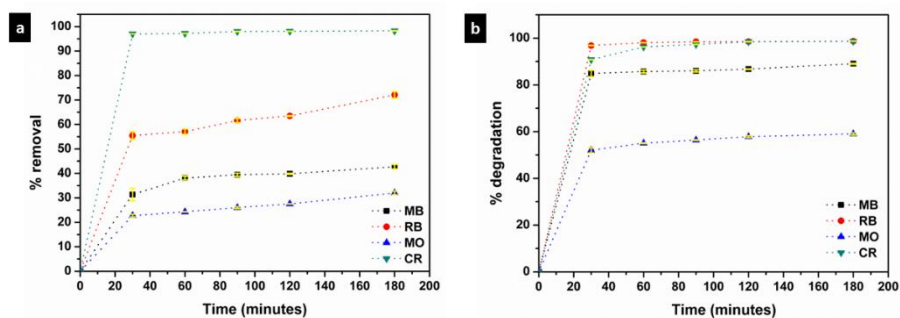
Figure 5.11– Removal of MB, RB, MO, and CR by **a)** adsorption (Reaction conditions: adsorbent dosage -1000 mg.L^{-1}, MB - 3 ppm, RB – 4ppm, MO-15 ppm, and CR-45 ppm) and **b)** Fenton-like catalytic degradation (Reaction conditions: adsorbent dosage -1000 mg.L^{-1}, H_2O_2 -0.098 mol.L^{-1}, MB - 5 ppm, RB – 5ppm, MO-15 ppm, and CR-45 ppm) over ZC BAT nanostructures.

The optimum initial concentrations of MB, RB, MO, and CR were taken as 3, 4, 15, and 45 ppm respectively for the adsorption studies. The removal efficiencies obtained by ZC BAT over a time of 180 minutes towards MB, RB, MO, and CR were found to be 42.7, 72.1, 32.0, and 98.2 % respectively. ZC BAT core-shell compositions exhibited the highest removal efficiency towards CR.
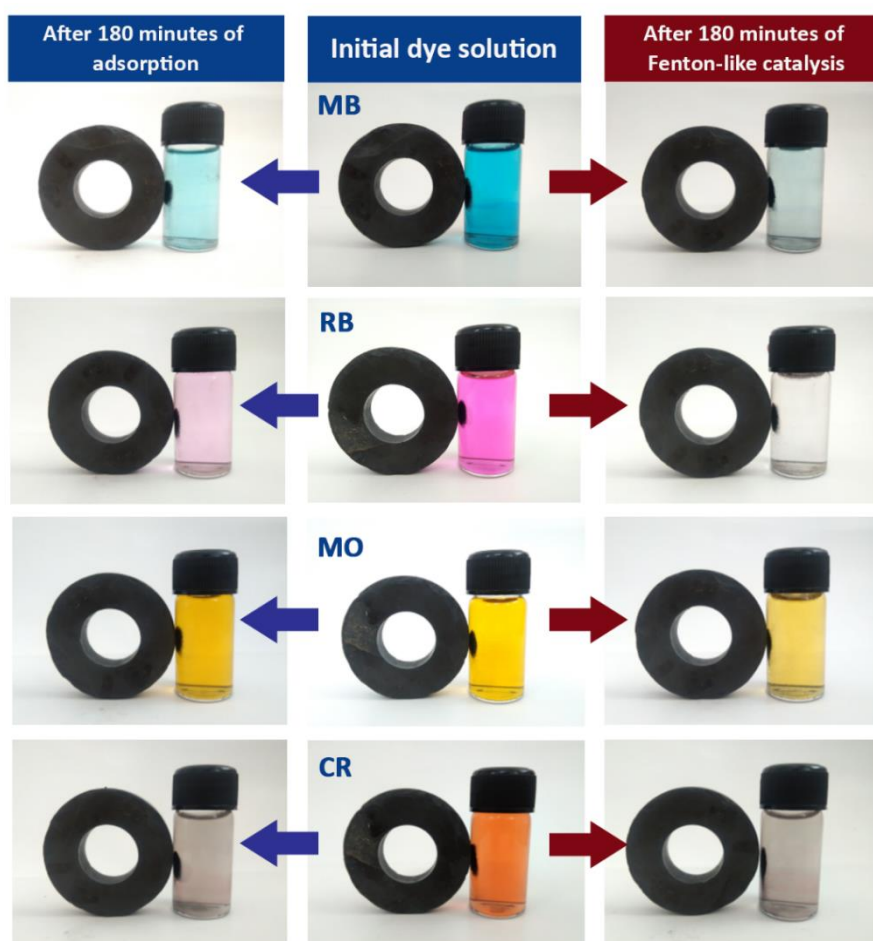
Figure 5.12 – Initial and final stages of adsorption and Fenton-like catalysis of MB, RB, MO, and CR dye solutions by ZC BAT nanostructures.

In the case of MB, RB and MO adsorption alone was not sufficient to achieve the complete removal of the dye molecules. To complement the process of adsorptive removal, Fenton-like catalytic degradation of the dye molecules was introduced. In the presence of H_2O_2, ZC BAT can act as Fenton-like catalysts; and their degradation performance towards MB, RB, MO, and CR is given in **Figure 5.11b**. ZC BAT nanostructures exhibited a degradation percentage of 89.2, 98.7, 59.3, and 98.6 % towards MB, RB, MO, and CR respectively. The optimum concentrations of MB, RB, MO, and CR for catalytic degradation studies were taken as 5, 5, 15, and 45 ppm respectively. The synergic action of adsorption and Fenton-like catalysis yield better removal efficiencies. Except for MO, all the other three dyes showed degradation efficiencies higher than 89 %. The effect of ZC BAT on MB, RB, MO, and CR dye solutions as an adsorbent and as a Fenton-like catalyst is shown in **Figure 5.12**. The practical demonstration of the magnetic recovery of the ZC BAT nanostructures before and after the adsorption/ catalysis is evident in **Figure 5.12**.
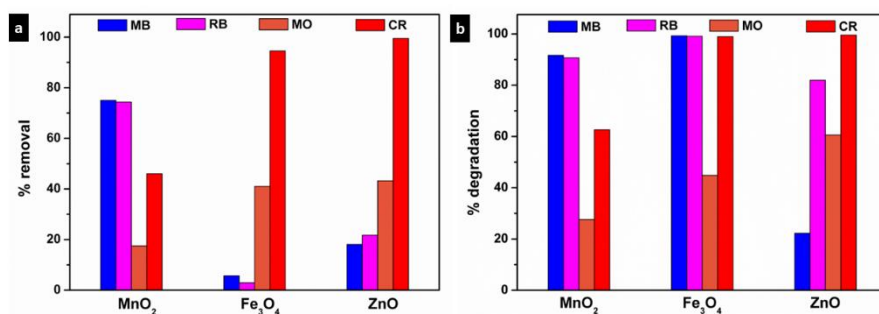
Figure 5.13 – Removal percentages of MB, RB, MO, and CR by **a)** adsorption and **b)** Fenton-like catalytic degradation over zinc-carbon battery-derived MnO_2, Fe_3O_4, and ZnO.

Table 5.3 –Zeta potential, adsorption, and degradation efficiencies of zinc-carbon battery derived MnO_2, Fe_3O_4, ZnO, and ZC BAT nanostructures towards MB, RB, MO, and CR.

	Zeta potential (mV)	Adsorption efficiency (%)				Degradation efficiency by Fenton-like catalysis (%)			
		MB	RB	MO	CR	MB	RB	MO	CR
MnO_2	-13.1	75.0	74.4	17.5	46.0	91.6	90.7	27.6	62.6
Fe_3O_4	8.42	5.6	2.9	41.0	94.6	99.3	99.1	44.9	98.9
ZnO	-13.1	18.1	21.7	43.2	99.6	22.2	82.0	60.5	99.6
ZC BAT	2.09	42.7	72.1	32.0	98.2	89.2	98.7	59.3	98.6

The adsorption as well as Fenton-like catalytic activity of the zinc-carbon battery-derived MnO_2, Fe_3O_4, and ZnO towards MB, RB, MO, and CR were studied individually and the results are represented in **Figures 5.13a** and **5.13b** respectively. The zeta potential, adsorption, and catalytic removal efficiencies obtained for individual components as well as for ZC BAT compositions are given in **Table 5.3**. The variation in adsorption capacity and degradation efficiency can be accounted for in terms of electrostatic and surface Van der Waals interactions. The role of individual components in the process of adsorption and degradation process is explained in detail in the later sections.

5.2.9 Factors affecting adsorption and catalytic degradation

5.2.9.1 Effect of initial concentration

The influence of initial dye concentration on the adsorption and catalytic degradation efficiencies was studied in detail by choosing 5 different concentrations of each of the dyes. The dye adsorption and

dye degradation by Fenton-like catalysis were carried out under varying dye concentrations and the observed trends are represented in **Figure 5.14**.
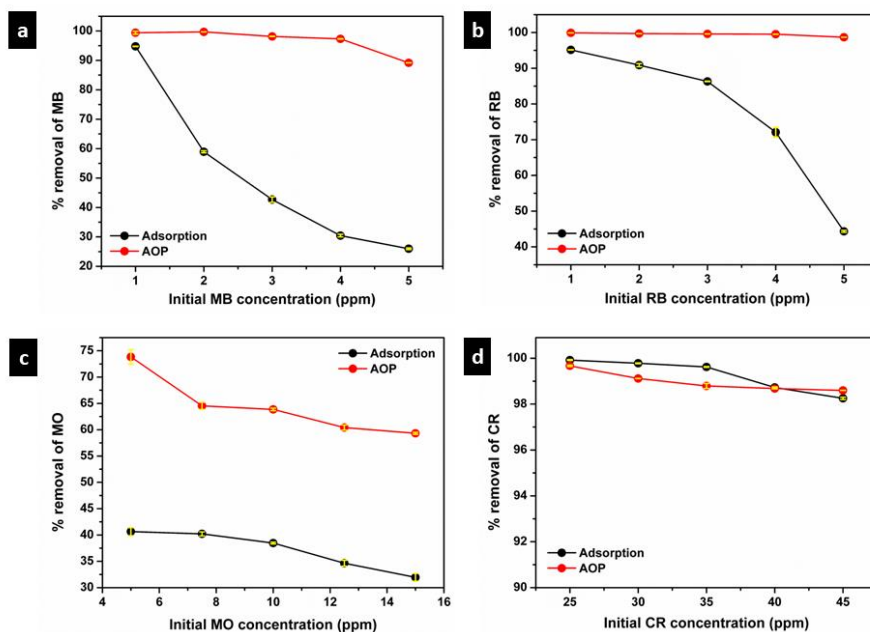
Figure 5.14 – The effect of varying concentrations of **a)** MB **b)** RB **c)** MO and **d)** CR on the adsorption and Fenton-like catalytic activity (AOP) of ZC BAT nanostructures.

In the case of MB and RB, the chosen concentrations are 1, 2, 3, 4 and 5 ppm. For MO, it was 5, 7.5, 10, 12.5, and 15 ppm and for CR, the concentrations under investigation are 25, 30, 35, 40, and 45 ppm. In the case of MB, the adsorption efficiency shown by ZC BAT decreases sharply from 94.8 % to 25.9 % with the increase in dye concentration. At the same time, the catalytic degradation efficiencies of ZC BAT remained above 89 % even at elevated MB concentrations. Similarly, for RB, the adsorption performance by ZC

Table 5.4 - Adsorption/catalytic efficiency of ZC BAT nanostructures with changing concentrations of MB, RB, MO and CR

Dye	Concentration (ppm)	Adsorption efficiency (%)	Fenton-like catalytic degradation efficiency (%)
MB	1	94.8	99.9
	2	58.9	99.7
	3	42.7	98.1
	4	30.4	97.3
	5	25.9	89.2
RB	1	95.2	99.9
	2	90.9	99.7
	3	86.3	99.6
	4	72.1	99.5
	5	44.3	98.7
MO	5	40.6	73.8
	7.5	40.2	64.5
	10	38.5	63.8
	12.5	34.6	60.4
	15	32.0	59.3
CR	25	99.9	99.7
	30	99.8	99.1
	35	99.6	98.8
	40	98.7	98.7
	45	98.2	98.6

BAT exhibited a decrease from 95.2 % to 44.3 % with an increase in concentration. Fenton-like catalytic degradation of RB was found to be highly efficient (>98 %) even at higher concentrations. However, MO adsorption efficiencies of ZC BAT reached only around 40.6 % even at lower concentrations. So ZC BAT is found to be less active

toward MO adsorption. In the case of catalytic degradation of MO using ZC BAT, the degradation efficiencies were found to be falling from 73.8 % to 59.3 % with a rise in MO concentration. In the case of MB, RB, and MO, there existed a large difference between the adsorption and degradation efficiencies. But in the case of CR, both adsorption and catalytic degradation efficiencies, were found to be greater than 98 %. The variation of adsorption and catalytic efficiency of ZC BAT nanostructures with changing concentrations of MB, RB, MO, and CR are given in detail in **Table 5.4**.

5.2.9.2 Effect of pH

The effect of pH on the adsorption performance of ZC BAT was evaluated by carrying out the adsorption experiments against MB, RB, MO, and CR under three different pH conditions (pH 3, pH 7, and
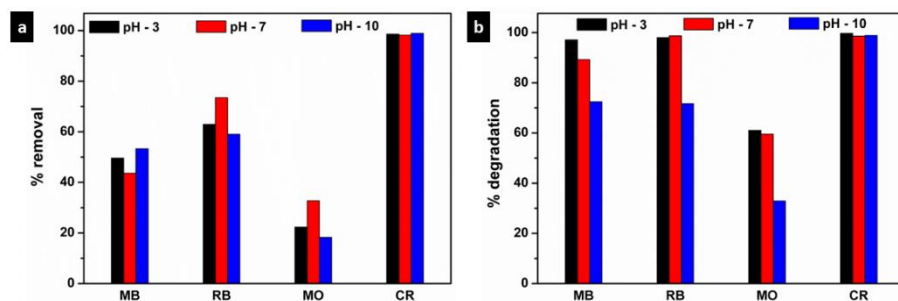
Figure 5.15 – The effect of different pH conditions on the a) adsorption and b) Fenton-like catalytic oxidation of MB, RB, MO, and CR by ZC BAT nanostructures.

pH 10); and the results are represented in **Figure 5.15a**. The variation in adsorption performances under different pH conditions can be accounted for in terms of pH_{pzc} of ZC BAT and pK_a of the dye molecules. The pH_{pzc} of ZC BAT nanostructures was determined

using the pH drift method and it was found to be 7.85 [46]. pH_{pzc} is the pH at which the adsorbent surface exhibits zero charge, at pH values lower than pH_{pzc}, the adsorbent surface will be positively charged and at pH values higher than pH_{pzc} the adsorbent surface will have a negative charge[47]. In the case of MB adsorption, at pH 3, the surface of the adsorbent will be positively charged since the pH_{pzc} of ZC BAT was higher than this value. The pK_a of cationic dye MB is 3.8 hence, at pH 3, MB is found to be in a less ionised form[48]. Thus, there will be less electrostatic repulsion between MB dye molecules and the ZC BAT surface, which favours adsorption. At pH 7, the ZC BAT surface remains positively charged and MB dye molecules are found in a highly ionised cationic form which causes electrostatic repulsion and an eventual decrease in adsorption efficiency. However, around pH 10, the ZC BAT surface becomes negatively charged and attracts cationic MB dye species which enhances the adsorption ability. Hence, the maximum MB adsorption was observed at pH 10. Upon considering the adsorption behaviour of RB on ZC BAT under different pH conditions, the best adsorption performance was obtained around pH 7. RB is a cationic dye having a pK_a value of 4.2 and it transforms into a Zwitter ionic form around pH 5[49, 50]. At pH 3, the ZC BAT surface is positively charged and RB molecules are in the protonated state. Irrespective of the electrostatic repulsion, the protonated RB molecules are capable of forming H bonds with the ZC BAT surface leading to adsorption. At pH 7, RB molecules transform to Zwitter ionic form and exhibit electrostatic attraction with ZC BAT surface which reflects in the form of increased adsorption. At alkaline pH, RB molecules get deprotonated and experience repulsion from

negatively charged ZC BAT surface which manifests as a reduction in adsorption efficiency[50]. Compared to MB, RB, and CR, MO is the species exhibiting minimum adsorption on ZC BAT under all pH conditions. The reason for the reduced adsorption of MO relative to the other 3 dyes will be discussed in the adsorption mechanism section. The variation in adsorption efficiency of ZC BAT towards MO, under different pH conditions can be explained similarly in terms of pH_{pzc} and pK_a. The pK_a value of MO is 3.4 and at pH 3, MO will be in less ionised form and to some extent shows electrostatic attraction with the positively charged ZC BAT surface[51]. At pH 7, MO is highly ionised to anionic species and can enter into electrostatic attraction with the ZC BAT surface which is positively charged. Under alkaline pH, there exists electrostatic repulsion between anionic MO species and negatively charged ZC BAT leading to a reduction in adsorption. The extent of CR adsorption remained around 98 % under all three different pH conditions. Here more than electrostatic interactions, Hydrogen bonding interactions between CR dye molecules and ZC BAT surface functional groups are the controlling factor for adsorption.

Besides the influence of pH on adsorption efficiency, the role of pH on the catalytic oxidation of dye molecules was also investigated. The Fenton-like catalytic oxidation of MB, RB, MO, and CR by ZC BAT nanostructures was carried out under three different pH conditions (pH-3,7, and 10). The percentage removals obtained for each dye under three different pH conditions are shown in **Figure 5.15b**. From the bar diagram, it can be seen that the catalytic degradation efficiencies are relatively higher under acidic conditions. This can be

attributed to the enhanced stability of H_2O_2 under acidic pH[52, 53]. At alkaline pH, the rate of decomposition of H_2O_2 is very high and as a result, the rate of formation of hydroxyl radicals on the ZC BAT surface decreases which in turn affects the degradation efficiency[54]. Also, Fe^{2+} easily gets converted to Fe^{3+} at pH>4 facilitating the Fe^{2+}/Fe^{3+} redox shuttle which is a crucial part of the Fenton-like catalytic oxidation mechanism[52, 55]. Thus, variations are observed in the degradation of MB, RB, and MO over ZC BAT with changes in pH conditions. In contrast, the degradation of CR over ZC BAT was almost constant under all three pH conditions. The enhanced adsorption of CR on ZC BAT through surface interactions can account for the retention of degradation efficiency under varying pH conditions.

5.2.10 Adsorption isotherms

Adsorption isotherms can explain the nature of the adsorption process and can give an idea about the adsorption capacity. Since adsorption forms an integral part of dye removal using ZC BAT, we have obtained and analysed adsorption isotherms of MB, RB, MO, and CR over ZC BAT. The adsorption isotherms were plotted after carrying out the adsorption experiments on ZC BAT using 5 different concentrations of each of MB, RB, MO, and CR. For MB and RB, the chosen concentrations are 1, 2, 3, 4, and 5 ppm. Whereas in the case of MO, the concentrations are 5, 7.5, 10, 12.5, and 15 ppm and for CR, the concentrations under investigation are 25, 30, 35, 40, and 45 ppm. Langmuir and Freundlich adsorption isotherms were plotted from the obtained data.
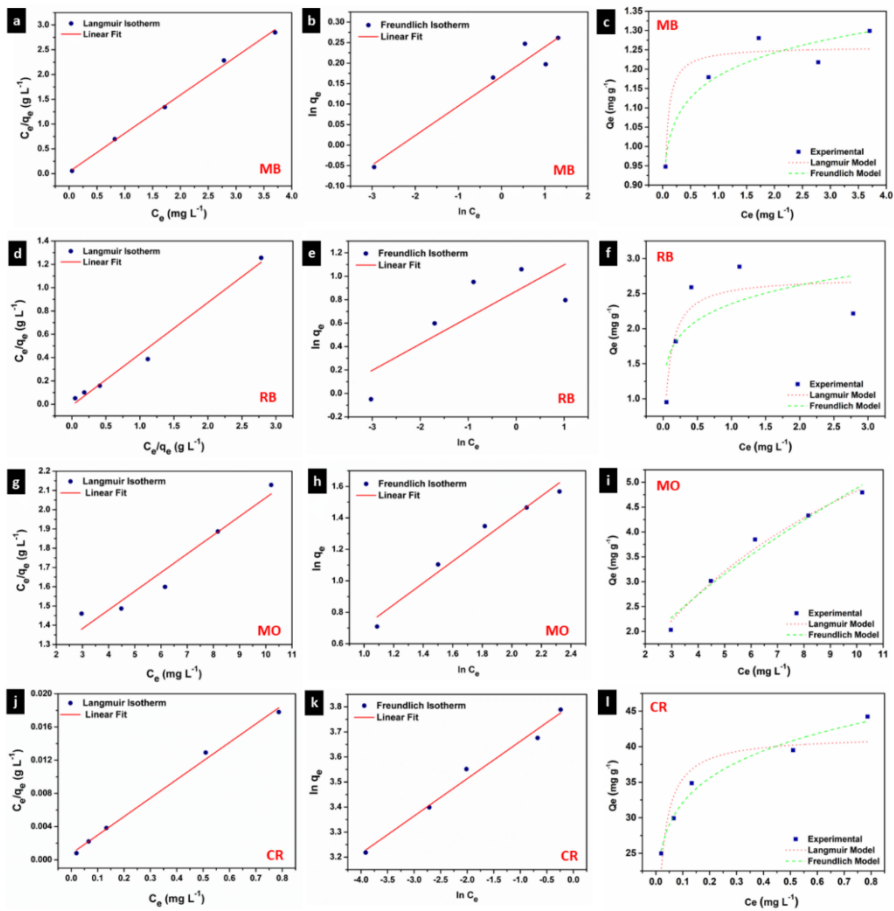
Figure 5.16 – Linearized **a, d, g, j)** Langmuir and **b, e, h, k)** Freundlich adsorption isotherms and **c, f, i, l)** non-linear adsorption isotherms obtained for MB, RB, MO and CR adsorption by ZC BAT nanostructures.

According to the Langmuir adsorption model,

$$q_e = \frac{q_m b C_e}{1 + b C_e} \qquad (5.1)$$

where, q_e, q_m, and b are the quantity of dye adsorbed at equilibrium, the maximum quantity of dye adsorbed per unit weight of the adsorbent, and Langmuir adsorption isotherm constant

respectively[56, 57]. The linearized Langmuir adsorption isotherms obtained for the adsorption of MB, RB, MO, and CR on ZC BAT nanostructures are given **in Figures 5.16a, 5.16d, 5.16g,** and **5.16j** respectively. The non-linear Langmuir and Freundlich adsorption isotherms are given together in **Figures 5.16c, 5.16f, 5.16i and 5.16l.** The parameters obtained after fitting the experimental data with the non-linear Langmuir adsorption model are given in **Table 5.5**.

Table 5.5 – The adsorption isotherm and fitting parameters obtained using Langmuir and Freundlich isotherm models for MB, RB, MO, and CR adsorption over ZC BAT nanostructures.

Dye	Langmuir			Freundlich		
	q_m $(mg \cdot g^{-1})$	b $(L \cdot mg^{-1})$	R^2	n	K_F $(mg^{(1-1/n)}$ $L^{1/n} \cdot g^{-1})$	R^2
MB	1.258	57.52	0.878	14.16	1.183	0.902
RB	2.735	12.94	0.760	6.524	2.355	0.356
MO	9.707	0.099	0.981	1.588	1.144	0.958
CR	41.56	58.28	0.808	6.780	45.12	0.975

Freundlich adsorption model which can account for multilayer adsorption is given by

$$q_e = K_f C_e^{1/n} \qquad (5.2)$$

where K_f and n are Freundlich adsorption isotherm constants[56, 57]. The Freundlich adsorption isotherms obtained for MB, RB, MO, and CR adsorption on ZC BAT are given in **Figures 5.16b, 5.16e,**

5.16h, and **5.16k** respectively. Here non-linear Freundlich adsorption model was used to carry out the fitting analysis of the experimental data and the resultant fitting and adsorption parameters are tabulated in **Table 5.5**.

The linear regression analysis of the experimental data carried out using Langmuir and Freundlich adsorption models revealed that the adsorption of MB, RB, and CR over ZC BAT follows the Langmuir model and MO obeys the Freundlich adsorption model. The agreement of MB, RB, and CR adsorption with the Langmuir model is obvious from the correlation coefficient R^2 values. The R^2 values obtained for MO adsorption indicate Freundlich adsorption. Thus, the agreement with the Langmuir adsorption model points out that the adsorption of MB, RB, and CR over ZC BAT can be regarded as monolayer adsorption over homogeneously distributed adsorbent sites. In the case of MO adsorption, the adsorption process is found to be heterogeneous multilayer adsorption.

5.2.11 Adsorption kinetics

Kinetic studies were performed to evaluate the rate of adsorption of MB, RB, MO, and CR on ZC BAT nanostructures. Pseudo-first-order and pseudo-second-order models were employed to carry out the linear regression analysis of the obtained experimental data. The optimum initial dye concentrations of 3 ppm for MB, 4 ppm for RB, 15 ppm for MO, and 45 ppm for CR were used for the kinetic studies. The optimum concentrations are the concentrations at which the maximum amount of dye adsorption (q_e) is shown by ZC BAT at equilibrium.

The pseudo-first-order model is given by

$$\log(q_e - q_t) = log q_e - \frac{k_1 t}{2.303} \qquad (5.3)$$

where, q_e is the amount of dye adsorbed at equilibrium, q_t is the amount of dye adsorbed over various time intervals, k_1 is the pseudo-first-order rate constant, and t is the time in minutes[58, 59].

According to the pseudo-second-order model,

$$\frac{t}{q_t} = \frac{1}{k_2 q_e^2} + \frac{t}{q_e} \qquad (5.4)$$

where, k_2 is the pseudo-second-order rate constant[58, 59]. The experimental adsorption data were fitted using pseudo-first-order and pseudo-second-order kinetic models and the obtained kinetic as well as fitting parameters are given in **Table 5.6**.

Table 5.6 - Pseudo-first-order and pseudo-second-order kinetic model parameters and fitting data.

Dye	Pseudo first-order model			Pseudo second order model			q_e experimental (mg.g^{-1})
	K_1 (min^{-1})	q_e (mg. g^{-1})	R^2	K_2 (g.mg^{-1} min^{-1})	q_e (mg. g^{-1})	R^2	
MB	0.020	0.849	0.807	0.054	1.36	0.977	1.30
RB	0.015	1.848	0.707	0.017	3.13	0.976	2.22
MO	0.013	3.368	0.763	0.008	5.25	0.999	4.79
CR	0.052	12.03	0.790	0.036	44.4	0.998	44.2

Figure 5.17 shows the fitted curves for the experimental data using pseudo-first and pseudo-second-order models. The correlation coefficient R^2 values indicate that the adsorption of all four dyes, i.e.

MB, RB, MO, and CR on ZC BAT follows pseudo-second-order kinetics.
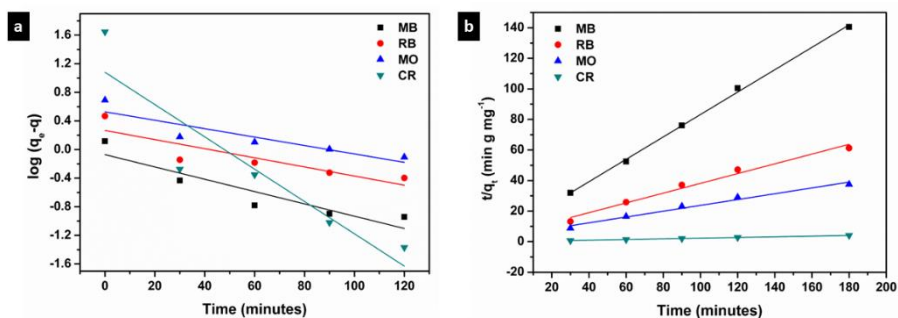
Figure 5.17 – a) Pseudo-first-order and b) pseudo-second-order kinetic plots for MB, RB, MO, and CR adsorption on ZC BAT nanostructures.

Also, the calculated and experimentally obtained q_e values are in good agreement in the case of the pseudo-second-order model. The pseudo-second-order kinetics reflects that the nature of adsorption is chemisorption and the adsorption capacity depends on the formation of chemical interactions between adsorbate and adsorbent surface functionalities[58, 59].

The effect of dye molecule diffusion on the adsorption process was evaluated with the help of liquid diffusion and intraparticle diffusion kinetic models. According to the liquid diffusion model,

$$\ln(1 - F) = -k_{fd}t \qquad (5.5)$$

where F is the fractional attainment of equilibrium ($F = \frac{q_t}{q_e}$) and k_{fd} is the film diffusion rate constant (min^{-1}). The experimental adsorption data was fitted with the liquid diffusion model as given in **Figure 5.18a** and the fitted data is given in **Table 5.7**.
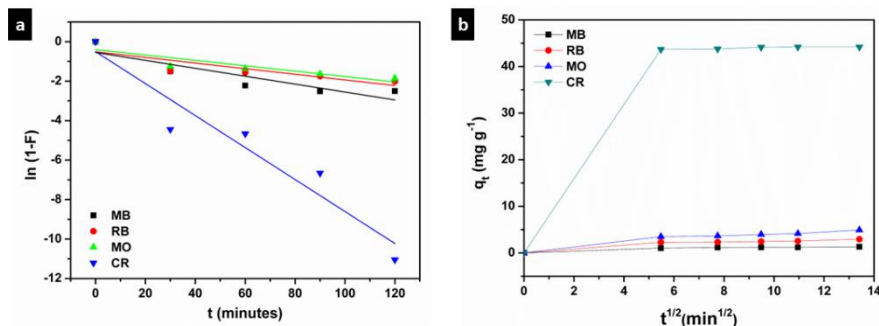
Figure 5.18 – a) Liquid diffusion and b) intraparticle diffusion model plots for MB, RB, MO, and CR adsorption on ZC BAT nanostructures.

If the adsorption process is fully controlled by liquid film diffusion, the plot of ln(1-F) against contact time t will be a straight line passing through the origin. The fitted parameters indicate that liquid film diffusion is not the sole determining factor for the adsorption of dye molecules over ZC BAT.

Besides the liquid diffusion model, the intraparticle diffusion kinetic model was also evaluated. According to the intraparticle diffusion model,

$$q_t = k_{id}t^{1/2} + c \qquad (5.6)$$

where k_{id} is the intraparticle diffusion rate constant (mg.g^{-1} min$^{-1/2}$), t is time and c (mg.g^{-1}) is the intercept which gives a measure of boundary layer thickness. The Weber– Morris intraparticle diffusion plot is shown in **Figure 5.18b** and the fitting parameters are given in **Table 5.7**. The existence of multilinearity in the intraparticle diffusion plot points out the presence of more than one adsorption rate- determining factor. So, the adsorption process can be regarded as a combined effect of electrostatic interactions, Van der Waals

interactions, liquid film diffusion and intraparticle diffusion over the developed ZC BAT nanostructures.

Table 5.7 - Liquid diffusion and intraparticle diffusion model parameters and fitting data.

Liquid diffusion model		
	K	**R^2**
MB	0.020	0.739
RB	0.014	0.645
MO	0.013	0.741
CR	0.081	0.896
Intraparticle diffusion model		
	K_{id1}	**C_1**	**R^2**
MB	0.093	0.240	0.779
RB	0.205	0.482	0.801
MO	0.344	0.659	0.859
CR	3.147	11.97	0.598

5.2.12 Kinetics of H_2O_2 decomposition

The decomposition of H_2O_2 into hydroxyl radicals is the crucial step involved in Fenton/Fenton-like oxidation reactions. Thus, understanding the kinetics of H_2O_2 decomposition by the Fenton-like catalysts is also important. Here, kinetic studies were carried out for the decomposition of H_2O_2 in the presence of individual zinc-carbon battery-derived components i.e., MnO_2, Fe_3O_4, and ZnO as well as using ZC BAT nanostructures.
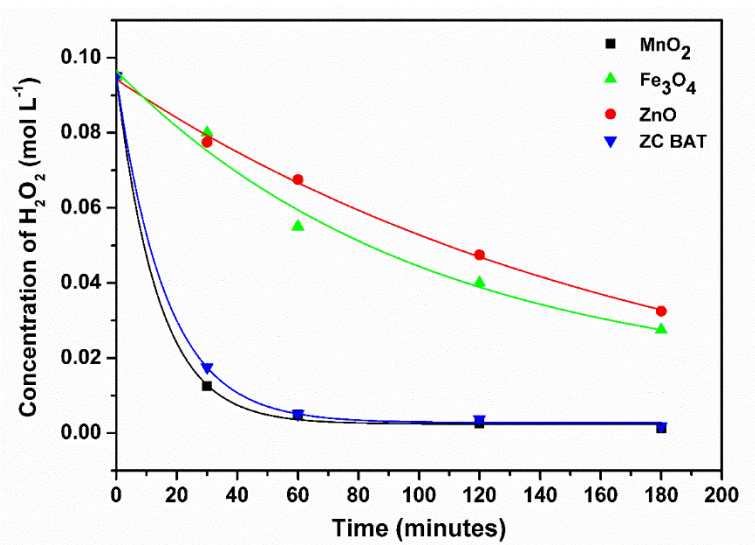
Figure 5.19 – First-order kinetic plots for the decomposition of H_2O_2 by MnO_2, Fe_3O_4, ZnO, and ZC BAT.

Table 5.8 – Rate constant and correlation coefficient values obtained upon fitting H_2O_2 decomposition reaction by MnO_2, Fe_3O_4, ZnO, and ZC BAT with First order kinetic model.

Sample	k_1	R^2
MnO_2	0.073	0.999
Fe_3O_4	0.010	0.970
ZnO	0.006	0.995
ZC BAT	0.061	0.999

The decomposition of H_2O_2 over time was evaluated by titrating a known volume of the reaction mixture against standardised $KMnO_4$. The decomposition of H_2O_2 follows first-order kinetics and the kinetic plot representing the decomposition of H_2O_2 with time is given in **Figure 5.19**[54]. The experimental data were fitted using the first-order kinetic model and the obtained correlation coefficient

R^2 values and first-order rate constants k_1 are given in **Table 5.8**. The highest decomposition rate of H_2O_2 is shown by MnO_2. Even though Fe_3O_4 and ZnO exhibited comparatively smaller rates of decomposition of H_2O_2, the combination of MnO_2, Fe_3O_4 and ZnO into core-shell nanostructures achieved a good catalytic decomposition rate.

5.2.13 Kinetics of Fenton like oxidation
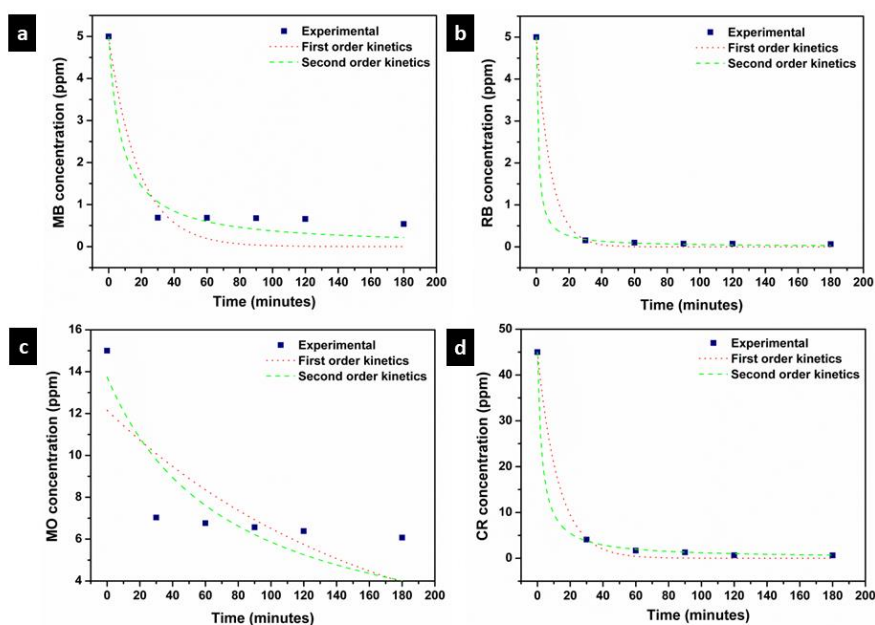
Figure 5.20 – a) First-order and b) second-order kinetic plots for the catalytic oxidation of a) MB b) RB c) MO and d) CR on ZC BAT nanostructures.

Fenton-like oxidation reactions usually follow either first-order or second-order kinetics. According to first-order kinetics,

$$C = C_o e^{(-k_1 t)} \qquad (5.7)$$

where, C_o is the initial dye concentration and k_1 is the first-order rate constant[52, 60].

The second-order rate expression is given by

$$C = \frac{C_o}{1+k_2 C_0 t} \qquad (5.8)$$

where, k_2 is the second-order rate constant[52, 60].

Fitting the experimentally obtained change in concentration of dyes over time, with first-order and second-order kinetic models yielded the first-order and second-order kinetic plots. The first and second-order kinetic plots obtained for the Fenton-like catalytic oxidation of MB, RB, MO, and CR are shown in **Figure 5.20**. The kinetic parameters and correlation coefficient R^2 values obtained using both first and second-order kinetic models are tabulated in **Table 5.9**.

Table 5.9 - First-order and second-order kinetic parameters and fitting data for the catalytic oxidation of a) MB b) RB c) MO and d) CR on ZC BAT nanostructures.

Dye	First order kinetics		Second order kinetics	
	R^2	k_1	R^2	k_2
MB	0.886	0.054	0.965	0.025
RB	0.998	0.115	0.999	0.182
MO	0.478	0.006	0.676	0.001
CR	0.997	0.078	0.999	0.008

Even though no clear distinction between the first and second kinetic models can be deduced, the correlation coefficient R^2 values suggest that catalytic oxidation of MB, RB, and CR are in best

agreement with the second-order kinetic model and the oxidation of MO follows first-order kinetics.

5.2.14 Mechanism of adsorption and Fenton-like oxidation

The mechanism behind the adsorption of MB, RB, MO, and CR dye species on ZC BAT nanostructures was evaluated carefully. Surface area, porosity, electrostatic interactions, and Van der Waals forces between adsorbent and adsorbate are the prime factors contributing to adsorption. MnO_2 derived from the zinc-carbon battery cathode material possesses good surface area due to the presence of activated carbon/graphitic carbon along with it. Even though Fe_3O_4 and ZnO possessed lower surface areas, their association with cathode material-derived MnO_2 improved the surface area as well as the porosity of the resultant ZC BAT core-shell nanostructures, as evident from the BET measurements. The improved surface area and porous networks enhanced the rate of adsorption of dye molecules. ZC BAT being mesoporous can also adsorb dye molecules into the mesopores. The dye intake into the pores depends on steric factors such as molecular size. The molecular sizes of MB, RB, MO, and CR are 1.44, 1.8, 1.2, and 2.3 nm respectively[61-63]. The smaller molecular size of MO relative to the pore diameter of ZC BAT (4.76 nm) allows the free movement of MO molecules through the pores without entrapment. Taking into consideration the role of electrostatic interactions, it can be seen that individually MnO_2 and ZnO have negatively charged surfaces (-13.1 mV for both) and the Fe_3O_4 surface is found to be positively charged (8.42 mV). At the same time, the ZC BAT surface managed to maintain a positive charge of 2.09 mV on its surface irrespective of the larger negative

zeta potentials of its constituents MnO_2 and ZnO. ZC BAT core-shell structures exhibited moderate adsorption performance towards cationic MB and RB, reduced adsorption performance towards MO, and a very good adsorption efficiency towards CR. Based on the pH_{pzc} of 7.85 for ZC BAT, it is evident that around the neutral pH of all the dye solutions, ZC BAT will be positively charged. Electrostatic repulsion between cationic MB and the positively charged ZC BAT surface will result in a reduction in the adsorption of MB on ZC BAT. In the case of RB, its existence in the Zwitter ionic form around neutral pH compensated electrostatic repulsions and yielded moderate adsorption[64]. CR showed enhanced adsorption on ZC BAT due to electrostatic as well as Van der Waals interactions. At the same time, despite having an electrostatic attraction between anionic MO and positively charged ZC BAT, its adsorption efficiency remained very low. All these observations point out that electrostatic interactions are not the sole determining factor of adsorption efficiency. Another crucial factor for adsorption efficiency is π-π electron donor-acceptor interactions between dye molecules and adsorbent[65]. While evaluating the adsorption capacity of individual components, the best adsorption performance was exhibited by MnO_2. Besides MnO_2 nanoparticles, the graphitic carbon/activated carbon content present in the zinc-carbon battery cathode material plays a crucial role in adsorption. Apart from high surface area and porous nature, the ability of graphitic carbon/activated carbon to form π-π conjugation with the aromatic rings of dye molecules also contributes to enhanced adsorption[66-68]. The π-π electron donor-acceptor interactions are evident from

the band around ~1530 cm^{-1} in the FT-IR spectra measured before and after dye adsorption on ZC BAT as shown by **Figure 5.21**.
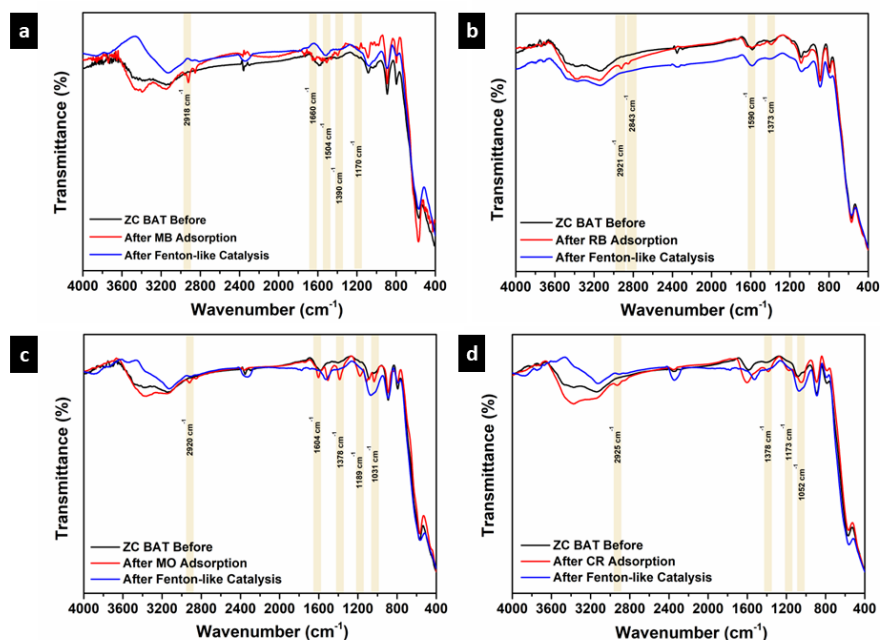
Figure 5.21 – FT-IR spectra obtained for ZC BAT nanostructures before adsorption, after adsorption, and after Fenton-like catalytic oxidation of a) MB b) RB c) MO, and d) CR dyes.

A slight shift as well as a reduction in intensity of the FT-IR band were observed after dye adsorption[69]. The reason for the reduced adsorption of MO can be deduced based on π-π donor-acceptor interactions. The functional groups such as -COOH, -CHO, etc. present on activated carbon act as π acceptors and thereby improve the adsorption of dye molecules such as MB, RB, and CR which have π electron donor character [65, 70]. Thus MB, RB, and CR can form π-π electron donor-acceptor interactions with conjugated rings of activated carbon or with its functional groups. Unlike MB, RB and CR, MO has got π electron acceptor character due to the presence of

electron-withdrawing SO_3^- group on the aromatic ring[70]. So, MO cannot form π-π electron donor-acceptor interactions with activated carbon which in turn affects the adsorption ability. Other important factors contributing to adsorption are Van der Waals interactions and hydrogen bonding interactions.

Except for MO, all the other three dyes have electron-rich aromatic rings having π electron donor character and can hence form electrostatic hydrogen bonding interactions with ZC BAT surface functional groups such as -COOH, -OH, etc. Also, the same π electron clouds of MB, RB, and CR can form n-π electron interactions with the lone pairs of electrons present on the oxygen atom of surface hydroxyl and carboxyl groups[71]. Dipole-dipole H-bonding interactions can also exist between the electronegative atoms such as N, S, O etc. in the dye molecules and H present in surface functional groups[71]. The H-bonding interactions are manifested by the shift and variation in -OH band intensities around ~3400 cm^{-1} in the FT-IR spectra given in **Figure 5.21**. The presence of the -COOH group in RB and the $-NH_2$ group in CR, further enhances the extent of H-bond formations with surface hydroxyls, and carboxyls as well as with absorbed water present on the surface of ZC BAT core-shell structures. Thus, the variation in adsorption efficiencies of ZC BAT towards MB, RB, MO and CR can be addressed in terms of surface characteristics and various interactions such as electrostatic, π-π electron conjugation, Van der Waals interactions and H-bonding.

The FT-IR spectra of ZC BAT nanostructures before and after the adsorption and after the Fenton-like catalysis of MB, RB, MO, and CR are given in **Figure 5.21. Figure 5.21a** shows the variation of FT-IR

spectra of ZC BAT before and after adsorption and Fenton-like catalysis on MB. Besides the characteristic vibrational bands of ZC BAT, the FT-IR spectra of ZC BAT after MB adsorption indicate bands corresponding to MB dye molecules. The bands that are exclusively present after MB adsorption are 2918 cm^{-1} corresponding to stretching vibrations of -CH$_3$ methyl groups, 1660 cm^{-1} corresponding to -C=N stretching vibrations in the ring, 1504 cm^{-1} band for aromatic -C=C stretching modes, 1390 cm^{-1} representing the symmetrical and asymmetrical bending modes of -CH$_3$ groups, and 1170 cm^{-1} corresponding to C=C skeleton of the aromatic ring[49, 72]. None of these bands are seen in the FT-IR spectra taken after Fenton-like catalysis which points out the complete degradation of MB dye molecules.

Figure 5.21b depicts the FT-IR spectra obtained for the adsorption and Fenton-like degradation of RB. The FT-IR spectra after RB adsorption exclusively show vibrational bands corresponding to methyl -CH bond stretching (2921, 2843 cm^{-1}), aromatic -C=N stretching (1590 cm^{-1}) and CH$_3$ stretching vibrations (1373 cm^{-1}). The absence of these bands after Fenton-like catalysis proves the complete degradation of RB molecules[49, 73]. In **Figure 5.21c**, FT-IR spectra of ZC BAT nanostructures after adsorption of MO show characteristic vibrational bands of MO at 2920, 1604, 1378 along with 1189 and 1031 cm^{-1} which corresponds to -CH$_3$ stretching, -N=N stretching, -C-N stretching and -C-H stretching vibrations of benzene ring respectively[74]. Upon Fenton-like catalysis, these characteristic peaks of MO vanished and the FT-IR spectra before and after Fenton-like catalysis look almost similar except for a shift

in the -OH stretching region. In the case of CR dye molecules as shown in **Figure 5.21d**, after adsorption the FT-IR spectra exhibited vibrational bands at 2925, 1378, 1173, and 1052 cm^{-1} representing -CH stretching, -CH bending, C-O-C asymmetrical stretching and C-O stretching respectively[75]. Here also the FT-IR spectra of ZC BAT looks clean without any traits of CR molecules after Fenton-like catalytic oxidation.

The possible mechanism for the degradation of dye molecules by ZC BAT in the presence of H_2O_2 can be explained in terms of the Fenton and Fenton-like catalytic oxidation process.
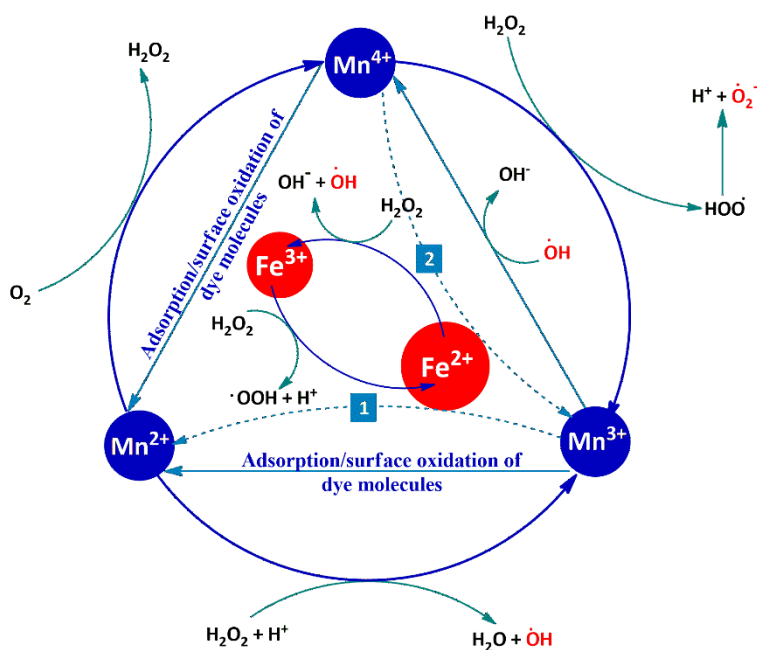
Scheme 5.1 – Mechanism of Fenton-like catalytic oxidation by ZC BAT nanostructures

The reaction of Fe^{2+} ions with H_2O_2 to yield hydroxyl radicals capable of oxidising organic contaminants forms the basis of Fenton reactions[7, 10]. The reaction of H_2O_2 causes the oxidation of Fe^{2+}

into Fe^{3+} ions. The Fe^{3+} ions can be reduced back to Fe^{2+} by H_2O_2 itself[7, 10]. The main limitation of Fenton reactions is the slower rate of reduction of Fe^{3+} back to Fe^{2+} compared to the rate of oxidation of Fe^{2+} into Fe^{3+}[76]. To overcome the deficient Fe^{3+}/Fe^{2+} reduction cycle in Fenton reactions, heterogeneous Fenton-like catalytic reactions were introduced[10, 77, 78]. Transition metals capable of showing variable oxidation states such as Mn, Cu, and Fe are commonly employed in Fenton-like catalysis[10, 78, 79]. Here the developed ZC BAT nanostructures can act as heterogeneous Fenton-like catalysts. Mn^{4+}-Mn^{3+} and Fe^{3+}-Fe^{2+} reduction cycles are mainly responsible for the catalytic activity. ZC BAT core-shell nanostructures consist of an outer shell of ZnO enveloping Fe_3O_4/MnO_2 cores. The major steps involved in the heterogeneous Fenton-like catalytic oxidations are the adsorption of organic moieties over the catalyst surface, in-situ generation of Reactive Oxygen Species (ROS) by the catalyst from H_2O_2 followed by oxidation of organic molecules, and the final step involves the desorption of oxidation products from the catalyst surface[10]. ZC BAT core-shell nanostructures are designed to carry out these steps in the best possible way. The activated carbon-containing MnO_2 core as well as the highly mesoporous ZnO surface layer enhances the extent of adsorption of dye molecules onto the ZC BAT surface. The porous nature of the ZnO shell enables the diffusion of dye molecules as well as H_2O_2 into the MnO_2 and Fe_3O_4 cores of the ZC BAT structure.

Now the crucial step involves the generation of hydroxyl and superoxide radicals by the decomposition of H_2O_2 by ZC BAT. Fe^{3+}-

Fe^{2+} and Mn^{4+}-Mn^{3+} are the main reduction cycles responsible for H_2O_2 decomposition as well as ROS generation. The catalytic mechanism can be accounted for in terms of the predominant oxidation states of Mn and Fe. The mechanism of catalytic oxidation in the presence of Fe^{3+}-Fe^{2+} and Mn^{4+}-Mn^{3+} redox cycles is illustrated in **Scheme 5.1**. The various reactions involved are as follows[10, 52, 54, 80-82].

$$Fe^{2+} + H_2O_2 \longrightarrow Fe^{3+} + \dot{H}O + OH^- \qquad (1)$$

$$Fe^{3+} + H_2O_2 \longrightarrow Fe^{2+} + H_2O + H^+ \qquad (2)$$

$$Mn^{4+} + H_2O_2 \longrightarrow H^+ + HO\dot{O} + Mn^{3+} \qquad (3)$$

$$HO\dot{O} + H_2O_2 \longrightarrow H\dot{O} + H_2O + O_2 \qquad (4)$$

$$HO\dot{O} \longrightarrow H^+ + O_2^- \qquad (5)$$

$$Mn^{2+} + H_2O_2 + H^+ \longrightarrow Mn^{3+} + HO\dot{} + H_2O \qquad (6)$$

$$Mn^{3+} + HO\dot{} \longrightarrow Mn^{4+} + OH^- \qquad (7)$$

$$Mn^{2+} + 2OH^- + 1/2 \, O_2 \longrightarrow Mn^{4+} + H_2O \qquad (8)$$
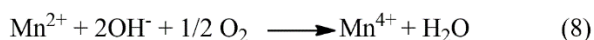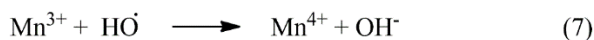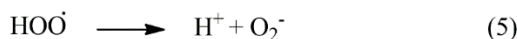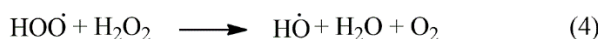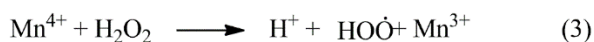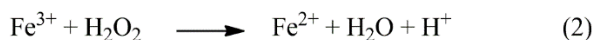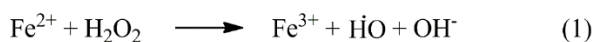
The various factors determining the adsorption process were discussed earlier. In the case of the Fe^{3+}-Fe^{2+} redox cycle, the interconversion between Fe^{3+} and Fe^{2+} occurs in the presence of H_2O_2 and the redox reactions are as given in equations 1 and 2. The standard reduction potentials of Mn^{3+}/ Mn^{2+} and Fe^{3+}/Fe^{2+} are 1.51 V and 0.77 V respectively[53, 83]. Thus, the reduction of Mn^{3+} to Mn^{2+} can also occur in the presence of Fe^{2+} as shown in pathway 1 in the scheme. Again, the standard reduction potential of Mn^{4+}/Mn^{3+} is found to be 0.95 V and Mn^{4+} can undergo a thermodynamically favourable reduction to Mn^{3+} in the presence of Fe^{2+} as given by pathway 2[84]. The dye molecules diffused into porous networks of the ZC BAT can undergo surface oxidation with Mn^{4+} of MnO_2 to yield

Mn^{3+} and Mn^{2+} [52, 80]. Similarly, Mn^{3+} present in ZC BAT undergoes reduction to yield Mn^{2+} upon surface oxidation of dye molecules. Also, the reduction of Mn^{4+} to Mn^{3+} can occur in the presence of H_2O_2 to yield hydroperoxyl radical first, which decomposes to superoxide radicals (eqn. 3 and eqn. 5)[81]. The oxidation of Mn^{2+} to Mn^{3+} occurs in the presence of H_2O_2 as shown in equation 6[10]. Hydroxyl radicals initiate the conversion of Mn^{3+} back to Mn^{4+} generating hydroxide ions (eqn. 7). At the same time, the reduced Mn^{2+} species can combine with dissolved oxygen in aqueous media to give Mn^{4+} (eqn. 8)[52]. The hydroxyl and superoxide radicals generated during these redox reactions are responsible for the catalytic degradation of dye molecules into simpler fragments which further decompose to give CO_2, H_2O, and other inorganic salts as byproducts[10]. The Fenton-like catalytic degradation of dye molecules was further confirmed by LC-MS analysis of the reaction mixture after attaining equilibrium. The above-proposed mechanism was also supported by the XPS data given in **Figure 5.6** where Fe^{3+}, Mn^{3+}, and Mn^{4+} are the majority oxidation states.

5.2.15 LC-MS analysis

The LC-MS analysis data of the dye solutions after 180 minutes of Fenton-like catalysis is given in **Figure 5.22**. Except for MO, no other dye solutions exhibited m/z values corresponding to their most intense peaks from the literature. For MB, the most intense peak is found at an m/z value of 284 which is absent in **Figure 5.22a**[85, 86]. In the case of RB, the reference pattern gives the most intense peak at 399.17 and a molecular ion peak at 443.23. In **Figure 5.22b**, there exists a small peak corresponding to the molecular ion peak of

RB and the most intense peak is absent[87]. **Figure 5.22c** clearly shows the most abundant peak of MO at m/z value 304, which indicates the presence of undissociated MO molecules in the reaction mixture[88]. In the case of CR, the most intense peak according to the literature is found at m/z = 571 and is found to be absent in the LC-MS data shown in **Figure 5.22**[89]. Thus the degradation of MB, RB, and CR dye molecules is evident from the LC-MS data.
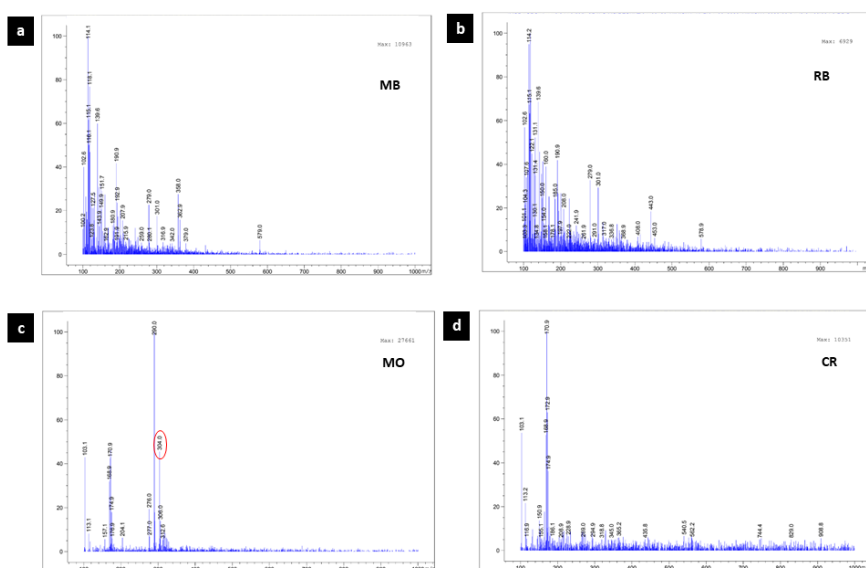
Figure 5.22- LC-MS analysis data of the a) MB b) RB c) MO and d) CR dye solutions after 180 minutes of Fenton-like catalysis using ZC BAT nanostructures.

The ROS responsible for the degradation of the dyes were identified by free radical quenching studies using isopropanol (IP) as the hydroxyl radical scavenger and chloroform (CF) as the superoxide radical scavenger[90, 91]. The catalytic oxidation of dyes by ZC BAT nanostructures was evaluated in the absence as well as in the presence of two different concentrations of the scavenging agents, IP

and CF. The degradation efficiencies obtained in the presence and absence of the radical scavengers are shown in **Figure 5.23**. The degradation efficiencies of MB and RB showed a rapid reduction with the introduction of IP which indicates that the reactive species
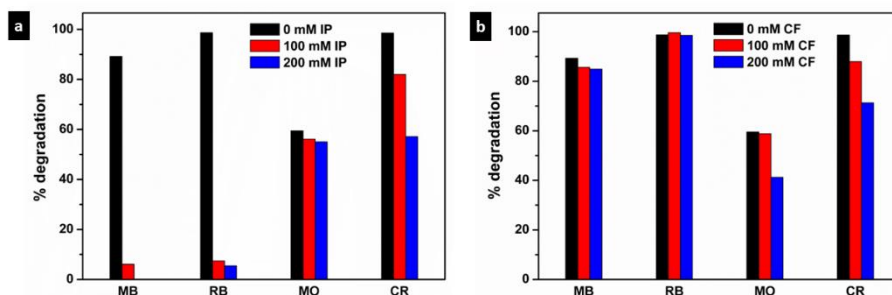
Figure 5.23 - The effect of radical scavengers a) IP and b) CF on the Fenton-like catalytic activity of ZC BAT towards MB, RB, MO, and CR.

responsible for catalytic oxidation are hydroxyl radicals. MO doesn't show any significant reduction in degradation efficiency with an increase in IP concentration. At the same time, CR degradation got retarded upon the addition of hydroxyl radical quencher which means that a part of the degradation process was carried out by hydroxyl radicals. As we investigated the effect of superoxide radical scavenger CF on the catalytic oxidation process, it was found that the cationic dye species MB and RB maintained their degradation efficiencies even in the presence of CF. Thus, superoxide radicals don't bear a prominent role in the degradation of MB and RB. In the case of MO, a reduction in degradation efficiencies was found with an increase in the concentration of CF. Similar is the case of CR, where a reduction in efficiencies was observed upon adding CF. It embarks on the role of superoxide radicals in the degradation of MO and CR.

5.2.16 Desorption, reusability and catalyst stability studies

Desorption experiments were carried out after the adsorption of MB, RB, MO, and CR on ZC BAT, and the desorption efficiencies are shown in **Figure 5.24**. The desorption efficiencies of adsorbed MB, RB, MO, and CR from ZC BAT were found to be 72.0, 85.0, 78.7, and 84.4 % respectively. Similarly, desorption efficiencies were found to be 0.66, 0.01, 6.71, and 0.53 % for MB, RB, MO, and CR after Fenton-like catalytic oxidation using ZC BAT. The reduced adsorption capacity of MO over ZC BAT itself can account for the decrease in catalytic oxidation of MO. Because the primary step of heterogeneous Fenton-like catalytic oxidation is adsorption. So complete degradation of the adsorbed MO content was not attained.
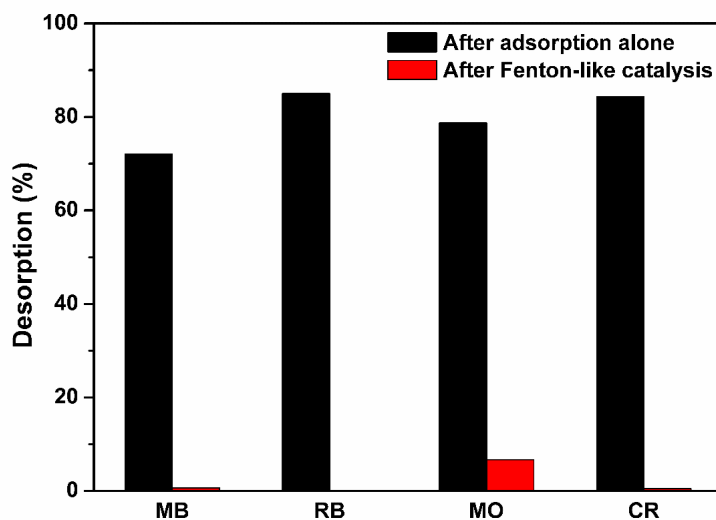
Figure 5.24 - Desorption percentages shown by ZC BAT nanostructures after adsorption and Fenton-like catalysis.

The reusability studies were performed separately for the adsorption and catalytic oxidation process. The removal efficiencies

obtained during three consecutive adsorptions as well as catalytic oxidation cycles are given in **Figure 5.25**. It is evident from **Figure 5.25** that ZC BAT core-shell structures show only a slight decrease in adsorption and catalytic efficiencies even after three cycles which makes ZC BAT a stable and reusable adsorbent/ Fenton-like catalyst. The Total Organic Carbon (TOC) content of the MB sample measured after the catalytic cycle is given in **Table 5.10**.
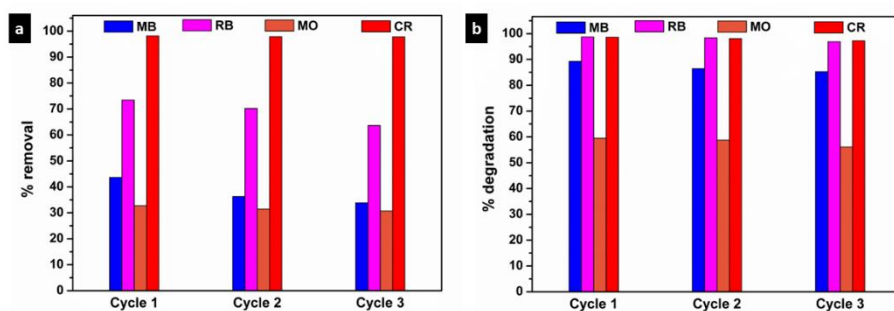
Figure 5.25 - a) Adsorption efficiency and b) Fenton-like catalytic efficiency of ZC BAT nanostructures during three consecutive adsorption/catalytic cycles.

The extent of metal ion leaching during the catalytic cycle was analysed using Atomic Absorption Spectroscopy (AAS) and the results are given in **Table 5.10**. The leached Fe, Mn and Zn concentrations were found to be within the permissible levels[92].

Table 5.10 - The leached Fe, Mn and Zn concentrations along with TOC content after the Fenton-like catalytic cycle

Catalyst	Fe (mg.L^{-1})	Mn (mg.L^{-1})	Zn (mg.L^{-1})	TOC (mg.L^{-1})
ZC BAT	0.176	2.74	6.915	2.19

The chemical stability of the ZC BAT catalyst was further confirmed by XRD analysis. As shown in **Figure 5.26** the XRD patterns obtained for pure and recycled ZC BAT nanostructures were found to be the same. No additional peaks or peak shifts were seen in the XRD profile of recycled ZC BAT.
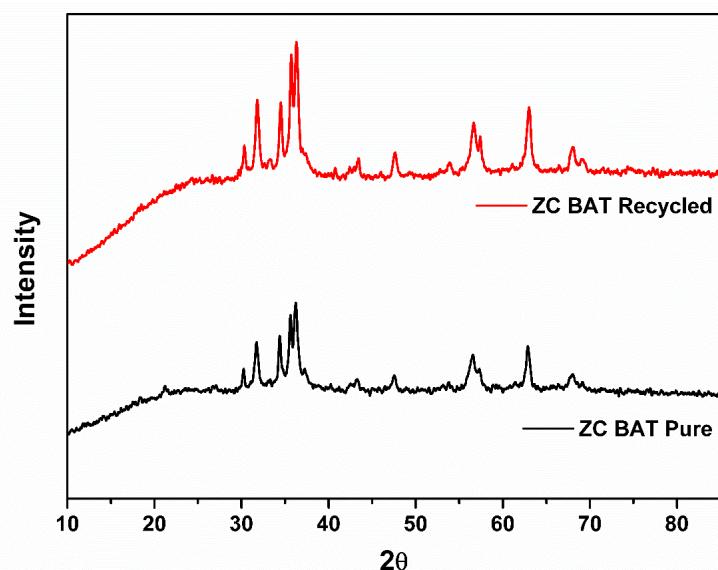
Figure 5.26 – XRD patterns obtained for pure and recycled ZC BAT nanostructures.

5.2.17 Thermal stability studies

The thermal stability of the developed ZC BAT nanostructures was evaluated with thermogravimetric analysis (TGA). The TGA plots of ZC BAT and its constituent components are given in **Figure 5.27**. From the TGA plots, it can be observed that the ZC BAT nanostructures display a gradual weight loss upon increasing the temperature to 800 °C. This weight loss can be attributed to the individual weight losses experienced by MnO_2 and Fe_3O_4 [93-95]. The zinc-carbon battery cathode-derived MnO_2 contains

activated/graphitic carbon content and the weight loss happens due to the decomposition of the carbon content. The weight loss shown by MnO_2 between 200 °C and 450 °C can be assigned to the decomposition of oxygen-containing functional groups[93, 95].
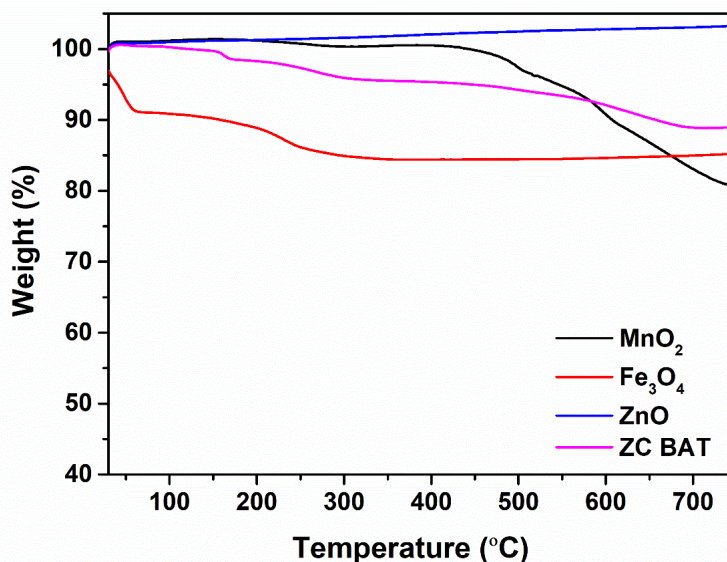
Figure 5.27 – TGA plots obtained for zinc-carbon battery-derived MnO_2, Fe_3O_4, ZnO and ZC BAT nanostructures

The further decrease in weight above 450 °C is due to the pyrolysis of the carbon network[95]. The zinc-carbon battery steel casing derived Fe_3O_4 also exhibited a gradual weight loss. For Fe_3O_4, the initial decrease in weight around 140 °C can be assigned to adsorbed moisture and a slight reduction in weight around 140-210 °C can be attributed to the oxidation of Fe_3O_4 to Fe_2O_3 [93]. There is no further weight loss observed for Fe_3O_4 above 300 °C. The TGA plots of ZnO indicate high thermal stability without any significant weight loss up to 800 °C. Even though the developed ZC BAT composition experienced gradual weight loss above 200 °C, they were found to be

thermally more stable than its constituents MnO_2 and Fe_3O_4 up to 800 °C. Thus, ZC BAT nanostructures were found to be highly stable around the operational temperatures of heterogeneous Fenton-like catalysts.

5.2.18 Comparison with reported Fenton-like catalysts

The Fenton-like catalytic activity of ZC BAT was compared with other reported catalysts and the details are tabulated in **Table 5.11**. From **Table 5.11**, we can distinguish ZC BAT as a potential Fenton-like catalyst due to its magnetic recoverability, efficiency, wide pH range of applicability, moderate H_2O_2 dosage and non-selective nature.

Table 5.11 - Comparison of Fenton-like catalytic performance of ZC BAT nanostructures with other available Fenton-like catalysts

Catalyst	Catalyst dosage (g.L⁻¹)	H_2O_2 dosage (mM.L⁻¹)	pH range	Pollutant	Degradation percentage (%)	References
Fe_3O_4	0.1	1	3	Methylene blue	100 % (30 minutes)	[96]
Fe_3O_4/RGO	0.1	0.8	3	Methylene blue	98 % (60 minutes)	[97]
GO/Fe_3O_4	0.2	22	3	Acid orange 7	100 % (180 minutes)	[98]
Activated carbon-FeOOH	1	10	7	Azo dye	98 % (240 minutes)	[99]

Fe$_2$O$_3$-MWCNTs	0.5	15	3.5	Acid orange II	94 % (30 minutes)	[100]
Fe$_3$O$_4$-γ Al$_2$O$_3$	1	44	3	4-chloro phenol	100 % (180 minutes)	[101]
Fe/ZSM-5	1	267	3.5	Reactive red	97 % (120 minutes)	[102]
FeVO$_4$	0.5	15	6.1	Methyl orange II	94.7 % (60 minutes)	[103]
LaFeO$_3$	0.1	26	5	Phenol	90 % (24 hours)	[104]
MnO$_2$	0.1	1450	6.1	Methylene blue	99 % (0.3 hours)	[16]
MnO$_2$-MWCNT	0.2	300	6	Reactive blue 19	99 % (180 minutes)	[105]
Manganese functionalised silicate nanoparticles	0.4	97	6	Methylene blue	100 % (240 minutes)	[106]
Mn$_3$O$_4$-FeS$_2$/Fe$_2$O$_3$	0.3	5	2.8	Orange II	99 % (60 minutes)	[107]
Mn-Ti HMS	1	10	7	Methylene Blue	63.9 % (120 minutes)	[108]
Mesoporous Cu/MnO$_2$	1	10	7.1	Benzotriazole	89 % (60 minutes)	[109]
Nickel foam supported Cu–MnO$_2$	1.1	-	3	p-nitro phenol	92.4 % (10 minutes) Microwave-	[110]

					enhanced Fenton-like catalysis	
Natural chalcopyrite	6	39.2	5.2	Rhodamine B	96.5 %	[111]
Surface-modified δ-MnO$_2$	0.01	-	6.5	Methylene blue	78.5 % (60 minutes)	[112]
Fe$_3$O$_4$@PDA-MnO$_2$	0.005	5 ml 30 % H$_2$O$_2$	3	Methylene blue	97.36 % (240 minutes)	[113]
MnO$_2$-templated iron oxide-coated diatomites	0.1	90	3	Methylene blue	99 % (120 minutes)	[114]
Chitosan-templated MnO$_2$ nanoparticles	1	30 mg. L^{-1}	7	Methylene blue	95.6 % (90 minutes)	[115]
ZC BAT **(Present work)**	1	98	3-10	Methylene blue (MB) Rhodamine B (RB) Methyl orange (MO) Congo red (CR)	89.2 % (MB) 98.7 % (RB) 59.3 % (MO) 98.6% (CR)	-

5.3. Conclusion

Affordable and efficient ways of water treatment are always under scientific investigation. Adsorption and Fenton-like catalysis are two prominent techniques for water treatment. It would be better if both adsorption and Fenton-like catalytic activity could be brought together in a single material. Here we have developed ZC BAT nanostructures from disposed zinc-carbon batteries as a magnetically retrievable material, capable of acting as an adsorbent as well as a heterogeneous Fenton-like catalyst. The developed ZC BAT has a core-shell design in which MnO_2 and Fe_3O_4 form the cores and mesoporous ZnO forms a shell around the cores. All the constituents of the developed ZC BAT nanostructures are exclusively derived from spent zinc-carbon batteries. Thus, we have achieved almost a full recycling of zinc-carbon batteries into a fully functional nanostructure for water purification. The adsorption and catalytic activities of the developed ZC BAT nanostructures were evaluated using MB, RB, MO, and CR as the model pollutants belonging to different categories. The adsorption and Fenton-like catalytic activity of ZC BAT towards the model pollutants were investigated separately and various factors affecting the adsorption/catalytic performance were evaluated. The mechanism of both adsorption and Fenton-like catalytic oxidation of dye molecules by ZC BAT core-shell nanostructures were discussed in detail. The investigation pointed out that the developed ZC BAT nanostructures are highly effective towards MB, RB, and CR irrespective of their cationic and anionic characteristics. Thus, an affordable, effective, and easy-to-operate adsorbent/Fenton-like catalyst has been developed by

recycling spent zinc-carbon batteries. Here we have addressed two major concerns, one regarding the disposal of spent zinc-carbon batteries and one regarding water purification or broadly saying, environmental remediation. It can be considered a small step towards achieving a circular economy and sustainable development.

5.4 References

1.   Ali, I., *New Generation Adsorbents for Water Treatment.* Chemical Reviews, 2012. **112**(10): p. 5073-5091.
2.   Dong, S., et al., *Recent developments in heterogeneous photocatalytic water treatment using visible light-responsive photocatalysts: a review.* RSC Advances, 2015. **5**(19): p. 14610-14630.
3.   Chew, C.M., et al., *Evaluation of ultrafiltration and conventional water treatment systems for sustainable development: an industrial scale case study.* Journal of Cleaner Production, 2016. **112**: p. 3152-3163.
4.   O'Shea, K.E. and D.D. Dionysiou, *Advanced oxidation processes for water treatment*. 2012, ACS Publications. p. 2112-2113.
5.   Oturan, M.A. and J.-J. Aaron, *Advanced oxidation processes in water/wastewater treatment: principles and applications. A review.* Critical Reviews in Environmental Science and Technology, 2014. **44**(23): p. 2577-2641.
6.   Wang, N., et al., *A review on Fenton-like processes for organic wastewater treatment.* Journal of Environmental Chemical Engineering, 2016. **4**(1): p. 762-787.
7.   Wang, S., *A comparative study of Fenton and Fenton-like reaction kinetics in decolourisation of wastewater.* Dyes and Pigments, 2008. **76**(3): p. 714-720.
8.   Nidheesh, P.V., *Heterogeneous Fenton catalysts for the abatement of organic pollutants from aqueous solution: a review.* RSC Advances, 2015. **5**(51): p. 40552-40577.
9.   Wang, J. and J. Tang, *Fe-based Fenton-like catalysts for water treatment: Catalytic mechanisms and applications.* Journal of Molecular Liquids, 2021. **332**: p. 115755.
10.   Hussain, S., E. Aneggi, and D. Goi, *Catalytic activity of metals in heterogeneous Fenton-like oxidation of wastewater contaminants: a review.* Environmental Chemistry Letters, 2021. **19**: p. 2405-2424.

11. Wang, W.-S., et al., *Preparation, catalytic efficiency and mechanism of Fe3O4/HNTs heterogeneous Fenton-like catalyst.* Materials Today Communications, 2023. **36**: p. 106821.

12. Xu, H.-Y., et al., *Fabricating a Fe3O4@HNTs nanoreactor to expedite heterogeneous Fenton-like reactions.* Materials Letters, 2023. **337**: p. 133985.

13. Ding, J., Y.-G. Sun, and Y.-L. Ma, *Highly Stable Mn-Doped Metal–Organic Framework Fenton-Like Catalyst for the Removal of Wastewater Organic Pollutants at All Light Levels.* ACS Omega, 2021. **6**(4): p. 2949-2955.

14. Qiu, M., et al., *ZnMn2O4 nanorods: an effective Fenton-like heterogeneous catalyst with t2g3eg1 electronic configuration.* Catalysis Science & Technology, 2018. **8**(10): p. 2557-2566.

15. Xing, Z., et al., *A novel Fenton-like catalyst and peroxymonosulfate activator of Mn3O4/λ-MnO2 for phenol degradation: Synergistic effect and mechanism.* Inorganic Chemistry Communications, 2023. **150**: p. 110396.

16. Kim, E.-J., et al., *Manganese oxide nanorods as a robust Fenton-like catalyst at neutral pH: Crystal phase-dependent behavior.* Catalysis Today, 2017. **282**: p. 71-76.

17. Šuligoj, A., et al., *Multicomponent Cu-Mn-Fe silica supported catalysts to stimulate photo-Fenton-like water treatment under sunlight.* Journal of Environmental Chemical Engineering, 2023. **11**(5): p. 110369.

18. Hammouda, S.B., et al., *Reactivity of novel Ceria–Perovskite composites CeO2- LaMO3 (MCu, Fe) in the catalytic wet peroxidative oxidation of the new emergent pollutant 'Bisphenol F': Characterization, kinetic and mechanism studies.* Applied Catalysis B: Environmental, 2017. **218**: p. 119-136.

19. Xu, L. and J. Wang, *Degradation of 2,4,6-trichlorophenol using magnetic nanoscaled Fe3O4/CeO2 composite as a heterogeneous Fenton-like catalyst.* Separation and Purification Technology, 2015. **149**: p. 255-264.

20. Do, Q.C., D.-G. Kim, and S.-O. Ko, *Catalytic activity enhancement of a Fe3O4@SiO2 yolk-shell structure for oxidative degradation of acetaminophen by decoration with copper.* Journal of Cleaner Production, 2018. **172**: p. 1243-1253.

21. Hussain, S., et al., *Enhanced ibuprofen removal by heterogeneous-Fenton process over Cu/ZrO2 and Fe/ZrO2 catalysts.* Journal of Environmental Chemical Engineering, 2020. **8**(1): p. 103586.

22. Keshtkar Vanashi, A. and H. Ghasemzadeh, *Copper(II) containing chitosan hydrogel as a heterogeneous Fenton-like catalyst for production of hydroxyl radical: A quantitative study.* International Journal of Biological Macromolecules, 2022. **199**: p. 348-357.

23. Wan, Z. and J. Wang, *Degradation of sulfamethazine using Fe3O4-Mn3O4/reduced graphene oxide hybrid as Fenton-like catalyst.* Journal of Hazardous Materials, 2017. **324**: p. 653-664.

24. Zhou, H., et al., *Hollow Meso-crystalline Mn-doped Fe3O4 Fenton-like catalysis for ciprofloxacin degradation: Applications in water purification on wide pH range.* Applied Surface Science, 2022. **590**: p. 153120.

25. Brahma, S., P. Arod, and S.A. Shivashankar, *Template-free, low temperature synthesis of binary and ternary metal oxide nanostructures.* MRS Online Proceedings Library, 2011. **1292**(1): p. 99-104.

26. Hsiao, M.-C., et al., *Preparation of Covalently Functionalized Graphene Using Residual Oxygen-Containing Functional Groups.* ACS Applied Materials & Interfaces, 2010. **2**(11): p. 3092-3099.

27. Wang, Z., et al., *Effect of Steam During Fischer–Tropsch Synthesis Using Biomass-Derived Syngas.* Catalysis Letters, 2017. **147**(1): p. 62-70.

28. Maleki, A., et al., *Palladium-decorated o-phenylenediamine-functionalized Fe3O4/SiO2 magnetic nanoparticles: A promising solid-state catalytic system used for Suzuki–Miyaura coupling reactions.* Journal of Physics and Chemistry of Solids, 2020. **136**: p. 109200.

29. Hassanzadeh-Afruzi, F., et al., *Facile synthesis of pyrazolopyridine pharmaceuticals under mild conditions using an algin-functionalized silica-based magnetic nanocatalyst (Alg@SBA-15/Fe3O4).* RSC Advances, 2023. **13**(15): p. 10367-10378.

30. Ferreira, S.H., et al., *Industrial Waste Residue Converted into Value-Added ZnO for Optoelectronic Applications.* ACS Applied Electronic Materials, 2020. **2**(7): p. 1960-1969.

31. Ryzhikov, A., I. Bezverkhyy, and J.-P. Bellat, *Reactive adsorption of thiophene on Ni/ZnO: Role of hydrogen pretreatment and nature of the rate determining step.* Applied Catalysis B: Environmental, 2008. **84**(3-4): p. 766-772.

32. Wen, J., et al., *Cleaner extraction of vanadium from vanadium-chromium slag based on MnO2 roasting and manganese recycle.* Journal of Cleaner Production, 2020. **261**: p. 121205.

33. Zhu, S., et al., *Efficient peroxymonosulfate (PMS) activation by visible-light-driven formation of polymorphic amorphous manganese oxides.* Journal of Hazardous Materials, 2022. **427**: p. 127938.

34. Terzyk, A.P., *The influence of activated carbon surface chemical composition on the adsorption of acetaminophen (paracetamol) in vitro: Part II. TG, FTIR, and XPS analysis of carbons and the temperature dependence of adsorption kinetics at the neutral pH.*

Colloids and Surfaces A: Physicochemical and Engineering Aspects, 2001. **177**(1): p. 23-45.

35.   Cao, H.T., et al., *Preparation and characterization of Al and Mn doped ZnO (ZnO: (Al, Mn)) transparent conducting oxide films.* Journal of Solid State Chemistry, 2004. **177**(4): p. 1480-1487.

36.   Wang, M., et al., *Efficiently enhancing electrocatalytic activity of α-MnO2 nanorods/N-doped ketjenblack carbon for oxygen reduction reaction and oxygen evolution reaction using facile regulated hydrothermal treatment.* Catalysts, 2018. **8**(4): p. 138.

37.   Huang, Z., et al., *High performance of Mn-Co-Ni-O spinel nanofilms sputtered from acetate precursors.* Scientific reports, 2015. **5**: p. 10899.

38.   Ai, Q., et al., *One-pot co-precipitation synthesis of Fe3O4 nanoparticles embedded in 3D carbonaceous matrix as anode for lithium ion batteries.* Journal of Materials Science, 2019. **54**(5): p. 4212-4224.

39.   Yamashita, T. and P. Hayes, *Analysis of XPS spectra of Fe2+ and Fe3+ ions in oxide materials.* Applied surface science, 2008. **254**(8): p. 2441-2449.

40.   Gupta, R. and S. Sen, *Calculation of multiplet structure of core p-vacancy levels.* Physical Review B, 1974. **10**(1): p. 71.

41.   Gupta, R. and S. Sen, *Calculation of multiplet structure of core p-vacancy levels. II.* Physical Review B, 1975. **12**(1): p. 15.

42.   Jijil, C.P., et al., *Nitrogen doping in oxygen-deficient Ca2Fe2O5: a strategy for efficient oxygen reduction oxide catalysts.* ACS applied materials & interfaces, 2016. **8**(50): p. 34387-34395.

43.   Xu, D., D. Fan, and W. Shen, *Catalyst-free direct vapor-phase growth of Zn 1– x Cu x O micro-cross structures and their optical properties.* Nanoscale research letters, 2013. **8**: p. 1-9.

44.   Sing, K.S., *Reporting physisorption data for gas/solid systems with special reference to the determination of surface area and porosity (Recommendations 1984).* Pure and applied chemistry, 1985. **57**(4): p. 603-619.

45.   Sing, K.S. and R.T. Williams, *Physisorption hysteresis loops and the characterization of nanoporous materials.* Adsorption Science & Technology, 2004. **22**(10): p. 773-782.

46.   Tang, D., et al., *Hierarchical porous carbon materials derived from waste lentinus edodes by a hybrid hydrothermal and molten salt process for supercapacitor applications.* Applied Surface Science, 2018. **462**: p. 862-871.

47.   Chowdhury, A.-N., et al., *Cobalt–nickel mixed oxide surface: A promising adsorbent for the removal of PR dye from water.* Applied Surface Science, 2010. **256**(12): p. 3718-3724.

48.   Kim, J.R. and E. Kan, *Heterogeneous photo-Fenton oxidation of methylene blue using CdS-carbon nanotube/TiO2 under visible light.*

Journal of Industrial and Engineering Chemistry, 2015. **21**: p. 644-652.

49.   Fang, Y., et al., *Complex formation via hydrogen bonding between rhodamine B and montmorillonite in aqueous solution.* Scientific reports, 2018. **8**(1): p. 229.

50.   Yu, Y., et al., *Benzene carboxylic acid derivatized graphene oxide nanosheets on natural zeolites as effective adsorbents for cationic dye removal.* Journal of hazardous materials, 2013. **260**: p. 330-338.

51.   Zhong, J.B., et al., *Photocatalytic decolorization of methyl orange in Bi2O3 suspension system.* Journal of Advanced Oxidation Technologies, 2012. **15**(2): p. 334-339.

52.   Ghasemi, H., et al., *Decolorization of wastewater by heterogeneous Fenton reaction using MnO2-Fe3O4/CuO hybrid catalysts.* Journal of Environmental Chemical Engineering, 2021. **9**(2): p. 105091.

53.   Li, K., et al., *Magnetic ordered mesoporous Fe3O4/CeO2 composites with synergy of adsorption and Fenton catalysis.* Applied Surface Science, 2017. **425**: p. 526-534.

54.   Do, S.-H., et al., *Hydrogen peroxide decomposition on manganese oxide (pyrolusite): kinetics, intermediates, and mechanism.* Chemosphere, 2009. **75**(1): p. 8-12.

55.   Jung, Y.S., et al., *Effect of pH on Fenton and Fenton-like oxidation.* Environmental Technology, 2009. **30**(2): p. 183-190.

56.   Foo, K.Y. and B.H. Hameed, *Insights into the modeling of adsorption isotherm systems.* Chemical engineering journal, 2010. **156**(1): p. 2-10.

57.   Wang, J. and X. Guo, *Adsorption isotherm models: Classification, physical meaning, application and solving method.* Chemosphere, 2020. **258**: p. 127279.

58.   Ebelegi, A.N., N. Ayawei, and D. Wankasi, *Interpretation of adsorption thermodynamics and kinetics.* Open Journal of Physical Chemistry, 2020. **10**(03): p. 166-182.

59.   Wang, J. and X. Guo, *Adsorption kinetic models: Physical meanings, applications, and solving methods.* Journal of Hazardous Materials, 2020. **390**: p. 122156.

60.   Xu, H.-Y., et al., *Heterogeneous Fenton-like discoloration of methyl orange using Fe3O4/MWCNTs as catalyst: kinetics and Fenton-like mechanism.* Frontiers of Materials Science, 2018. **12**(1): p. 34-44.

61.   Huang, J.-H., et al., *Adsorption of Rhodamine B and methyl orange on a hypercrosslinked polymeric adsorbent in aqueous solution.* Colloids and Surfaces A: Physicochemical and Engineering Aspects, 2008. **330**(1): p. 55-61.

62.   Jia, P., et al., *Removal of methylene blue from aqueous solution by bone char.* Applied sciences, 2018. **8**(10): p. 1903.

63. Swan, N.B. and M.A.A. Zaini, *Adsorption of Malachite Green and Congo Red Dyes from Water: Recent Progress and Future Outlook.* Ecological Chemistry and Engineering S, 2019. **26**: p. 119 - 132.

64. Bandaru, N., et al., *Benzene carboxylic acid derivatized graphene oxide nanosheets on natural zeolites as effective adsorbents for cationic dye removal.* Journal of hazardous materials, 2013. **260C**: p. 330-338.

65. C.R, M., et al., *Adsorption behaviour of reduced graphene oxide towards cationic and anionic dyes: Co-action of electrostatic and π – π interactions.* Materials Chemistry and Physics, 2017. **194**: p. 243-252.

66. Ramesha, G.K., et al., *Graphene and graphene oxide as effective adsorbents toward anionic and cationic dyes.* Journal of Colloid and Interface Science, 2011. **361**(1): p. 270-277.

67. Bernal, V., L. Giraldo, and J.C. Moreno-Piraján, *Physicochemical Properties of Activated Carbon: Their Effect on the Adsorption of Pharmaceutical Compounds and Adsorbate–Adsorbent Interactions.* C, 2018. **4**(4): p. 62.

68. Tran, H., et al., *Insights into the mechanism of cationic dye adsorption on activated charcoal: The importance of π–π interactions.* Process Safety and Environmental Protection, 2017. **107**: p. 168-180.

69. Tran, H.N., et al., *Insights into the mechanism of cationic dye adsorption on activated charcoal: The importance of π–π interactions.* Process Safety and Environmental Protection, 2017. **107**: p. 168-180.

70. Chen, X., et al., *Effective removal of methyl orange and rhodamine B from aqueous solution using furfural industrial processing waste: Furfural residue as an eco-friendly biosorbent.* Colloids and Surfaces A: Physicochemical and Engineering Aspects, 2019. **583**: p. 123976.

71. Swan, N.B. and M.A.A. Zaini, *Adsorption of malachite green and congo red dyes from water: recent progress and future outlook.* Ecological chemistry and engineering S, 2019. **26**(1): p. 119-132.

72. Pradhan, A.C., A. Paul, and G.R. Rao, *Sol-gel-cum-hydrothermal synthesis of mesoporous Co-Fe@ Al 2 O 3– MCM-41 for methylene blue remediation.* Journal of Chemical Sciences, 2017. **129**: p. 381-395.

73. Kooh, M.R.R., M.K. Dahri, and L.B. Lim, *The removal of rhodamine B dye from aqueous solution using Casuarina equisetifolia needles as adsorbent.* Cogent environmental science, 2016. **2**(1): p. 1140553.

74. Cyril, N., et al., *Catalytic degradation of methyl orange and selective sensing of mercury ion in aqueous solutions using green synthesized silver nanoparticles from the seeds of Derris trifoliata.* Journal of Cluster Science, 2019. **30**: p. 459-468.

75. Litefti, K., et al., *Adsorption of an anionic dye (Congo red) from aqueous solutions by pine bark.* Scientific Reports, 2019. **9**(1): p. 16530.

76. Sun, H., et al., *Ascorbic acid promoted magnetite Fenton degradation of alachlor: Mechanistic insights and kinetic modeling.* Applied Catalysis B: Environmental, 2020. **267**: p. 118383.

77. Zhu, Y., et al., *Strategies for enhancing the heterogeneous Fenton catalytic reactivity: A review.* Applied Catalysis B: Environmental, 2019. **255**: p. 117739.

78. Lu, S., et al., *Design and application of metal-organic frameworks and derivatives as heterogeneous Fenton-like catalysts for organic wastewater treatment: A review.* Environment international, 2021. **146**: p. 106273.

79. Cheng, M., et al., *Metal-organic frameworks for highly efficient heterogeneous Fenton-like catalysis.* Coordination Chemistry Reviews, 2018. **368**: p. 80-92.

80. Dassanayake, R.S., et al., *One-pot synthesis of MnO_2–chitin hybrids for effective removal of methylene blue.* International Journal of Biological Macromolecules, 2016. **93**: p. 350-358.

81. Dawadi, S., et al., *Degradation of methylene blue using hydrothermally synthesized α-manganese oxide nanostructures as a heterogeneous Fenton catalyst.* Journal of Nanomaterials, 2022. **2022**.

82. Pham, V.L., D.-G. Kim, and S.-O. Ko, *Mechanisms of methylene blue degradation by Nano-sized β-MnO 2 particles.* KSCE Journal of Civil Engineering, 2020. **24**: p. 1385-1394.

83. López-Ortega, A., et al., *Galvanic Replacement onto Complex Metal-Oxide Nanoparticles: Impact of Water or Other Oxidizers in the Formation of either Fully Dense Onion-like or Multicomponent Hollow MnOx/FeOx Structures.* Chemistry of Materials, 2016. **28**(21): p. 8025-8031.

84. Wei, J., et al., *Hierarchical porous nanosheets of Co-Mn bimetallic oxide from deep eutectic solvent for highly efficient peroxymonosulfate activation.* Nano Research, 2023: p. 1-11.

85. Zhang, X., et al., *Determination of methylene blue and its metabolite residues in aquatic products by high-performance liquid chromatography–tandem mass spectrometry.* Molecules, 2021. **26**(16): p. 4975.

86. Martin, N. and Y. Leprince-Wang, *HPLC-MS and UV–Visible Coupled Analysis of Methylene Blue Photodegradation by Hydrothermally Grown ZnO Nanowires.* physica status solidi (a), 2021. **218**(24): p. 2100532.

87. Ferreira, B.R., et al., *Fragmentation reactions of rhodamine B and 6G as revealed by high accuracy orbitrap tandem mass spectrometry.* Journal of the Brazilian Chemical Society, 2017. **28**: p. 136-142.

88.   Chen, T., et al., *Study on the photocatalytic degradation of methyl orange in water using Ag/ZnO as catalyst by liquid chromatography electrospray ionization ion-trap mass spectrometry.* Journal of the American Society for Mass Spectrometry, 2008. **19**(7): p. 997-1003.

89.   Smith, G.D., et al., *Forensic dye analysis in cultural heritage: unraveling the authenticity of the earliest Persian knotted-pile silk carpet.* Forensic Science International: Synergy, 2021. **3**: p. 100130.

90.   Hislop, K.A. and J.R. Bolton, *The Photochemical Generation of Hydroxyl Radicals in the UV–vis/Ferrioxalate/H2O2 System.* Environmental Science & Technology, 1999. **33**(18): p. 3119-3126.

91.   Šihor, M., et al., *Photocatalytic Oxidation of Methyl Tert-Butyl Ether in Presence of Various Phase Compositions of TiO2.* Catalysts, 2020. **10**(1): p. 35.

92.   Organization, W.H., *Guidelines for drinking-water quality, 4th edn, incorporating the 1st addendum.* World Health Organization, Geneva. https://www. who. int/water_sanitation_ health/publications/drinking-water-quality-guidelines-4-including-1st-addendum/en/. Accessed, 2019. **13**.

93.   Liang, Y. and W. Lu, *Gamma-irradiation synthesis of Fe 3 O 4/rGO nanocomposites as lithium-ion battery anodes.* Journal of Materials Science: Materials in Electronics, 2020. **31**: p. 17075-17083.

94.   Wang, S., et al., *Adsorption of acetic acid and hydrogen sulfide using NaOH impregnated activated carbon for indoor air purification.* Engineering Reports, 2020. **2**(1): p. e12083.

95.   Farivar, F., et al., *Thermogravimetric analysis (TGA) of graphene materials: Effect of particle size of graphene, graphene oxide and graphite on thermal parameters.* C, 2021. **7**(2): p. 41.

96.   Wei, X., et al., *Shape-Dependent Fenton-Like Catalytic Activity of Fe3O4 Nanoparticles.* Journal of Environmental Engineering, 2020. **146**(3): p. 04020005.

97.   Yang, B., et al., *Enhanced heterogeneous Fenton degradation of Methylene Blue by nanoscale zero valent iron (nZVI) assembled on magnetic Fe3O4/reduced graphene oxide.* Journal of Water Process Engineering, 2015. **5**: p. 101-111.

98.   Zubir, N.A., et al., *Structural and functional investigation of graphene oxide–Fe3O4 nanocomposites for the heterogeneous Fenton-like reaction.* Scientific Reports, 2014. **4**(1): p. 4594.

99.   Wu, J., et al., *Heterogeneous Fenton-like degradation of an azo dye reactive brilliant orange by the combination of activated carbon–FeOOH catalyst and H2O2.* Water Science and Technology, 2013. **67**(3): p. 572-578.

100.   Deng, J., X. Wen, and Q. Wang, *Solvothermal in situ synthesis of Fe3O4-multi-walled carbon nanotubes with enhanced*

heterogeneous Fenton-like activity. Materials Research Bulletin, 2012. **47**(11): p. 3369-3376.

101. Munoz, M., et al., *A ferromagnetic γ-alumina-supported iron catalyst for CWPO. Application to chlorophenols.* Applied Catalysis B: Environmental, 2013. **136-137**: p. 218-224.

102. Yaman, Y.C., G. Gündüz, and M. Dükkancı, *Degradation of CI Reactive Red 141 by heterogeneous Fenton-like process over iron-containing ZSM-5 zeolites.* Coloration Technology, 2013. **129**(1): p. 69-75.

103. Deng, J., et al., *FeVO4 as a highly active heterogeneous Fenton-like catalyst towards the degradation of Orange II.* Applied Catalysis B: Environmental, 2008. **84**(3): p. 468-473.

104. Rusevova, K., et al., *LaFeO3 and BiFeO3 perovskites as nanocatalysts for contaminant degradation in heterogeneous Fenton-like reactions.* Chemical Engineering Journal, 2014. **239**: p. 322-331.

105. Fathy, N.A., et al., *Oxidative degradation of RB19 dye by a novel γ-MnO2/MWCNT nanocomposite catalyst with H2O2.* Journal of Environmental Chemical Engineering, 2013. **1**(4): p. 858-864.

106. Tušar, N.N., et al., *Manganese Functionalized Silicate Nanoparticles as a Fenton-Type Catalyst for Water Purification by Advanced Oxidation Processes (AOP).* Advanced Functional Materials, 2012. **22**(4): p. 820-826.

107. Xu, Y., et al., *Efficient photocatalytic removal of orange II by a Mn3O4–FeS2/Fe2O3 heterogeneous catalyst.* Journal of Environmental Management, 2020. **253**: p. 109695.

108. Song, H., et al., *Manganese functionalized mesoporous molecular sieves Ti-HMS as a Fenton-like catalyst for dyes wastewater purification by advanced oxidation processes.* Journal of Environmental Chemical Engineering, 2016. **4**(4, Part A): p. 4653-4660.

109. Zhang, Y., et al., *Degradation of benzotriazole by a novel Fenton-like reaction with mesoporous Cu/MnO2: Combination of adsorption and catalysis oxidation.* Applied Catalysis B: Environmental, 2016. **199**: p. 447-457.

110. Shen, T., et al., *Application of nickel foam supported Cu–MnO2 in microwave enhanced Fenton-like process for p-nitrophenol removal: Degradation, synergy and mechanism insight.* Journal of Cleaner Production, 2023. **397**: p. 136442.

111. Yang, J., et al., *Heterogeneous Fenton degradation of persistent organic pollutants using natural chalcopyrite: effect of water matrix and catalytic mechanism.* Environmental Science and Pollution Research, 2022. **29**(50): p. 75651-75663.

112. Ma, Z., et al., *Hydrothermal synthesis and characterization of surface-modified δ-MnO2 with high Fenton-like catalytic activity.* Catalysis Communications, 2015. **67**: p. 68-71.

113. Pan, X., et al., *Fenton-like catalyst Fe3O4@polydopamine-MnO2 for enhancing removal of methylene blue in wastewater.* Colloids and Surfaces B: Biointerfaces, 2019. **181**: p. 226-233.
114. He, Y., et al., *Evaluation of MnO2-templated iron oxide-coated diatomites for their catalytic performance in heterogeneous photo Fenton-like system.* Journal of Hazardous Materials, 2018. **344**: p. 230-240.
115. Yang, J., et al., *Immobilization of chitosan-templated MnO2 nanoparticles onto filter paper by redox method as a retrievable Fenton-like dip catalyst.* Chemosphere, 2021. **268**: p. 128835.

Chapter 6

Colour Tunable Cool Pigments Based on $TiZn_2O_4$ Inverse Spinels
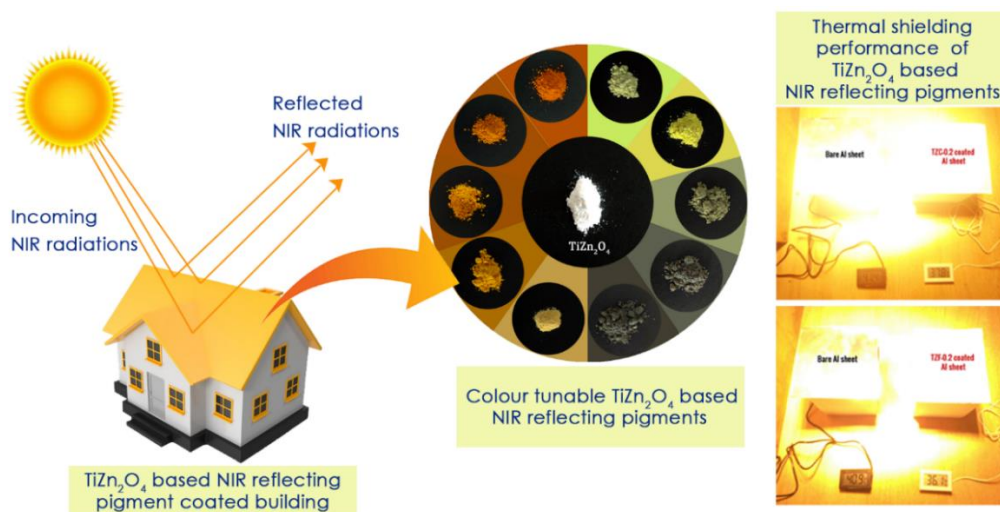
A new class of near-infrared (NIR) reflecting yellow and orange cool pigments based on $TiZn_2O_4$ inverse spinels were synthesized. The colour tuning in pure $TiZn_2O_4$ was made possible by the substitution of octahedral Zn^{2+} ions by Cu^{2+} and Fe^{3+} ions separately. By the incorporation of Cu^{2+} and Fe^{3+} ions into the inverse spinel lattice in varying amounts, a series of pigment compositions having colours ranging from greenish-yellow to reddish-brown was obtained. The developed pigments exhibited moderate to high NIR reflectance ranging from 47.61 to 87.81 %. $TiZn_2O_4$ based NIR reflecting pigment provided an interior 4.8 °C cooler than an uncoated roofed interior. Cu^{2+} and Fe^{3+} doped $TiZn_2O_4$ systems were found to be highly stable and eco-friendly cool pigment candidates capable of achieving better thermal conditioning and impressive energy conservation.

6.1 Introduction

Colour plays a crucial role in conveying information, creating memories, determining moods, and even in decision-making. In such a way, inorganic pigments capable of imparting colours also affect us. There is a wide range of inorganic pigments available in the market spanning over a broad range of colours[1, 2]. The investigations for more attractive and affordable pigments with better characteristics are still on. The development of environmentally benign inorganic pigments is one of the prime objectives of pigment manufacturers. The presence of elements such as Cd, Cr and Pb in pigment compositions is discouraged nowadays[3, 4]. Lead Tin Oxide ($PbSnO_3$), Cadmium Sulfide (CdS), Nickel Titanate ($NiTiO_3$), $Al_2O_3:Cr^{3+}$ (corundum), Cadmium red (CdS: CdSe), etc. are some of the conventional inorganic pigments in the yellow-orange-red colour range in use[5-9]. The presence of heavy metals in these pigments is a deterrent to their commercial use. Such pigments can cause serious health and environmental hazards [10, 11]. Synthesis of efficient substitutes for hazardous pigments without compromising optical characteristics and stability is one of the challenges faced by manufacturers. Environmental friendliness, economic viability and high stability are the main objectives of present-day pigment research [12-15]. Apart from the aesthetic aspects, functional properties of pigments such as solar reflectance, magnetic nature, corrosion inhibition etc. are also under exploration [1, 16]. Earth's temperature has risen by 0.18 ℃ per decade since 1981[17]. The rising global temperature will lead to a climatic catastrophe if left unaddressed. About 52 % of solar spectra consist

of NIR[18]. These NIR radiations are responsible for the heat build-up from solar radiation. To deal with the heat build-up inside buildings, cooling facilities which consume an immense amount of energy are in use. Here arises the significance of NIR reflecting cool pigment coatings, which has an instantaneous effect as well as a long-term impact on rising global temperatures [19, 20]. The instant effect is nothing but the cooler interiors provided by the NIR reflecting pigment-coated buildings even amid high solar irradiance. The long-term impact occurs from the energy conserved by the utilization of cool coatings instead of air conditioning and other cooling appliances. In the long run, conservation of the energy spent on cooler interiors can lead to a more sustainable and eco-friendly mode of energy utilization.

We have chosen a less explored $TiZn_2O_4$, inverse spinel system as our parent material for investigation[21]. By incorporating Cu^{2+} and Fe^{3+} ions into the $TiZn_2O_4$ lattice, we have developed a series of pigment compositions with colours ranging from greenish-yellow to reddish-brown. Here we report, $TiZn_2O_4$-based pigments as affordable, high NIR reflecting and eco-friendly replacements for many of the environmentally malign and high-cost commercial pigments.

6.2 Results and Discussion

6.2.1 *X-ray Diffraction Studies*

The XRD pattern of TZ, i.e. the undoped version of $TiZn_2O_4$ along with the reference pattern is shown in **Figure 6.1**. The XRD pattern of TZ can be indexed to a cubic crystal structure belonging to the Fd-3m space group (JCPDS00-025-1164)[21]. $TiZn_2O_4$ has an inverse

spinel structure in which half of the Zn^{2+} ions occupy the tetrahedral voids and the other half occupy octahedral voids along with Ti^{4+} ions in the lattice[22].
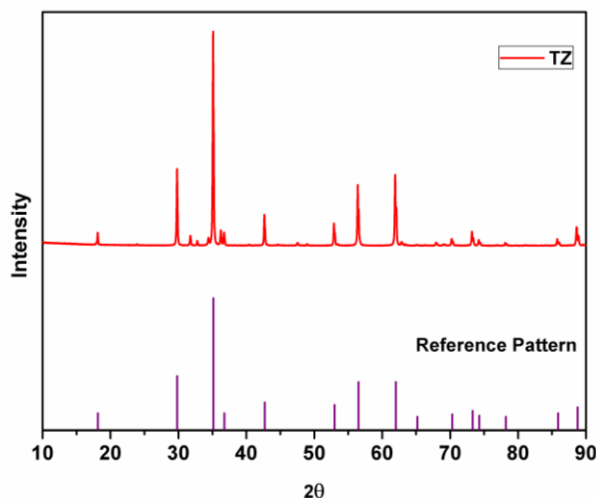
Figure 6.1 - XRD pattern of $TiZn_2O_4$ with the reference pattern

The XRD patterns of the synthesized Cu doped $TiZn_2O_4$ compositions having the general formula, $TiZn_{2-x}Cu_xO_4$ (where x ranges from 0 to 1) are given in **Figure 6.2**. Upon examination, Cu^{2+} doped variants i.e. TZC-0.2, TZC-0.4, TZC-0.6, TZC-0.8 and TZC-1 were also found to belong to cubic crystal structure with Fd-3m space group. In addition to the cubic $TiZn_2O_4$ phase, the XRD pattern of TZC-0.2 and TZC-0.4 exhibited ZnO, TZC-0.6 showed TiO_2 and TZC-0.8 and TZC-1 contained CuO phase in negligible amounts. Since $TiZn_2O_4$ has got inverse spinel structure, upon Cu^{2+} doping the Zn^{2+} ions present in the octahedral sites of the inverse spinel lattice were replaced by Cu^{2+} ions. Crystal field stabilization energy of Cu^{2+} plays a crucial role here [23, 24]. Even after doping of Cu^{2+} ions into the $TiZn_2O_4$

lattice, the XRD patterns showed no significant phase changes or additional peaks except the minute ZnO, TiO_2 and CuO peaks.
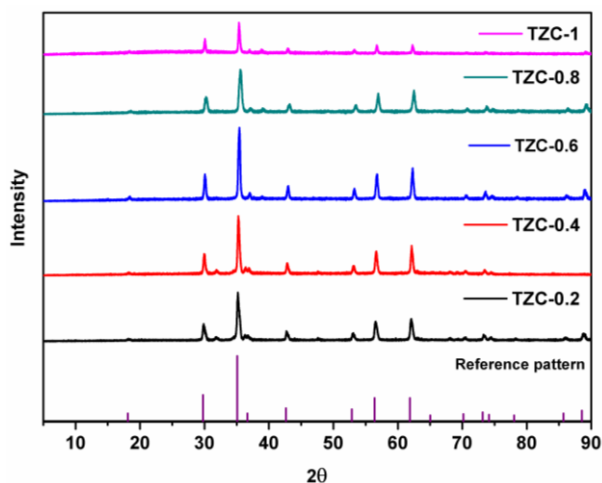
Figure 6.2- X-ray diffraction patterns of the synthesized Cu^{2+} doped $TiZn_2O_4$ compositions

Upon close examination, the XRD patterns of Cu^{2+} doped variants showed a narrow shift towards higher 2θ values. This can be attributed to the slightly smaller ionic radii of Cu^{2+}(73 pm) compared to Zn^{2+} (74 pm) ions. To understand the TZ crystal structure and the changes occurring in the lattice upon doping with Cu^{2+} ion, we have carried out Rietveld refinement studies of the synthesized samples. **Figure 6.3** shows the crystal structures drawn from the lattice parameters obtained by the Rietveld refinement of TZ and TZC-0.4. The experimental and refined patterns obtained after the Rietveld refinement of TZ and other Cu^{2+} doped $TiZn_2O_4$ candidates are given in **Figure 6.4**. The lattice parameters obtained for TZ and Cu^{2+} doped $TiZn_2O_4$ compositions after Rietveld refinement are shown in **Table 6.1**.
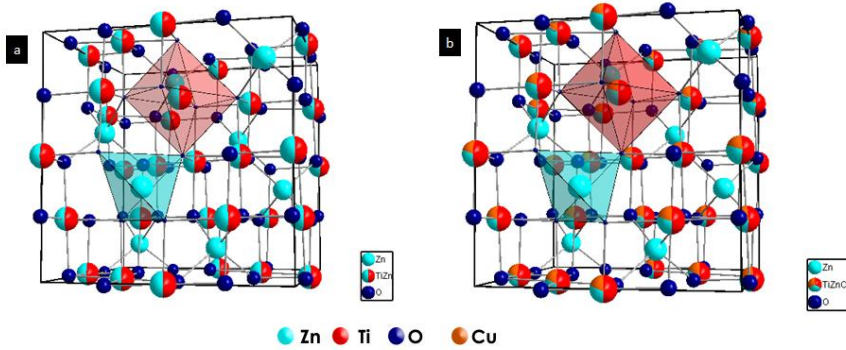
Figure 6.3- Crystal structures of a) TZ and b) TZC-0.4 obtained through Rietveld refinement studies
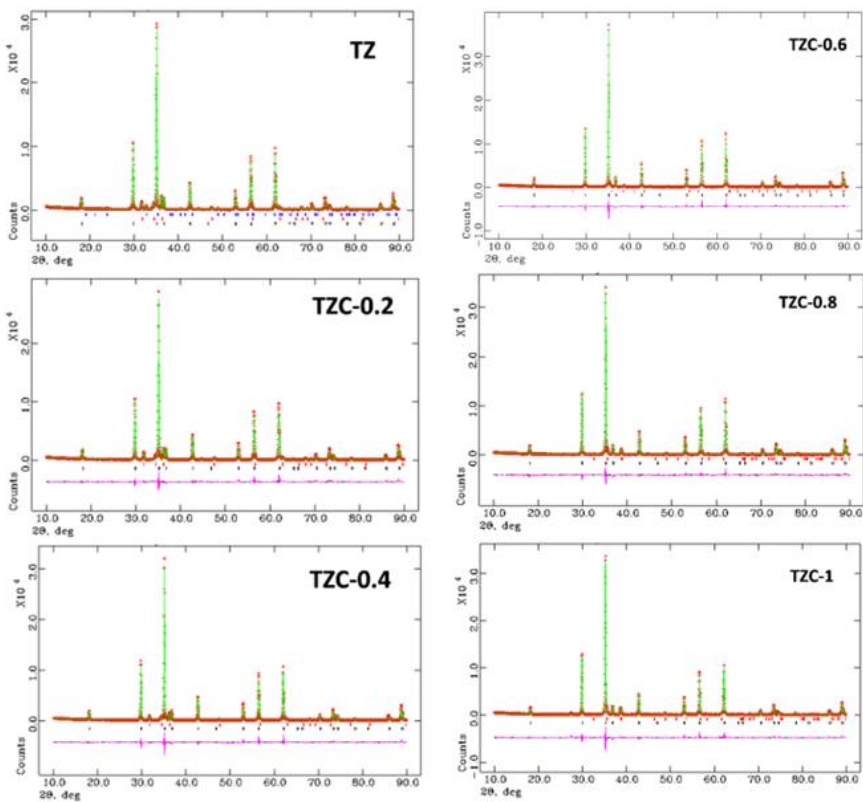
Figure 6.4 - The experimental and refined patterns obtained on Rietveld analysis of TZ, TZC-0.2, TZC-0.4, TZC-0.6, TZC-0.8 and TZC-1 samples

Table 6.1 - The reliability factors and lattice parameters obtained for TZ and $TiZn_{2-x}Cu_xO_4$ series by Rietveld refinement studies

Samples	χ^2	wRp (%)	Rp (%)	a(Å)	Volume
TZ	3.75	9.55	7.40	8.4650(0)	606.6
TZC-0.2	3.65	9.37	7.24	8.4596(0)	605.4
TZC-0.4	4.24	10.44	8.14	8.4542(0)	604.3
TZC-0.6	5.32	8.51	11.44	8.4510(0)	603.6
TZC-0.8	3.79	9.64	7.22	8.4493(5)	603.2
TZC-1	4.81	10.90	8.18	8.4367(0)	600.5

Rietveld refinement was performed for all the samples using the structural parameter of cubic $TiZn_2O_4$. Refinement of the XRD patterns with these parameters proceeded smoothly[21]. **Table 6.1** shows a reduction in lattice parameters and cell volume with an increase in Cu^{2+} doping. The decrease in lattice parameters and cell volume can be attributed to the smaller ionic radii of Cu^{2+} relative to Zn^{2+}. The refinement data obtained show that the doping of Cu^{2+} into the $TiZn_2O_4$ went as planned. The fractional coordinates, sites occupied and extent of occupancy of each atom upon completion of Rietveld refinement of pristine and Cu^{2+} doped $TiZn_2O_4$ compositions are given in **Table 6.2**. The observed XRD patterns are in good agreement with the calculated Cu^{2+} doped $TiZn_2O_4$ models. The extent of agreement is evident from the χ^2, R_p and wRp values obtained upon refining. The reduction in lattice volume and cell edge lengths due to the incorporation of Cu^{2+} ions is evident from the refinement data.

Table 6.2 - The fractional coordinates, sites occupied and extent of occupancy obtained upon Rietveld refinement for TZ and Cu^{2+} doped $TiZn_2O_4$ compositions

TZ						
Atom	**Site**	**x**	**y**	**z**	U_{iso}	Occupancy
Zn (1)	8a	0.125	0.125	0.125	0.01745	1
Ti	16d	0.5	0.5	0.5	0.00953	0.5
Zn (2)	16d	0.5	0.5	0.5	0.01975	0.5
O	32e	0.2588	0.2588	0.2588	0.01897	1
TZC-0.2						
Atom	**Site**	**x**	**y**	**z**	U_{iso}	Occupancy
Zn (1)	8a	0.125	0.125	0.125	0.01831	1
Ti	16d	0.5	0.5	0.5	0.00848	0.5
Zn (2)	16d	0.5	0.5	0.5	0.01802	0.4
Cu	16d	0.5	0.5	0.5	0.00908	0.1
O	32e	0.2592	0.2592	0.2592	0.01937	1
TZC-0.4						
Atom	**Site**	**x**	**y**	**z**	U_{iso}	Occupancy
Zn (1)	8a	0.125	0.125	0.125	0.01849	1
Ti	16d	0.5	0.5	0.5	0.00748	0.5
Zn (2)	16d	0.5	0.5	0.5	0.01528	0.3
Cu	16d	0.5	0.5	0.5	0.01698	0.2
O	32e	0.2589	0.2589	0.2589	0.02028	1
TZC-0.6						
Atom	**Site**	**x**	**y**	**z**	U_{iso}	Occupancy
Zn (1)	8a	0.125	0.125	0.125	0.02135	1

Ti	16d	0.5	0.5	0.5	0.01398	0.5
Zn (2)	16d	0.5	0.5	0.5	0.01331	0.2
Cu	16d	0.5	0.5	0.5	0.01701	0.3
O	32e	0.2577	0.2577	0.2577	0.02291	1
TZC-0.8						
Atom	Site	x	y	z	U_{iso}	Occupancy
Zn (1)	8a	0.125	0.125	0.125	0.01915	1
Ti	16d	0.5	0.5	0.5	0.01069	0.5
Zn (2)	16d	0.5	0.5	0.5	0.00132	0.1
Cu	16d	0.5	0.5	0.5	0.02192	0.4
O	32e	0.2604	0.2604	0.2604	0.02022	1
TZC-1						
Atom	Site	x	y	z	U_{iso}	Occupancy
Zn	8a	0.125	0.125	0.125	0.01876	1
Ti	16d	0.5	0.5	0.5	0.01396	0.5
Cu	16d	0.5	0.5	0.5	0.02094	0.5
O	32e	0.2570	0.2570	0.2570	0.02313	1

The Fe^{3+} doped $TiZn_2O_4$ compositions having the general formula $TiZn_{2-x}Fe_xO_{4+\delta}$ (where x = 0.2, 0.4, 0.6, 0.8, 1 and $\delta=x/2$) showed XRD patterns identical to that of the cubic structure of $TiZn_2O_4$. The XRD patterns of $TiZn_{2-x}Fe_xO_{4+\delta}$ series are given in **Figure 6.5**.

From the XRD data, it is evident that the Fe^{3+} doped $TiZn_2O_4$ structures belong to the Fd-3m space group. The proposed crystal structure for a $TiZn_{2-x}Fe_xO_{4+\delta}$ composition involves an inverse spinel structure in which Fe^{3+} ions are expected to occupy the octahedral

sites and site allocation is given by the formula $Ti_{(oh)}Zn_{1(Td)}Zn_{1-x(oh)}Fe_{x(Oh)}O_{4+\delta}$.
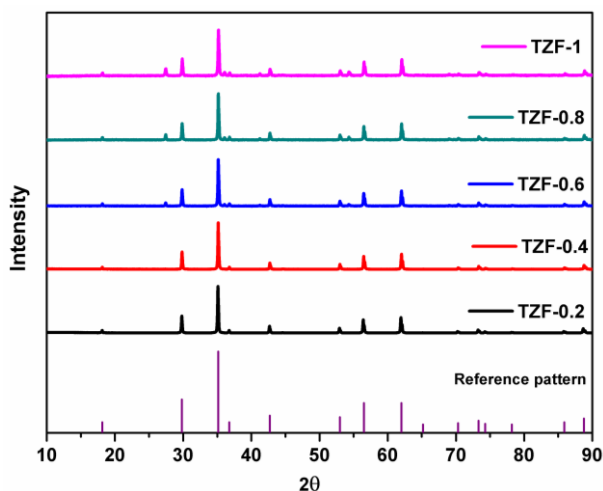
Figure 6.5 - X-ray diffraction patterns of the synthesized Fe^{3+} doped $TiZn_2O_4$ compositions

The allocation of Fe^{3+} into the octahedral sites is confirmed with the help of Rietveld refinement and XPS in the later section. The doping of Fe^{3+} into the octahedral Zn^{2+} positions was manifested as a shift in the XRD peaks towards a higher 2θ value. This is mainly due to the smaller ionic radii of Fe^{3+} compared to Zn^{2+}. The replacement of octahedral Zn^{2+} ions by Fe^{3+} may result in a reduction of lattice distances. The effect of Fe^{3+} doping on the $TiZn_2O_4$ crystal structure was evaluated with the help of Rietveld refinement. Similar to the Cu^{2+} doped $TiZn_2O_4$ compositions, the cubic structure was taken as the starting model for refinement. The refined crystal structure for TZF-0.4 is shown in **Figure 6.6**.

The experimental and refined patterns for Fe^{3+} doped $TiZn_2O_4$ are given in **Figure 6.7**. The lattice parameters for TZ and $TiZn_{2-x}Fe_xO_{4+\delta}$

are listed in **Table 6.3** along with refinement reliability factors. In addition, refinement parameters along with atom positions and site occupancies of Fe^{3+} doped $TiZn_2O_4$ compositions are provided in **Table 6.4**. The lattice distances obtained by refinement studies show a gradual decrease with an increase in Fe^{3+} ion doping into the lattice. The smaller ionic radii of Fe^{3+} compared to Zn^{2+} ions are responsible for this reduction.
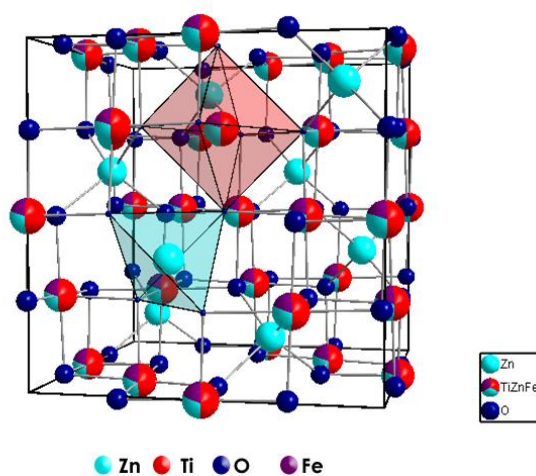
Figure 6.6- Crystal structures of TZF-0.4 obtained through Rietveld refinement studies

Table 6.3 - The reliability factors and lattice parameters obtained for TZ and $TiZn_{2-x}Fe_xO_4$ series by Rietveld refinement studies

Samples	χ^2	wRp (%)	Rp (%)	a(Å)	Volume
TZ	3.75	9.55	7.40	8.4650(0)	606.6
TZF-0.2	3.82	4.48	3.28	8.4615(0)	605.8
TZF-0.4	3.81	3.79	2.66	8.4511(0)	603.6
TZF-06	1.71	3.74	2.79	8.4491(0)	603.2
TZF-0.8	1.89	3.59	2.59	8.4497(0)	603.3
TZF-1	1.29	2.80	2.15	8.4493(0)	603.2
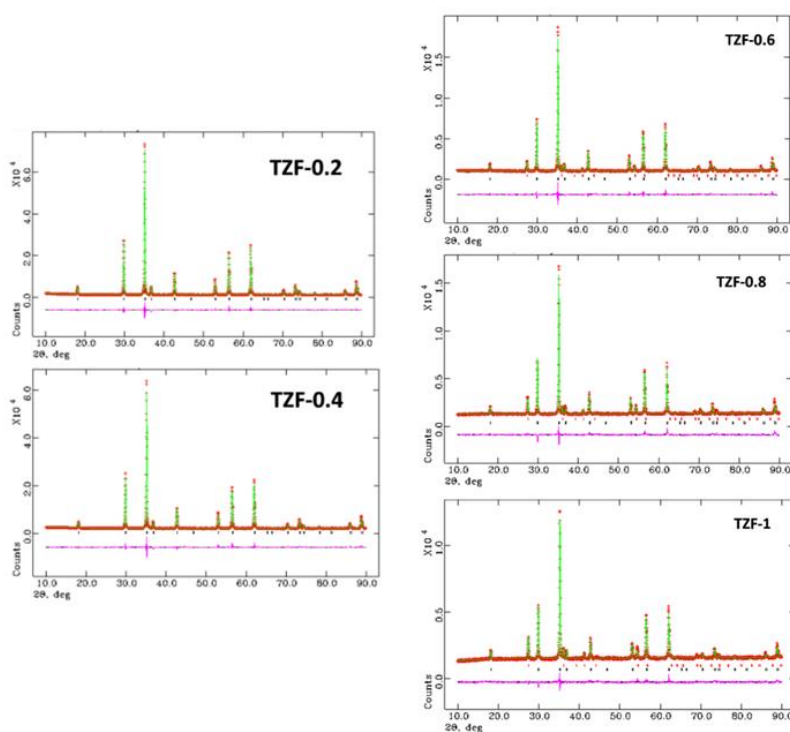
Figure 6.7 - The experimental and refined patterns obtained on Rietveld analysis of TZF-0.2, TZF-0.4, TZF-0.6, TZF-0.8 and TZF-1 samples

Table 6.4 - The fractional coordinates, sites occupied and extent of occupancy obtained upon Rietveld refinement Fe^{3+} doped $TiZn_2O_4$ compositions

TZF-0.2						
Atom	**Site**	**x**	**y**	**z**	U_{iso}	**Occupancy**
Zn (1)	8a	0.125	0.125	0.125	0.0124	1
Ti	16d	0.5	0.5	0.5	0.0047	0.5
Zn (2)	16d	0.5	0.5	0.5	0.0161	0.4
Fe	16d	0.5	0.5	0.5	0.0013	0.1
O	32e	0.2584	0.2584	0.2584	0.0136	1

TZF-0.4						
Atom	**Site**	**x**	**y**	**z**	**U_{iso}**	**Occupancy**
Zn (1)	8a	0.125	0.125	0.125	0.0167	1
Ti	16d	0.5	0.5	0.5	0.0102	0.5
Zn (2)	16d	0.5	0.5	0.5	0.0163	0.3
Fe	16d	0.5	0.5	0.5	0.0065	0.2
O	32e	0.25868	0.25868	0.25868	0.0183	1
TZF-0.6						
Atom	**Site**	**x**	**Y**	**z**	**U_{iso}**	**Occupancy**
Zn (1)	8a	0.125	0.125	0.125	0.0178	1
Ti	16d	0.5	0.5	0.5	0.0034	0.5
Zn (2)	16d	0.5	0.5	0.5	0.0067	0.2
Fe	16d	0.5	0.5	0.5	0.0250	0.3
O	32e	0.25915	0.25915	0.25915	0.0167	1
TZF-0.8						
Atom	**Site**	**x**	**y**	**z**	**U_{iso}**	**Occupancy**
Zn (1)	8a	0.125	0.125	0.125	0.0199	1
Ti	16d	0.5	0.5	0.5	0.0250	0.5
Zn (2)	16d	0.5	0.5	0.5	0.0250	0.1
Fe	16d	0.5	0.5	0.5	0.0250	0.4
O	32e	0.25990	0.25990	0.25990	0.0152	1
TZF-1						
Atom	**Site**	**x**	**y**	**z**	**U_{iso}**	**Occupancy**
Zn	8a	0.125	0.125	0.125	0.0214	1
Ti	16d	0.5	0.5	0.5	0.0250	0.5
Fe	16d	0.5	0.5	0.5	0.0021	0.5
O	32e	0.26022	0.26022	0.26022	0.0135	1

To confirm the successful doping of Fe^{3+} ions into the octahedral sites, we have carried out XRD refinement studies using three different starting models. The first model has the general formula, $Ti_{(oh)}Zn_{1(Td)}Zn_{1-x(oh)}Fe_{x(Oh)}O_{4+\delta}$ where the Fe^{3+} ions are completely allotted to the octahedral sites. The second one, $Ti_{(oh)}Zn_{1(Oh)}Zn_{1-x(Td)}Fe_{x(Td)}O_{4+\delta}$ has all the Fe^{3+} ions occupying the tetrahedral voids. The third model assumes an equal distribution of Fe^{3+} ions between octahedral and tetrahedral voids i.e., $Ti_{(oh)}Zn_{1-x/2(Oh)}Fe_{x/2(Oh)}Zn_{1-x/2(Td)}Fe_{x/2(Td)}O_{4+\delta}$. After the completion of refinement using all three models, a comparison of the chi-square, Rp and wRp values given in **Table 6.5** revealed that the general composition of Fe^{3+} doped $TiZn_2O_4$ samples is $Ti_{(oh)}Zn_{1(Td)}Zn_{1-x(Oh)}Fe_{x(Oh)}O_{4+\delta}$.

Table 6.5 - The reliability factors and lattice parameters obtained for three different models of site allocation in $TiZn_{2-x}Fe_xO_4$ by Rietveld refinement studies

	χ^2	wRp (%)	Rp (%)	a(Å)	Volume
Model 1	3.82	4.48	3.28	8.4615(0)	605.8
Model 2	6.121	5.67	4	8.4604(2)	605.6
Model 3	6.522	5.85	4.06	8.4575(2)	604.9

Refinement details of models 2 and 3 are given in **Figure 6.8** and **Table 6.6**. Thus, it is evident that both Cu^{2+} and Fe^{3+} ions are getting placed into the octahedral sites in the inverse spinel lattice of $TiZn_2O_4$. The percentages of main and secondary phases calculated

from Rietveld refinement for each of the developed compositions are given in **Table 6.7**.
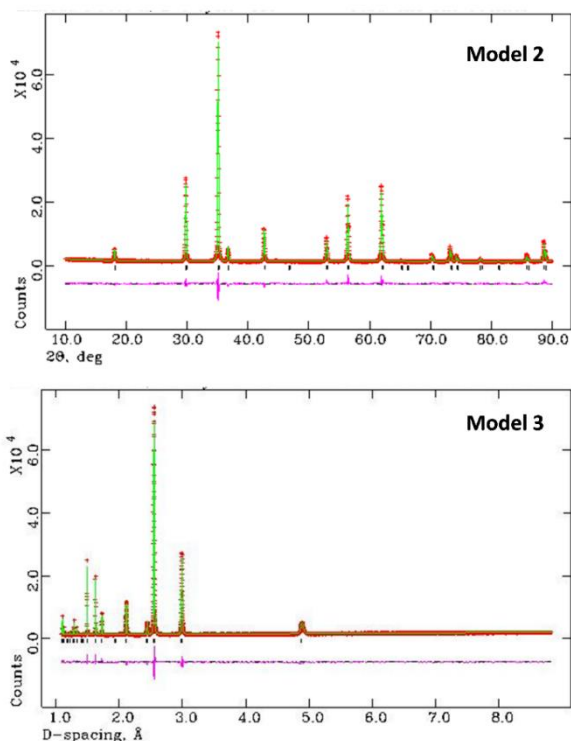
Figure 6.8 - The experimental and refined patterns obtained on Rietveld analysis of TZF-0.2 as per models 2 and 3.

Table 6.6 - The fractional coordinates, sites occupied and extent of occupancy obtained upon Rietveld refinement for TZF-0.2 as per models 2 and 3.

Model 2						
Atom	**Site**	**x**	**y**	**z**	**U_{iso}**	**Occupancy**
Zn (1)	8a	0.125	0.125	0.125	0.01240	0.8
Ti	16d	0.5	0.5	0.5	0.01245	0.5
Zn (2)	16d	0.5	0.5	0.5	0.02060	0.5
Fe	8a	0.125	0.125	0.125	0.02500	0.2

O	32e	0.2572	0.2572	0.2572	0.01976	1
Model 3						
Atom	**Site**	**x**	**y**	**z**	**U$_{iso}$**	**Occupancy**
Zn (1)	8a	0.125	0.125	0.125	0.01456	0.9
Ti	16d	0.5	0.5	0.5	0.01055	0.5
Zn (2)	16d	0.5	0.5	0.5	0.01936	0.45
Fe (1)	8a	0.125	0.125	0.125	0.01986	0.1
Fe (2)	16d	0.5	0.5	0.5	0.0250	0.05
O	32e	0.2585	0.2585	0.2585	0.0250	1

Table 6.7 - The percentages of main and secondary phases calculated through Rietveld refinement for the developed pigment compositions.

Composition	Percentage of phases present
TZ	90.01 % (Main phase) 7.57 % (ZnO), 2.37 % (ZnTiO$_3$)
TZC-0.2	91.29 % (Main phase), 8.70 % (ZnO)
TZC-0.4	93.7 % (Main phase), 6.3 % (ZnO)
TZC-0.6	99.5 % (Main phase), 0.49 % (TiO$_2$)
TZC-0.8	94.36 % (Main phase), 5.63 % (CuO)
TZC-1	92.73 % (Main phase), 7.26 % (CuO)
TZF-0.2	100 % (Main phase)
TZF-0.4	100 % (Main phase)
TZF-0.6	90.72 % (Main phase), 9.2 % (TiO$_2$)
TZF-0.8	86.65 % (Main phase), 13.34 % (TiO$_2$)
TZF-1	77.11 % (Main phase), 22.88 % (TiO$_2$)

6.2.2 XPS Analysis

The XPS measurements were carried out mainly to confirm the oxidation state and site of occupancy of Fe in $TiZn_{2-x}Fe_xO_{4+\delta}$ compositions. Cu^{2+} has CFSE considerations towards the octahedral sites, which was further confirmed by Rietveld refinement studies[24]. So TZC series doesn't require any additional assurance on its Cu^{2+} site of occupancy. Such a conclusion cannot be made in the case of Fe^{3+} doped samples without XPS measurements. Here we have performed the XPS analysis of TZF-0.2 as a model system.
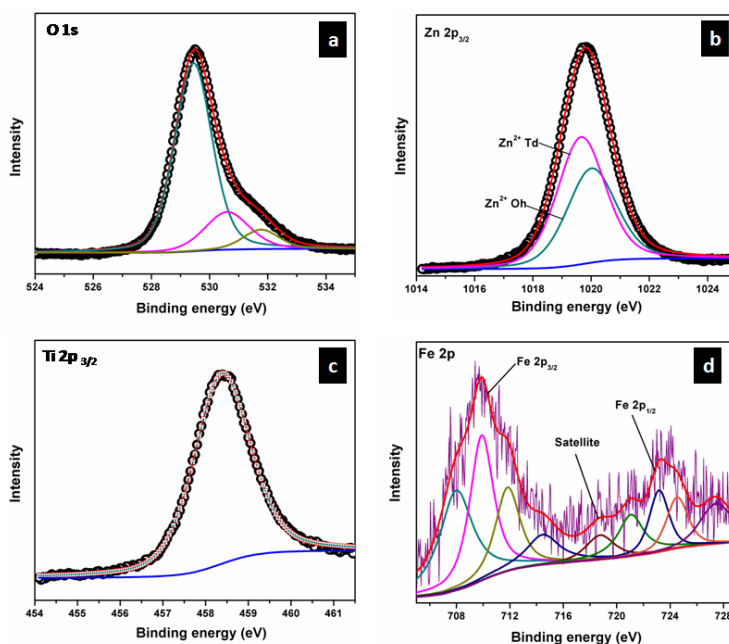

Figure 6.9 – High resolution XPS of a) O 1s b) Zn $2p_{3/2}$ c) Ti $2p_{3/2}$ and d) Fe 2p core levels in TZF-0.2

The XPS spectra of TZF-0.2 in the regions of O, Ti, Zn and Fe are given in **Figure 6.9**. The O 1s signal of TZF-0.2 shown in **Figure 6.9a**, can be deconvoluted into three peaks with binding energies centred on

529.7, 531.6 and 532.8 eV which corresponds to lattice oxygen, oxygen-deficient regions and surface hydroxyl groups respectively[25]. In the case of Zn^{2+}, the peaks corresponding to Zn $2p_{3/2}$ and Zn $2p_{1/2}$ states were observed at binding energies of 1021 and 1044 eV [26]. To confirm the distribution of Zn^{2+} among the octahedral and tetrahedral sites, we have carried out the deconvolution of the Zn $2p_{3/2}$ peak. From the literature, it was evident that the $2p_{3/2}$ signal which appears at 1019 eV corresponds to Zn^{2+} ions occupying tetrahedral sites and signal around 1021 eV corresponds to octahedral site occupying Zn^{2+} ions[27]. Here we have deconvoluted the Zn $2p_{3/2}$ signal into two peaks corresponding to Zn^{2+} ions occupying octahedral and tetrahedral sites as shown in **Figure 6.9b**. In the case of Ti, Ti^{4+} has a single peak centred at 458.3 which belongs to Ti $2p_{3/2}$ state of octahedral coordination as in **Figure 6.9c**[25].

Also, the Fe $2p_{3/2}$ peak of TZF-0.2 is observed at 709.8 eV and the Fe $2p_{1/2}$ peak is observed at 723.3 eV respectively[25]. The presence of a satellite peak at 718.6 eV confirmed the oxidation state of Fe as +3[28, 29]. Apart from this, due to spin-orbital and electrostatic interactions present in high spin early transition metal ions, each of the Fe $2p_{3/2}$ and $2p_{1/2}$ peaks can be deconvoluted into four peaks as shown in **Figure 6.9d**[30, 31]. The fitting of Fe 2p XPS into four multiplets further ensured the presence of Fe^{3+} ions in octahedral sites[31, 32]. Thus, the XPS measurements are found to be in exact agreement with Rietveld refinement data and expected stoichiometries.
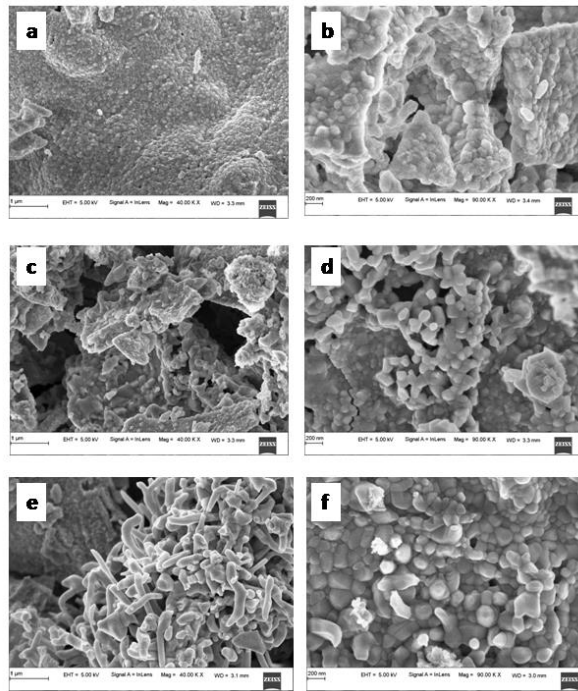
6.2.3 FE-SEM

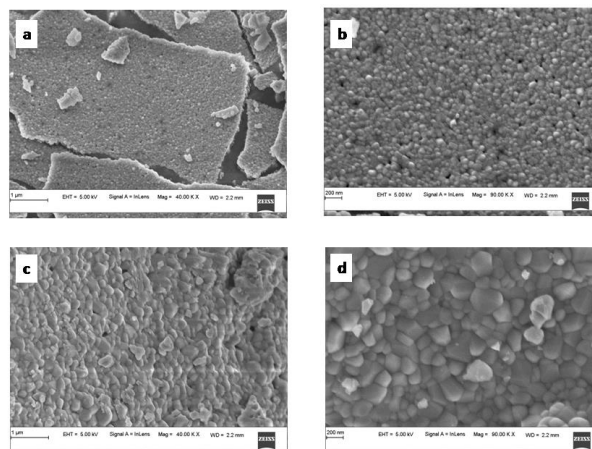**Figure 6.10** – FE-SEM images of a,b) TZ c,d) TZC-0.2 and e,f) TZC-0.4 samples

Figure 6.11 – FE-SEM images of a,b) TZF-0.2 and c,d) TZC-0.4 samples

The SEM micrographs of TZ, TZC-0.2 and TZC-0.4 are given in **Figure 6.10**. The SEM images show extended aggregation of particles and the aggregates are found to be in the micrometre regime. With Cu^{2+} doping, there is a variation in the shape of the aggregates. The particles are getting transformed from the spherical form into needle-like structures with an increase in Cu^{2+} dopant amount. **Figure 6.10** shows that, in the case of TZF-0.2 and TZF-0.4, the extent of aggregation is somewhat similar to that found in TZ. From **Figure 6.11**, TZF-0.2 is found to have flake-like aggregates which are smaller than that of TZF-0.4. The increment in the size of the aggregates results in a reduction in NIR reflectance[33].

6.2.4 UV-Visible Diffuse Reflectance Studies
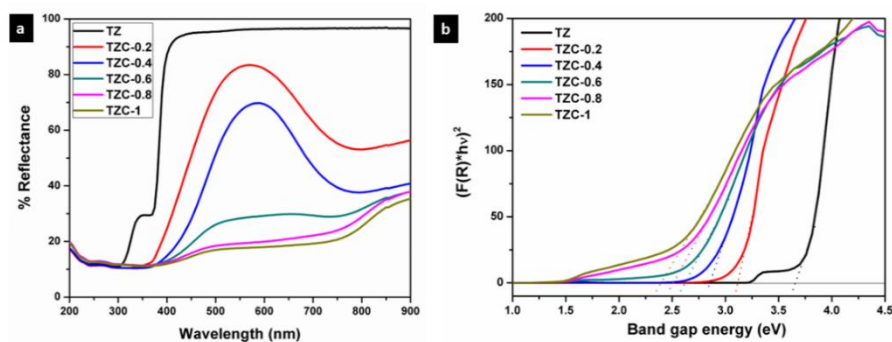
Figure 6.12 – a) UV-Visible diffuse reflectance spectra and b) Kubelka Munk plots of Cu^{2+} doped $TiZn_2O_4$ pigments

The UV-Visible diffuse reflectance spectra of Cu^{2+} doped $TiZn_2O_4$ pigment powders are given in **Figure 6.12a**. Here we can see that the undoped $TiZn_2O_4$, i.e. TZ shows no characteristic absorption in the visible region and as a result, it appears white. With the incorporation of Cu^{2+} ions into the $TiZn_2O_4$ lattice, a gradual shift of the absorption edges towards the higher wavelength is seen. This

bathochromic shift can be explained by the bandgap measurements made using the Kubelka-Munk function. The bandgaps of all the developed Cu^{2+} doped $TiZn_2O_4$ compositions are given in **Table 6.8**. From **Figure 6.12b**, the gradual decrease in bandgaps which is responsible for the bathochromic shift is evident. All the Cu^{2+} doped variants exhibited absorptions in the visible region. The absorption in the region 740-800 nm can be attributed to the ^2E_g -$^2T_{2g}$ transition in a d^9 octahedral system[34].
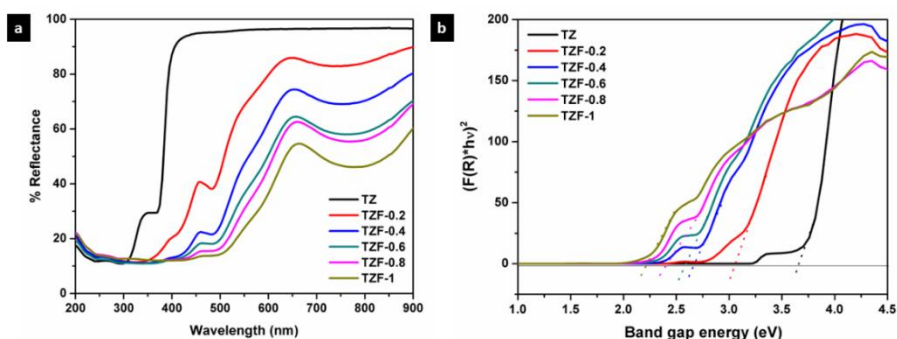
Figure 6.13 – a) UV-Visible diffuse reflectance spectra and b) Kubelka Munk plots of Fe^{3+} doped $TiZn_2O_4$ pigments

One such absorption centred around 800 nm helps in imparting a green tint to TZC-0.2. At the same time, for TZC-0.4, the absorption is around 780 nm which accounts for its yellow colour. Upon increasing the Cu^{2+} ion concentration, the absorption band gets broader and extends all over the visible region. Thus, the compositions got darker on increasing the Cu^{2+} concentration.

In the case of Fe^{3+} doped $TiZn_2O_4$ pigment powders, the observed changes in the diffuse reflectance spectra are shown in **Figure 6.13a**. TZ which has no significant absorption in the visible region gradually shows absorptions within 350 and 900 nm with the

introduction of Fe^{3+} into the $TiZn_2O_4$ structure. The changes in optical properties for TZF-0.2, TZF-0.4, TZF-0.6, TZF-0.8 and TZF-1 are due to the incorporation of Fe^{3+} into the octahedral sites of $TiZn_2O_4$ lattice as confirmed by the XRD refinement studies. Among the absorptions shown by Fe^{3+} doped $TiZn_2O_4$, the one around 380 nm can be attributed to $^6A_1(^6S) \rightarrow {}^4E(^4D)$ transition[34]. Again the absorptions around 430 and 470 nm are due to the $^6A_1(^6S) \rightarrow {}^4E$ $(^4G)$and $^6A_1(^6S) \rightarrow {}^4A_1(^4G)$ transitions. The Fe^{3+} doped samples show a significant reduction in reflectance around 650 and 800 nm, which results from $^6A_1(^6S) \rightarrow {}^4T_2(^4G)$ and $^6A_1(^6S) \rightarrow {}^4T_1(^4G)$ bands[34, 35]. With an increase in Fe^{3+} dopant concentration, the $^6A_1(^6S) \rightarrow {}^4T_2(^4G)$ and $^6A_1(^6S) \rightarrow {}^4T_1(^4G)$ bands get more superior and the absorption becomes broader and extends over the range of 500-900 nm. The extension of the absorption edges towards higher wavelengths due to the gradual decrease in bandgap with an increase in dopant Fe^{3+} ion concentration is shown in **Figure 6.13b**. The calculated bandgap values are given in **Table 6.9**. Here we can see that TZF-0.2 shows a light yellowish-orange colour which gradually transforms into orange and brownish-orange as we move along the series. The yellowish-orange colour in TZF-0.2 arises due to the absorption of visible light in the violet-indigo region and TZF-0.2 appears in the complementary yellowish-orange colour. In the case of TZF-0.4, the absorption extends towards the violet-blue region and a corresponding increase in orange hue is observed. As we move from TZF-0.4 to TZF-1 i.e. with an increasing concentration of Fe^{3+} ions in $TiZn_2O_4$, the absorptions are found to be in the blue-green region. The extension of visible light absorption towards the green region manifests as an increase in the orange colour intensity.
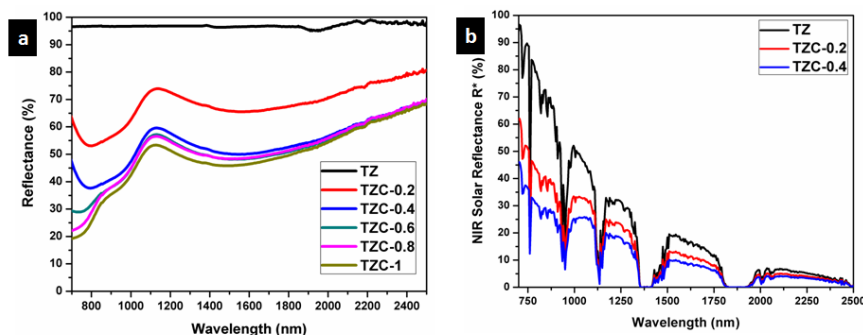
6.2.5 Near-Infrared Reflectance Analysis

Figure 6.14 – a) NIR reflectance spectra of Cu^{2+} doped $TiZn_2O_4$ pigment powders and b) solar reflectance spectra of TZ, TZC-0.2 and TZC-0.4 samples

The NIR reflectance in the range 700-2500 nm, for the Cu^{2+} doped $TiZn_2O_4$ samples, is given in **Figure 6.14** along with solar reflectance spectra for TZ, TZC-0.2 and TZC-0.4. Pure $TiZn_2O_4$ (TZ) shows a solar reflectance of 96.76 % in the NIR region. Compared to TZ, the NIR reflection is less for Cu^{2+} doped $TiZn_2O_4$ compositions. Percentage NIR reflectance decreases with an increase in the amount of Cu^{2+} ions. Even though there is a reduction in reflectance along with the Cu^{2+} doped series, TZC-0.2 and TZC-0.4 exhibited attractive colours along with considerable solar reflectance values. The NIR reflectance R^* values for the developed Cu^{2+} incorporated $TiZn_2O_4$ pigment samples along with $BiPO_4$, an already reported yellow pigment are given in **Table 6.8**[36].

The NIR reflectance of Fe^{3+} doped $TiZn_2O_4$ samples was also determined. The NIR reflectance spectra of the Fe^{3+} incorporated pigment series are given in **Figure 6.15**.
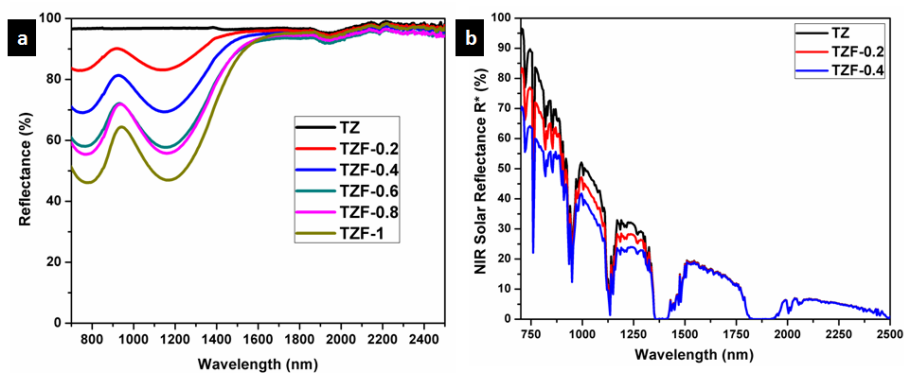
Figure 6.15 – a) NIR reflectance spectra of Fe^{3+} doped $TiZn_2O_4$ pigment powders and b) solar reflectance spectra of TZ, TZF-0.2 and TZF-0.4 samples

The percentage of NIR reflectance R* values for Fe^{3+} doped $TiZn_2O_4$ pigments and commercial $BiVO_4$ are given in **Table 6.9**. Both TZF-0.2 and TZF-0.4 exhibited percentage NIR reflectance values higher than $BiVO_4$[37]. Compared to the percentage reflectance of TZ, there is a reduction of reflectance around the 700-1600nm region, with the substitution of Zn^{2+} ions in octahedral sites with Fe^{3+} ions. The introduction of chromophore Fe^{3+} ions into the $TiZn_2O_4$ lattice enhances the visual appearance by imparting different shades of orange colour to the samples. The observed colours ranged from yellowish-orange to reddish-brown. Despite having a reduction in solar reflectance across the Fe^{3+} doped series, TZF-0.2 and TZF-0.4 are showing promising solar reflectance values of 87.81 and 77.83 % respectively.

6.2.6 Chromatic studies

As part of analysing the chromatic characteristics of the developed pigments, the CIE Lab colour coordinates were measured. **Figure**

6.16 shows the photograph of developed $TiZn_2O_4$-based pigment powders. The CIE *L*a*b** parameters of TZ and Cu^{2+} doped compositions along with $BiPO_4$ are listed in **Table 6.8**.

With the incorporation of Cu^{2+} chromophore, there is a decrease in lightness coordinate, *L**. At the same time, there is an initial reduction in *a** value due to the green tint attributed to the Cu^{2+} doping in TZC-0.2, which becomes less negative with a further increase in the Cu^{2+} dopant amount. The increase in yellowish hue from TZ to TZC-0.4 is evident from the rise in *b** values. The *b** values start decreasing from TZC-0.6 onwards. The lightness coordinate *L** also shows a reduction in values, with an increase in Cu^{2+} chromophore concentration. Even though inferior to $BiPO_4$ in NIR reflectance, TZC-0.2 and TZC-0.4 exhibited superior yellow hues compared to $BiPO_4$[36]. The CIE lab coordinates for Fe^{3+} doped compositions are given in **Table 6.9** along with commercial $BiVO_4$. Here also a reduction in lightness coordinates with an increase in Fe^{3+} content was observed. Again, as the dopant Fe^{3+} concentration increases, the orange tint was found to be increasing which manifests as an increment in *a** and *b** coordinates.
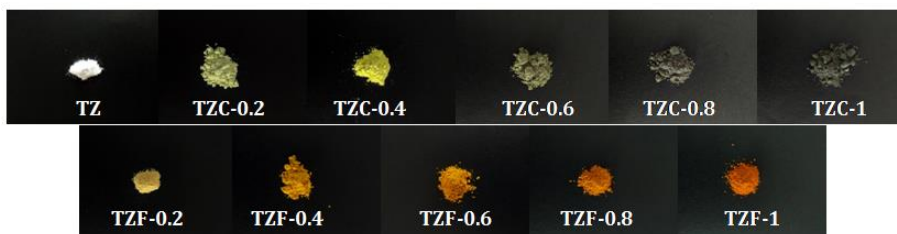
Figure 6.16- Photographs of developed $TiZn_2O_4$-based pigment powders.

Table 6.8 - Bandgap, Percentage NIR Reflectance and CIE *L*a*b** parameters of pure and Cu^{2+} doped $TiZn_2O_4$ compositions

	Band gap (eV)	**NIR reflectance** (R*)	*L**	*a**	*b**	**c**	**hᵒ**
TZ	3.54	96.76 %	98.41	-0.05	0.99	0.99	92.89
TZC-0.2	3.12	62.83 %	91.12	-7.50	24.18	25.32	107.23
TZC-0.4	2.93	47.61 %	82.92	-5.48	36.41	36.82	98.56
TZC-0.6	2.65	43.19 %	59.61	-2.44	14.13	14.34	99.79
TZC-0.8	2.51	41.90 %	50.88	-0.66	7.04	7.07	95.36
TZC-1	2.39	39.13 %	48.84	-1.08	6.28	6.37	99.76
BiPO₄*	3.657	86.40 %	96.85	-0.27	0.64	0.69	112.87

Table 6.9 - Bandgap, Percentage NIR Reflectance and CIE *L*a*b** parameters of pure and Fe^{3+} doped $TiZn_2O_4$ compositions

	Band gap (eV)	**NIR reflectance** (R*)	*L**	*a**	*b**	**c**	**h°**
TZ	3.54	96.76 %	98.41	-0.05	0.99	0.99	92.89
TZF-0.2	3.07	87.81 %	84.81	6.92	31.72	32.47	77.693
TZF-0.4	2.69	77.83 %	73.70	14.49	37.78	40.46	69.016
TZF-0.6	2.57	68.73 %	66.97	16.39	32.84	36.70	63.47
TZF-0.8	2.29	67.44 %	63.27	19.55	31.54	37.11	58.207
TZF-1	2.19	60.43 %	57.68	19.70	25.29	32.06	52.081
BiVO₄*	2.40	73.51 %	82.43	4.25	76.26	76.38	86.81

The TZF series exhibited an enhanced red hue represented by the rise in *a** coordinate with an increase in Fe^{3+} doping. The *b** values clearly show that the yellow hue increases from TZ to TZF-0.4 and then starts diminishing. Fe^{3+} doped variants managed to retain attractive orange to brownish-orange shades even with increased dopant concentrations. The TZF-0.2 and TZF-0.4 managed to exhibit considerable yellow hues even without the use of hazardous elements. Even though commercial $BiVO_4$ exhibited superior yellow colour, TZF-0.2 and TZF-0.4 compositions have higher NIR reflectance and more economic viability[37].
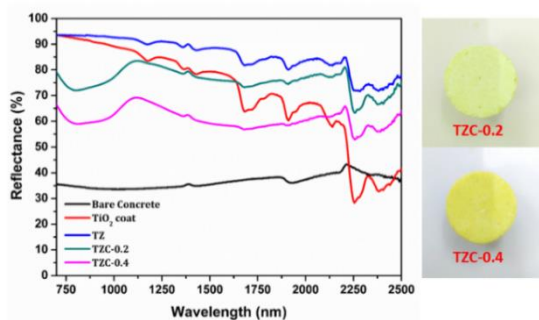
6.2.7 Coating studies

Figure 6.17 – NIR reflectance spectra of coated TZ, TZC-0.2 and TZC-0.4 in comparison with TiO_2 and bare concrete coatings.

The NIR reflectance values were calculated for the selected pigment coatings over concrete and Al sheet substrates. **Figure 6.17** shows the NIR reflectance spectra of TZ, TZC-0.2 and TZC-0.4 coatings over concrete in comparison with bare concrete and TiO_2 coating. **Figure 6.18** shows the NIR reflectance spectra of TZ, TZF-0.2 and TZF-0.4 pigment coatings on concrete along with bare concrete and TiO_2 coatings. The NIR reflectance R* values calculated according to the ASTM model for the

selected pigment coatings are listed in **Table 6.10** along with their CIE *L*a*b** coordinates.
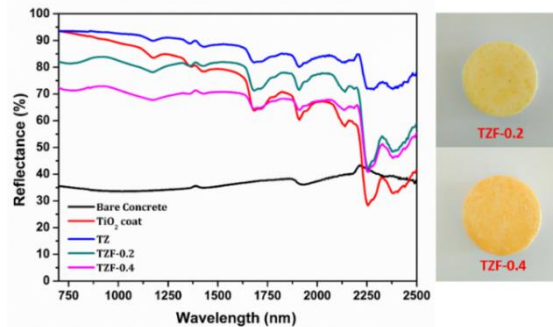

Figure 6.18 – NIR reflectance spectra of coated TZ, TZF-0.2 and TZF-0.4 in comparison with TiO$_2$ and bare concrete coatings.

Table 6.10 – Percentage NIR reflectance, R* values and CIE L*a*b* coordinates for the selected pigment coatings over concrete

Sample	R*	L*	a*	b*
Concrete	34.94 %	61.911	0.055	3.952
TiO$_2$ coat	85.17 %	97.686	-0.221	0.473
TZ	89.31 %	96.532	0.006	4.085
TZC-0.2	76.28 %	95.283	-4.067	11.812
TZC-0.4	61.91 %	88.809	-3.294	14.894
TZF-0.2	79.38 %	85.127	4.797	18.588
TZF-0.4	69.26 %	85.768	4.98	26.445

Figure 6.19 shows the NIR reflectance spectra of TZ, TZC-0.2 and TZC-0.4 coatings over Al sheet in comparison with bare Al sheet and TiO$_2$ coating. **Figure 6.20** shows the NIR reflectance spectra of TZ, TZF-0.2 and TZF-0.4 pigment coatings on the Al sheet. The NIR reflectance, R* values calculated according to the ASTM model for the selected pigment coatings over the Al sheet are listed in **Table 6.11** along with their CIE *L*a*b**coordinates.
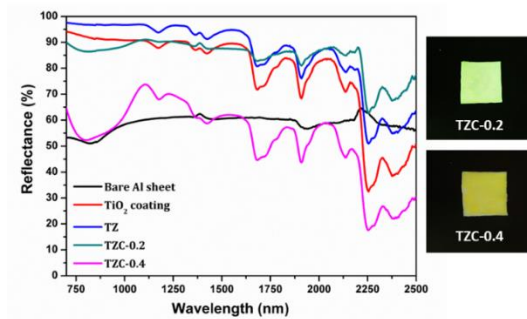
Figure 6.19 – NIR reflectance spectra of coated TZ, TZC-0.2 and TZC-0.4 in comparison with TiO$_2$ coating and bare Al sheet.
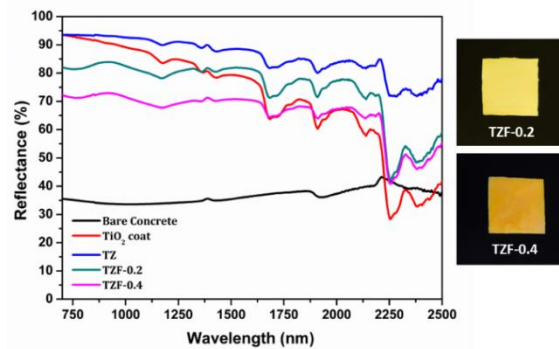

Figure 6.20 – NIR reflectance spectra of coated TZ, TZF-0.2 and TZF-0.4 in comparison with TiO$_2$ coating and bare Al sheet.

Table 6.11 – Percentage NIR reflectance, R* values and CIE L*a*b* coordinates for the selected pigment coatings over the Al sheet

Sample	R*	L*	a*	b*
Bare Al sheet	56.65 %	78.329	-0.12	0.995
TiO$_2$ coating	88.56 %	98.426	-0.443	0.59
TZ	94.20 %	99.285	-0.19	0.461
TZC-0.2	87.53 %	96.956	-1.279	4.76
TZC-0.4	58.65 %	91.099	-4.127	25.043
TZF-0.2	90.59 %	95.427	1.07	7.784
TZF-0.4	74.57 %	77.834	13.869	42.26

6.2.8 Thermal shielding studies

Thermal shielding performance of two of the best pigment compositions, i.e., TZC-0.2 and TZF-0.2 were evaluated. As described in the experimental section, foam boxes roofed with coated and uncoated Al sheets were placed under an IR lamp (40 cm above the roof) and separate temperature sensors were inserted into the foam boxes to monitor the interior temperature. To evaluate the thermal shielding performance, time-dependent temperature measurements were made for 1 hour. We have carried out the thermal shielding analysis for TZC-0.2 and TZF-0.2 separately and compared it with that of uncoated Al sheet roofing. The time-dependent temperature measurements made for TZC-0.2 and TZF-0.2 coated roofs along with bare Al sheets are shown in Figure 6.21.
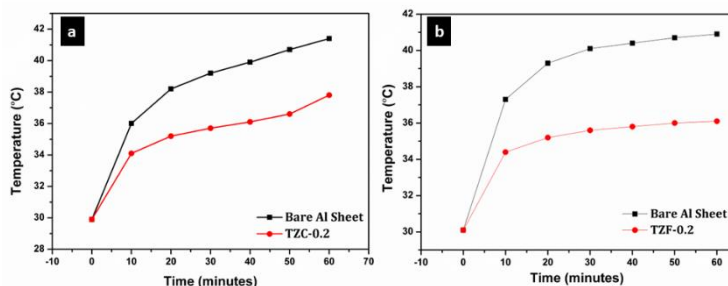
Figure 6.21 – Time-dependent temperature measurements obtained for a) TZC-0.2 and b) TZF-0.2 coated Al sheet roofing along with bare Al sheet.

The time-temperature plots indicate a steady increase in temperature with time initially and then gradually stabilized over 1 hour. **Figure 6.22a and b** show the difference in interior temperatures observed after 1 hour of IR irradiation for the TZC-0.2 and TZF-0.2 coated and uncoated Al roofing. TZC-0.2 coating provided an interior 3.6 °C cooler than the uncoated roofing interior temperature. In the case of TZF-0.2, the

observed temperature difference was 4.8 °C. Thus, the overall results suggest that TZC-0.2 and TZF-0.2 are promising cool pigment candidates with good NIR reflectance characteristics.

Figure 6.22 – Difference in interior temperatures observed after thermal shielding studies using **a)** TZC-0.2 and **b)** TZF-0.2 coated Al sheet roofing in comparison with bare Al sheet roofing.
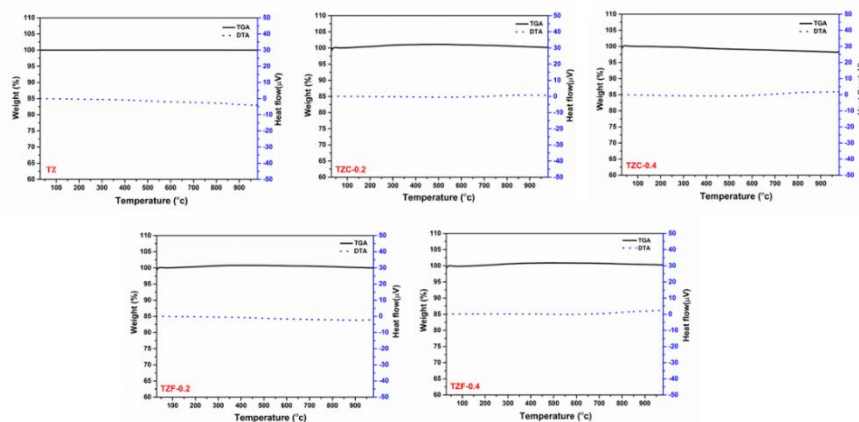
6.2.9 Thermal stability studies

Figure 6.23 – TGA and DTA curves of TZ, TZC-0.2, TZC-0.4, TZF-0.2 and TZF-0.4 pigment powders

The thermal stability of the developed pigments was studied using thermogravimetric analysis. The thermogravimetric analysis of TZ, TZC-

0.2, TZC-0.4, TZF-0.2 and TZF-0.4 was carried out in presence of air in the temperature range of 30-1000 °C. TGA and DTA results, given in **Figure 6.23** show that the developed pigment compositions exhibit high thermal stability, even above 900 °C. There is no significant weight loss observed or no phase changes in the temperature range of 30-1000 °C. High thermal stability is an essential requirement for NIR-reflecting pigments. So, these compositions can be considered promising pigment candidates.

6.2.10 Chemical stability studies

The chemical stability of the developed pigments towards acid and alkaline environments was evaluated by treating them with 5 % HNO_3 and 5 % NaOH solutions. The resistance of the selected pigment compositions towards chemically aggressive environments was studied by weighing out 0.5 g of pigment and then treating it with acid/alkaline solutions accompanied by constant stirring. After 30 minutes, the pigment samples were collected by centrifugation, washed and dried. The dried powders were then subjected to chromatic studies to measure their CIE *L*a*b** coordinates. The NIR reflectance of the pigments was also measured after the acid/alkali treatment. The obtained CIE *L*a*b**coordinates are listed in **Table 6.12** along with the colour difference ΔE* calculated. XRD analysis of three selected pigment compositions was also carried out after chemical treatment. The XRD patterns obtained can be indexed to the cubic $TiZn_2O_4$ phase and are exactly in agreement with the XRD patterns of untreated samples (**Figure 6.24**). Even after acid/alkali treatment, the pigments have retained their colour characteristics and NIR reflectance without significant changes. Thus, the developed $TiZn_2O_4$-based compositions are found to be resistant to harsh chemical environments, which makes them suitable for commercial application.

Table 6.12 - CIE *L*a*b** coordinates, colour difference ΔE* and percentage NIR reflectance obtained after acid/alkali treatment of the developed pigment samples.

| Sample	Untreated				HNO$_3$					NaOH				
	R*	L*	a*	b*	R*	L*	a*	b*	(ΔE*)	R*	L*	a*	b*	(ΔE*)
TZ	96.76 %	98.41	-0.05	0.99	96.8 %	98.51	-0.22	1.26	0.33	95.63 %	97.03	0.33	2.72	2.24
TZC-0.2	62.83 %	91.12	-7.50	24.18	62.02 %	90.87	-7.48	24.27	0.27	61.25 %	90.59	-7.32	26.25	2.14
TZC-0.4	47.61 %	82.92	-5.48	36.41	47.34 %	83.02	-5.41	36.63	0.25	46.32 %	82.94	-4.65	36.92	0.98
TZF-0.2	87.81 %	84.81	6.92	31.72	86.82 %	84.90	6.56	30.88	0.93	83.73 %	83.20	7.43	31.99	1.71
TZF-0.4	77.83 %	73.70	14.49	37.78	77.25 %	72.93	15.09	38.15	1.05	76.45 %	72.76	14.92	37.36	1.12
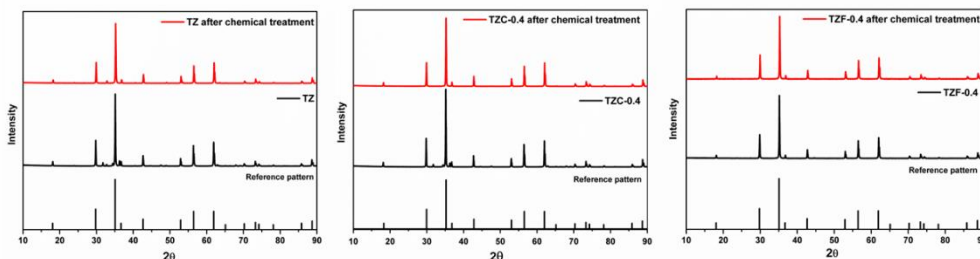
Figure 6.24 - XRD patterns of TZ, TZC-0.4 and TZF-0.4 after chemical treatment, given in comparison with XRD patterns of reference and untreated samples.

6.3 Conclusion

Here $TiZn_2O_4$-based NIR reflecting inorganic pigments which are economically affordable and eco-friendly were developed through citric acid fuel-assisted solution combustion strategy. Optical properties of the inverse spinel structured $TiZn_2O_4$ lattice were modified with the incorporation of Cu^{2+} and Fe^{3+} ions as chromophores capable of imparting attractive hues and reducing band gaps. The replacement of octahedral Zn^{2+} ions by Cu^{2+} and Fe^{3+} ions in varying amounts resulted in a series of pigment colours ranging from greenish-yellow to reddish-brown. The resulting crystal structures were characterised well and site allocations and lattice changes were understood in detail with the help of Rietveld refinement of XRD patterns. Four among the ten developed compositions were selected for application as possible NIR reflecting pigments. They exhibited percentage NIR reflectance ranging from 47.61 to 87.81 % and showed very high thermal and chemical stability. Pure $TiZn_2O_4$ showed a very high NIR reflectance of 96.76 % which is comparable with commercial TiO_2 pigments. The thermal shielding studies conducted using two of the selected pigment candidates showed a reduction in

interior temperature by 3.6 °C for Cu^{2+} doped $TiZn_2O_4$ and 4.8 °C for Fe^{3+} doped $TiZn_2O_4$ coated roofing relative to uncoated roofed interiors. Thus Cu^{2+} and Fe^{3+} doped $TiZn_2O_4$ pigments can ensure better thermal conditioning of buildings with zero cost to the environment. Apart from tackling the urban heat island effect, these pigments have the capability for energy conservation over the long term. Further modifications of the $TiZn_2O_4$ lattice with suitable dopants and synthetic strategies may result in pigments with enhanced optical and solar reflectance properties.

6.4 References

1. Pfaff, G., *Inorganic pigments*. 2017: de Gruyter.
2. Speight, J.G., *Chapter Three - Industrial Inorganic Chemistry*, in *Environmental Inorganic Chemistry for Engineers*, J.G. Speight, Editor. 2017, Butterworth-Heinemann. p. 111-169.
3. Gramm, G., et al., *Environmentally benign inorganic red pigments based on tetragonal β-Bi2O3.* Dyes and Pigments, 2019. **160**: p. 9-15.
4. Divya, S. and S. Das, *New red pigments based on Li3AlMnO5 for NIR reflective cool coatings.* Ceramics International, 2021. **47**(21): p. 30381-30390.
5. Kato, M., et al., *Synthesis of reddish pink pigment by addition of Mg2+ into (Al, Cr) 2O3 corundum.* Journal of the Ceramic Society of Japan, 1999. **107**(1242): p. 181-183.
6. Wang, J.-L., et al., *Synthesis and characterization of NiTiO3 yellow nano pigment with high solar radiation reflection efficiency.* Powder technology, 2013. **235**: p. 303-306.
7. Eroles, A. and A. Friedberg, *Color and structural character of CdS-CdSe pigments.* Journal of the American Ceramic Society, 1965. **48**(5): p. 223-227.
8. Heck, M., T. Rehren, and P. Hoffmann, *The production of lead–tin yellow at Merovingian Schleitheim (Switzerland).* Archaeometry, 2003. **45**(1): p. 33-44.
9. Wanrooij, P., et al., *Extraction of CdS pigment from waste polyethylene.* Journal of applied polymer science, 2006. **100**(2): p. 1024-1031.
10. White, K., et al., *An investigation of lead chromate (crocoite-PbCrO4) and other inorganic pigments in aged traffic paint samples from Hamilton, Ohio: implications for lead in the environment.* Environmental Earth Sciences, 2014. **71**(8): p. 3517-3528.

11. Liu, H., et al., *Sunlight mediated cadmium release from colored microplastics containing cadmium pigment in aqueous phase.* Environmental Pollution, 2020. **263**: p. 114484.

12. Jansen, M. and H.P. Letschert, *Inorganic yellow-red pigments without toxic metals.* Nature, 2000. **404**(6781): p. 980-982.

13. Coccato, A., L. Moens, and P. Vandenabeele, *On the stability of mediaeval inorganic pigments: a literature review of the effect of climate, material selection, biological activity, analysis and conservation treatments.* Heritage Science, 2017. **5**(1): p. 1-25.

14. Jose, S., et al., *Recent advances in infrared reflective inorganic pigments.* Solar Energy Materials and Solar Cells, 2019. **194**: p. 7-27.

15. Thejus, P.K., K.V. Krishnapriya, and K.G. Nishanth, *A cost-effective intense blue colour inorganic pigment for multifunctional cool roof and anticorrosive coatings.* Solar Energy Materials and Solar Cells, 2021. **219**: p. 110778.

16. Sarkodie, B., et al., *Characteristics of pigments, modification, and their functionalities.* Color Research & Application, 2019. **44**(3): p. 396-410.

17. Noaa, N., *State of the climate: Global climate report for annual 2018.* URL www. ncdc. noaa. gov/sotc/global/201813, 2019.

18. Akbari, H., et al., *Cool color roofing materials.* California Energy Commission PIER Program; Heat Island Group, Lawrence Berkeley National Laboratory: Berkeley, CA, USA, 2006.

19. Synnefa, A., M. Santamouris, and K. Apostolakis, *On the development, optical properties and thermal performance of cool colored coatings for the urban environment.* Solar energy, 2007. **81**(4): p. 488-497.

20. Sharma, R., S. Tiwari, and S.K. Tiwari, *Highly reflective nanostructured titania shell: a sustainable pigment for cool coatings.* ACS Sustainable Chemistry & Engineering, 2018. **6**(2): p. 2004-2010.

21. Millard, R.L., R.C. Peterson, and B.K. Hunter, *Study of the cubic to tetragonal transition in Mg2TiO4 and Zn2TiO4 spinels by 17O MAS NMR and Rietveld refinement of X-ray diffraction data.* American Mineralogist, 1995. **80**(9-10): p. 885-896.

22. Souza, S., et al., *Influence of pH on iron doped Zn 2 TiO 4 pigments.* Journal of Thermal Analysis and Calorimetry, 2005. **79**(2): p. 451-454.

23. Lu, X., et al., *Influence of inverse spinel structured CuGa2O4 on microwave dielectric properties of normal spinel ZnGa2O4 ceramics.* Journal of the American Ceramic Society, 2018. **101**(4): p. 1646-1654.

24. Burdett, J.K., G.D. Price, and S.L. Price, *Role of the crystal-field theory in determining the structures of spinels.* Journal of the American Chemical Society, 1982. **104**(1): p. 92-95.

25. Arillo, M., et al., *Surface characterisation of spinels with Ti (IV) distributed in tetrahedral and octahedral sites.* Journal of alloys and compounds, 2001. **317**: p. 160-163.

26. Vinuthna, C., et al., *Characterization of Co1–XZnxFe2O4 nano spinal ferrites prepared by citrate precursor method.* Int. J. Eng. Res. Appl., 2013. **3**: p. 654-660.

27. Steinike, U., et al., *Formation and surface structure of Ti–Zn-double oxides and Zn ferrite.* Chemical Papers, 1998. **52**(3): p. 147-151.

28. Dhankhar, S., et al., *Anomalous room temperature magnetoresistance in brownmillerite Ca 2 Fe 2 O 5.* RSC Advances, 2015. **5**(112): p. 92549-92553.

29. Liu, J., M. Zeng, and R. Yu, *Surfactant-free synthesis of octahedral ZnO/ZnFe2O4 heterostructure with ultrahigh and selective adsorption capacity of malachite green.* Scientific reports, 2016. **6**(1): p. 1-10.

30. Aghavnian, T., et al., *Determination of the cation site distribution of the spinel in multiferroic CoFe2O4/BaTiO3 layers by X-ray photoelectron spectroscopy.* Journal of Electron Spectroscopy and Related Phenomena, 2015. **202**: p. 16-21.

31. Gupta, R. and S. Sen, *Calculation of multiplet structure of core p-vacancy levels.* Physical Review B, 1974. **10**(1): p. 71.

32. McIntyre, N. and D. Zetaruk, *X-ray photoelectron spectroscopic studies of iron oxides.* Analytical Chemistry, 1977. **49**(11): p. 1521-1529.

33. Peoples, J., et al., *A strategy of hierarchical particle sizes in nanoparticle composite for enhancing solar reflection.* International Journal of Heat and Mass Transfer, 2019. **131**: p. 487-494.

34. Reddy, S.L., T. Endo, and G.S. Reddy, *Electronic (absorption) spectra of 3d transition metal complexes.* Advanced aspects of spectroscopy, 2012: p. 4-48.

35. Granone, L.I., et al., *Effect of the degree of inversion on the photoelectrochemical activity of spinel ZnFe2O4.* Catalysts, 2019. **9**(5): p. 434.

36. Ding, C., et al., *Hydrothermal synthesis and characterization of novel yellow pigments based on V 5+ doped BiPO 4 with high near-infrared reflectance.* RSC advances, 2018. **8**(35): p. 19690-19700.

37. Thejus, P. and K. Nishanth, *Rational approach to synthesis low-cost BiVO4–ZnO complex inorganic pigment for energy efficient buildings.* Solar Energy Materials and Solar Cells, 2019. **200**: p. 109999.

Chapter 7

Conclusions and Future Outlook
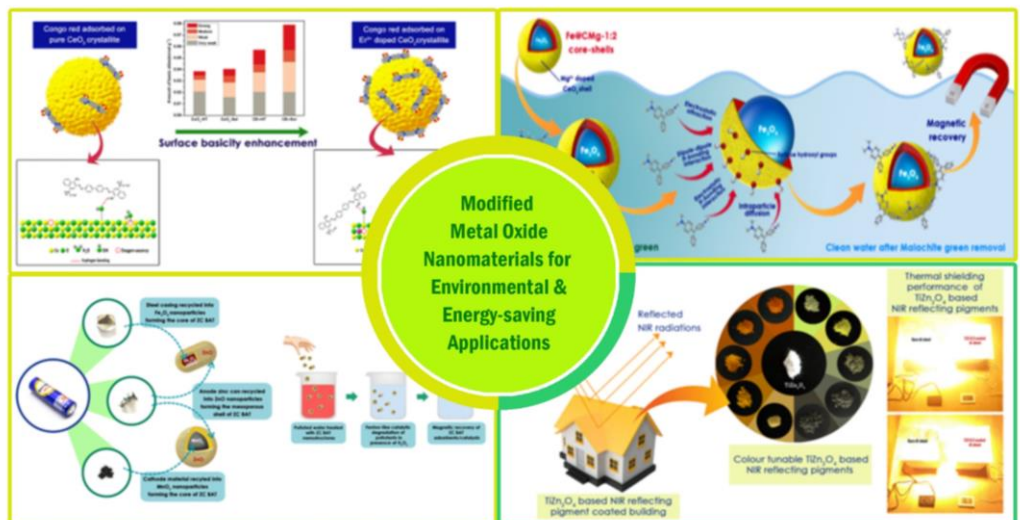
A brief summary of the entire research work is provided in this chapter, along with an outlook for the future. The highlights of the research works carried out are presented here. Future possibilities of the developed nanomaterials for sustainability were briefly discussed.

7.1 Conclusions

Metal oxide nanomaterials have immense applications in energy and environmental fields. Presently a large number of research works are undergoing for the development of efficient and affordable metal oxide nanomaterials. Various strategies such as doping, formation of nanocomposites, heterojunctions and core-shells are being employed for the fabrication of efficient, cost-effective and stable metal oxide nanomaterials. In the present thesis, we have focused mainly on two of the most significant fields of application of metal oxide nanomaterials i.e., environmental and energy-saving applications. So, the entire thesis was divided into two parts, one discussing the environmental aspects of modified metal oxide nanomaterials especially water treatment while the other part deals with the energy-saving aspects related to NIR reflecting inorganic pigments. The entire thesis was formulated according to the sustainable development goals adopted by the United Nations. The present thesis addresses sustainable development goals six and seven among the 17 goals. While goal six aims for clean water and sanitation, goal seven emphasizes affordable and clean energy. The division of the thesis into two sections can also be seen in terms of sustainable development goals 6 and 7. Under the environmental objective of the present work, comes the development of modified metal oxide nanomaterials for water treatment application. Wastewater treatment by utilizing the adsorption and Fenton-like catalytic activity of various metal oxide nanomaterials and their modifications were mainly investigated. The second part of the thesis, i.e. the energy saving objective discusses in detail the development of NIR reflecting pigments based on Cu^{2+} and Fe^{3+} substituted $TiZn_2O_4$ compositions. These cool pigments are capable of

providing cooler interiors and thereby reducing the energy spent on cooling purposes.

This thesis has seven chapters. Chapter 1 gives a brief introduction to sustainable development and discusses in detail the measures adopted for achieving sustainability. Chapter 1 also discusses in brief about nanomaterials and their properties. Environmental and energy applications of nanomaterials were reviewed in detail. The use of nanomaterials for water treatment applications was explored in the literature. The literature survey was carried out and presented with special emphasis on adsorbents and Fenton-like catalysts. The significance of modified metal oxide-based adsorbents and Fenton-like catalysts was well established. Energy applications of nanomaterials were also incorporated and remarkable research outputs were highlighted. Out of the various energy-related applications of nanomaterials, the energy-saving aspect of NIR reflecting cool pigments was described in detail. A literature survey of NIR reflecting inorganic pigments with remarkable solar reflectance and colour characteristics was carried out and was incorporated within this chapter. Chapter 1 provides us with the ways of employing nanomaterials to achieve sustainable development by focusing on two of the vital aspects of sustainability i.e., environmental remediation and energy conservation.

Chapter 2 gives an account of the materials and experimental procedures used during the present studies.

Chapters 3, 4 and 5 come under the environmental objective of the research work. Chapter 3 reports the synthesis of surface basicity-enhanced CeO_2 adsorbents by sol-gel and sol-hydrothermal methods for

water treatment. The surface basicity enhancement was achieved by doping Er^{3+} ions into the CeO_2 lattice. The enhancement in surface basicity was evaluated by CO_2-TPD studies and correlated to Er^{3+} doping. The rapid and selective adsorption of Congo red by modified CeO_2 was investigated and an adsorption mechanism was proposed with hydrogen bonding as the major factor controlling the adsorption process. Here increase in surface basicity results in a greater extent of hydrogen bonding which in turn is responsible for the rapid and selective adsorption of Congo red over mesoporous Er^{3+} doped CeO_2. Thus, the use of surface-active sites as a tool for regulating the selectivity and efficiency of an adsorbent material is well established in this chapter.

Chapter 4 deals with the development of a novel adsorbent material capable of efficient selective adsorption and magnetic recovery. The developed core-shell nanostructure was composed of Fe_3O_4 cores encapsulated within a shell of mesoporous Mg^{2+} doped CeO_2. The selectivity of the developed Fe@CMg-1:2 core-shells towards malachite green was investigated in detail. The mechanism and nature of the adsorption were evaluated with the help of five different adsorption isotherm models. Adsorption kinetic studies were also carried out and a mechanism for the selective adsorption of malachite green was proposed. Thus Fe@CMg-1:2 core-shells are found to be highly efficient, cost-effective, selective, stable, reusable and magnetically retrievable adsorbent materials for the removal of hazardous malachite green from water. The fabricated core-shell structure can be further subjected to surface functionalization or tuning to achieve selective adsorption of various classes of pollutants.

Chapter 5 reports the recycling of spent zinc-carbon batteries into nanostructures capable of performing dual functions as adsorbents and as Fenton-like catalysts. Core-shell nanostructures with MnO_2 and Fe_3O_4 nanoparticles forming the core and mesoporous ZnO forming a shell around them were derived exclusively from disposed Zinc-carbon batteries. The adsorption and Fenton-like catalytic activity of the developed nanostructures were investigated towards four different dye pollutants. Adsorption isotherms as well as adsorption kinetics were studied in addition to the kinetics of Fenton-like catalysis. The mechanisms of adsorption and Fenton-like catalytic activity of developed Zinc-carbon battery-derived nanostructures were discussed in detail. The reusability and stability of the developed adsorbent/catalysts were found suitable for practical application. Here water treatment and waste management were brought together from a circular economic perspective. As we look at the environmental objective of the thesis, we can observe a gradual evolution of the developed nanomaterials over the first three working chapters. The first working chapter dealt with the tuning of adsorption efficiency and selectivity. In the second working chapter, we developed an upgraded adsorbent material which is magnetically recoverable, selective and highly effective. The third working chapter dealt with a further evolved version of a nanomaterial capable of environmental remediation. Here besides pollutant removal ability, the developed nanomaterial exhibited pollutant degradation capability via an advanced oxidation process. Another interesting attribute was the recycling of spent zinc-carbon batteries which has also given a circular economic perspective to the research carried out.

Chapter 6 which falls under the energy-saving objective of the present thesis, reports the design and development of NIR reflecting inorganic pigments based on $TiZn_2O_4$ inverse spinels. A series of NIR reflecting inorganic pigments having colours ranging from greenish yellow to reddish brown were synthesized by substituting Cu^{2+} and Fe^{3+} ions into $TiZn_2O_4$ lattice by a citric acid-based solution combustion method. The developed pigment compositions were well characterised and structural elucidation was carried out with the help of Rietveld refinement. The synthesized series of cool pigments exhibited NIR reflectance values ranging from 47.6 to 87.8 %. The practical applicability of the developed pigment compositions was evaluated by carrying out thermal shielding and stability studies. A reduction in interior temperature by 3.6 ^oC for Cu^{2+} doped $TiZn_2O_4$ and 4.8 ^oC for Fe^{3+} doped $TiZn_2O_4$ coated roofs was obtained relative to uncoated roofed interiors during thermal shielding studies. Thus, the developed pigment compositions were found to be economically affordable, stable and high NIR reflecting in nature. Considerable energy conservation can be achieved by the coating of these cool pigments over roofs and walls. The economic affordability, stability and eco-friendliness of the developed cool pigments require special mention. The developed NIR reflecting pigments have an energy conservation advantage and the energy saving aspect in the long run can contribute to sustainable development.

7.2 Future Outlook

From the environmental perspective, the prospects of the present research work involve the design and development of environmental remediation processes which are affordable, efficient and practically applicable. The evolution of such processes requires even extensive

research on nanomaterials. Efforts should be carried out to further improve the efficiency, selectivity and reusability of the developed adsorbent materials. Affordability of the adsorbents can be further enhanced by employing cost-effective synthetic routes and modification techniques. Additional ways of tuning surface features of the adsorbent and catalyst materials should be explored. The effect of a wide range of cost-effective dopants can be investigated and efforts can be made to further improve the performance of the developed nanomaterials. Attempts should be made to overcome the limited adsorption capacity of metal oxide nanomaterials. The effectiveness of the fabricated nanomaterials towards other classes of potential pollutants such as heavy metal ions, PPCPs (Pharmaceuticals and Personal Care Products), pesticides and other hazardous organic molecules should be evaluated. The recycling of various waste materials into potential nanostructures for environmental remediation can be investigated. The fabrication of the modified metal oxide nanomaterials into commercial devices for water treatment can be considered. The future possibilities of the energy-saving objective of the present work involve the commercialization of the developed NIR reflecting pigment candidates. Synthesis of NIR reflecting pigments of more colour hues based on the $TiZn_2O_4$ inverse spinel system by the substitution of various other metal ion chromophores. Efforts should be made to further enhance the NIR reflectance of the $TiZn_2O_4$-based pigment compositions.

Publications
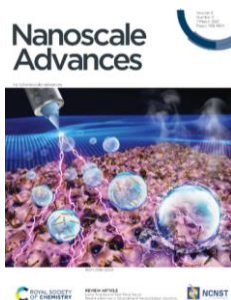
Joshy, Deepak, Seena Chakko, Yahya A. Ismail, and Pradeepan Periyat. "Surface basicity mediated rapid and selective adsorptive removal of Congo red over nanocrystalline mesoporous CeO_2." Nanoscale Advances 3, no. 23 (2021): 6704-6718.

Joshy, Deepak, Nimisha Kuruvangattu Puthenveettil, Yahya A. Ismail, and Pradeepan Periyat. "Mechanistic investigation of mesoporous Mg^{2+} doped CeO_2 encapsulated Fe_3O_4 core-shells for the selective adsorptive removal of malachite green." Results in Engineering 20 (2023): 101409.
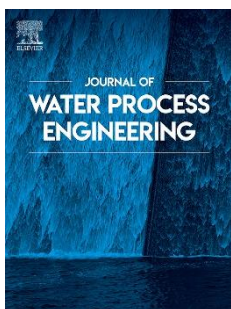
Deepak Joshy, Chamundi P. Jijil, Yahya A. Ismail, Pradeepan Periyat, "Spent zinc-carbon battery derived magnetically retrievable Fenton-like catalyst for water treatment - A circular economical approach." Journal of Water Process Engineering, 58 (2024):104812.
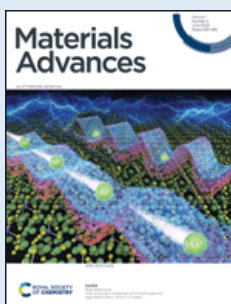
Joshy, Deepak, Chamundi P. Jijil, Sheethu Jose, Yahya A. Ismail, and Pradeepan Periyat. "Colour tunable cool pigments based on $TiZn_2O_4$ inverse spinels." Materials Advances 3, no. 16 (2022): 6584-6596.

Joshy, Deepak, Soumya B. Narendranath, Yahya A. Ismail, and Pradeepan Periyat. "Recent progress in one dimensional TiO_2 nanomaterials as photoanodes in dye-sensitized solar cells." Nanoscale Advances 4, no. 24 (2022): 5202-5232.


Kumaran, Akhila A., Ritu Gopal, Chamundi P. Jijil, **Deepak Joshy**, N. K. Hijas, Suresh Babu Adukamparai Rajukrishnan, and Renuka Neeroli Kizhakayil. "Reduced graphene oxide-5, 10, 15, 20-tetraphenylporphyrin non-covalent conjugate for interference-free Cd^{2+} monitoring in aqueous solutions." Journal of Environmental Chemical Engineering 11, no. 3 (2023): 109918.

Sreekandan, Sreelakshmi, Anjitha Thadathil, **Deepak Joshy**, Kannan Vellayan, and Pradeepan Periyat. "Synthesis of 2, 3-dihydroquinozoline-4 (1H)-Ones using magnetically retrievable nickel based nanocatalyst." Results in Engineering 15 (2022): 100552.
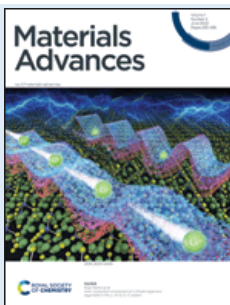
Thadathil, Anjitha, Hareesh Pradeep, **Deepak Joshy**, Yahya A. Ismail, and Pradeepan Periyat. "Polyindole and polypyrrole as a sustainable platform for environmental remediation and sensor applications." Materials Advances 3, no. 7 (2022): 2990-3022.
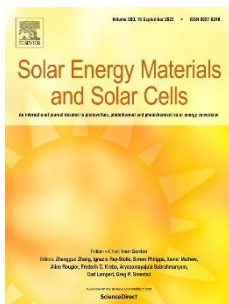
Jose, Sheethu, **Deepak Joshy**, Soumya B. Narendranath, and Pradeepan Periyat. "Recent advances in infrared reflective inorganic pigments." Solar Energy Materials and Solar Cells 194 (2019): 7-27.

Kavil, Jithesh, P. M. Anjana, **Deepak Joshy**, Ameya Babu, Govind Raj, P. Periyat, and R. B. Rakhi. "gC_3N_4/CuO and gC_3N_4/Co_3O_4 nanohybrid structures as efficient electrode materials in symmetric supercapacitors." RSC advances 9, no. 66 (2019): 38430-38437.

Jose, Sheethu, Soumya B. Narendranath, **Deepak Joshy**, N. V. Sajith, MR Prathapachandra Kurup, and Pradeepan Periyat. "Low temperature synthesis of NIR reflecting bismuth doped cerium oxide yellow nano-pigments." Materials Letters 233 (2018): 82-85.

Presentations

1. Poster presentation in International Conference "Frontiers in Chemical Sciences FCS 2022" organized by the Department of Chemistry, University of Calicut.

2. Poster presentation in International Conference on Energy & Environment ICEE 2K19 organized by T.K.M College of Arts & Science, Kollam, India.

Check for updates

Surface basicity mediated rapid and selective adsorptive removal of Congo red over nanocrystalline mesoporous CeO₂†

Deepak Joshy,[a] Seena Chakko,[a] Yahya A. Ismail [ID][a] and Pradeepan Periyat [ID] *[ab]

Herein we first report surface basicity mediated rapid and selective adsorptive removal of organic pollutants over nanocrystalline mesoporous CeO₂. The role of surface features in controlling the selectivity and efficiency of adsorption is well known. Nevertheless, the possibility of tuning the adsorption capacity and selectivity of adsorbents through their surface characteristics remains less explored. In this work, the surface basicity of mesoporous CeO₂ nanoparticles was improved by Er^{3+} doping under two different reaction conditions: via sol–gel and sol–hydrothermal methods. The nature and amount of surface basic sites were determined with the help of CO_2 temperature programmed desorption (TPD). The adsorption capacity and selectivity of four different CeO₂ samples were investigated using Congo red, methyl orange, and methylene blue as the model pollutants. From the adsorption studies, Er^{3+} doped CeO₂ synthesized by the sol–gel method, having the highest amount of surface basic sites, proved to be the most efficient and highly selective adsorbent among the four developed variants of CeO₂ towards Congo red. According to the proposed mechanism, surface basicity can be employed as a controlling parameter capable of tuning the adsorption capacity as well as the selectivity of CeO₂ towards organic pollutants.

Introduction

CeO₂ is one of the most widely employed semiconducting metal oxides in the field of catalysis and environmental remediation,[1–5] mainly due to (i) its high abundance and low cost,[6] (ii) wide band-gap, non-toxicity and high stability,[7] (iii) tendency for oxygen uptake into the lattice and the possibility of a reversible transition redox system between Ce^{3+} and Ce^{4+} (ref. 8 and 9) and (iv) the chance of formation of solid solutions with other oxides.[6] CeO₂ has already emerged as a promising choice for a wide range of catalytic processes such as a promoter in three-way catalysts in automobiles,[10,11] solid oxide fuel cells,[12,13] reforming of hydrocarbons,[14–16] water gas shift reaction,[17–19] CO oxidation,[20–22] catalytic combustion of volatile organic compounds (VOC's),[23–26] hydrogenation of alkynes,[27,28] syngas conversion to alcohols,[29] thermochemical water splitting,[30,31] photocatalysis[32–34] etc. Nevertheless, efforts to further improve its catalytic efficiency are still in progress.[35] Besides this, the environmental remediation applications of CeO₂ mainly include photocatalytic degradation[36,37] and adsorptive removal of pollutants from water resources.[38,39]

Textile and dyestuff industries are some of the major sources of water pollution, as they release dye species into water resources. The total world production of dyes is around 700 000 tonnes annually. About 10–15% of these dyes are lost during their application and a major share is discharged into water bodies. Many of these dyes have a very complex chemical structure and are found to be non-biodegradable. Studies have revealed that many of these dyes are carcinogenic and mutagenic in nature. In addition, the dyes may be present in different forms in different aqueous environments. In such cases we should be able to tune our remediation techniques according to the requirements of the target dye molecules. For example, Congo red is such a widely employed benzidine-based azo dye for various applications such as in textile, printing, plastic, rubber and dyeing industries. Due to its high water solubility, Congo red can disperse easily in water resources. Also depending on pH, Congo red is capable of being present in different ionic forms in water. Such a malign and widely distributed water pollutant should be treated individually by highly efficient means.[40–42] Adsorptive removal is one such effective way to remove organic pollutants. While developing the adsorbent material, we have focused on Congo red as our target pollutant.

The adsorption capacity and selectivity of an adsorbent depend on several factors such as high surface area, porosity,

[a]Department of Chemistry, University of Calicut, Kerala, India, 673635. E-mail: pperiyat@uoc.ac.in

[b]Department of Environmental Studies, Kannur University, Kerala, India. E-mail: pperiyat@kannuruniv.ac.in

† Electronic supplementary information (ESI) available. See DOI: 10.1039/d1na00412c

Mechanistic investigation of mesoporous Mg^{2+} doped CeO_2 encapsulated Fe_3O_4 core-shells for the selective adsorptive removal of malachite green

Deepak Joshy [a], Jijil Chamundi P [a], Nimisha Kuruvangattu Puthenveettil [a], Yahya A. Ismail [a], Pradeepan Periyat [b],[*]

[a] Department of Chemistry, University of Calicut, Kerala, 673635, India
[b] Department of Environmental Studies, Kannur University, Kerala, India

ARTICLE INFO

ABSTRACT

Economically viable, easy to operate and highly efficient techniques for water treatment are one of the basic amenities that should be provided to every individual in our society. Here we have developed $Fe_3O_4@Mg^{2+}$ doped CeO_2 core-shells by a co-precipitation route as magnetically retrievable adsorbents which are highly selective towards hazardous malachite green. The developed core-shell nanostructures were well-characterised using XRD, FE SEM, HR TEM, XPS, BET, VSM and TGA. The developed Fe@CMg-1:2 core-shells exhibited a removal efficiency of 95.1% towards Malachite green. Various parameters affecting the adsorption activity were investigated in detail. The nature, extent and mechanism of the adsorption were evaluated using various adsorption isotherm and kinetic models. Dubinin-Radushkevich (D-R), Freundlich and Temkin adsorption models were used to fit the isotherm data and the maximum adsorption capacity (q_m) was found to be 18.44 mg g^{-1} according to Dubinin-Radushkevich (D-R) model. It was found that the selective adsorption of malachite green over Fe@CMg-1:2 core-shells follows heterogeneous multilayer adsorption which obeys pseudo-second-order kinetics. The developed Fe@CMg-1:2 core-shells also exhibited high thermal stability and reusability. Fe@CMg-1:2 core-shells retained 82.4% removal efficiency even after four successive reusability cycles. Easy separation, high selectivity and cost-effectiveness are the highlights of the developed mesoporous Mg^{2+} doped CeO_2 encapsulated Fe_3O_4 core-shell structures.

1. Introduction

Industrialization and the growing global population have caused a wide variety of social, economic and environmental effects. Among them, the one that requires the highest priority is environmental issues caused by the changing global trends. Water pollution is a serious environmental scenario, the world is facing nowadays. The unavailability of clean water sources and the lack of efficient and cost-effective methods for water purification are always topics of serious concern. Industrial and agricultural activities released a wide variety of pollutants into water in significant quantities [1,2]. The major category among those released pollutants is dyes expelled from various sources such as textile, leather, food processing and plastic industries [3–6]. The unchecked release of these dyes into water sources without proper treatment can cause severe problems to aquatic life as well as to humans [7–9]. The released dyes are of different types having different chemical structures and properties falling under different categories such as

cationic, anionic, azo, acidic and basic dyes [10]. Malachite green is a cationic basic dye widely employed in food processing and pharmaceutical industries [11]. Malachite green is directly employed as a dye over a broad variety of substrates such as cotton, silk, leather, plastic, wood and paper [12]. Malachite green when present in quantities higher than permitted levels can cause adverse effects. Besides being carcinogenic as well as teratogenic, malachite green can cause infections, damage to vital organs and developmental disorders [11,13]. So, the effective treatment of the discharged malachite green content in waterbodies from various sources is inevitable. Being regarded as one of the most dangerous dye pollutants, malachite green requires a selective and highly effective removal strategy.

Several water treatment techniques such as reverse osmosis [14], ultrafiltration [15,16], coagulation-flocculation [17], photocatalysis [18,19], adsorption [20–23], advanced oxidation process etc. are used for the removal of pollutants from water sources [9,24,25]. Some of these techniques are found to be effective for the removal of Malachite

* Corresponding author.
E-mail address: pperiyat@kannuruniv.ac.in (P. Periyat).

Spent zinc-carbon battery derived magnetically retrievable Fenton-like catalyst for water treatment - A circular economical approach

Deepak Joshy [a], Chamundi P. Jijil [a], Yahya A. Ismail [a], Pradeepan Periyat [b,*]

[a] Department of Chemistry, University of Calicut, Kerala 673635, India
[b] Department of Environmental Studies, Kannur University, Kerala, India

A R T I C L E   I N F O

A B S T R A C T

Discarded zinc-carbon batteries were effectively recycled into magnetically retrievable nanostructures which can perform dual roles as adsorbent and Fenton-like catalysts. The developed nanostructures were made exclusively from various components of spent zinc carbon batteries. The otherwise thrown-away discarded zinc-carbon batteries were thus given a novel role in water treatment. The adsorbent/catalyst design consists of MnO$_2$ and Fe$_3$O$_4$ cores surrounded by a shell of mesoporous ZnO. The adsorption and Fenton-like catalytic performance of the developed nanostructures were studied in detail by employing Methylene blue (MB), Rhodamine B(RB), Methyl orange (MO), and Congo red (CR) as the model pollutants. Various factors influencing the adsorption and catalytic activity were investigated and a detailed mechanism was thereby proposed for the degradation of model pollutants. Thus, a novel approach of Fenton-like catalyst synthesis was introduced emphasizing the principles of the circular economy. The spent zinc-carbon battery-derived adsorbents/Fenton-like catalysts are found to be highly effective, affordable, easy to use, and easy to regenerate.

1. Introduction

Dyes are one of the largest classes of organic compounds responsible for water pollution. The dyeing of plastic, textile, and printing industries is mainly responsible for expelling the dyes into water resources. The high chemical stability and non-biodegradability of these molecules make them potentially harmful to humans and aquatic life. Besides the dye molecules; pharmaceutical drugs, pesticides, and other harmful organic compounds are also present at alarming levels in water sources. The dye molecules can be taken as model pollutants representing various classes of water contaminants. Various strategies such as adsorption [1], photocatalysis [2], ultrafiltration [3], and Advanced Oxidation Process (AOP) [4,5] are in practice for the removal of these pollutants from water. Among the various AOPs available, one of the promising and widely used methods is Fenton-like catalysis [6]. Fenton-like catalysis is the modified version of the Fenton reaction; which is the aqueous phase oxidation process in the presence of ferrous ions and H$_2$O$_2$ [7–9]. The process involves the generation of hydroxyl radicals which are capable of degrading organic pollutants in water. However, conventional Fenton reactions have a narrow pH range of activity, an ineffective Fe^{3+}-Fe^{2+} redox cycle, and production of iron sludge under

acidic conditions; which reduces their catalytic activity [7,10]. Heterogeneous Fenton-like catalysts were introduced to overcome the limitations of Fenton catalysts. Fenton-like catalysis can be regarded as an environmentally friendly heterogeneous process capable of generating a large amount of reactive oxygen species (ROS) which can degrade organic contaminants into CO$_2$, H$_2$O, and various other inorganic species [6]. Heterogeneous Fenton-like catalysis can ensure a wide pH range of activity, minimum input of chemicals, better regeneration of catalysts, and minimal amount of iron sludge generation [8–10]. Besides the most commonly employed Fe^{3+} containing iron-based catalysts, several other transition metals like Ce, Mn, Cu, and Co which are capable of showing multiple oxidation states are also used as heterogeneous Fenton-like catalysts. Fe$_3$O$_4$ forms a major component of several Fenton-like catalysts [11,12] . The presence of transition metals such as Mn [13–17], Ce [18,19], and Cu [20–22] along with conventional Fenton-like catalysts can further enhance the catalytic activity by taking part in hydroxyl radical generation and by speeding up the Fe^{3+} to Fe^{2+} conversion [10]. The association of transition metals like Mn, Ce, and Cu with Fe$_3$O$_4$ can yield highly stable, non-toxic, and economically affordable Fenton-like catalysts [19,20,23,24].

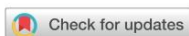As we look from a circular economy perspective, the development of

---

PAPER

Check for updates

Colour tunable cool pigments based on TiZn$_2$O$_4$ inverse spinels†

Deepak Joshy,[a] Chamundi P. Jijil,[a] Sheethu Jose,[b] Yahya A. Ismail [iD][a] and Pradeepan Periyat [iD] *[c]

A new class of near-infrared (NIR) reflecting yellow and orange cool pigments based on TiZn$_2$O$_4$ inverse spinels were synthesized. The colour tuning in pure TiZn$_2$O$_4$ was made possible by the substitution of octahedral Zn^{2+} ions by Cu^{2+} and Fe^{3+} ions separately. By the incorporation of Cu^{2+} and Fe^{3+} ions into the inverse spinel lattice in varying amounts, a series of pigment compositions having colours ranging from greenish-yellow to reddish-brown was obtained. The developed pigments exhibited moderate to high NIR reflectance ranging from 47.61 to 87.81%. The TiZn$_2$O$_4$ based NIR reflecting pigment provided an interior 4.8 °C cooler than an uncoated roofed interior. Cu^{2+} and Fe^{3+} doped TiZn$_2$O$_4$ systems were found to be highly stable and eco-friendly cool pigment candidates capable of achieving better thermal conditioning and impressive energy conservation.

Introduction

Colour plays a crucial role in conveying information, creating memories, determining moods, and even in decision making. In such a way, inorganic pigments capable of imparting colours also have an effect on us. There are a wide range of inorganic pigments available in the market spanning over a broad range of colours.[1,2] The investigations for more attractive and affordable pigments with better characteristics are still on. The development of environmentally benign inorganic pigments is one of the prime objectives of pigment manufacturers. The presence of elements such as Cd, Cr and Pb in pigment compositions is discouraged nowadays.[3,4] Lead tin oxide (PbSnO$_3$), cadmium sulfide (CdS), nickel titanate (NiTiO$_3$), Al$_2$O$_3$:Cr^{3+} (corundum), cadmium red (CdS:CdSe), *etc.* are some of the conventional inorganic pigments in the yellow-orange-red colour range in use.[5–9] The presence of heavy metals in these pigments is a deterrent to their commercial use. Such pigments can cause serious health and environmental hazards.[10,11] Synthesis of efficient substitutes for hazardous pigments without compromising the optical characteristics and stability is one of the challenges faced by manufacturers. Environmental friendliness, economic viability and high stability are the main objectives of present-day pigment research.[12–15] Apart from the aesthetic aspects, the functional properties of pigments such as solar reflectance, magnetic nature, corrosion inhibition, *etc.* are

also under exploration.[1,16] Earth's temperature has risen by 0.18 °C per decade since 1981.[17] The rising global temperature will lead to a climatic catastrophe if left unaddressed. About 52% of the solar spectrum consist of NIR.[18] These NIR radiations are responsible for the heat build-up from solar radiation. To deal with the heat build-up inside buildings, cooling facilities which consume an immense amount of energy are in use. Here arises the significance of NIR reflecting cool pigment coatings, which has an instantaneous effect as well as a long-term impact on rising global temperature.[19,20] The instant effect is nothing but the cooler interiors provided by the NIR reflecting pigment-coated buildings even in the midst of high solar irradiance. The long-term impact occurs from the energy conserved by the utilization of cool coatings instead of air conditioning and other cooling appliances. In the long run, conservation of the energy spent on cooler interiors can lead to a more sustainable and eco-friendly mode of energy utilization.

We have chosen the less explored TiZn$_2$O$_4$ inverse spinel system as our parent material for investigation.[21] By incorporating Cu^{2+} and Fe^{3+} ions into the TiZn$_2$O$_4$ lattice, we have developed a series of pigment compositions with colours ranging from greenish-yellow to reddish-brown. Here we report TiZn$_2$O$_4$-based pigments as affordable, high NIR reflecting and eco-friendly alternatives to many of the environmentally malignant and high-cost commercial pigments.

Experimental

Materials

Zinc nitrate (Zn(NO$_3$)$_2$·6H$_2$O, Alfa Aesar, 98%), titanium isopropoxide (Ti(OCH(CH$_3$)$_2$)$_4$, Aldrich Chemistry, 97%), cupric

[a] Department of Chemistry, University of Calicut, Kerala, 673635, India
[b] Department of Chemistry, Central University of Kerala, 671316, India
[c] Department of Environmental Studies, Kannur University, Kerala, India.
  E-mail: pperiyat@kannuruniv.ac.in